Evaluation of Surficial Non-Liquefiable Soil Layer Impacts on Liquefaction Surface Manifestation of the West Tennessee Area Based on Finite Difference Methods

By

Hamed Tohidi

A Dissertation

Submitted in Partial Fulfillment of the

Requirements for the Degree of

Doctor of Philosophy

Major: Civil Engineering

The University of Memphis

Fall 2022

Acknowledgements

I really and truly appreciate all the support I received from the Civil Engineering Department at the University of Memphis during the completion of my doctoral degree. Foremost, I would like to thank from the bottom of my heart my advisor, Dr. David Arellano, for his continuous support, patience, motivation, and immense knowledge. His guidance helped me in all the steps of researching and writing this dissertation. I could not have imagined having a better advisor for my Ph.D. study. Besides my advisor, my gratitude and appreciation go to my Ph.D. committee: Dr. Chris Cramer, Dr. Ashraf Elsayed, Dr. Roger Meier, and Dr. Shahram Pezeshk, chair of the Civil Engineering Department who provided many opportunities for me during my time as a graduate student at the University of Memphis.

I owe a deep sense of gratitude to Dr. Chris Cramer, Center for Earthquake Research and Information, for his kind and unlimited support during my dissertation. I strongly acknowledge his cooperation in developing the liquefaction hazard maps for this study.

I would also like to thank the Department of Housing and Urban Development (HUD). This study was partially supported by a Department of Housing and Urban Development National Disaster Resilience Award.

Finally, my deepest gratitude goes to my family for supporting me throughout my Ph.D.

Abstract

An investigation of the impact of shear strength and thickness of non-liquefiable soil layers on the surface manifestation of liquefaction based on finite difference numerical methods and to investigate the liquefaction potential of the West Tennessee area was performed by (1) analyzing liquefaction potential of Lake, Dyer, Lauderdale, and Tipton Counties, which are in West Tennessee and within or near the New Madrid Seismic Zone, based on the liquefaction potential indices of LPI and LPI_{ISH} methods; (2) developing a numerical model to perform liquefaction analysis ; (3) validating the developed numerical model in FLAC based on the evaluation of New Zealand data and observations; (4) performing sensitivity analysis of the overall FLAC model to shear strength and thickness of non-liquefiable soil layers; (5) adjusting the LPI_{ISH} procedure to incorporate the effects of shear strength and thickness of non-liquifiable soil layers based on the numerical model and sensitivity results; (6) performing liquefaction potential analysis of West Tennessee based on the LPI_{ISH}.

A comparison of the LPI- and LPI_{ISH}-based Liquefaction Probability Curves (LPCs) for the probability of LPI and LPI_{ISH} exceeding 5, which provides the probability that liquefaction surface manifestation can occur based on the threshold of 5, revealed that the probability of liquefaction surface manifestation provided by the LPI_{ISH} method is significantly lower than the probability of liquefaction surface manifestation provided by the LPC based on the LPI method, mainly at higher ratios of PGA/MSF, i.e., more intense earthquake scenarios for the West Tennessee Area. The results of this study indicate two primary reasons that the LPI-based LPC predicts a higher probability of liquefaction surface manifestation than the LPI_{ISH}-based LPC. First, the LPI_{ISH} method includes the impact of non-liquefiable layers on liquefaction surface manifestation by incorporating a limiting non-liquefiable layer thickness whereby surficial

manifestation is not expected to puncture through the non-liquefiable layer regardless of the thickness of the underlying liquefiable layer while LPI does not consider the impact of non-liquefiable soil layers. Second, LPI_{ISH} incorporates a power-law depth weighting function that provides for shallower liquefiable layers to contribute more to surficial manifestation than deeper layers. Therefore, because the weighting function between the two methods is based on different statistical methods, the contribution of soil layers to liquefaction surface manifestation is different between LPI and LPI_{ISH} methods. Additionally, the results of the numerical analysis of this study using FLAC software show that liquefaction surface manifestation occurrence is very sensitive to the thickness and shear strength of upper non-liquefiable soil layers. The LPI_{ISH} method is adjusted in this study by considering the impact of shear strength and thickness of upper non-liquefiable layers and a new LPC is developed for the West Tennessee area. By comparing the adjusted LPI_{ISH}-based LPC with LPI_{ISH} and LPI-based LPCs in this study, it is shown that the adjusted LPI_{ISH}-based LPC predicts a liquefaction probability significantly different than LPI and LPI_{ISH}-based LPCs.

Table of Contents

LIST OF TABLES

LIST OF FIGURES

CHAPTER 1. INTRODUCTION

This chapter presents a general discussion of this study followed by the current state of practice, problem statement, research goal and objectives, research approach, and the organization of this dissertation.

1.1 General Discussion of The Topic

Earthquakes cause soil liquefaction, which leads to serious damage all around the world, especially in areas near major fault zones. Liquefaction is defined as the development of excess pore water pressure in loose saturated granular soil layers due to seismic shaking. During AN earthquake there is not enough time for excess pore pressure to dissipate, so the soil loses its effective stress, triggering liquefaction. The soil no longer has high strength and stiffness, so it behaves as a liquid and starts to flow. In the absence of a thick non-liquefiable crust, the liquefied soil may flow to the ground surface, or if the upper layer has a high shear strength and the liquefied soil cannot penetrate through it to the ground surface, it may flow laterally. The parameters of ground shaking, as well as the density and initial effective stress of the soil, all play a role in whether or not liquefaction occurs and the extent of the liquefaction. Other parameters that impact the possibility of liquefaction triggering include soil type, soil fabric, age, and the orientation and amounts of pre-earthquake shear forces (State of the art and practice of earthquake-induced soil liquefaction and its consequences, 2021). The other important parameter that must be considered in the liquefaction potential analysis of any area is the near-surface geology and topography of the area. For instance, the West Tennessee area studied in this research consists of three primary geologic units (Lowlands, Intermediates-terraces, and Uplands) that differ in their elevation and near-surface geology. For this study, the liquefaction potential analysis is limited to the Lowlands

unit because it is the most liquefaction-prone geologic unit in West Tennessee and many liquefaction features have been observed in this area.

Liquefaction is a major source of damage during or shortly after earthquakes. Therefore, evaluation of the liquefaction potential of areas near major seismic zones is important. One of the most common ways of presenting the liquefaction potential of any region is liquefaction hazard maps. Detailed liquefaction hazard maps can be developed based on a combination of liquefaction potential indices and the geology of any specific region. Different liquefaction potential indices consider different criteria in the evaluation of liquefaction severity at a soil profile location. The main difference between liquefaction potential indices is a consideration of the impact of non-liquefiable soil layers on liquefaction surface manifestation.

The West Tennessee area is located within and adjacent to the New Madrid Seismic Zone, which is one of the major seismic zones and a potential source of earthquakes in the southern and midwestern United States. As part of a five-year seismic and liquefaction hazard mapping project for four western Tennessee counties (Lake, Dyer, Lauderdale, and Tipton) began in 2017 under a Disaster Resilience Competition grant from the U.S. Department of Housing and Urban Development (HUD) to the State of Tennessee, the liquefaction potential index (LPI) developed by Iwasaki (1978-1982) and the modified LPI procedure known as $LPI_{ISH,}$ developed by Maurer et al. (2015), have been utilized to analyze liquefaction potential and to develop liquefaction hazard maps. In Chapters 2 and 3, more details will be provided about these frameworks.

1.2 Current State of Practice

Many regions in the world have experienced soil liquefaction and its consequences. Some of those regions are Japan, New Zealand, the United States, and Nepal. For example, earthquakes

in 1811 and 1812 triggered severe liquefaction across a 150-kilometer length of the Mississippi River from the Memphis area north (State of the art and practice of earthquake-induced soil liquefaction and its consequences, 2021). In 1886, an earthquake in Charleston, South Carolina, produced significant liquefaction and ground displacements. During the 1964 earthquake in Alaska, liquefaction may have led to tsunami deaths by undermining delta fronts. In 1971, liquefaction nearly caused a dam to overtop and the reservoir at the terminal of the Los Angeles Aqueduct above the San Fernando Valley to discharge, flooding thousands of homes below the dam. The city of Kobe, Japan, has yet to recover economically from the 1995 Hyogo-ken Nanbu earthquake's liquefaction-related devastation to the city's port. During the 2010-2011 earthquake series in Christchurch, New Zealand, liquefaction resulted in the destruction of 15,000 houses; the most damaging earthquakes were in the range of magnitude of 6 to 7 with a mean of 6.2 (State of the art and practice of earthquake-induced soil liquefaction and its consequences, 2021).

So, according to the previous paragraph, evaluation of the liquefaction probability of areas susceptible to earthquakes can prevent and mitigate many life losses, infrastructure collapses, and economic damages. In the past 60 years, various methods have been developed to predict the liquefaction probability. Most of them are still being used by researchers, although many of them have been improved since then. Liquefaction evaluation methods are of two types: those which evaluate the liquefaction triggering potential and those which predict the consequences of liquefaction occurrence (State of the art and practice of earthquake-induced soil liquefaction and its consequences, 2021).

Liquefaction and its repercussions are still one of the most active fields of geotechnical engineering study and development. In 1998, the technical community agreed to employ an empirical stress-based approach for liquefaction triggering assessment known as the "simplified

method," which was first established in 1971. This is still the most widely utilized strategy in practice. By 2004, however, credible organizations had proposed improvements to the procedure, with many of them focusing on two different approaches. Both of those alternate ways have now been refined, and new methods and adjustments have been proposed. Practitioners must now choose from a variety of strategies, often without first recognizing their limitations (State of the art and practice of earthquake-induced soil liquefaction and its consequences, 2021).

The current state of practice on liquefaction triggering assessment is limited, for example, with the degree of saturation below the groundwater table, at great depths, beneath the sloping ground, in gravelly soils, in soils with a significant component of fine-grained particles (i.e., silt and clay), in Holocene-age soils due to aging effects, or in Pleistocene-aged (and older) soils. There is a scarcity of evidence to back up processes for estimating the effects of liquefaction triggering. There are significant ambiguities in the application of methodologies to forecast liquefaction triggering and its repercussions (State of the art and practice of earthquake-induced soil liquefaction and its consequences, 2021).

1.3 Problem Statement, Research Goal and Objectives

From the results of the HUD project on liquefaction hazard analysis of West Tennessee for the four counties of Lake, Dyer, Lauderdale, and Tipton, it has been observed that the LPI- and LPI_{ISH}-based liquefaction hazard maps are significantly different from each other in all four counties and for all geologic units. The LPI_{ISH}-based liquefaction hazard maps show a lower probability of liquefaction than the LPI-based liquefaction hazard maps. The main reason for the difference is the impact of non-liquefiable soil layers on liquefaction surface manifestation that is considered in the LPI_{ISH} framework.

Additionally, both the LPI and LPI_{ISH} methods have some limitations that will be presented later in this proposal. One key limitation of both the LPI and LPI_{ISH} methods is that neither considers the effect of soil shear strength. Therefore, the goal of this study is to evaluate liquefaction potential by considering the impact of shear strength and thickness of non-liquefiable soil layers on the surface manifestation of liquefaction based on finite difference numerical methods. This study will provide detail liquefaction hazard analysis in West Tennessee by considering the impact of thickness and strength of non-liquefiable soil layers. The goal is to investigate the impact of the upper non-liquefiable soil layer and thickness on the liquefaction surface manifestation potential of a liquefiable layer properly in stratified soil profile.

1.4 Research Approach

Initially, this study investigates the liquefaction surface manifestation potential of the West Tennessee area using the current liquefaction potential indices of LPI and LPI_{ISH} combined with the simplified procedure to develop the liquefaction probability curves and liquefaction hazard maps. A comparison will be made between the results of different methods for a better understanding of the impact of non-liquefiable layers on the liquefaction potential of a soil profile.

In the next step of the analysis, this study will numerically evaluate the impact of non-liquefiable soil layers on the liquefaction surface manifestation potential of liquefiable soil layers in stratified soil profiles by considering the shear strength and thickness of different soil layers. This study employs the Fast Lagrangian Analysis of Continua (FLAC) tool. First, the model is developed in FLAC, and then it is calibrated based on actual earthquakes and site observations with liquefaction surface manifestation records. Furthermore, the sensitivity of the model to different soil parameters including thickness and shear strength will be investigated. Based on the

numerical analysis results, a correlation between thickness and shear strength of soil layers will be developed to consider the impact of both thickness and shear strength of different soil layers in a soil profile on liquefaction surface manifestation.

1.5 Dissertation Organization

This dissertation is set out as follows: Chapter 2 provides a literature review on liquefaction that includes the simplified method of liquefaction analysis, liquefaction potential indices including the LPI and LPI_{ISH} methods, and an overview of the finite difference and finite element numerical methods related to liquefaction analysis. Chapter 3 is "Methodology" which goes through the verification of the liquefaction analysis of west Tennessee, the introduction of the geology of the study, the LPI and LPI_{ISH} analysis of the West Tennessee area, followed by the finite difference numerical model as well as verification of the written FLAC code and calibration of the model for this study by performing liquefaction analysis of various sites. Chapter 3 will also go through the methodology of analysis of shear strength and thickness of different soil layers. Chapter 4 summarizes the results of LPI- and LPI_{ISH}-based liquefaction analysis of West Tennessee followed by sensitivity analyses and correlation of shear strength and thickness of different soil layers with liquefaction surface manifestation. Finally, Chapter 5 outlines the key conclusions of this study and suggestions for possible future studies.

CHAPTER 2. REVIEW OF LIQUEFACTION EVALUATION PROCEDURES

The purpose of this chapter is to introduce liquefaction and its consequences, the background of liquefaction triggering evaluation methods, and an introduction to the numerical methods of liquefaction analysis that will be used in this study.

2.1 Liquefaction

Liquefaction is one of the consequences of an earthquake in which a loose saturated soil layer loses shear strength because of the development of excess pore water pressure from the cyclic stress imposed by the earthquake. Due to the build-up of pore pressure in the soil profile during the dynamic loading of an earthquake, the effective stress decreases. In the other words, due to the upward propagation of shear waves of the earthquake from bedrock through the soil profile in a short amount of time, there is not enough time for excess pore water pressure that develops due to cyclic shaking to dissipate. Therefore, excess pore pressure builds up within the soil pores. Equation (2.1) provides the shear strength of soil based on the Mohr-Coulomb failure criterion, and Equation (2.2) is the general equation for computing effective stress in soil.

$$\tau = c' + \sigma' tan\emptyset' \tag{2.1}$$

$$\sigma' = \sigma - u \tag{2.2}$$

where c' is soil effective cohesion, σ' is vertical effective stress, $\emptyset'$ is drained friction angle, u is pore water pressure, τ is shear strength, and σ is total vertical stress. Equation (2.1) indicates that the shear strength of soil is dependent on the effective stress in the soil. Equation (2.2) indicates that the effective stress decreases with an increase in pore water pressure. Thus, during an

earthquake, if excess pore water pressure increases, effective stress decreases and the shear strength decreases as well. Liquefaction occurs when the increase in excess pore water pressure results in zero effective stress, which is the condition that the soil particles are no longer in contact. For soils with no effective cohesion such as sands, when excess pore water pressure results in zero effective stress, shear strength is also zero and the soil behaves like a liquid.

Sladen et al. (1985) define soil liquefaction as follows:

"Liquefaction is a phenomenon wherein a mass of soil loses a percentage of its shear resistance, when subjected to monotonic, cyclic, or shock loading, and flows in a manner resembling a liquid until the shear stresses acting on the mass are as low as the reduced shear resistance."

The importance of soil liquefaction was first recognized by Casagrande (1936), however, the main progression in the analysis of soil liquefaction due to seismic loading was started in 1964 after the catastrophic Niigata, Japan and Anchorage, Alaska earthquakes. On Friday, March 27, 1964, a strong seismic motion of 9.2 Richter, with a rupture approximately 25 km under the surface, shook Alaska for 4.5 minutes and the earthquake destroyed/damaged numerous bridges and buildings and caused massive landslides. The other earthquake of 1964 that brought soil liquefaction to the attention of researchers was the strong earthquake of June 16, 1964, with a magnitude of 7.5, in Niigata, Japan. During the Niigata earthquake, massive sand liquefaction caused irretrievable damage to more than ten thousand buildings as well as bridges, highways, and utilities. Since 1964, soil liquefaction has become one of the most interesting topics in geotechnical engineering all around the world, and to date, after 56 years, soil liquefaction is still being studied based on different empirical, experimental, and numerical analyses.

Generally, the main consequences of soil liquefaction are lateral spread, ground oscillation, loss of bearing capacity, flow failure, ground settlement, sand blow, and sand dike (National

Research Council, 1985; Robertson et al., 1992; Tuttle et al., 2018). A general description of the soil liquefaction consequences is briefly defined next.

- Lateral Spread: occurs when soil liquefaction causes movement of sloping ground laterally. According to Varnes (1978), lateral spread is the most common result of soil liquefaction. Tuttle et al. (2002a) provide an example of lateral spread that happened in India (Figure 2.1).

Figure 2.1. Lateral spread example (from Tuttle et al., 2002a).

- Ground oscillation: occurs on flat grounds where the liquefied layer oscillates back and forth as a ground wave shape. It occurs on flat ground due to inertial forces applied above or within the liquefied zone (Youd, 2003) as shown in Figure 2.2.

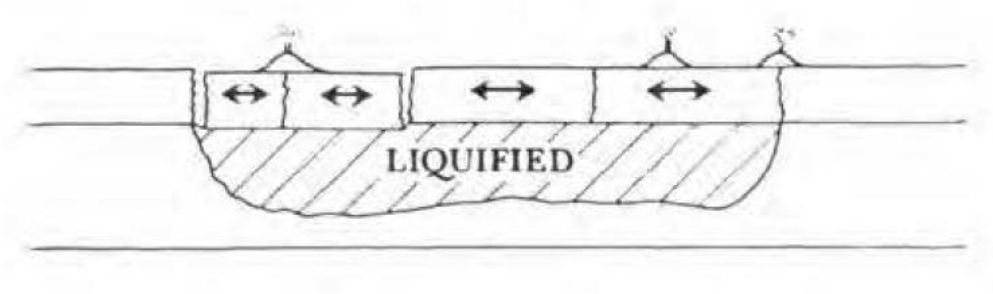

Figure 2.2 Schematic of ground oscillation due to soil liquefaction (After Youd, 1993).

- Loss of bearing capacity: bearing capacity failure because of a decrease in soil shear strength is another common consequence of liquefaction that causes building settlement and tilting. The near-surface liquefied layers cause the soil supporting a foundation to lose bearing capacity, consequently, settlement and overturning of structures occur (Figure 2.3).

Figure 2.3. Bearing capacity failure due to Niigata earthquake, 1964.

- Flow failure: Robertson (2010) presents that flow failure is the result of lateral movements of a sediment layer that has been liquefied on sloping ground steeper than 3^{o}. Additionally, flow failure is known as the most catastrophic liquefaction consequence because it can occur on land or underwater and it displaces a large mass of soil several miles at a velocity

of tens of miles per hour (Tuttle et al. 2018, USGS). Figure 2.4 illustrates an example of flow failure.

Figure 2.4. Sand heap landslide on 27 March 2020 at the Guizhou Commercial Concrete Co., Ltd. in Guiyang (Image from News 163, Source Media: Xinhua Net Editor: Huang Jiadi_NNB6466).

- Ground settlement: occurs due to the dissipation of excess pore water pressure that takes place after the earthquake.
- Sand blow: due to the occurrence of liquefaction in the soil layers, the upward seepage ejects sand on the ground surface as the shape of a cone; it is also known as a sand volcano (Tuttle et al. 2018) (see Figure 2.5).
- Sand dike (filled fissure): sand dike occurs when water pressure forces a liquefied sand layer upward. In the other words, it is the path of the sand blow (see Figure 2.5).

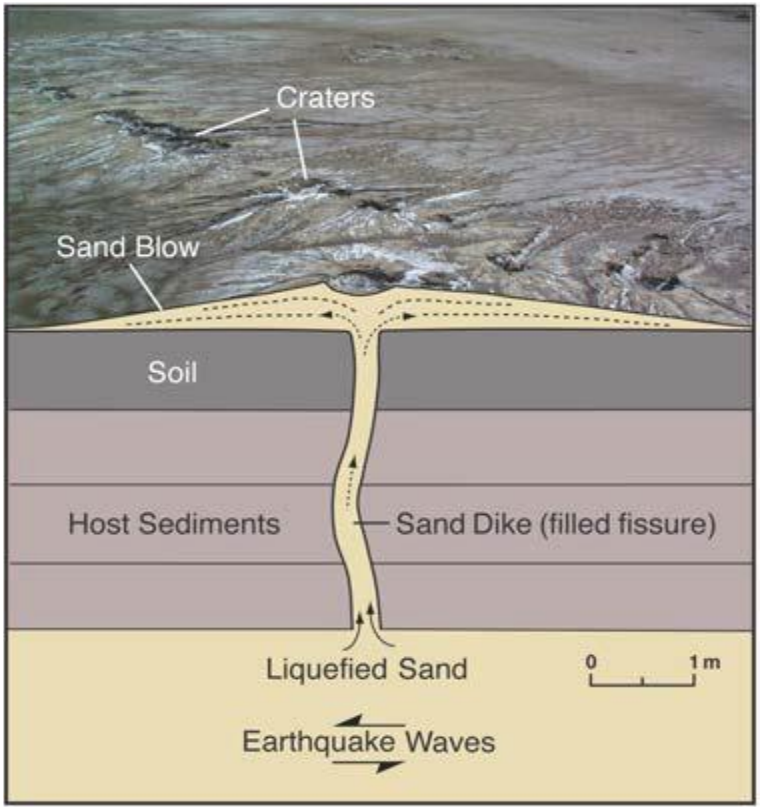

Figure 2.5. Overview of sand blow and sand dike (from NUREG-2015).

In this study, numerical analyses will be performed to model liquefaction surface manifestation (i.e., sand blows).

2.2 New Madrid Seismic Zone

The West Tennessee area is located within and adjacent to the New Madrid seismic zone, which is one of the major seismic zones in the United States. The New Madrid seismic zone potentially can impact the states of Illinois, Indiana, Missouri, Arkansas, Kentucky, Tennessee, Oklahoma, and Mississippi (see Figure 2.6). According to the Missouri Department of Natural Resources, the New Madrid seismic zone is the most active area in the United States and the fault line is 150 miles long. The New Madrid seismic zone is responsible for the huge and catastrophic earthquakes of 1811 and 1812 that occurred in Saint Louise, Missouri (USGS,

https://www.usgs.gov/programs/earthquake-hazards/new-madrid-seismic-zone). During 1811 and 1812, a sequence was generated by the New Madrid seismic zone, three of which were very large with magnitudes between 7 and 8. During the 1811 and 1812 earthquakes, liquefaction and the resulting lateral spreading were severe and widespread. Sand blows formed over an extremely large area of about 10,400 square kilometers. Effects of liquefaction extended about 200 km northeast of the New Madrid seismic zone in White County, Illinois, 240 km to the north-northwest near St. Louis, Missouri, and 250 km to the south near the mouth of the Arkansas River. In the New Madrid region, sand blows can still be seen on the surface today (USGS).

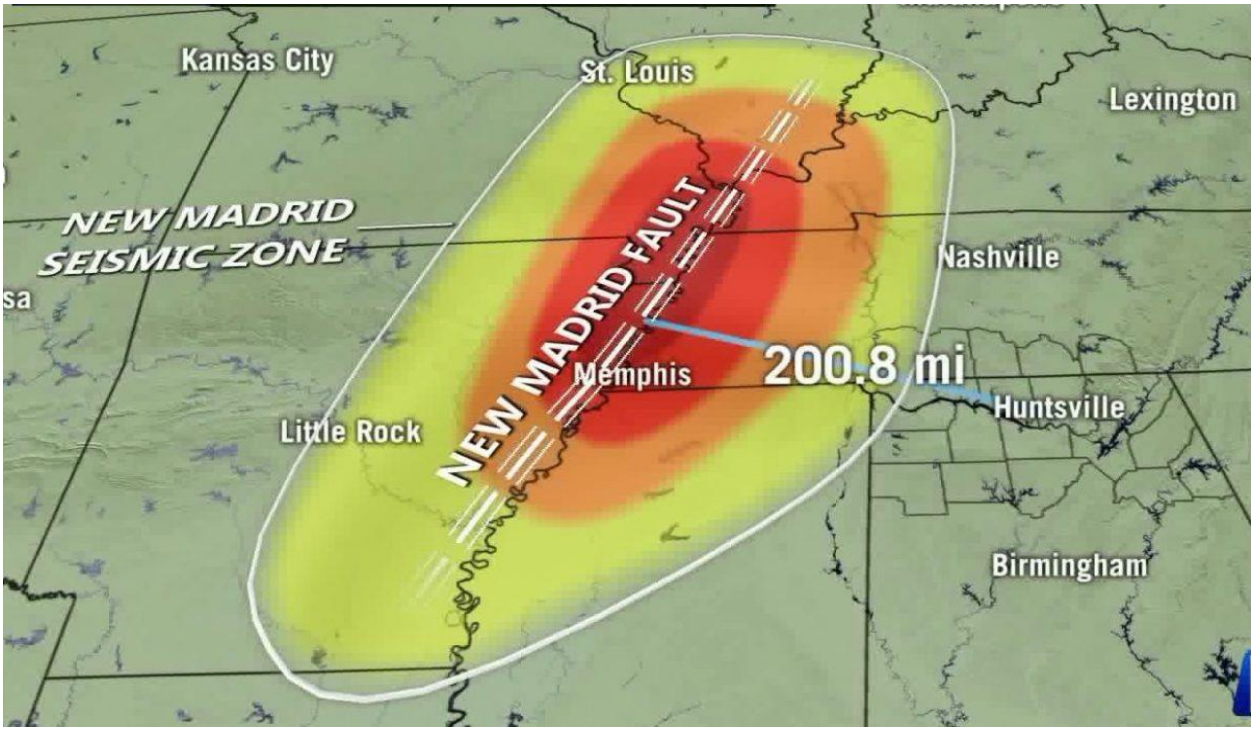

Figure 2.6. New Madrid fault zone (Six, 2021).

2.3 Evaluation of Liquefaction Triggering

This section covers the background and procedure of the simplified method of liquefaction analysis developed by Seed and Idriss (1971) that will be utilized in this study. This section will

also go through the relationship between the simplified method and liquefaction potential indices of LPI (Iwasaki, 1978-1982) and LPI_{ISH} (Maurer, 2015) as well as the detail of LPI and LPI_{ISH} methods that are used in this study.

2.3.1 Simplified Method of Liquefaction Analysis

After the Niigata and Alaska earthquakes (1964), Seed and Idriss (1967) developed a general simplified procedure to evaluate the soil liquefaction potential of cohesionless soils. They considered the following factors that impact liquefaction potential based on laboratory investigations and field observations:

- The characteristics of the soil.
    - The soil types.
    - The relative density or void ratio.
- The initial stresses acting on the soil.
    - The initial confining pressures.
- The characteristics of the earthquake.
    - The intensity of ground shaking.
    - Duration of ground shaking.

Considering the above factors, Seed and Idriss (1967) presented a four-step general procedure for evaluating liquefaction potential:

1. Determination of shear stress time history produced by the earthquake.
2. Conversion of the shear stress time history of the earthquake into an equivalent number of uniform stress cycles as a function of depth as shown by the cyclic stress developed for N cycles by the earthquake motions curve in Figure 2.7.

3. Estimation of the required number of cycles that induces liquefaction at various depths based on the cyclic triaxial lab tests of Sacramento River Sand using the equivalent number of uniform cycles from Step 2 as shown by the cyclic stress-causing liquefaction in the N cycles curve in Figure 2.7.
4. Determination of the liquefiable zones by comparing the shear stresses caused by the earthquake from Step 2 with the estimation of cycles that induce liquefaction from Step 3. As shown by the zone of liquefaction designation in Figure 2.7, the zone of liquefaction is the zone where the equivalent number of uniform stress cycles exceeds the cyclic stress-causing liquefaction.

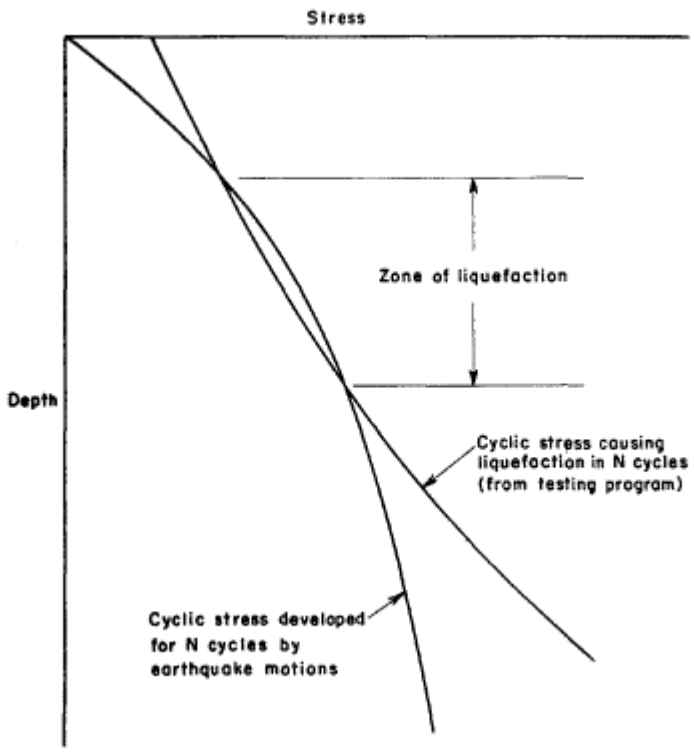

Figure 2.7. Method of evaluating liquefiable zone (from Seed and Idriss, 1967).

In 1971, Seed and Idriss presented the simplified procedure for evaluating liquefaction that consisted of three evaluations:

1. Simplified procedure for evaluating stresses induced by the earthquake.
2. Simplified procedure for evaluating stresses causing liquefaction.
3. Evaluation of liquefaction potential.

To evaluate the stresses induced by an earthquake, the simplified method consists of a relationship in which the maximum shear stress on the soil is defined as:

$$\tau_{max} = \frac{\gamma h}{g} \cdot a_{max} \tag{2.3}$$

where γ is the unit weight of the soil, h is the depth of the soil, g is gravity acceleration, and a_{max} is the maximum ground acceleration.

In reality, the soil column behaves as a deformable body and not as a rigid body, hence a coefficient of stress reduction by depth (r_d) has been applied to Equation (2.3) to compute the τ_{max} using Equation (2.4):

$$\tau_{max} = \frac{\gamma h}{g} \cdot a_{max} \cdot r_d \tag{2.4}$$

As shown in Figure 2.8, the magnitude of shear stress that occurs during an earthquake in the field varies from cycle to cycle. Based on the shear stress time history of the Niigata earthquake, Seed and Idriss determined that the average shear stress induced by the earthquake was about 65% of the maximum shear stress. Thus, they suggested a reduction of 0.65 to Equation (2.4) and the use of Equation (2.5) to estimate the average shear stress (τ_{ave}):

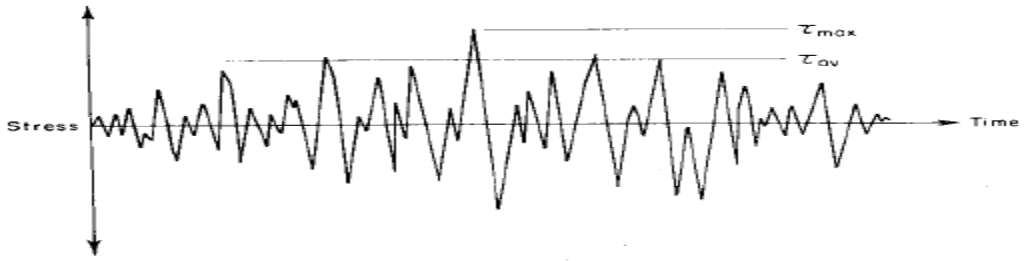

Figure 2.8. Shear stress time history of Niigata earthquake (Seed and Idriss, 1971).

$$\tau_{ave} = 0.65 \cdot \frac{\gamma h}{g} \cdot a_{max} \cdot r_d \qquad (2.5)$$

Based on the duration of the ground shaking as a function of earthquake magnitude, Seed and Idriss, using site response analysis, computed the shear stress variations at depths of 5, 15, 25, 35, and 45 ft. for the first 30 seconds of the earthquake. To determine if the shear stress variation causes liquefaction on Sacramento River sand at various depths, the actual stress time history of the earthquake had to be converted to a uniform number of stress cycles so that the equivalent series could be compared with lab test results under the same equivalent number of stress cycles. Using the obtained uniform number of shear stress cycles at each depth, Seed and Idriss determined the average magnitude of major stresses. The remaining smaller stress cycles (smaller than major stresses) were estimated to be equivalent to a number of uniform cycles according to the average magnitude of major stresses. In the other words, Seed and Idriss (1971), to compare the irregular stress cycles of the earthquake with the results of laboratory tests under uniform stress cycles by giving a weighting factor to each stress cycle of the earthquake, converted the irregular stress cycles of the earthquake to an equivalent uniform stress cycle. Thus, Seed and Idriss (1971) proposed a typical equivalent number of uniform stress cycles for various magnitudes as provided in Table 2.1.

Table 2.1. Equivalent number of uniform stress cycles for earthquake magnitudes of 7 to 8 determined by response analysis.

Earthquake Magnitude	Equivalent number of uniform stress cycles
7	10
7.5	20
8	30

The combination of values from Table 2.1 and Equation (2.5) provides a simplified procedure to compute the Cyclic Stress Ratio (CSR) induced by the stress of an earthquake at any depth. The CSR in the field was expressed as $\frac{\tau_{ave}}{\sigma_v'}$ and is given by:

$$CSR = \frac{\tau_{ave}}{\sigma_v'} = 0.65(\frac{a_{max}}{g})(\frac{\sigma_v}{\sigma_v'})r_d \qquad (2.6)$$

Evaluating stresses causing liquefaction is the second evaluation of the simplified procedure. To evaluate the stresses causing liquefaction, the results of the cyclic triaxial tests were expressed by the stress ratio of $\frac{\sigma_{dc}}{2\sigma_a}$ causing liquefaction in 10 and 30 cycles (for magnitudes of 7 to 8 from Table 2.1), in which σ_{dc} is the cyclic deviator stress and σ_a is the initial ambient pressure under which the sample was consolidated. Equation (2.7) provides the CSR that will result in liquefaction at a given depth, which is also interpreted as Cyclic Resistance Ratio (CRR) against CSR induced by the earthquake:

$$CRR = \left(\frac{\tau_{\mathrm{ave}}}{\sigma'_v}\right) = \left(\frac{\sigma\mathrm{dc}}{2\sigma\mathrm{a}}\right) Cr \frac{Dr}{50} \qquad (2.7)$$

where Cr is a correction factor of lab test data, and Dr is relative density.

The third evaluation of the simplified procedure for evaluating liquefaction consists of comparing the CSR and CRR values of Equations (2.6) and (2.7) respectively. If the CSR from Equation (2.6) is equal to or greater than the CRR of Equation (2.7) at a given depth, then

liquefaction at that depth is possible. The Factor of Safety (FS) at a given depth in a soil profile is a function of the simplified procedure (Seed and Idriss, 1971) and is determined using the equation:

$$FS = \frac{CRR}{CSR} \cdot MSF.K_{\sigma}.K_{\alpha} \tag{2.8}$$

in which *FS* is the factor of safety against liquefaction at a specific depth, *CRR* is the cyclic resistance ratio of soil against liquefaction as determined by Equation (2.7), *CSR* is the cyclic stress ratio due to cyclic loading of the earthquake and is computed by Equation (2.6), *MSF* is a magnitude scaling factor that corrects for magnitudes other than 7.5 and is computed using the revised relationship by Idriss (1999) as follows:

$$MSF = 6.9\exp\left(\frac{-M_W}{4}\right) - 0.06, M_W > 5.2 \tag{2.9}$$

$$MSF = 1.82, M_W \leq 5.2 \tag{2.10}$$

K_{α} in Equation (2.8) is a correction factor for the sloping ground, which is considered 1 in this study because the West Tennessee area consists of relatively flat terrain, and K_{σ} is an overburden correction factor for soil layers with overburden pressure of greater than 100 KPa, and is computed by:

$$K_{\sigma} = \left(\frac{\sigma'_{v0}}{P_a}\right)^{f-1} \tag{2.11}$$

where P_a is the atmospheric pressure and is equal to 100 KPa, and in $f - 1$, f is an exponent function in a range of 0.6-0.8.

The CRR of the simplified procedure of Seed and Idriss (1971) was initially based on the SPT resistance, i.e., SPT N-values. Since 1971, the CRR of the simplified procedure has been

extended to include Cone Penetration Test (CPT), Becker Penetration Test (BPT), Dilatometer Testing (DMT), and Shear Wave Velocity (V_s) measurements. In this study, the CRR is computed based on SPT N-values because of the availability of SPT data within the area of the study. The CRR procedure based on the SPT data of Youd and Idriss (2001) is given by:

$$CRR_{7.5} = \left(\frac{1}{34-(N_1)_{60CS}} + \frac{(N_1)_{60CS}}{135} + \frac{50}{(10((N_1)_{60CS})+45)^2} - \frac{1}{200}\right) \qquad (2.12)$$

where $(N_1)_{60CS}$ is corrected N-value for clean sand and is given by:

$$(N_1)_{60CS} = \alpha + \beta((N_1)_{60}) \qquad (2.13)$$

where α and β are functions of fines content (FC) and are estimated as provided in Table 2.2.

Table 2.2. Values of α and β for different ranges of FC.

Fines Content (FC)	α	β
FC ≤ 5 %	α = 0	β = 1.0
5%<FC <35 %	$\alpha = \exp\left[1.76 - \left(\frac{190}{FC^2}\right)\right]$	$\beta = \left[0.99 + \left(\frac{FC^{1.5}}{1000}\right)\right]$
FC ≥ 35%,	α = 1.2	β = 5

Note that for FC ≤ 5, $(N_1)_{60cs}$ is equal to $(N_1)_{60}$, which is the corrected SPT N-value for field conditions and is calculated by:

$$(N_1)_{60} = N \cdot C_N \cdot C_E \cdot C_B \cdot C_R \cdot C_S \qquad (2.14)$$

where N is the measured standard penetration resistance, C_N is the overburden correction factor, and is computed by $\left(\frac{P_a}{\sigma'_{v0}}\right)^{0.5}$, C_E is the hammer energy ratio correction factor, C_B is the borehole diameter correction factor, C_R is the rod length correction factor, and C_S is a correction factor for samplers with or without liners.

The calculated FS from the procedure explained in this section will then be utilized to compute the liquefaction potential indices which will be discussed in the following section.

2.3.2 Liquefaction Potential Indices

The primary purpose of the simplified method is to evaluate the potential of liquefaction triggering at some depth in a soil profile, but it does not evaluate or consider the potential for liquefaction manifestation at the ground surface. One of the most common ways to evaluate the severity of liquefaction surface manifestation is by combining liquefaction potential indices with the simplified method. Two of the main liquefaction potential indices considered in this study are:

1. LPI developed by Iwasaki 1978-1982 and,
2. LPI_{ISH} presented in Maurer's framework 2015.

To estimate the liquefaction severity of a soil profile at the ground surface, Iwasaki (1978-1982) proposed a liquefaction potential index, known as LPI, based on an evaluation of liquefied and non-liquefied sites of six earthquakes that occurred in Japan between 1891 and 1978. The LPI of Iwasaki evaluates the liquefaction potential of a soil column to a depth of 20 meters. That depth was chosen because the liquefaction of liquefiable layers below 20 m has a minor impact on liquefaction surface manifestation (Iwasaki, 1982). Iwasaki's method gives a weight of contribution to liquefaction surface manifestation to all liquefiable soil layers that is a linear function of depth. Iwasaki's method does not consider the impact of non-liquefiable soils within the soil profile. A liquefiable soil layer in Iwasaki's method was defined as saturated loose sandy soil. Iwasaki's LPI is expressed as follows:

$$LPI = \sum_{z=0}^{20m} F(z) \cdot w(z) \cdot dz \tag{2.15}$$

where z is the depth (0 to 20 m), dz is the differential increment of depth; $w(z)$ is the weighting function, which is equal to $10 - 0.5z$; and $F(z)$ is the severity. $F(z)$ is a function of Factor of Safety (FS) as provided by the following relationships: $F(z)=1 - FS$ for $0 \leq FS \leq 1$ and $F(z)=0$ for FS >1.

Ishihara (1985) assessed the influence of a non-liquefiable capping soil layer near the ground surface on the surficial manifestation of liquefaction of an underlying liquefiable soil layer. In Ishihara's method, a liquefiable layer was defined as a saturated loose sand layer with an SPT N-value less than 10. As shown in Figure 2.9a, he plotted observations of liquefaction surface manifestation using the thickness of the non-liquefied capping layer, *H1*, and the liquefied strata, *H2*. Ishihara proposed a single boundary curve between observed cases of liquefaction manifestation and cases of no observed manifestation to predict liquefaction surface manifestation as a function of *H1* and *H2* for peak ground acceleration (PGA) of 0.2g. Figure 2.9b shows boundary curves for additional earthquake PGAs. From the boundary curves shown in Figure 2.9b, for each specific PGA, there is an H_1 threshold above which liquefaction surface manifestations may not form, regardless of *H2* (Maurer, 2015). Figure 1b suggests a threshold *H1* of about 3 m for PGA of 0.2g and H_1 increases with PGA. However, a limiting surficial cap thickness is not included in the LPI procedure provided by Equation (2.15) nor is the shear strength of the non-liquefiable capping soil layer considered.

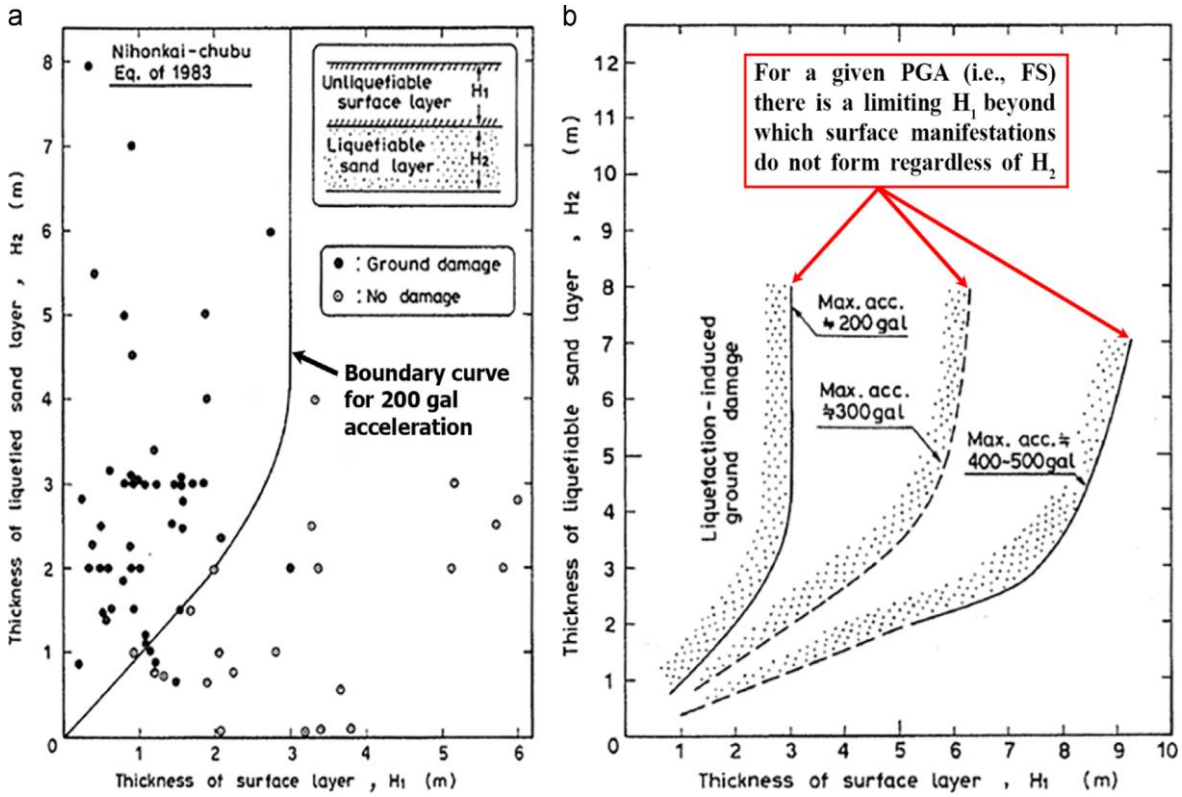

Figure 2.9. Liquefaction Boundary Curves a) for a single PGA value of 0.2g proposed by Ishihara, 1985 b) for different PGAs (after Ishihara, 1985) (Figure from Maurer et al., 2015).

Since the LPI procedure does not consider the characteristics of non-liquefiable soil layers such as thickness and strength on liquefaction ground surface manifestation, Maurer et al. (2014; 2015) indicated that Iwasaki's method generally overpredicted the severity of liquefaction manifestation based on observations of the Canterbury earthquakes of New Zealand. Moreover, Maurer et al. (2015) claimed that Ishihara's criteria are not the most suitable indicator of liquefaction damage observed in Canterbury due to the difficulty of representing multiple interbedded non-liquefiable layers within a site-specific soil profile as two simple layers. Thus, by modifying Ishihara's boundary curves, Maurer presented an alternative liquefaction potential index denoted as LPI_{ISH}. Maurer's framework is summarized in Equations (2.16) to (2.18).

$$LPI_{ISH} = \int_{H1}^{H1+H2} F(FS)\frac{25.56}{z}dz \tag{2.16}$$

$$F(FS) = \begin{cases} 1 - FS\ if\ FS \leq 1 \cap H1 \times m(FS) \leq 3 \\ 0 \qquad\qquad\qquad\qquad otherwise \end{cases} \tag{2.17}$$

$$m(FS) = \exp\left(\frac{5}{25.56(1-FS)}\right) - 1 \tag{2.18}$$

where *H1* and *H2* are the bounds of a liquefiable layer, *F(FS)* is the factor of safety-related function, *z* is depth, and *dz* is the differential increment of depth. The function *m(FS)* is an initial slope, unique to each boundary curve, for identification of liquefaction-induced damage and manifested at the ground surface (after Ishihara 1985) (Figure 2.9b). In Maurer's framework, each boundary curve is assumed to consist of two straight lines with slopes of m and ∞ (see Figure 2.10a and Figure 2.10b). The slope *m* can be utilized to relate *H1* and *H2* by $H2 = H1 \cdot m$ as can be seen in Figure 2.10. Thus, *m* provides a non-liquefiable soil layer thickness, *H1*, whereby surficial liquefaction manifestation may not occur.

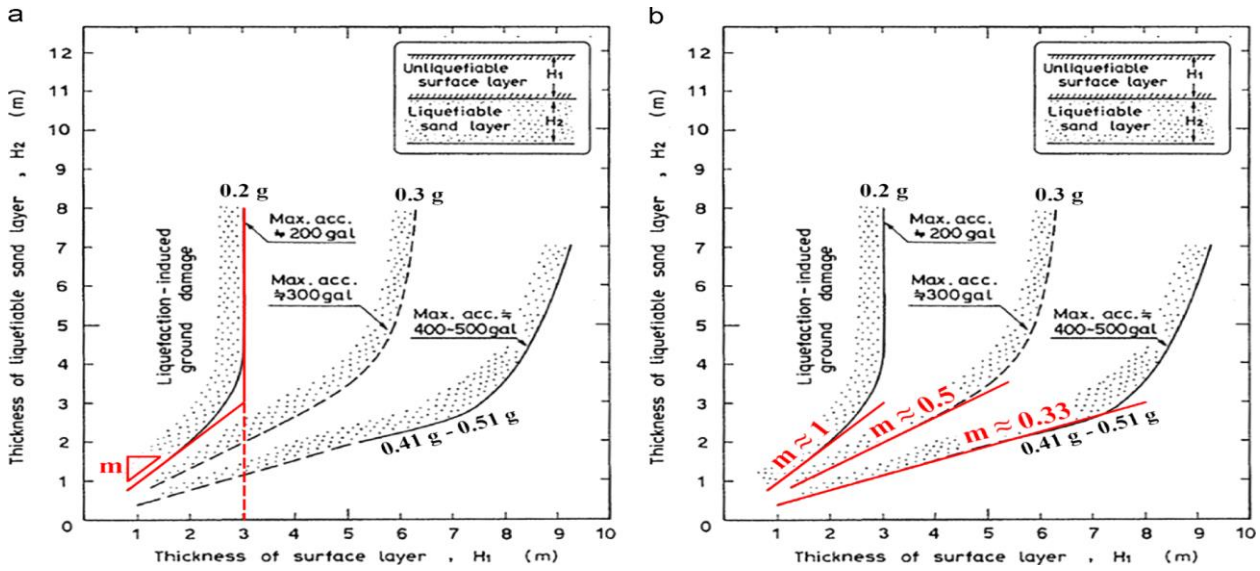

Figure 2.10. Unique slope of each boundary curve that relates H1 to H2 (Figure from Maurer et al., 2015).

The key differences between the LPI_{ISH} framework and the LPI framework are:

- LPI_{ISH} incorporates the concept of a limiting non-liquefiable cap layer thickness whereby surficial liquefaction manifestation may not occur.
- Inherently, the LPI method assumes that all liquefiable soil layers through a 20 m soil profile contribute to liquefaction surface manifestation as a function of depth.
- The LPI_{ISH} utilizes a power-law depth weighting function to represent the contribution of a liquefiable soil layer to surface manifestation instead of the linear depth weighting function that is used in the framework of Iwasaki's LPI (see Figure 2.11). In the LPI_{ISH} framework, shallower liquefiable layers at depths between 0 and 3 m, i.e., liquefiable layers closer to the ground surface, contribute more to the surficial manifestation of liquefaction than for depths between 3 and 20 m.

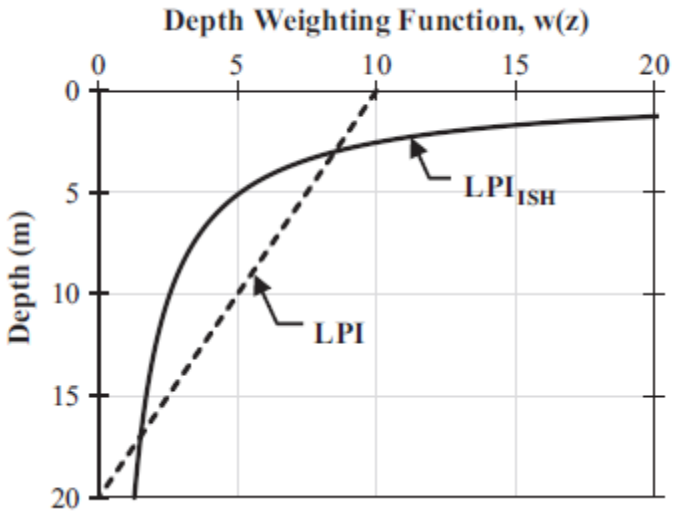

Figure 2.11. Depth weighting functions of LPI and LPI$_{ISH}$ (from Maurer 2015).

The LPI and LPI$_{ISH}$ methods have been used by various researchers to assess liquefaction hazards as well as the performance of these indices based on post-liquefaction surface manifestation evidence (Green, 2014; Maurer and Green, 2015; Maurer, 2016; Chung and Rogers, 2017; Rhodes, 2017). Green (2014), following the field observations from the Darfield 2010 and Christchurch 2011 earthquakes of New Zealand, indicates that the LPI framework is generally consistent in the prediction of moderate to severe liquefaction surface manifestations while there is inconsistency between the LPI and field observations of less severe liquefaction manifestations which could be improved by considering the impact of non-liquefiable crust characteristics.

Bowen and Jacka (2013), evaluated the performance of Ishihara's method and compared it with field observations of the Canterbury, New Zealand earthquakes. They concluded that the liquefaction predictions based on Ishihara's method may be unconservative in the prediction of no damage for the sites where thin liquefiable layers are near the ground surface because the observations from the Canterbury earthquakes revealed significant damages due to the liquefaction of thin liquefiable layers that were present near the ground surface of these sites.

Furthermore, Van Ballegooy et al. (2014) and Maurer et al. (2014) found the performance of LPI inconsistent with field observations in a significant number of site predictions in Christchurch, New Zealand. Additionally, Maurer and Green (2015) and Maurer (2016) evaluated the performance of LPI and LPI_{ISH}. They claim that the performance of LPI was found to be more inconsistent with field observations than LPI_{ISH} performance. LPI was found to overpredict liquefaction surface manifestation.

Other researchers have evaluated the performance of LPI in the prediction of liquefaction surface manifestation. Chung and Rogers (2017) found that the LPI tends to overpredict liquefaction surface manifestation. They propose that not considering the influences of non-liquefiable soils on liquefaction hazards may cause the overprediction of the LPI approach. Therefore, they suggest a liquefaction reduction number that is combined with LPI as a supplement to improve the performance of LPI.

Rhodes (2017) addressed the impact of non-liquefiable layers in a soil profile on liquefaction surface manifestation. She claims that "non-liquefiable crust thickness has a significant impact on whether liquefaction is manifested at the ground surface when liquefaction occurs in deeper layers". Additionally, she presented that the interaction between liquefiable and non-liquefiable soil layers has a predominant effect on the liquefaction potential of a soil column. In the simplified method and LPI of Iwasaki, it is assumed that soil layers act independently of each other.

In another study done by Bowen and Jacka (2013), from the observations of the Canterbury earthquakes, they presented that a non-liquefiable crust thicker than 3.5-4 m prevents liquefaction surface manifestation no matter how thick the lower liquefiable soil layer is. This conclusion is not considered in the methods of Iwasaki and Ishihara, which may result in overprediction of

liquefaction. Bowen and Jacka (2013) also claim that the impact of the thickness of liquefiable and non-liquefiable soil layers on liquefaction surface manifestation is even more significant than the impact of ground shaking intensity.

In summary although the two indices of LPI and LPI_{ISH} have been used by many researchers, both have some limitations. Some of the limitations of the LPI method are:

- It significantly overpredicts the probability of liquefaction, especially for sites having stratified soils consisting of both liquefiable and non-liquefiable soils.
- It is less applicable at sites with predominantly silty or clayey soils.
- It assumes that each liquefiable soil layer contributes to the damage potential at the ground surface without considering the impact of upper non-liquefiable soil layers near the ground surface.

Limitations of the LPI_{ISH} method are:

- Ishihara's boundary curve was based on observations of only two earthquakes with a limited range of ground accelerations.
- Although the method considers the impact of non-liquefiable layers, the influence of the capping and/or interbedded non-liquefiable layers on surficial manifestation is complex and further research is needed to fully understand the effects.
- It does not include the influence of the shear strength of non-liquefiable layers and applied stress imposed by the liquefiable layer on the non-liquefiable layer in the evaluation of liquefaction potential.

Furthermore, from the studies done by Ishihara (1985), Naesgaard et al., (1998), and Andersen et al., (2007) it can be concluded that the presence of a thick non-liquefiable layer with

high shear strength over a liquefiable layer can stop liquefaction surface manifestation even if liquefaction has occurred in the underlying liquefiable layer.

Thus, the focus of this dissertation is to evaluate the influence of shear strength and thickness of upper non-liquefiable layers and the applied stress imposed by the liquefiable layer on the non-liquefiable layer in the evaluation of liquefaction potential.

2.4 Numerical Methods Related to Liquefaction Analysis

In the past decade, in addition to experimental and empirical methods of liquefaction potential analysis, numerical methods have received significant attention from researchers. Some advantages of numerical methods include analyzing the interaction between soil layers, modeling water flow during analysis, monitoring the pore water pressure situation during analysis, and obtaining the impact of earthquake motion on soil properties. Due to these advantages, numerical methods have been utilized by many researchers to perform liquefaction analysis (Rhodes, 2017; Daftari, 2015; Ziotopoulou, 2010).

2.4.1 FEM and FDM Application in Geotechnical Engineering

In geotechnical engineering, numerical methods are defined in five categories: finite difference methods, finite element methods, discrete element methods, boundary element methods, and boundary/combined element methods. The most common numerical methods to evaluate liquefaction potential are Finite Difference Methods (FDM) and Finite Element Methods (FEM). The FDM and FEM are employed in different commercially available software programs to find a solution to engineering problems. For example, PLAXIS uses FEM numerical methods to solve geotechnical problems. FLAC (Fast Lagrangian Analysis of Continua) is a software tool that

utilizes FDM methods. Both FLAC and PLAXIS are common software programs that are utilized by geotechnical consulting firms. FLAC is the software that is employed in this study. FLAC programs are available to perform two-dimensional and three-dimensional analyses. The focus of this study is two-dimensional analysis. FLAC also has built-in material models such as Mohr-Coulomb, Elastic, Hoek-Brown, etc., to investigate the behavior of soil and rock. In FLAC, it is possible to change the mesh size of the model to fit it with the specific dynamic (earthquake) loading that is applied for dynamic analysis of liquefaction problems. An overview of FLAC is provided next.

2.4.2 Background of Numerical Analysis of Liquefaction

Numerical modeling has been utilized by many researchers to evaluate the impact of liquefaction on shallow foundations, deep foundations, building settlements, soil-structure interaction in liquefiable soils, etc., (Taiebat 1999, Elgamal et al., 2002, Chang et al., 2008, Caballero and Razavi, 2008, Shahir and Pak, 2010, Karamitros et al., 2013, Asgari et al., 2014, Mehrzad et al., 2016, Karimi and Dashti, 2016, Moghadam et al., 2017, Ziotopoulou and Montgomery, 2017, Forcellini, 2020, Karafagka et al., 2021, Özcebe et al., 2021). Besides numerical modeling, liquefaction analysis based on the physics of soil has been conducted in the study "Can geotechnical liquefaction indices serve as predictors of foundation settlement" done by Bullock and Dashti (2021).

All of the above-cited studies involved site-specific analysis and most of them were done in a fully liquefiable soil deposit without the presence of any non-liquefiable soils. For example, Liyanathirana (2002) presented a numerical model of liquefaction analyses of a complete saturated

soil deposit with the presence of no non-liquefiable soil layers. In another study, Liyanathirana (2007) numerically modeled soil liquefaction in sloping ground with all loose sand deposits.

However, to perform regional liquefaction hazard analysis, researchers typically utilize liquefaction potential indices and geology (Chung and Rogers, 2011, Cramer et al., 2008, Dixit and Jangid, 2012, Goda et al., 2011, Green et al., 2020, Holzer, 2008, Holzer et al., 2006, Hossain et al., 2020, Kayabasi and Gokceoglu, 2018, Kim et al., 2021, Lenz and Biase, 2007, Maurer et al., 2019, Maurer et al., 2014, Maurer et al.,2015, Muley et al., 2018, Papathanassiou et al.,2015, Rahman et al., 2015, SDonmez, 2003, Tint et al., 2018, Toprak and Holzer, 2003, Wang and Chen, 2018, Wang et al., 2017, Youd and Perkins, 1987, Zhang et al., 2016). Bullock and Dashti (2021) mention that liquefaction potential indices are common tools to evaluate the risk of liquefaction for both specific sites and regions. They also claim that because the liquefaction potential indices were generated based on liquefaction surface manifestation, their correlation with the evaluation of liquefaction damage to foundations is not as good as their correlation with land damage due to liquefaction.

According to the literature review that has been done for this research, numerical analysis of liquefaction has been conducted by many researchers to evaluate lateral spreading (Soroush, 2004), perform site response analysis for sites with liquefiable layers (Wu, 2014), perform numerical analysis of pore pressure generation during an earthquake (Vargas, 2015), perform numerical evaluation of liquefaction potential of a specific soil and compare the results with centrifuge tests on that specific soil (Byrne, 2004), evaluate flow slides due to liquefaction (Reid, 2013), evaluate the response of shallow foundations as a result of liquefaction (Mehrzad, 2016), and assess the impact of liquefaction on underground structures and earth structures, dams, pile bridge abutments, and slopes (Chian, 2014, and Wang, 2004, and Ma, 2008, and Armstrong, 2015,

and Bastani, 2003). From the literature, there is missing research on the numerical evaluation of liquefaction surface manifestation of stratified soil profiles that consist of liquefiable and non-liquefiable soil layers that consider various soil and earthquake parameters for a specific region. Therefore, the goal of this study is to evaluate the liquefaction potential that considers the impact of shear strength and thickness of non-liquefiable soil layers on the surface manifestation of liquefaction based on finite difference numerical methods and to investigate the liquefaction surface manifestation potential of the West Tennessee area based on the adjusted LPI_{ISH} procedure.

Furthermore, as part of the literature search of this study, it was shown that the conventional liquefaction potential indices of LPI and LPI_{ISH} that are used to evaluate the liquefaction surface manifestation potential of a soil profile have limitations. In the next chapter, it will be shown and discussed that the LPI- and LPI_{ISH}-based liquefaction hazard maps of the West Tennessee area provide significantly different results that may cause an over/under prediction of liquefaction surface manifestation potential for the area that is vulnerable to seismic motions of New Madrid seismic zone.

CHAPTER 3. METHODOLOGY

3.1. Introduction

The goal of this study is to evaluate the liquefaction potential that considers the impact of shear strength and thickness of surficial non-liquefiable soil layers on the surface manifestation of liquefaction based on finite difference numerical methods To accomplish this goal the research methodology consists of the following primary tasks:

1. Perform liquefaction analysis of West Tennessee based on LPI and LPI_{ISH} methods coupled with the simplified procedure of Seed and Idriss (1971) and compare the results.
2. Develop a FLAC model and code to perform liquefaction surface manifestation potential analysis and verify the FLAC models to perform liquefaction analysis based on evaluation of the Wildlife site in California.
3. Perform additional evaluation of the written code in FLAC for this study based on the Christ Church data and observations from four sites.
4. Perform sensitivity analysis of the liquefaction potential of the FLAC models by varying the shear strength and thickness of surficial non-liquefiable soil layers.
5. Statistical correlation analysis between shear strength, thickness and liquefaction surface manifestation

The entire procedure of this dissertation study is summarized in the following flowchart (Figure 3.1).

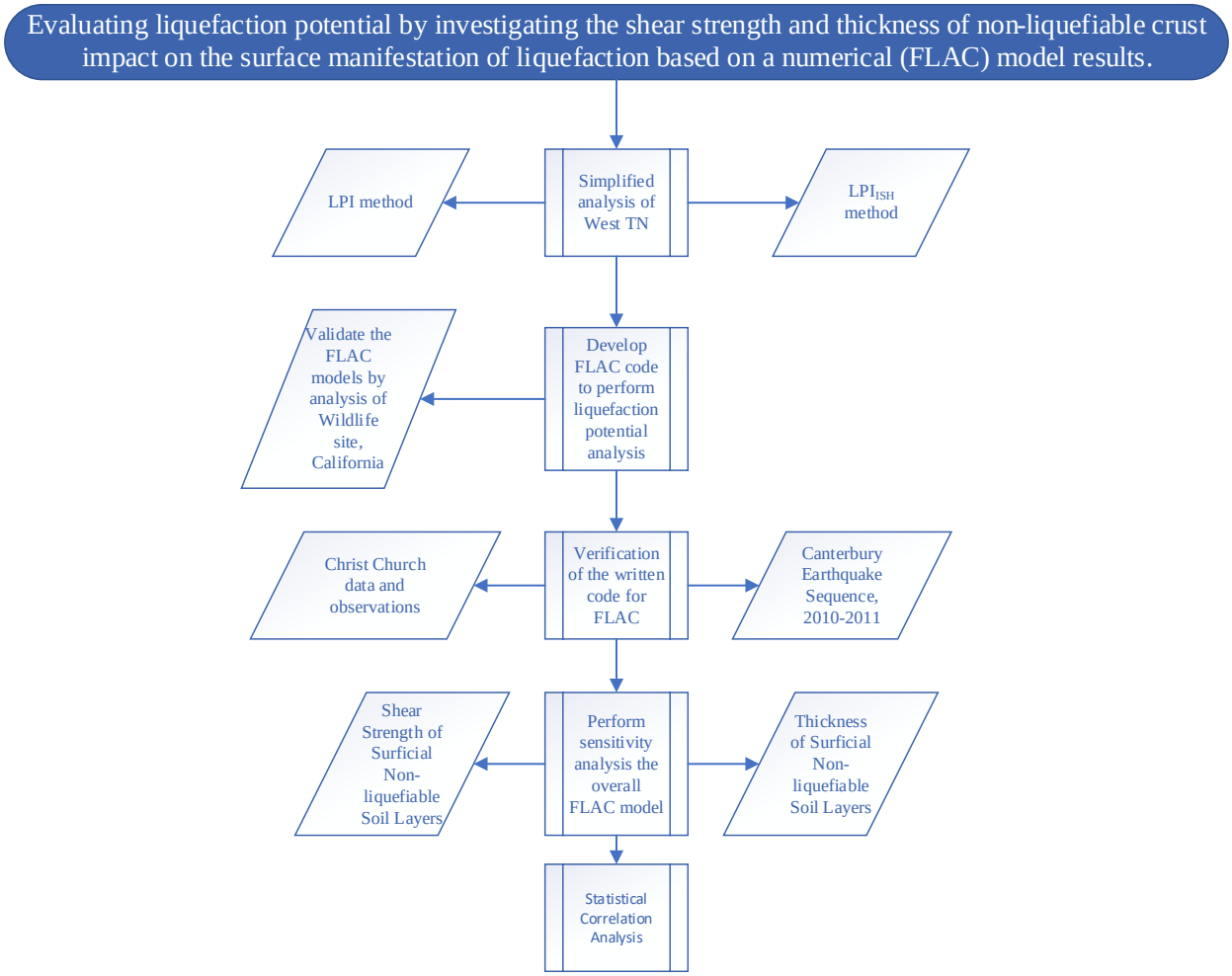

Figure 3.1. Flow chart of the entire procedure of the dissertation study.

3.2. Liquefaction Analysis of West Tennessee Area

The West Tennessee area is located within and near the New Madrid Seismic Zone (NMSZ) which is one of the major seismic zones of the United States; therefore, this area is vulnerable to seismic risk. The NMSZ is in southeastern Missouri, northeastern Arkansas, western Tennessee, western Kentucky, and southern Illinois. The NMSZ is responsible for three major earthquakes with a magnitude of 7 or larger that occurred between Dec. 16, 1811, and Feb. 7, 1812.

The 1811-1812 earthquakes of NMSZ affected almost 5,500 square miles of the Mississippi and Ohio river valleys with landslides, fissures, sand blows, lateral spreads, subsidence, submergence, and uplift (Missouri Department of Natural Resource at https://dnr.mo.gov). The NMSZ lies within the northern part of the Mississippi Embayment, which is a large sedimentary basin formed during the Cretaceous period. The Mississippi Embayment passes through parts of Alabama, Arkansas, Illinois, Kentucky, Louisiana, Mississippi, Missouri, Tennessee, and Texas (Imlay, 1949 and Morgan, 1983). Therefore, the West Tennessee area is within both the NMSZ, and the Mississippi Embayment as shown in Figure 3.2.

Figure 3.2. Mississippi Embayment (Image source: Wikimedia Commons by Kbh3rd, April 2010).

3.2.1. Geology of the Area

The soil profiles of the West Tennessee area are stratified and consist of liquefiable and non-liquefiable soil layers. The West Tennessee area consists of three primary near-surface geologic units of Lowland, Intermediate, and Upland. The Lowlands are at an elevation of less than 81 m and consist of Holocene (< 12 ka) river floodplain alluvium (Saucier, 1994; Ritenour et al., 2007). In general, the alluvium consists of surface silt and clay overbank sediment that overlies

laterally accreted sand and gravel sediment. Between elevations of 81 m and 107 m are the Intermediate units. The Intermediate unit includes loess overlying Finley, Hatchie, and Humboldt terraces and loess overlying Eocene strata, and all Intermediate units are covered with Peoria loess (wind-blown silt) (Cramer et al., 2020a, 2020b). The Upland unit is at an elevation > 107 m and is loess covered high-level terrace of the ancestral (~ 3.6 Ma) Mississippi/Ohio river (Van Arsdale et al., 2007; Odum et al., in review). This high-level terrace alluvium, called the Upland Complex, consists of sand and gravel that is regionally a major source of aggregate (Van Arsdale et al., 2012; Lumsden et al., 2016). For this study, the liquefaction potential analysis has been done for the lowlands which are the most liquefaction-prone geologic unit because of the presence of river floodplain alluvium and shallow groundwater levels.

3.2.2. West Tennessee Liquefaction Hazard Analysis Based on LPI and LPI_{ISH}

As part of a five-year seismic and liquefaction hazard mapping project for four western Tennessee counties of Lake, Dyer, Lauderdale, and Tipton that began in 2017 under a Disaster Resilience Competition grant from the U.S. Department of Housing and Urban Development to the State of Tennessee (HUD project), both LPI and LPI_{ISH} approaches were utilized to develop liquefaction hazard maps. The results of analyses show that the liquefaction probability curves, and liquefaction hazard maps obtained from the LPI and LPI_{ISH} methods are different. The LPI_{ISH}-based liquefaction hazard maps significantly show a lower probability of liquefaction than the LPI-based liquefaction hazard maps. Significantly the inconsistency between LPI- and LPI_{ISH}-based liquefaction hazard maps is because of the key differences between the two frameworks, especially the impact of non-liquefiable layers on the surficial manifestation of liquefaction that is considered in the LPI_{ISH} but not the LPI procedure that was indicated in Section 2.3.

Regional liquefaction hazard maps have been developed by various researchers (Holzer, 2012; Cramer et al., 2008, 2019, 2020a, b, 2021, and 2022) for preliminary assessment of liquefaction hazards. Usually, liquefaction hazard mapping is developed based on surficial geology maps only; however, these types of maps cannot predict the severity of the liquefaction probability of a region. However, by combining the geological and geotechnical data of a region, one can develop liquefaction hazard maps that provide liquefaction potential conditions.

Two common types of hazard maps are probabilistic- and deterministic-based hazard maps. These maps are designed to give the general public as well as land-use planners, utilities, and lifeline owners a better tool to assess their risk from earthquake damage.

In this study, LPCs were developed using the three-step procedure utilized by Rix and Romero-Hudock (2006), Tohidi et al. (2021), and Cramer et al. (2019, 2020a, 2020b, 2021, and 2022), and each step is described in this section.

Step 1: Calculate the Factor of Safety (FS) of soil layers of each soil boring against liquefaction using the Simplified method (Seed and Idriss, 1971) in which:

$$FS = \frac{CRR_{7.5}}{CSR} \cdot MSF \cdot K_{\sigma} \cdot K_{\alpha} \tag{3.1}$$

where $CRR_{7.5}$ is the cyclic resistance ratio at a magnitude of 7.5, which is the capacity of the soil to resist liquefaction, CSR is the cyclic stress ratio and represents the exerted dynamic stress induced by an earthquake on the soil, and MSF is a magnitude scaling factor that corrects for magnitudes other than 7.5 and is computed using the revised relationship by Idriss (1999):

$$MSF = 6.9 \exp\left(\frac{-M_W}{4}\right) - 0.06, M_W > 5.2 \tag{3.2}$$

$$MSF = 1.82, M_W \leq 5.2 \tag{3.3}$$

K_α in Equation (3.1) is a correction factor for the sloping ground, which is considered 1 in this study because the terrain of West Tennessee is generally flat to sloping, and K_σ in Equation (3.1) is an overburden correction factor for soil layers with overburden pressure > 100kPa, and is computed using:

$$K_\sigma = \left(\frac{\sigma'_{v0}}{P_a}\right)^{f-1} \tag{3.4}$$

where σ'_{v0} is the vertical effective overburden stress; P_a is the atmospheric pressure and is equal to 100 kPa, and f is an exponent function in a range of 0.6-0.8.

CSR is given by:

$$CSR = 0.65(\frac{a_{max}}{g})(\frac{\sigma_v}{\sigma'_v})r_d \tag{3.5}$$

where $a_{\max}$ is the peak ground acceleration, g is the acceleration due to gravity (9.8 m/sec^2), σ_v is the total vertical overburden stress, and r_d is the stress reduction coefficient and is computed by the revised equation suggested by Idriss (1999):

$$r_d = \exp\left(\alpha(z) + \beta(z)M_W\right) \tag{3.6}$$

where $\alpha(z) = -1.012 - 1.12\sin(\frac{z}{11.7} + 5.133)$, and $\beta(z) = 0.106 + 0.118\sin(\frac{z}{11.3} + 5.142)$.

The CRR is computed using Equation (3.7) developed by Youd and Idriss (2001) and recommended by NCEER (1996):

$$CRR_{7.5} = \left(\frac{1}{34-(N_1)_{60CS}} + \frac{(N_1)_{60CS}}{135} + \frac{50}{(10((N_1)_{60CS})+45)^2} - \frac{1}{200}\right) \quad (3.7)$$

where $N1_{60CS}$ is the corrected N-value for clean sand and is given by:

$$(N_1)_{60CS} = \alpha + \beta((N_1)_{60}) \quad (3.8)$$

where $\left(\frac{P_a}{\sigma'_v}\right)^{0.5}$ is known as the correction for effective overburden stress; P_a = atmospheric pressure in the same units as vertical effective stress (σ'_v) or P_a is 100 kPa if σ'_v is in KPa. The values of α and β are functions of fines content (FC) as shown in Table 3.1. FC is defined as the percentage of silt and clay in granular soils.

Table 3.1. Values of α and β for different ranges of FC.

Fines Content (FC)	α	β
FC ≤ 5 %	α = 0	β = 1.0
5% < FC < 35 %	$\alpha = \exp\left[1.76 - \left(\frac{190}{FC^2}\right)\right]$	$\beta = \left[0.99 + \left(\frac{FC^{1.5}}{1000}\right)\right]$
FC ≥ 35%,	α = 1.2	β = 5

Note that for FC ≤ 5, $(N_1)_{60cs}$ is equal to $(N_1)_{60}$ which is the corrected SPT N-value of the field and is calculated by:

$$(N_1)_{60} = N \cdot C_N \cdot C_E \cdot C_B \cdot C_R \cdot C_S \quad (3.9)$$

where N is measured standard penetration resistance, C_N is the overburden correction factor and is computed by $\left(\frac{P_a}{\sigma'_{v0}}\right)^{0.5}$, C_E is the hammer energy ratio correction factor, C_B is the borehole diameter correction factor, C_R is the rod length correction factor, and C_S is a correction factor for samplers with or without liners. For this study because the information of hammer type, borehole diameter, rod length and sampler liner were not available, the correction factors were not utilized.

Step 2: Calculate liquefaction potential indices based on the LPI and LPI_{ISH} procedures at each soil boring location. The LPI was developed to predict the severity of liquefaction potential and it is expressed as follows (Iwasaki, 1978-1982):

$$LPI = \int_0^{20\ m} F(z) \cdot w(z) \cdot dz \tag{3.10}$$

where z is the depth, dz is the differential increment of depth, F(z) is the severity, which is a function of Factor of Safety (FS), $F(z)=1 - FS$ for $0 \leq FS \leq 1$, and $F(z)=0$ for FS >1, and $w(z)$ is the linear weighting function which is equal to 10 - 0.5z.

The second liquefaction potential index that has been used in this study to develop the LPC is the LPI_{ISH} procedure developed by Maurer et al. (2015) and is summarized in Equations (3.11), (3.12), and (3.13).

$$LPI_{ISH} = \int_{H1}^{H1+H2} F(FS) \frac{25.56}{z} dz \tag{3.11}$$

$$F(FS) = \begin{cases} 1 - FS\ if\ FS \leq 1 \cap H1 \times m(FS) \leq 3 \\ 0 \qquad\qquad otherwise \end{cases} \tag{3.12}$$

$$m(FS) = \exp\left(\frac{5}{25.56(1 - FS)}\right) - 1 \tag{3.13}$$

where *H1* and *H2* are bounds of a liquefiable layer, F(FS) is the severity, which is a factor of safety-related function, z is depth, and dz is the differential increment of depth. The *m(FS)* term is an initial slope that is unique to each boundary curve shown in Figure 3.3. In Maurer's framework, it is assumed that each boundary curve can be defined by two straight lines with slopes of m and

∞ (see Figure 3.3a and Figure 3.3b). The thicknesses *H1* and *H2* are related to m by $H2 = H1 \cdot m$ as can be seen in Figure 3.3.

The boundary curves that are shown in Figure 3.3 indicate that there is *H1* threshold for each specific PGA that can minimize the potential for liquefaction surface manifestation occurrence regardless of *H2*. Maurer et al. (2015) noted from Figure 3.3b that when $H1 \times m$ exceeds about 3 m (~10 ft) for a given PGA of 0.2g, surficial manifestation is not expected regardless of the thickness of the liquefiable layer, *H2*. The limiting surficial crust thickness changes with PGA according to Figure 3.3b; for example, with PGA of 0.3g, the limiting thickness is about 6 m. This limiting non-liquefiable layer thickness is included in Equation (3.12) by the relationship of $H1 \times m$ for each boundary curve of Figure 3.3 b. The ratio of *25.56/z* in Equation (3.11) is the LPI_{ISH} power-law depth weighting function shown in Figure 2.11. The power-law weighting function represents the contribution of a liquefiable soil layer to surface manifestation. Liquefiable layers closer to the ground surface at depths between 0 and 3 m (~10 ft) contribute more to the surficial manifestation of liquefaction and liquefiable soils layers at depths between 3 and 20 m (~10 and 66 ft) contribute less.

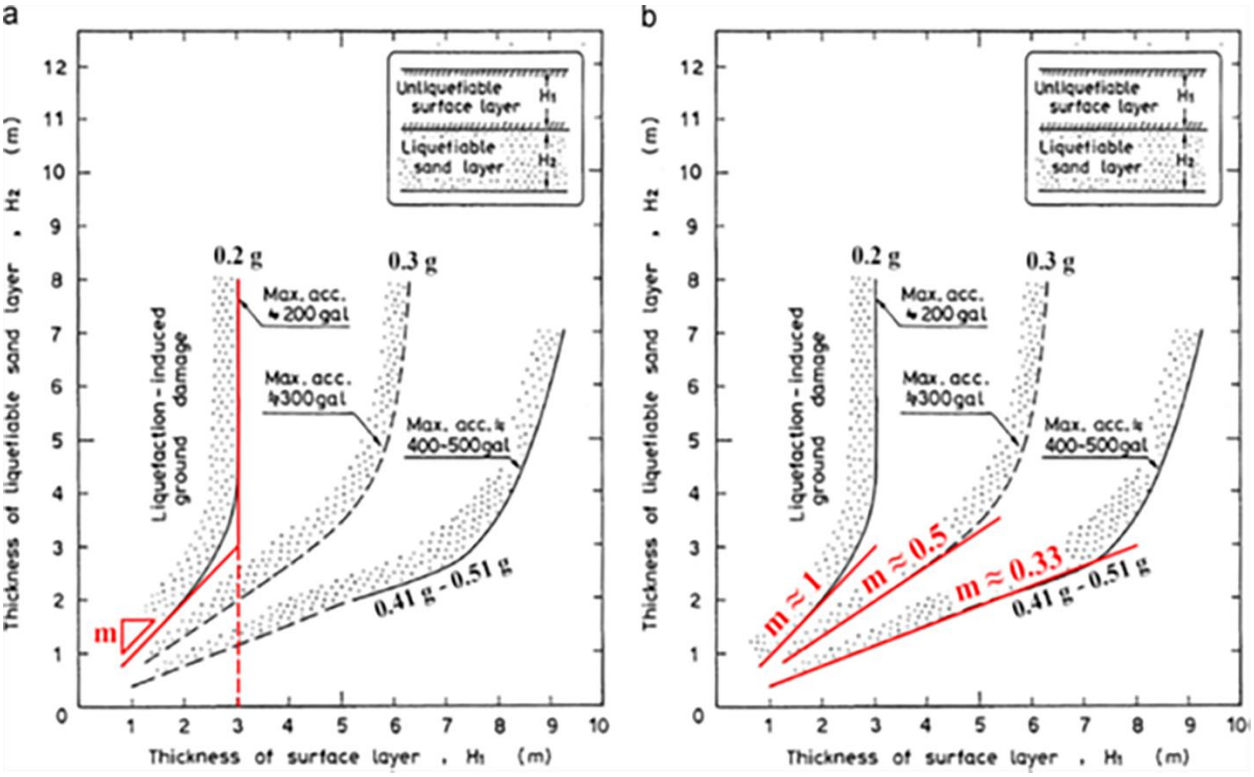

Figure. 3.3. Unique slope of each boundary curve that relates H1 to H2 (after Ishihara, 1985).

In summary, the primary difference between the LPI and LPI_{ISH} methods is that the LPI_{ISH} method includes the impact of non-liquefiable layers on liquefaction surface manifestation by incorporating a limiting non-liquefiable layer thickness whereby surficial manifestation from an underlying liquefiable layer is not expected regardless of the thickness of the underlying liquefiable layer. Additionally, LPI_{ISH} incorporates a power-law depth weighting function that statistically allows shallower liquefiable layers to contribute more to surficial manifestation than deeper layers. In the other words, since the LPI_{ISH} method considers the impact of non-liquefiable layers on liquefaction surface manifestation by incorporating a limiting non-liquefiable layer thickness and the LPI method does not, the factor of safety-related parameter (F) in Equations (3.10) and (3.11) is different. Thus, the liquefaction severity is different between the two methods. Also, because the weighting function between the two methods is based on different statistical

methods, the contribution of soil layers to the liquefaction surface manifestation is different between the LPI and LPI_{ISH} methods.

In this study, the LPI and LPI_{ISH} were determined at each boring location for peak ground acceleration (PGA) values of 0.1, 0.2, 0.3, 0.4, 0.5, 0.6, 0.7, 0.8, 0.9, and 1.0g and earthquake magnitudes (M_w) of 5, 5.5, 6, 6.5, 7, 7.5, and 8 (Cramer et al. 2019, 2020a, 2020b, 2021, and 2022). Thus, LPI and LPI_{ISH} are determined for each of the 70 possible combinations of PGA and M_w (i.e., 70 earthquake scenarios).

Step 3: After the determination of LPI and LPI_{ISH} at each boring location, the distribution of the number of soil boring locations (frequency) of a given range of LPI and LPI_{ISH} values was determined for every individual combination of PGA and M_w earthquake scenario for the Lowlands and non-lowlands (intermediate and upland) geologic units of all five West Tennessee counties by creating a MATLAB code. As noted previously, P[LPI>5] provides the probability that liquefaction surface manifestation can occur based on Iwasaki's threshold of 5, and based on Maurer's framework, liquefaction surface manifestation is expected where LPI $\geq$ 5 and is not expected where LPI < 5. LPCs can be developed based on the distribution of P[LPI>5] with the ratio of PGA/MSF.

Additionally, the approach of Cramer et al. (2006, 2008, 2014, 2018, 2019, 2020a, b, 2021, and 2022) for including the effects of local geology in seismic and liquefaction hazard estimates has been used in this study. First, a seismic hazard model is used to generate hard rock seismic hazard curves (probabilistic exceedance vs. ground motion level) and estimates (scenario). At each site (grid point), the 3D geology model developed for Lake County (Cramer et al., 2019; Weathers and Van Arsdale, 2019) is sampled to generate a seismic velocity and geotechnical soil profile above bedrock, which is then used to generate a site amplification distribution as a function

of input rock motion via soil profile randomization (Cramer et al., 2006). The rock hazard curves and estimates are then converted to site-specific curves and estimates using the site amplification distribution at a site, and the procedure of Cramer (2003, 2005) for probabilistic hazard curves and average site amplification for a given ground motion level for scenario estimates. For liquefaction hazard at a site (grid point), the Lake County LPC developed in this study is applied to the geology-specific PGA hazard value for a given level of exceedance (probabilistic) or scenario estimate to provide the probability of exceeding a specified LPI value (liquefaction hazard) (Cramer et al., 2008). The 2014 USGS National Seismic Hazard Project's seismic hazard model (Petersen et al., 2014) sources and regional ground motion attenuation were used to generate the hard rock hazard curves and scenario estimates that were then converted to geology-specific hazard curves and estimates from which hazard maps were generated. Probabilistic maps are for 2% and 5% exceedance in 50 years. Deterministic maps have been generated for M_w 6.9 "Dawn" aftershock on the Cottonwood Grove Fault (SW segment of NMSZ), and M_w 5.8 hypothetical Lake County earthquake (source model from Cramer et al., 2019). Further information regarding hazard map generation can be found in Cramer et al. (2006, 2008, 2014, 2018, 2019, 2020a, b, 2021, and 2022). More detail on developing the LPCs of each County is provided next.

3.2.3. Subsurface Data Collection of West Tennessee Counties

3.2.3.1. Lake County

Subsurface data that were collected within Lake County consisted of Standard Penetration Test (SPT) resistance or "N-value", shear wave velocity (V_s), Cone Penetration Test (CPT), and groundwater level. A summary of the procedures used to collect these data is presented next. Soil boring logs that included soil classifications based on the Unified Soil Classification System

(USCS) and SPT-N values were obtained from the Memphis District of the U.S. Army Corps of Engineers (USACE), Tennessee Department of Transportation (TDOT), Tennessee Department of Economic & Community Development (TNECD), Construction Materials Laboratory, Inc., and Joel B. Spaulding & Company, Inc. Table 3.2 shows the total number of soil boring logs that were received from each organization and Figure 3.4 shows the general locations of all 2,075 soil borings that were obtained.

Table 3.2. Summary of the total number of borings.

Organization	Number of Boring Logs
USACE	2004
Joel B. Spaulding & Company, Inc.	4
Construction Materials Laboratory, Inc.	42
TDOT	10
TNECD	15
Total	2075

The initial soil boring selection screening criteria can be summarized as:

- Borings must extend to a depth of 20 m (66 ft) or greater.
- The borings must include SPT-N values.
- The boring locations must have latitude and longitude coordinates.

The above screening criteria are similar to the screening criteria used in developing the liquefaction probability curves incorporated in the Seismic Hazard Maps for Memphis and Shelby County (Cramer et al. 2018; Cramer et al. 2015) except that a minimum depth of 66 ft (20 m) was used instead of 49 ft (15 m) because a minimum depth of 66 ft (20 m) of soil data is required to determine the liquefaction probability index.

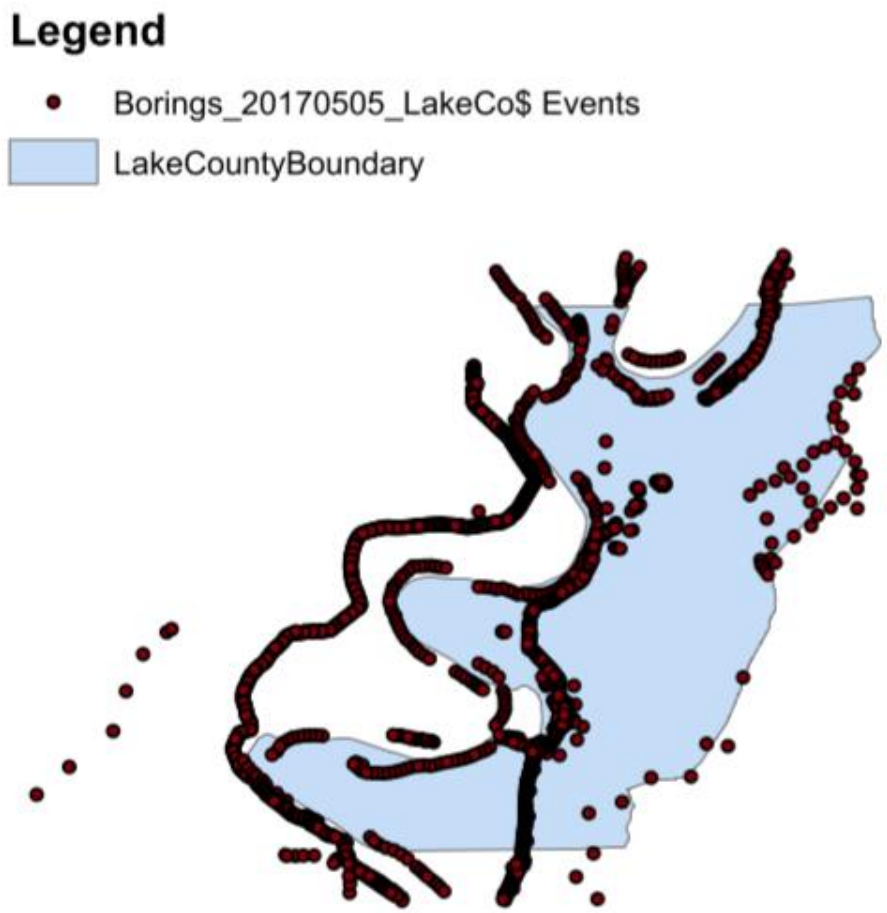

Figure 3.4. Geotechnical boring locations.

As shown in Figure 3.4 and provided in Table 3.3, 859 of the 2,075 borings are located inside Lake County. Additionally, only 189 of the 859 borings within Lake County had some SPT N-values. Unfortunately, a majority of these 189 borings did not meet the minimum desired depth of 66 ft (20 m) nor did the borings have N-values at a majority of intervals through the full minimum desired 66 ft (20 m) depth. The procedure to develop liquefaction probability curves requires that N-values be available for a majority of the minimum desired 66 ft (20 m) depth. Only 33 of the 189 soil borings within Lake County had N-values for a minimum desired 66 ft (20 m)

depth. These 33 borings, locations of which are shown in Figure 3.5, were used in the liquefaction analysis of Lake County and Table 3.3 summarizes the description of Lake County soil boring logs.

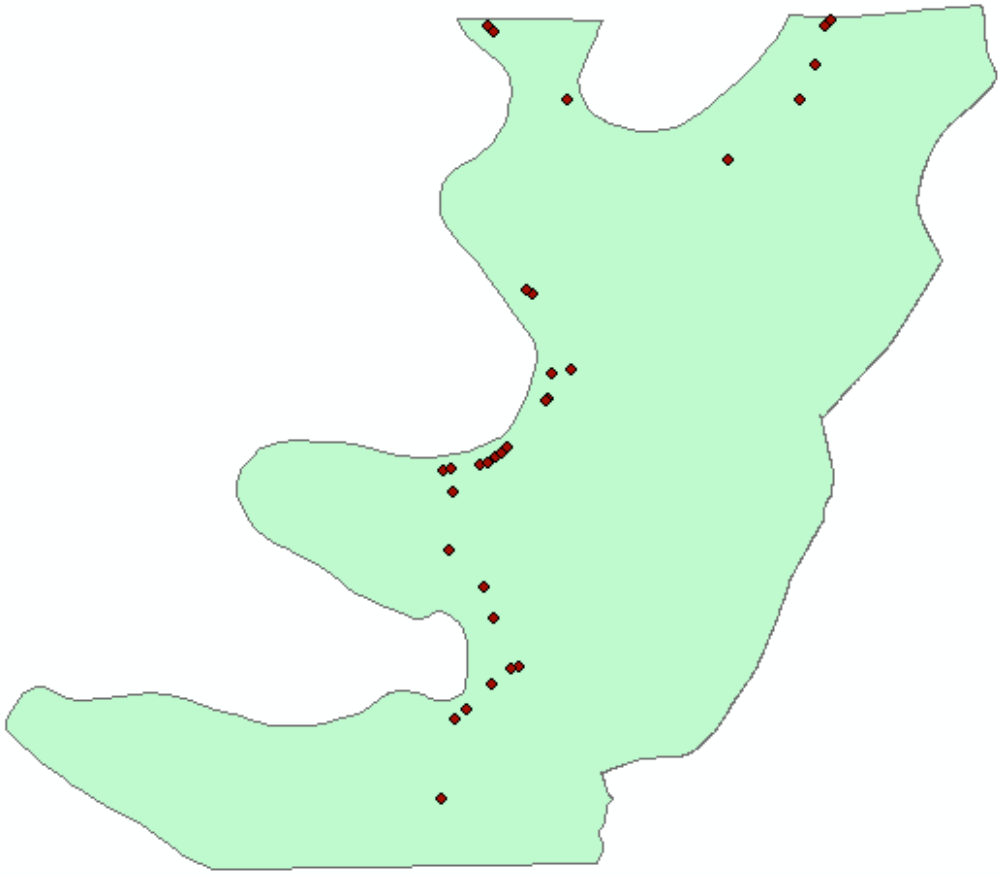

Figure 3.5. Locations of SPT borings.

Table 3.3. Summary of the soil borings location and frequency of SPT N-values.

Organization	Total Borings	Outside-County	Inside-County	Inside County but No N-values provided	Inside County with some N-values provided	Inside County with many N-values provided & min. 60 ft deep
USACE	2004	1203	801	670	131	33
Construction Materials Laboratory, Inc.	42	9	33	0	33	0
Joel Spaulding & Company, Inc.	4	4	0	0	0	0
TDOT	10	0	10	0	10	0
TNECD	15	0	15	0	15	0
Total	2075	1216	859	670	189	33

For Lake County, in addition to SPT borings data, a total of 26 shear wave velocity or V_s profiles were measured and also obtained from various studies as shown in Table 3.4 and Figure 3.6. Among the 26 V_s profiles, four of those did not have a specific location but all others were located inside Lake County or within a buffer zone defined herein as within 4 km (2.5 miles) of the County's boundary lines. Only one profile (HUD-8) was discarded due to a lack of data to a depth of 20 m (66 ft.). Thus, a total of 25 shear wave velocity profiles were used in the liquefaction analysis of Lake County.

Table 3.4. Summary of shear wave velocity profiles.

Shear Wave Velocity Data	Total Profiles	Profiles Used in Analysis
HUD	14	13
Finprostats (Cramer 2018)	1	1
Rosenblad (Rosenblad 2007)	2	2
Wynnburg (Pezeshk et al. 1998)	1	1
GaTech (Mayne 2005)	2	2
CUSSO (Woolery et al. 2016)	2	2
OBN (Holzer et al. 2011)	4	4
TOTAL	26	25

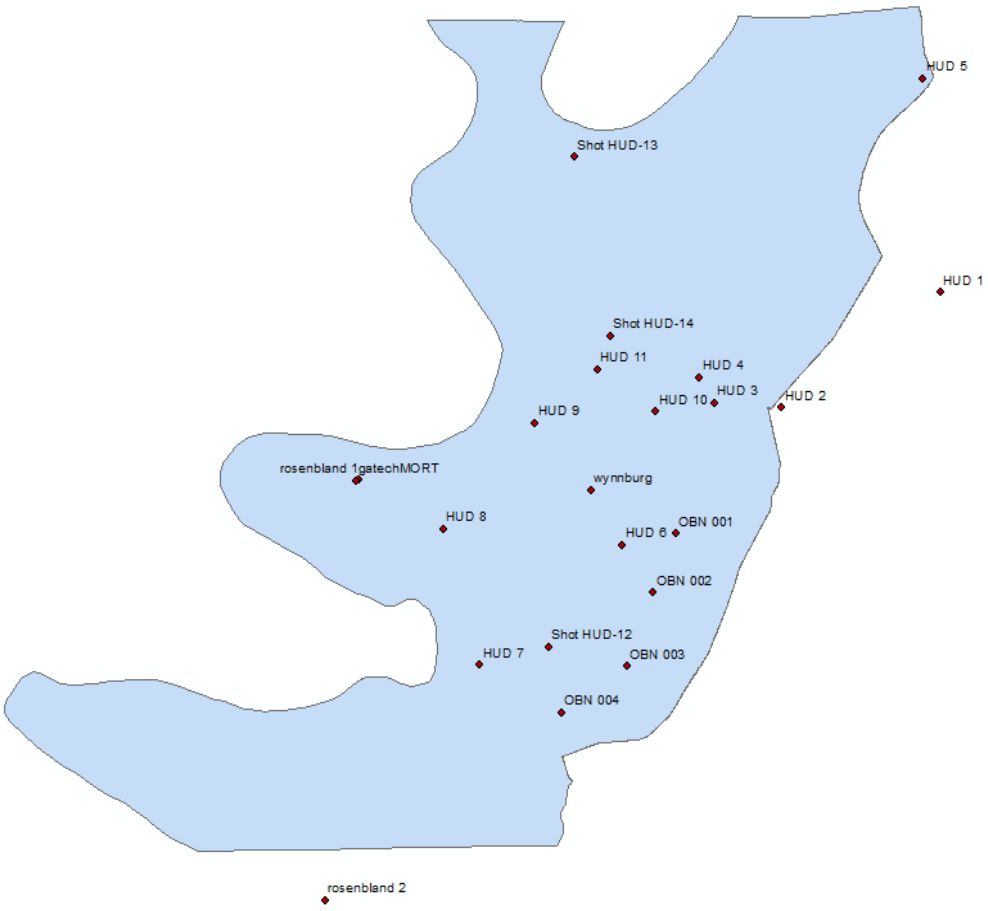

Figure 3.6. Location of shear wave velocity profiles.

To develop the preliminary LPCs of Lake County the groundwater level data were obtained from Holzer's study. Holzer et al. (2011) did a study to develop liquefaction probability curves (LPCs) for 14 surficial geologic deposits within the U.S. Holzer's study presented LPCs for three different types of surficial geological deposits in the Mississippi embayment area that included floodplain point bar, abandoned channel, and flood basin. Holzer et al. developed LPCs for each surficial geologic deposit and groundwater levels of 1.5 and 5 m. Thus, each geologic deposit was represented by two LPCs, one for each groundwater level, and Holzer et al. developed a total of six LPCs for the three different types of surficial geological deposits located in the Mississippi

embayment area. A preliminary LPC for Lake County was developed based on the average of the six LPCs which represents an average groundwater level of 3.25 m, which is the average of groundwater levels of 1.5 m and 5 m.

Supplemental groundwater level data were obtained from the United States Geological Survey (USGS) groundwater data website (https://maps.waterdata.usgs.gov). Groundwater level data within Lake County was provided by USGS for 15 water wells inside Lake County as shown in Figure 3.7. Seven of these wells were active, meaning that water levels are currently obtained, and eight are inactive. A total of 30 water level records with readings obtained between 1984 and March 2018 were available on the USGS website (Table 3.5).

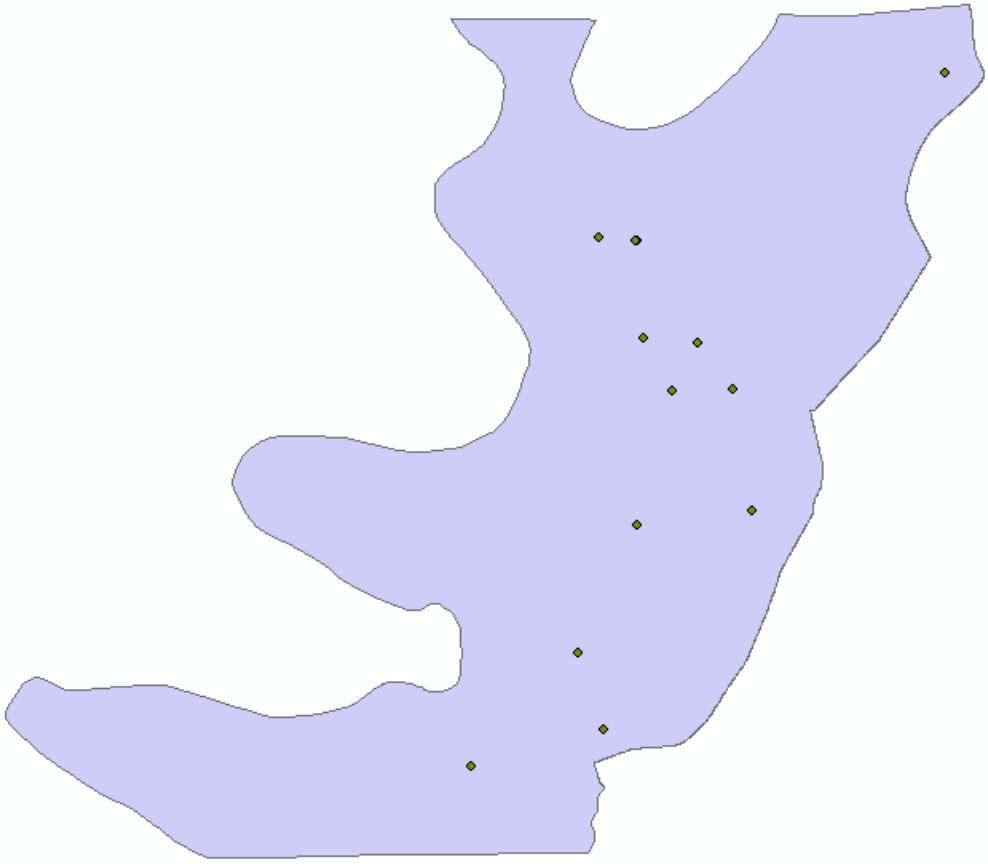

Figure 3.7. USGS wells within Lake County.

Table 3.5. Summary for the period of record periodic water levels of wells inside Lake County.

Well NO.	Period of Reading	Level (ft)	Level (m)
G042	7/23/1984	22	6.70
E003	10/7/1985	13.52	4.12
E003	3/14/2007	10.94	3.33
E021	10/7/1985	20.82	6.34
E021	3/14/2007	22.53	6.86
H-5 REELFOOT	7/17/1986	3.62	1.10
H-6	7/23/1986	5.4	1.64
H-7	7/23/1986	5.5	1.67
G040	8/13/1987	29	8.83
G040	5/13/2009	27.55	8.39
G040	6/28/2011	28.62	8.72
G040	5/17/2013	29.58	9.01
G040	6/9/2015	28.61	8.72
G040	4/11/2017	29.17	8.89
C002	Jun-16	4.7	1.43
B002	Jun-16	5.79	1.76
B002	4/3/2018	3.7	1.12
G044	Jun-16	15.4	4.69
G044	4/3/2018	16.15	4.92
E034	Jun-16	5.39	1.64
E034	4/3/2018	3.95	1.20
E035	Jun-16	8	2.43
E035	4/3/2018	6.97	2.12
E036	Jun-16	4.23	1.28
E036	4/3/2018	3.28	0.99
G043	Jun-16	20.38	6.21
G043	3/1/2018	23.76	7.24
G043	4/3/2018	22.47	6.84
G045	3/1/2018	22.03	6.71
G045	4/3/2018	20.77	6.33

An approximate average water level for Lake County was found based on the records of these 15 wells using three different methods:

- Based on the average readings each year. Because the wells had readings in different years, I classified the well readings based on the year of reading and got

an average of all readings in a specific year. The overall average was calculated based on the average of each specific year and used as a single GWL in the analysis.

- Based on the average of all readings. In this method, the average of all 30 readings was computed and used as a single groundwater level in the analysis.
- Based on the average readings of each well. Some of the wells had multiple readings in different years, in this method, the average of all readings of each well was calculated and used as a single groundwater level for each well. The overall average groundwater level was computed based on the single average level of each well.

Table 3.6 shows the results of the three methods.

Table 3.6. Groundwater level estimation using USGS data.

Water level based on the average of each year (meter)	6.5
Water level based on the average of all readings (meter)	4.7
Water level based on the average of each well (meter)	3.7

To develop the finalized LPCs of Lake County (after preliminary LPCs) additional groundwater level data of Lake County was provided by a groundwater elevation contour map developed by Schrader (2007). Schrader used the groundwater flow model of the northern Mississippi embayment that was developed by the U.S. Geological Survey Office of Ground-Water Resources Program as part of the Mississippi Embayment Regional Aquifer Study (MERAS). The groundwater elevation contour map covers approximately 70,000 square miles and includes Alabama, Arkansas, Illinois, Kentucky, Louisiana, Mississippi, Missouri, and Tennessee. The map is based on data from 748 water level measurements obtained in spring 2007 from 309 wells in Arkansas, 7 wells in Kentucky, 116 wells in Louisiana, 150 wells in Mississippi, 6 wells in Missouri, and 160 wells in Tennessee. Figure 3.8 shows the groundwater elevation contour

lines, which are based on the National Geodetic Vertical Datum (NGVD) of 1929, that extend through Lake County. As shown in Figure 23, the groundwater levels in Lake County are predominantly between elevations 260 and 280 ft, a difference of 20 ft.

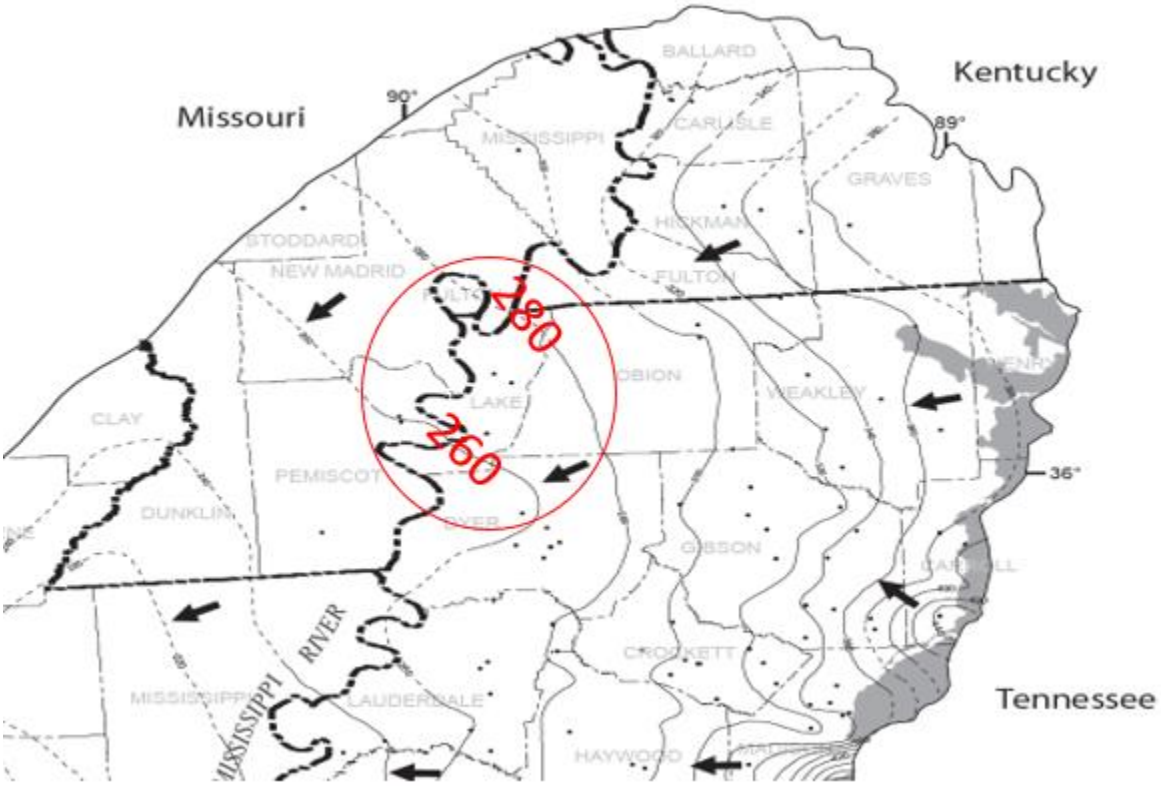

Figure 3.8. USGS groundwater level contour map (Schrader 2007).

Figure 3.9 shows the groundwater level contour map generated from the Schrader (2007) map. ArcMap was utilized to project the groundwater elevation contour map on a shapefile boundary of Lake County and the two contour lines of 260 ft. and 280 ft. were digitized and located on the Lake County shapefile. Using ArcMap, the groundwater elevation contour map for the entire County was generated. Then the summarized SPT boring logs and shear wave velocity profiles were located on the groundwater contour map shown in Figure 24 and using the ArcMap interpolation tool, Inverse Distance Weighting (IDW), the groundwater level was interpolated for

all borings and profiles. Because the SPT and V_s database did not have ground surface elevations at each boring and profile location, ground surface elevation was estimated using Light Detection and Ranging (LiDAR) map that was received from the geology team in ArcMap format. The SPT borings and V_s profiles were located on the LiDAR map and the ground surface elevations were interpolated for all borings and profiles. The groundwater depth of each profile was computed by subtracting the groundwater elevation from the ground surface elevation.

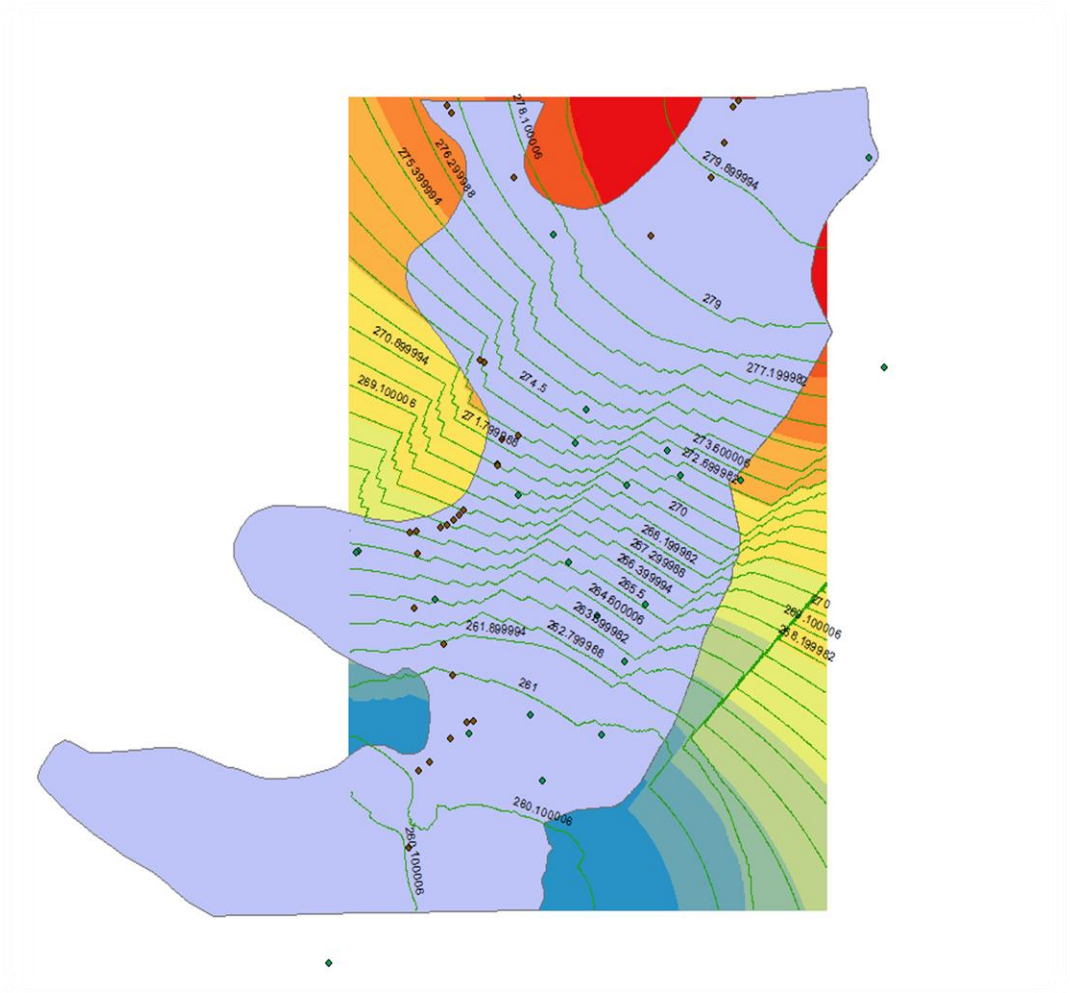

Figure 3.9 Groundwater level contour map for Lake County (red points represent soil borings and green points represent shear wave velocity profile locations).

3.2.3.2. Dyer County

Soil boring logs containing soil classifications based on the USCS and SPT-N values were obtained from the USACE and the TDOT. Table 3.7 shows the total number of soil boring logs that were received from each organization.

Table 3.7. Summary of the total number of borings.

Organization	Number of Boring Logs
USACE	993
TDOT	140
Total	1133

The USACE soil boring logs were selected based on the same selection criteria used for Lake County. The initial selection criteria only yielded data from 30 borings because many boring logs did not include N-values to a depth of 20 m (66 ft). Therefore, to include additional boring data in the development of LPCs, the screening criteria were revised to accept boring logs with most N-values included to a depth of 15 m (50 ft) instead of 20 m (66 ft) based on the following procedure:

- Missing N-values for any depth at a given boring location were estimated by using the same N-value for a given N-value above or below the depth of the missing N-value if the overlying and underlying soil had the same soil classification.
- If the soil layers above and below the layer of a missing N-value did not have the same classification or did not have an N-value in a given boring, the N-value was extracted from the closest boring for the same classification and the same depth as the classification and depth of the missing N-value.

The modified boring log screening criteria added 54 boring locations to the 30 boring locations that met the initial screening criteria. Thus, the total number of USACE borings selected

for the development of LPCs is 84. As shown in Figure 3.10, the most boring locations are along the Mississippi River located along the western edge of Dyer County.

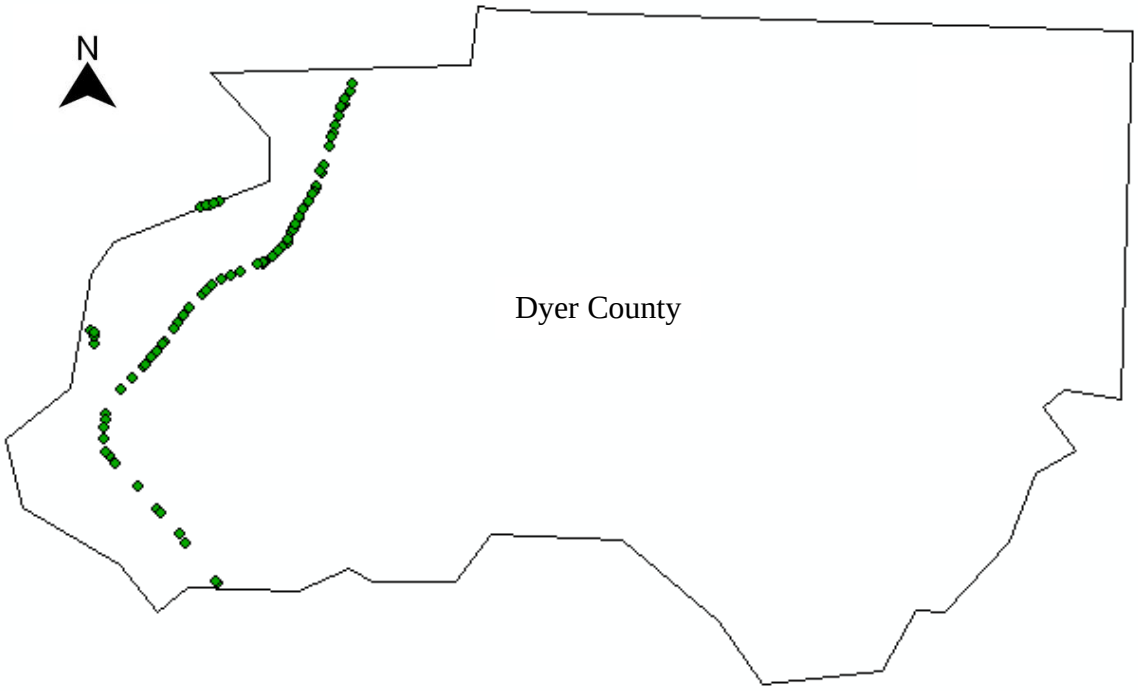

Figure 3.10. Locations of selected USACE SPT borings.

Dyer county consists of three primary geologic units: lowland, intermediate, and upland. Intermediate includes loess overlying Finley, Hatchie, and Humboldt terraces and loess overlying Eocene strata. Figure 3.11 shows the distribution of the geologic units and the USACE boring locations about these geologic units (Cramer et al., 2020a). As shown in Figure 3.11, all 84 USACE boring locations are located within the lowland geologic unit of Dyer County.

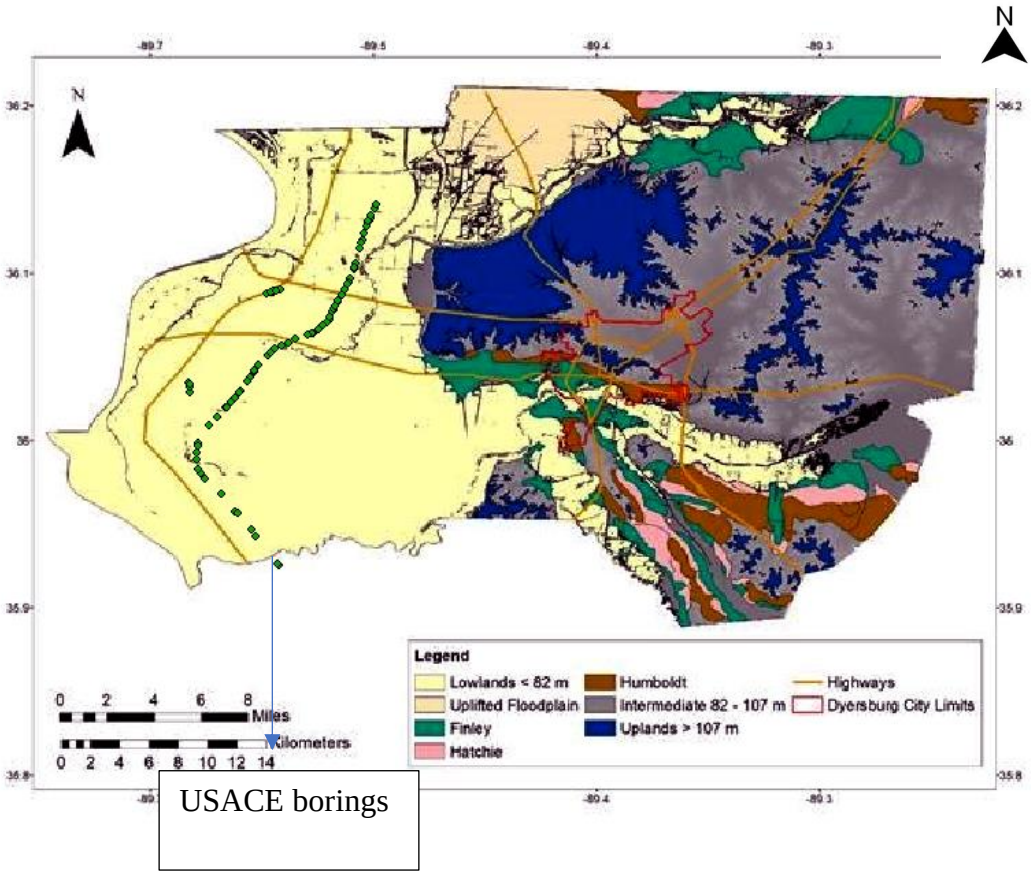

Figure 3.11. Locations of USACE selected borings on the geology map.

In addition to USACE boring logs, a total of 140 soil boring logs were received from TDOT as shown in Table 3.7. The same screening criteria utilized in the selection of USACE boring logs were used to select TDOT boring logs for use in the development of LPCs. The TDOT boring logs did not provide a coordinate location of where the boring was obtained. Either a project location map (without scale) or a general project location description was available. Using Google Earth and Google Map, the location of the projects was estimated and used as the project location for all soil borings of a project to find the geologic unit of the borings and to interpolate the GWL of each boring using the GWL contour map described later in this section. Figure 3.12 shows the 17 TDOT project locations in relation to the distribution of the geologic units of Dyer County.

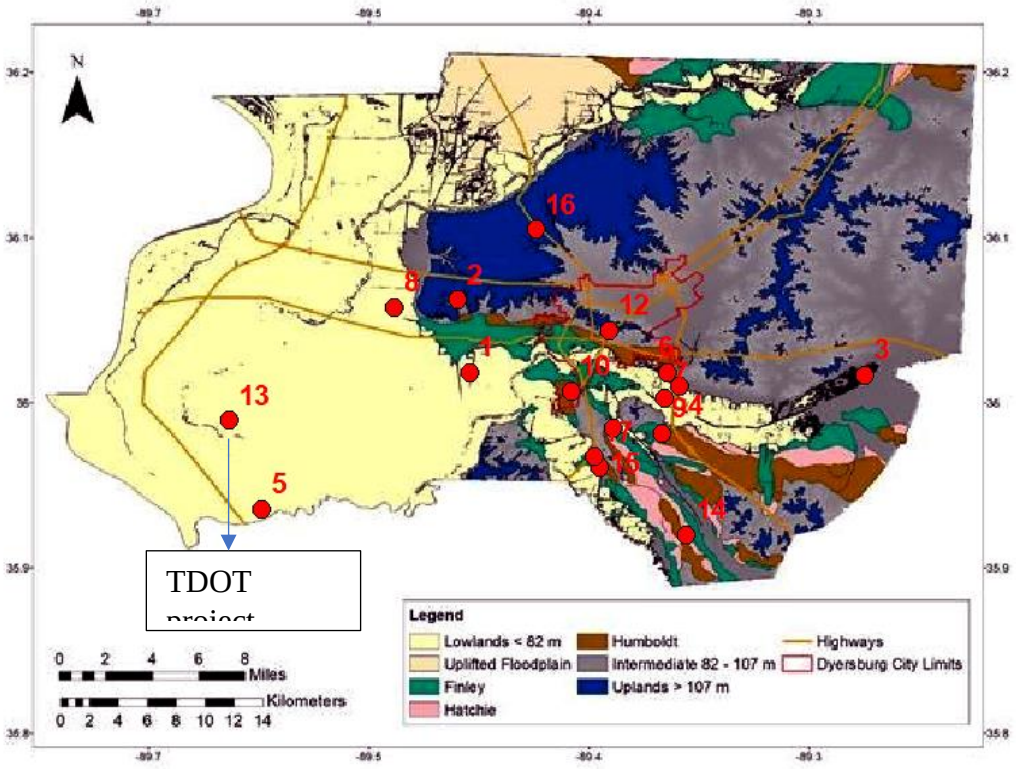

Figure 3.12. TDOT project locations.

Table 3.8 provides the distribution of the 54 boring locations with the geologic units for the 17 project locations shown in Figure 3.12.

Table 3.8. Summary of the soil borings of TDOT based on geology.

Geology	Number of Borings	Project No. on Map
Lowland	34	5-8-9-10-13-16
Intermediate	22	1-3-4-6-7-11-12-14-15-17
Upland	2	2

Table 3.9 summarizes the total number of borings selected for use in developing LPCs within Dyer County based on the geologic unit.

Table 3.9. Summary of the total number of SPT borings for each geologic unit.

Geology	Organization	USACE	TDOT	Total
Lowland		84	34	118
Intermediate		0	22	22
Upland		0	2	2

To develop the GWL contour map of Dyer County, a similar procedure to develop the water level contour map of Lake County (Cramer et al., 2019) was used. The primary source for establishing the GWL contour map within the surface alluvial aquifer for Dyer County was the GWL contour map shown in Figure 3.13, which was developed by Schrader (2008).

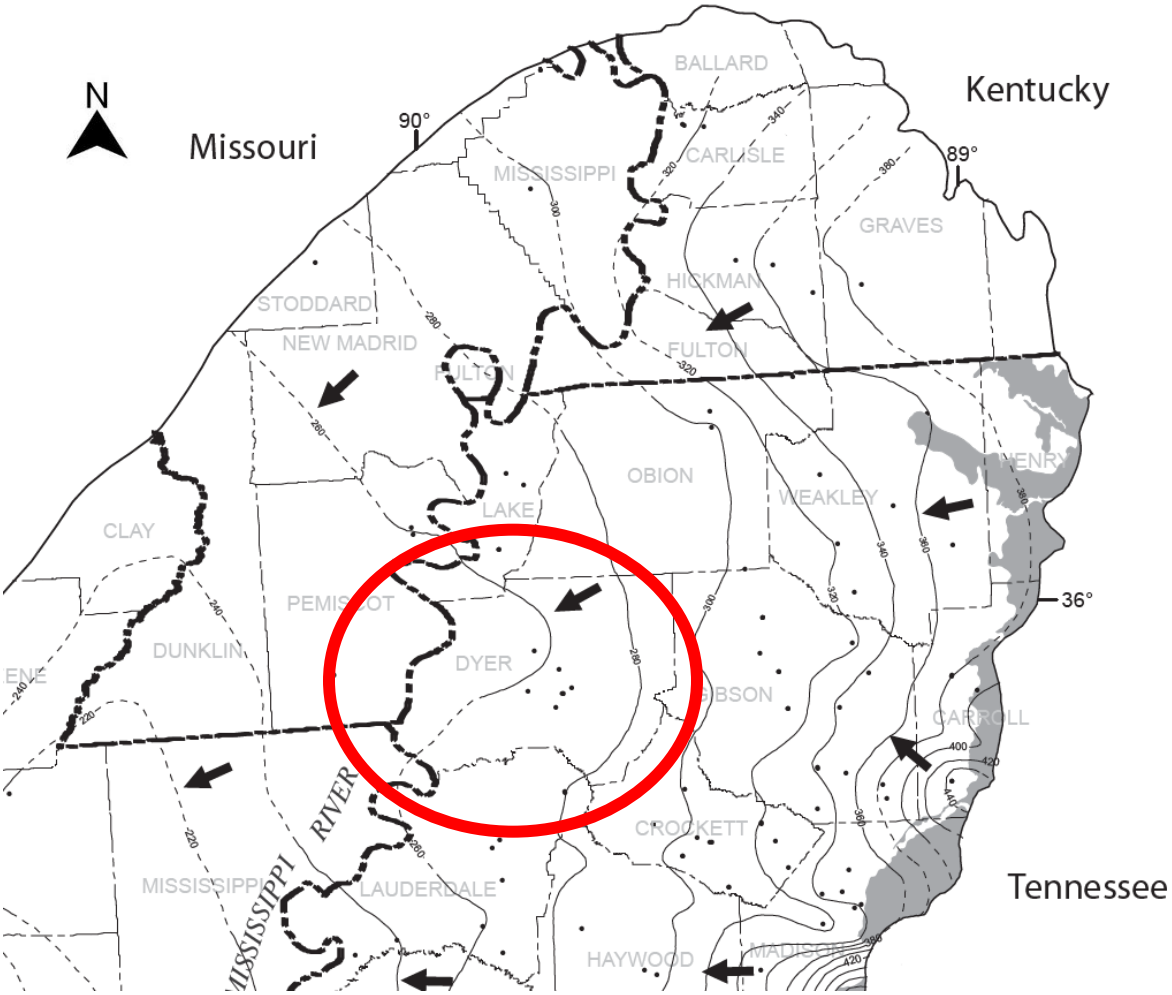

Figure 3.13. USGS groundwater level contour map (Schrader 2008) in the surface alluvium aquifer.

Using ArcMap, the contour lines were digitized on a shapefile boundary of Dyer County and the contour map was developed by the Inverse Distance Weighting (IDW) method. Figure 3.14 shows the GWL contour map of Dyer County that was used to develop the LPCs.

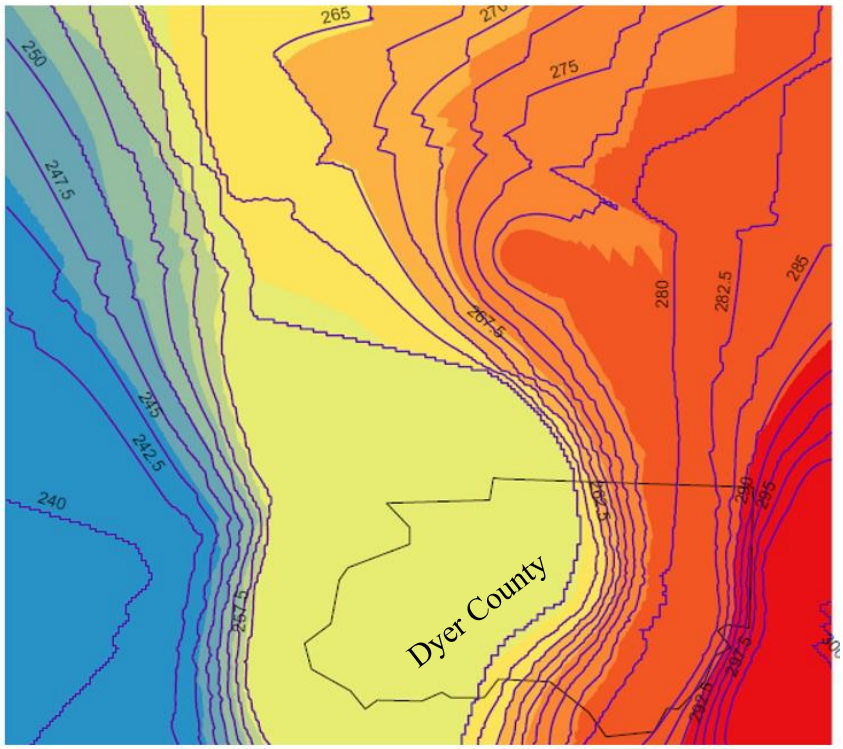

Figure 3.14 Groundwater level contour map for Dyer County (Contour lines are in ft.-NGVD 1929).

To verify the accuracy of the above GWL contour map, additional groundwater data for eight wells within Dyer County were obtained from the USGS groundwater database (https://maps.waterdata.usgs.gov). Wells are all periodic, meaning that water levels are recorded at a specific time of the year. As shown in Figure 3.15, all eight USGS water wells are in the lowest elevation areas of the GWL contour map.

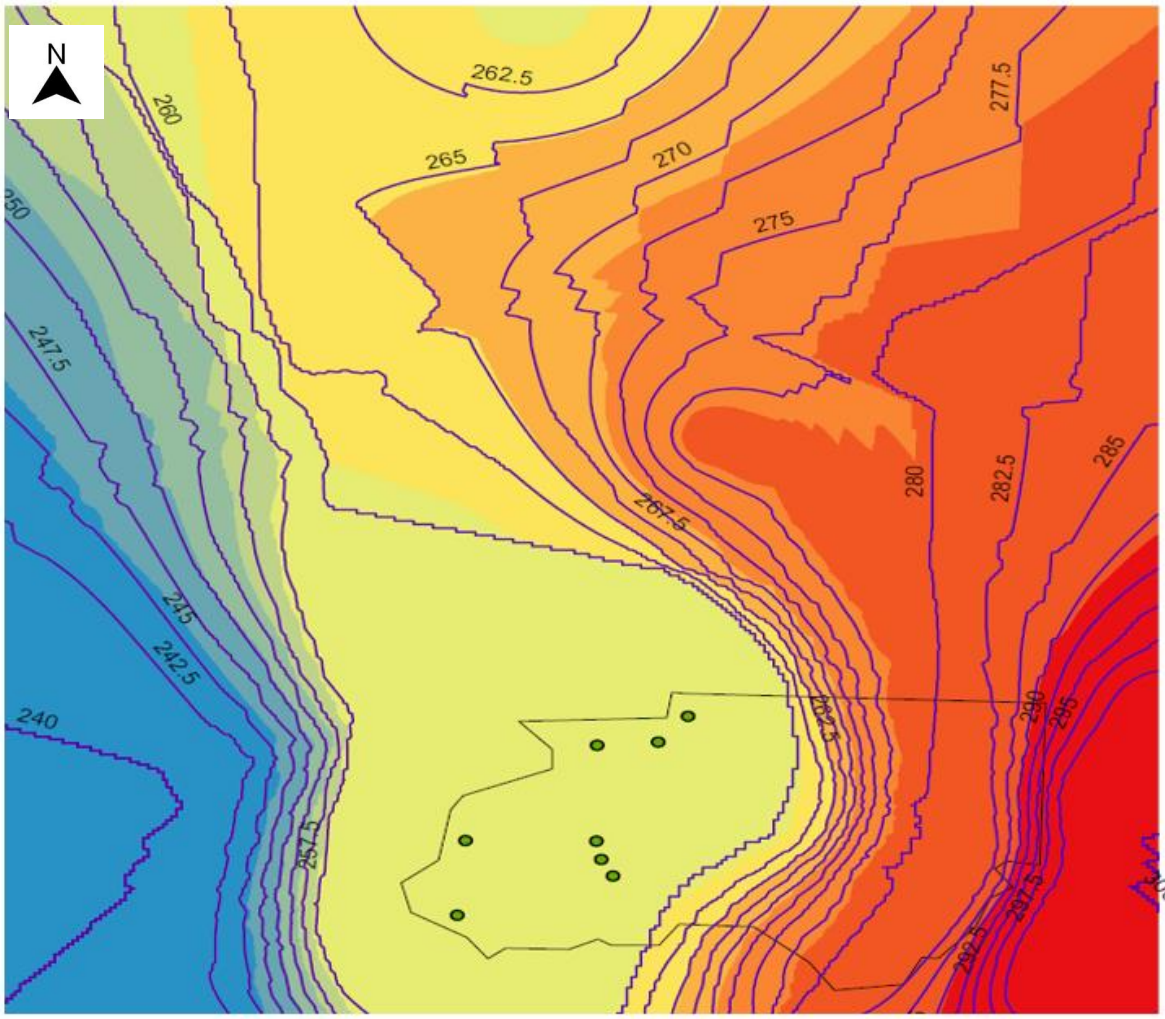

Figure 3.15. Location of USGS wells on the contour map of the water table elevation in the alluvial aquifer.

Because the wells had periodic readings and various recorded water level data, an average of the lowest and highest water table elevations of each well was calculated. For each USGS well, the GWL was interpolated from the contour map and the interpolated level was compared with the computed average of the lowest and highest GWL of each well. As provided in Table 3.10, for four wells the average is slightly higher than the interpolated GWL from the contour map, and for four wells the average is slightly lower than the contour map level for each specific well.

Additionally, the overall average of the lowest and highest readings of wells with the overall average GWL obtained from the contour map for wells was compared. As shown by the last row of Table 3.10, the difference between the average readings of all wells and the average interpolated levels from the contour map is 0.75 ft. (0.2 m).

Table 3.10. Comparison of contour map level for USGS wells and the average of lowest and highest readings of wells.

Well NO.	Average Readings (ft-NGVD of 1929)	Contour Map (ft-NGVD of 1929)	Difference between contour map and wells readings (ft)
1	257	249	8
2	257	258	-1
3	257	255	2
4	257	255	2
5	257	254	3
6	260	268	-8
7	260	265	-5
8	260	267	-7
Overall average	258.125	258.875	0.75

Because there is no water well data available within higher elevation parts of the county, and there is a good agreement between USGS well data and the contour map, the GWL contour map shown in Figure 3.14 was used to interpolate the GWL at each soil boring location.

3.2.3.3. Lauderdale County

For Lauderdale County, SPT soil boring logs were received from the USACE, and the TDOT. From the USACE total of 350 boring logs, and from the 69 TDOT projects, a total of 250 boring logs were obtained. To use SPT soil borings in the development of LPCs, there are specific

criteria for selecting borings for analysis. At first, the USACE boring logs were selected based on the selection criteria used in developing the LPCs of the Lake and Dyer counties Seismic and Liquefaction Hazard Maps (Cramer et al. 2019, 2020). The selection criteria of the USACE soil boring logs yielded data from 71 boring logs out of a total of 350, and 279 of the USACE boring logs were discarded. Figure 3.16 indicates the distribution of the selected boring logs of USACE within Lauderdale County. As shown in Figure 3.16, the most boring locations are along the northwestern edge of Lauderdale County.

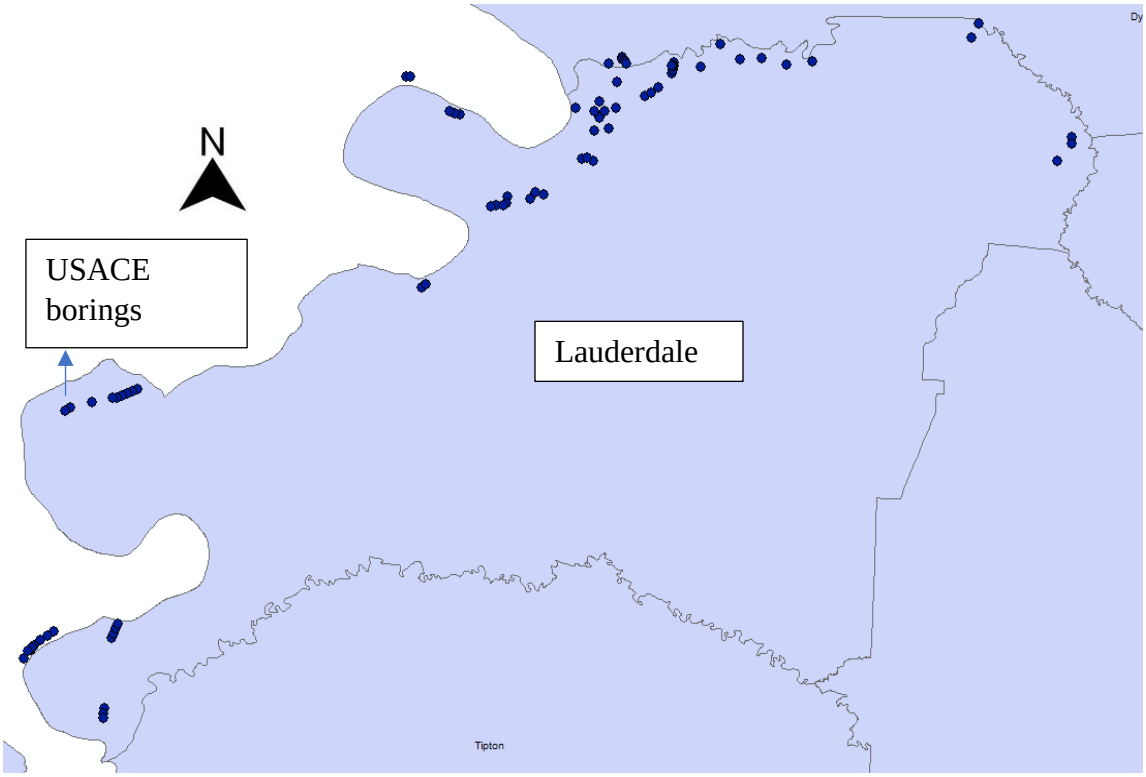

Figure 3.16. Locations of selected USACE SPT borings.

For Lauderdale County, a total of 250 SPT soil boring logs from 69 TDOT projects were received. As in Dyer County, the main issue of TDOT boring logs in Lauderdale County was the

unavailability of coordinate locations of borings. The TDOT projects had only a project location map (without scale) or general project location description. Based on either the project location map or the general project location description, the coordinates of project locations were estimated using Google Maps and Google Earth. The coordinate location of a project was used for all soil borings of a project to find the surface geologic unit of the borings and to estimate the GWL of each boring based on the GWL contour map, which will be discussed later in this section.

Thirty-nine TDOT projects, including a total of 138 boring logs, were selected and added to the database of liquefaction analysis of Lauderdale County to develop LPCs. Figure 3.17 shows the location of 39 selected TDOT projects within Lauderdale County.

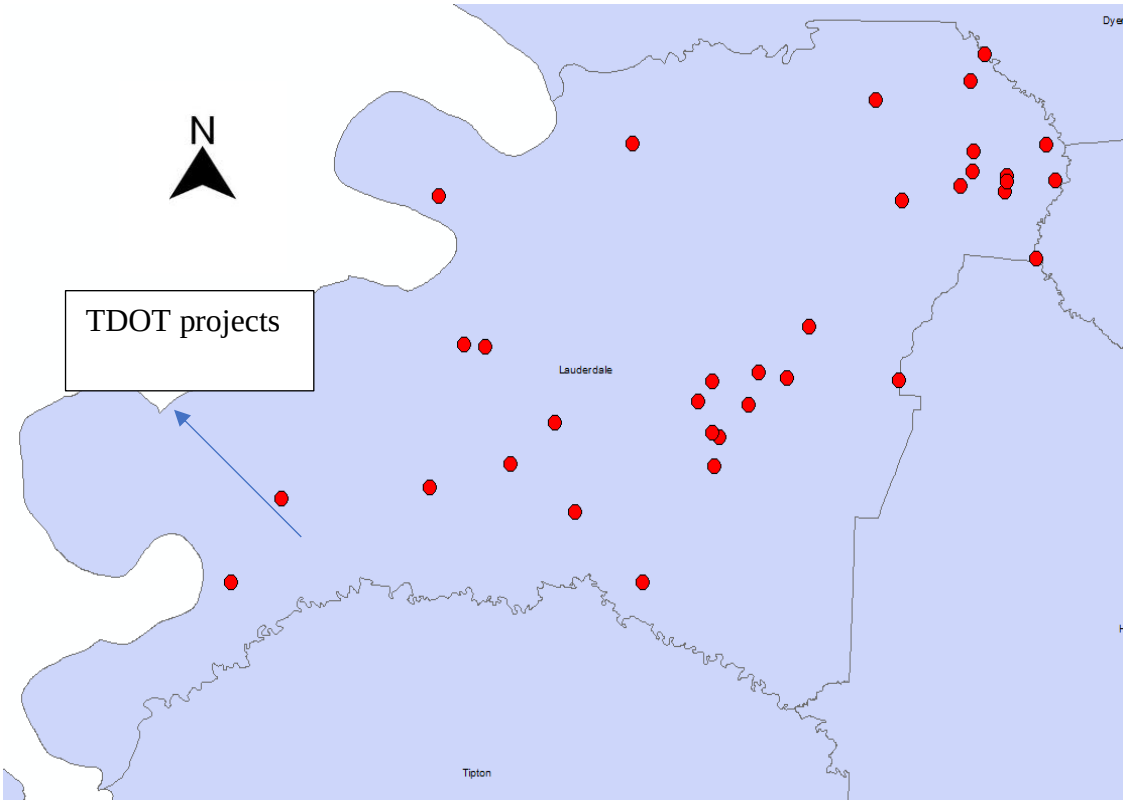

Figure 3.17. TDOT project locations.

Similar to Dyer County, Lauderdale County also consists of three primary surface geologic units: lowland (elevations below 80 meters), intermediate (elevation between 80 and 107 meters), and upland (elevations above 107 meters). Figure 3.18 depicts the surface geology map of Lauderdale County.

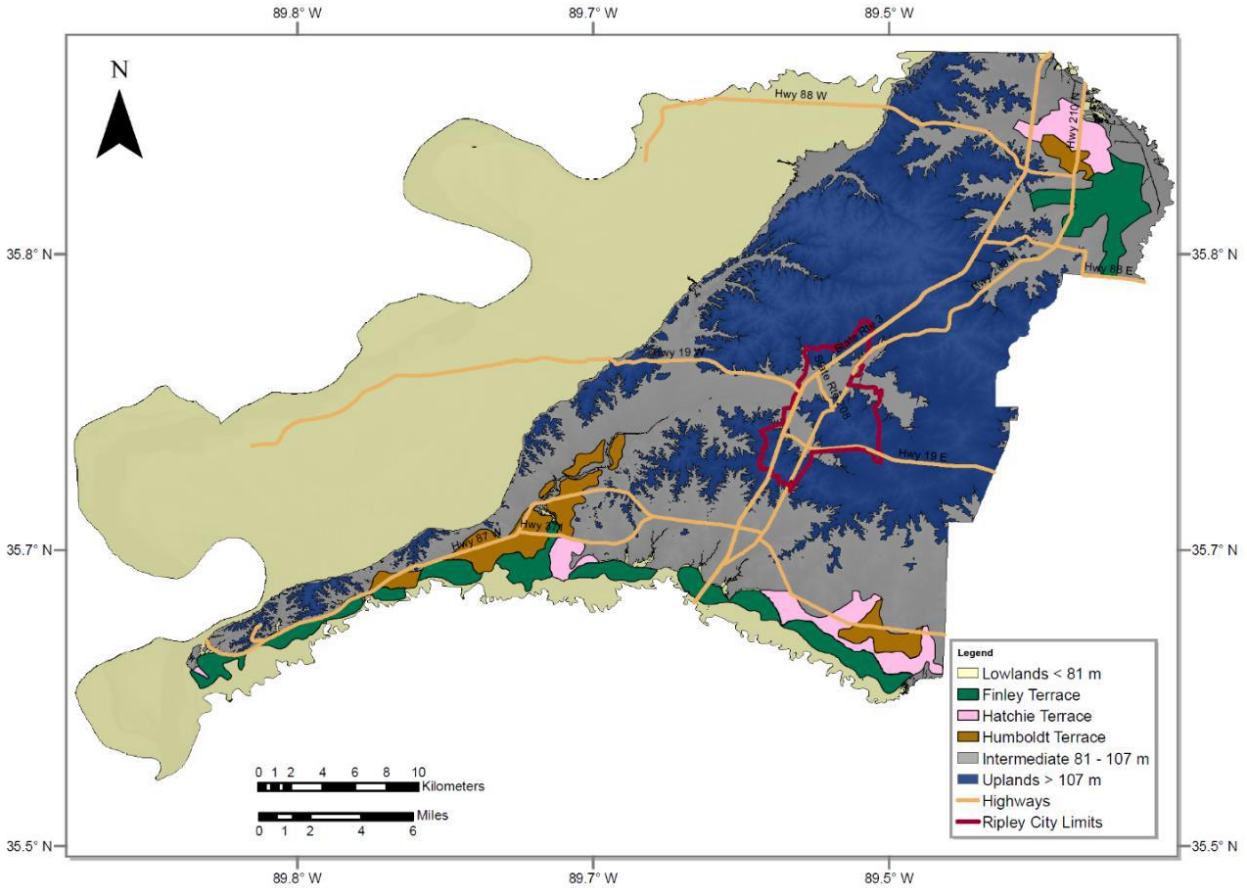

Figure 3.18. Surface geology map of Lauderdale County.

To develop LPCs for each primary surficial geology unit separately, the boring logs had to be classified for each surface geologic unit. The distribution of selected borings from USACE and TDOT on the surface geology map of Lauderdale County is illustrated in Figure 3.19. Among the total of 209 boring logs selected from USACE and TDOT borings, 153 are in the lowland, 47 are

in the intermediate, and 9 are in the upland parts of Lauderdale County. Table 3.11 provides a summary of the geological classification of boring logs.

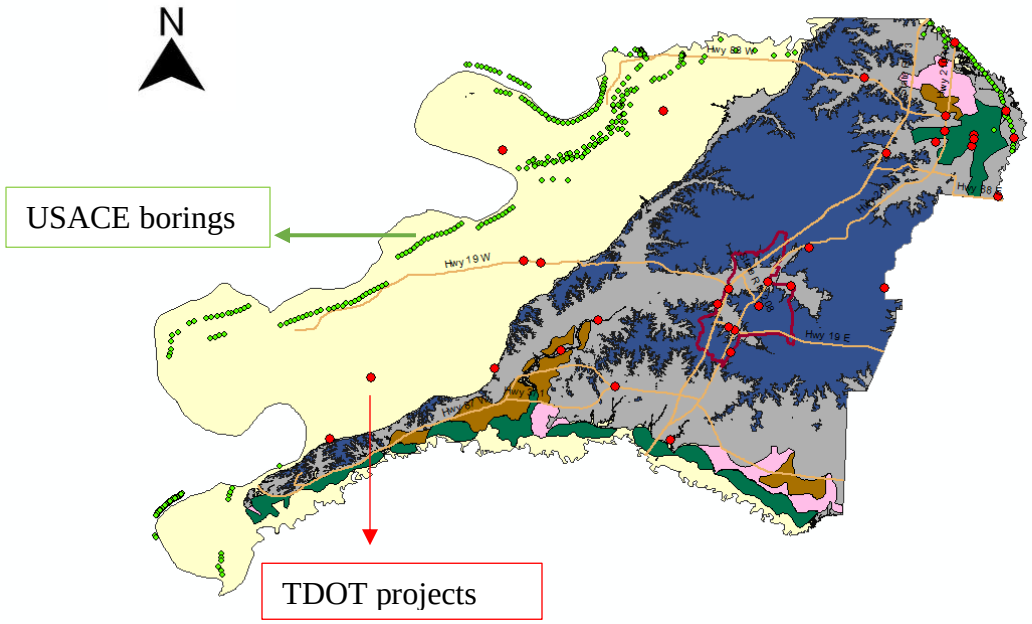

Figure 3.19. Soil boring logs location on the surface geology map.

Table 3.11. Summary of the number of borings in each geology.

	LOWLAND	INTERMEDIATE	UPLAND
TDOT	86	44	8
USACE	67	3	1
TOTAL	**153**	**47**	**9**

To estimate the GWL at each soil boring location within Lauderdale County, the same procedure that was used as for Lake and Dyer counties (Cramer et al., 2019, 2020). The GWL contour map for Lauderdale County was established based on the groundwater level contour map within the surface alluvial aquifer of the Mississippi Embayment developed by Schrader (2008).

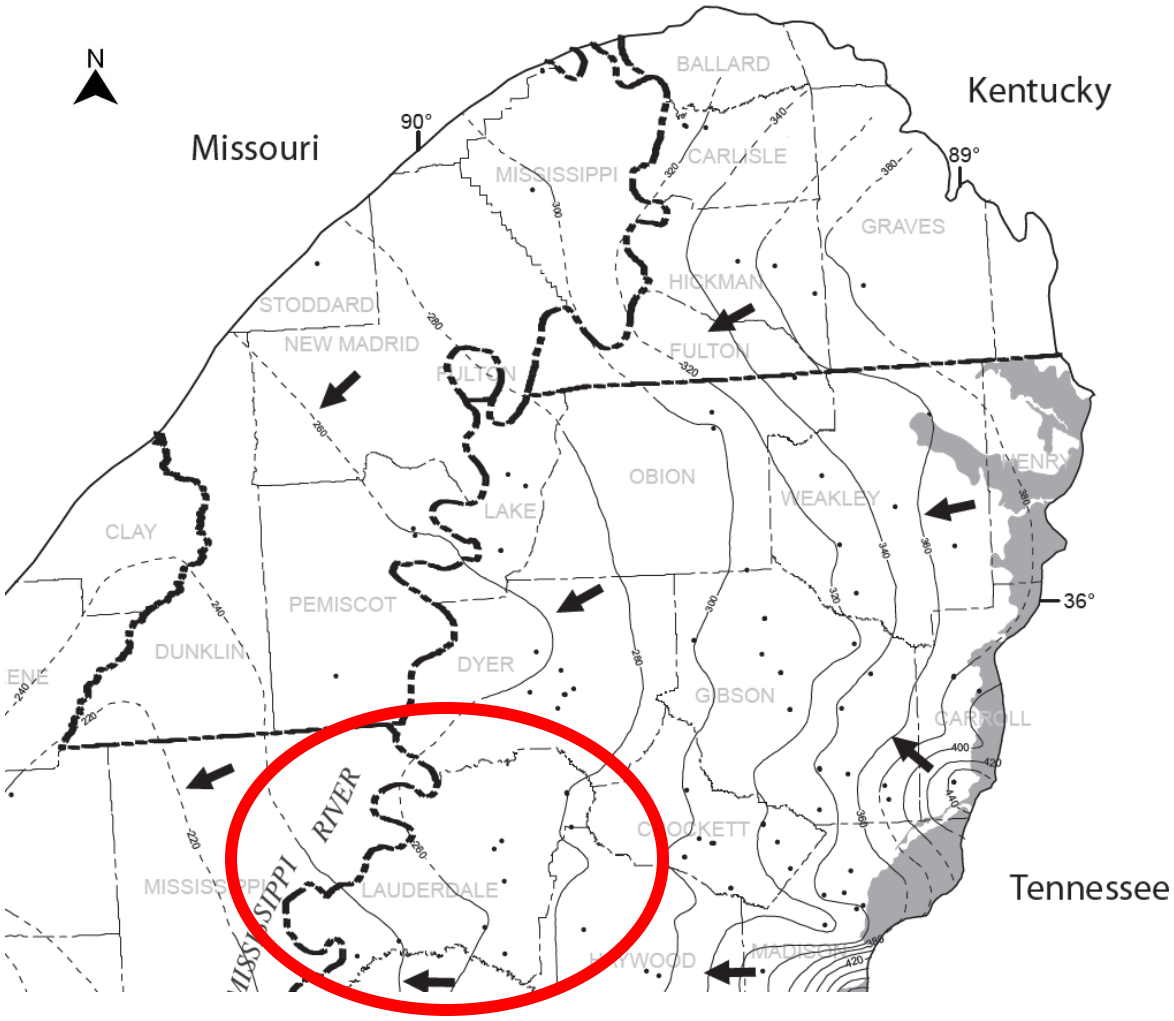

Figure 3.20. USGS groundwater level contour map (Schrader 2008).

To establish the GWL contour map that covers the entire area of Lauderdale County with an appropriate interval between the contour lines, I utilized the contour lines of 200, 220, 240, 260, 280, and 300 ft. National Geodetic Vertical Datum of 1929 (NGVD 29) from Schrader's map (Figure 3.20). The interpolated contour lines were imported in ArcMap and digitized on the 2D boundary shapefile of Lauderdale County. There are various tools to generate a contour map in ArcMap, however, to be consistent with Lake and Dyer counties, the IDW tool was used to create the GWL contour map of Lauderdale County. Figure 3.21 indicates the generated GWL contour map of Lauderdale County in the format of a raster file.

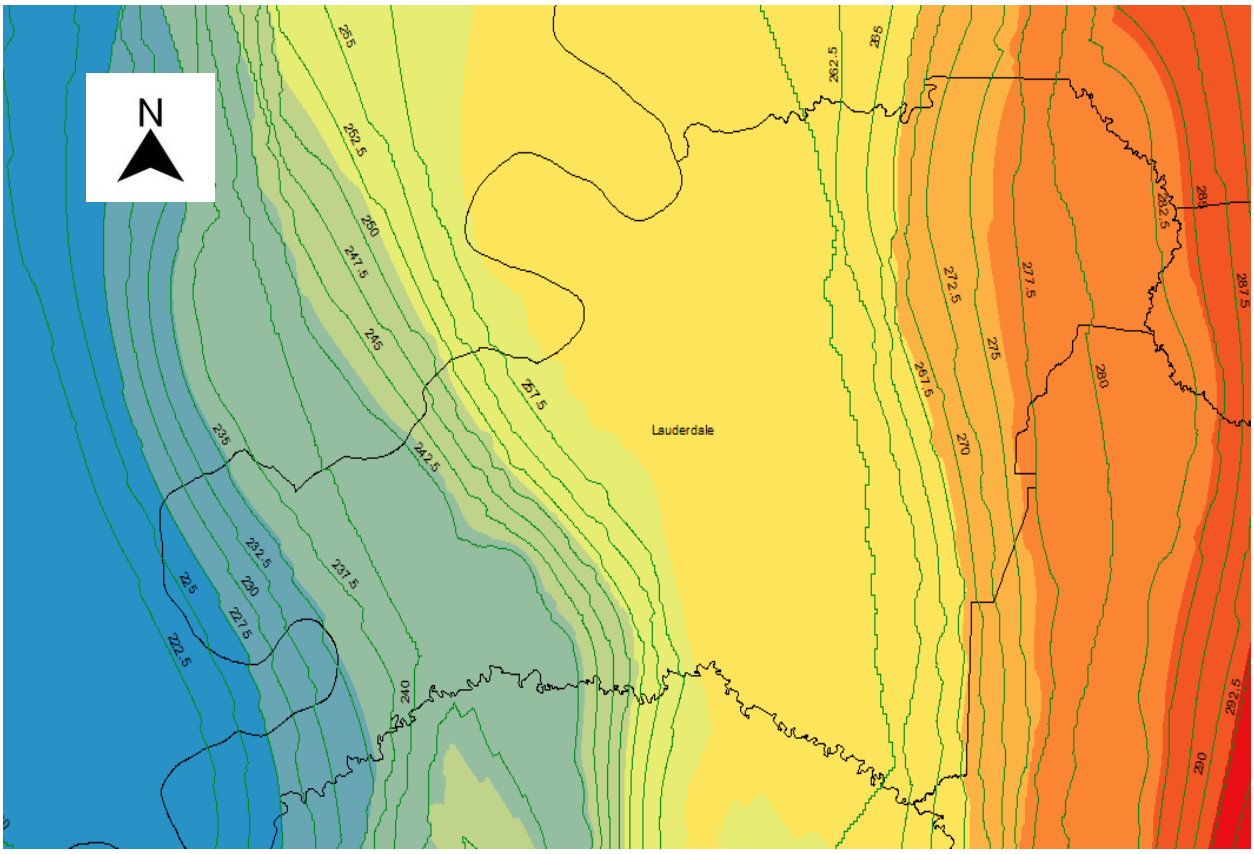

Figure 3.21. Groundwater level contour map for Lauderdale County.

To verify the accuracy of the GWL contour map, additional groundwater data from nine water wells within Lauderdale County were obtained from the United States Geological Survey (USGS) groundwater data website (https://maps.waterdata.usgs.gov). Figure 3.22 shows the location of the USGS wells on the GWL contour map of Lauderdale County.

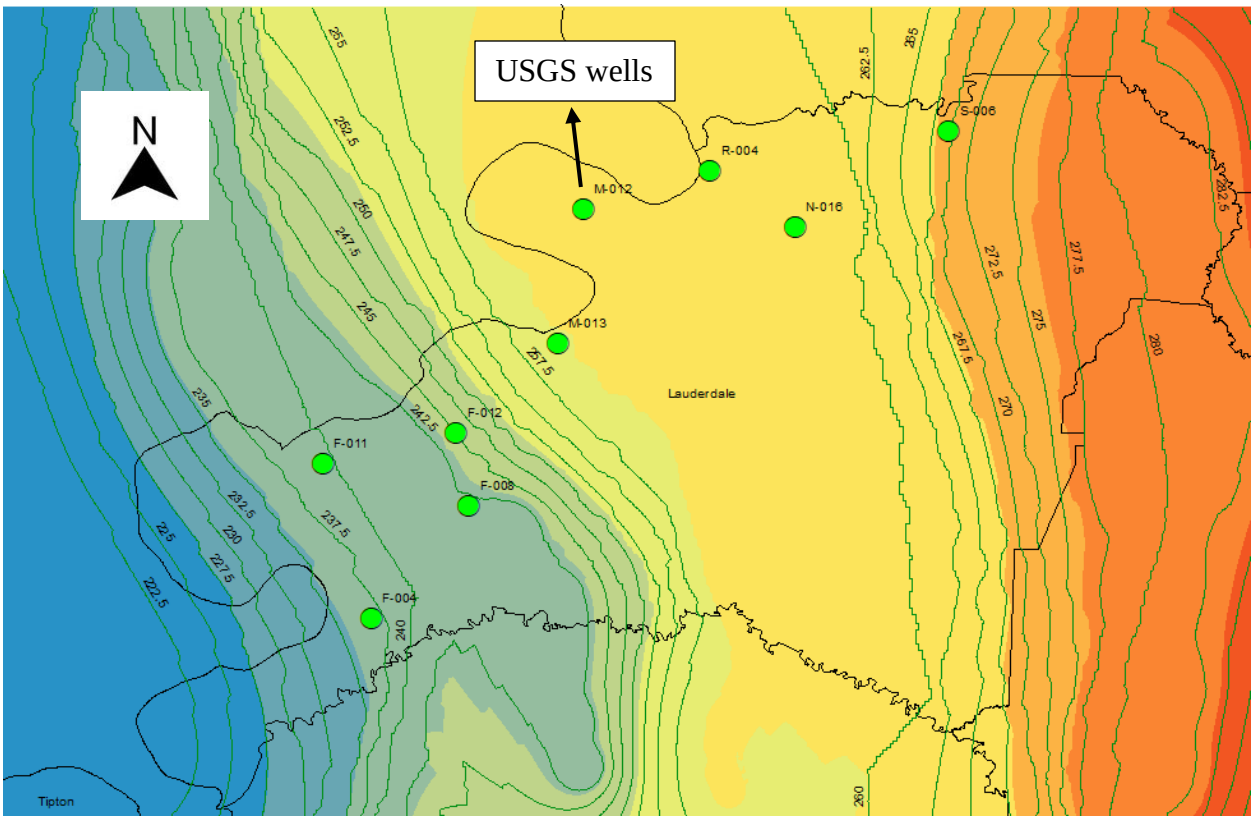

Figure 3.22. Location of USGS wells on the contour map.

By comparing the interpolated GWL of wells from the contour map with the actual groundwater level of wells provided in Table 3.12, there is only a 4.5 ft. difference between the overall average of the actual level of wells and the measured level of wells from the contour map. Besides, it must be considered that because the geodetic datum of GWL data of wells from USGS is NAVD 1988 and the GWL of the contour map is in the geodetic datum of NGVD 1929, the conversion might have impacted the result.

Table 3.12. Comparison of contour map level for USGS wells and the average of lowest and highest readings of wells.

Well ID	Average Readings (ft-NGVD of 1929)	Contour Map (ft-NGVD of 1929)	Difference between contour map and wells readings (ft)
F-009	230	237	+7
F-004	240	237	-3
F-008	236	242	+6
F-011	238	239	+1
F-012	241	245	+4
M-013	252	258	+6
N-016	256	260	+4
M-012	251	260	+9
R-004	258	260	+2
S-006	265	270	+5

3.2.3.4. Tipton County

For Tipton County, a total of 113 SPT soil borings within Tipton County were received from three organizations: USACE, TDOT, and Construction Material Laboratory, Inc. The total number of soil boring logs that were obtained from each organization is provided in Table 3.13.

Table 3.13. Summary of the total number of borings.

Organization	Number of Boring Logs
USACE	53
TDOT	31
Construction Material Lab, Inc.	29
Total	113

For the boring logs of the USACE and soil borings of bridge projects that were received from Construction Material Laboratory, Inc., the coordinate locations were provided by the organizations but like Dyer and Lauderdale counties, the TDOT boring logs did not provide a coordinate location of where the boring was obtained. TDOT data had only a project location map

(without scale) or a general project location description. Using Google Earth and Google Map, the location of the projects was estimated, and the project location was used for all soil borings of a project to find the geologic unit of the borings and to interpolate the GWL of each boring using the GWL contour map described later in this section.

Using the same criteria that were utilized to select SPT soil boring logs of the Lake, Dyer, and Lauderdale counties Seismic and Liquefaction Hazard Maps (Cramer et al., 2019, 2020a, 2020b) in developing the LPCs, the boring logs of Tipton County were selected. Thus, a total of 66 out of 113 received boring logs within Tipton County were selected: 16 from USACE, 33 from 9 TDOT projects, and 17 from Construction Material Laboratory, Inc. Figure 3.23 shows the locations of selected soil boring logs within Tipton County.

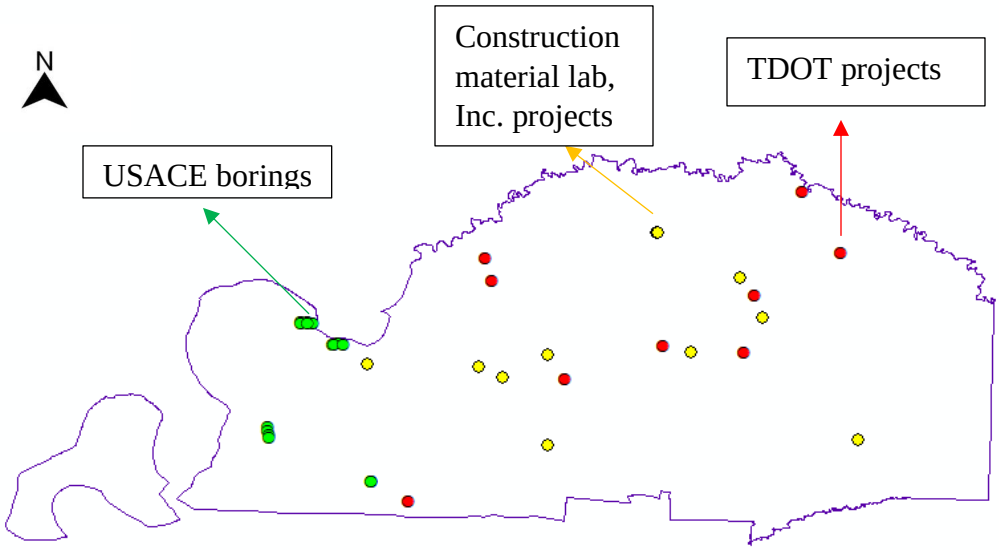

Figure 3.23. Locations of selected USACE SPT borings.

Tipton County consists of three primary geologic units: lowland, intermediate, and upland. Intermediate includes loess overlying Finley, Hatchie, and Humboldt terraces and loess overlying Eocene strata. Figure 3.24 shows the surface geology map of Tipton County.

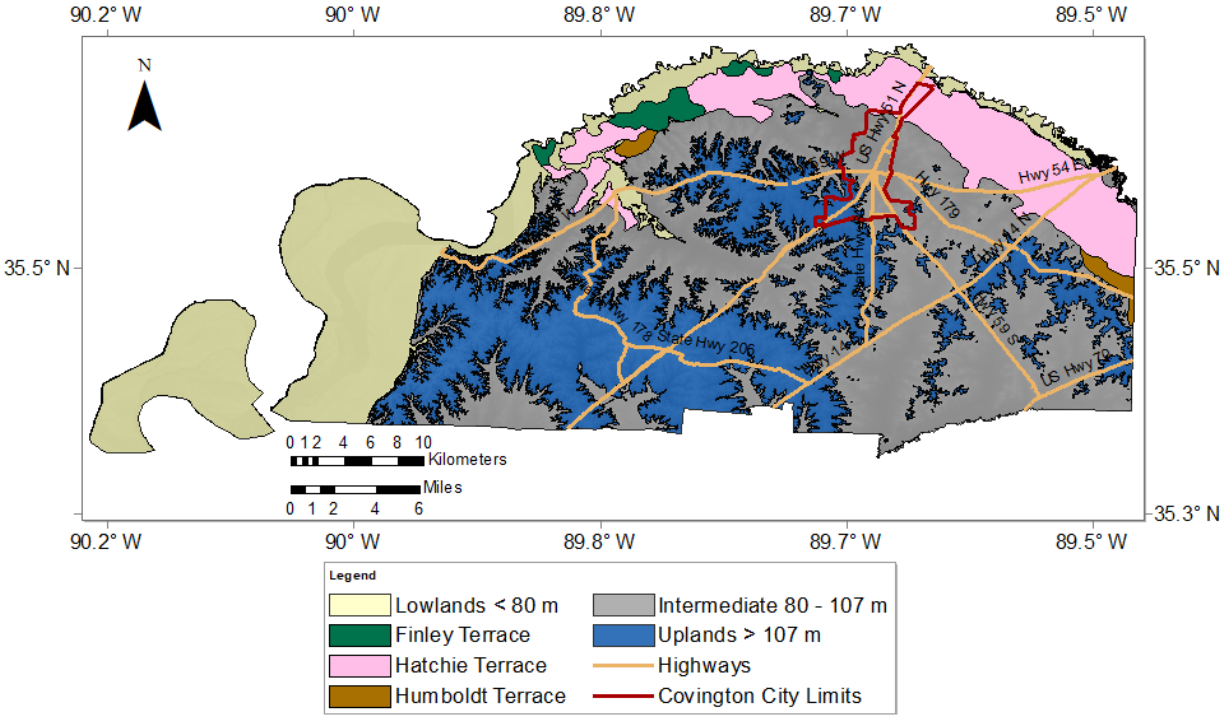

Figure 3.24. Surface geology map of Tipton County.

Like Dyer and Lauderdale counties, due to the variety of surficial geologic units, the selected SPT soil boring logs from the previous section must be classified for each geologic unit to develop specific LPCs for each geologic unit. Figure 3.25 illustrates the distribution of the geologic units and the boring locations in relation to geologic units. Table 3.14 provides the total number of selected boring logs within each geologic unit.

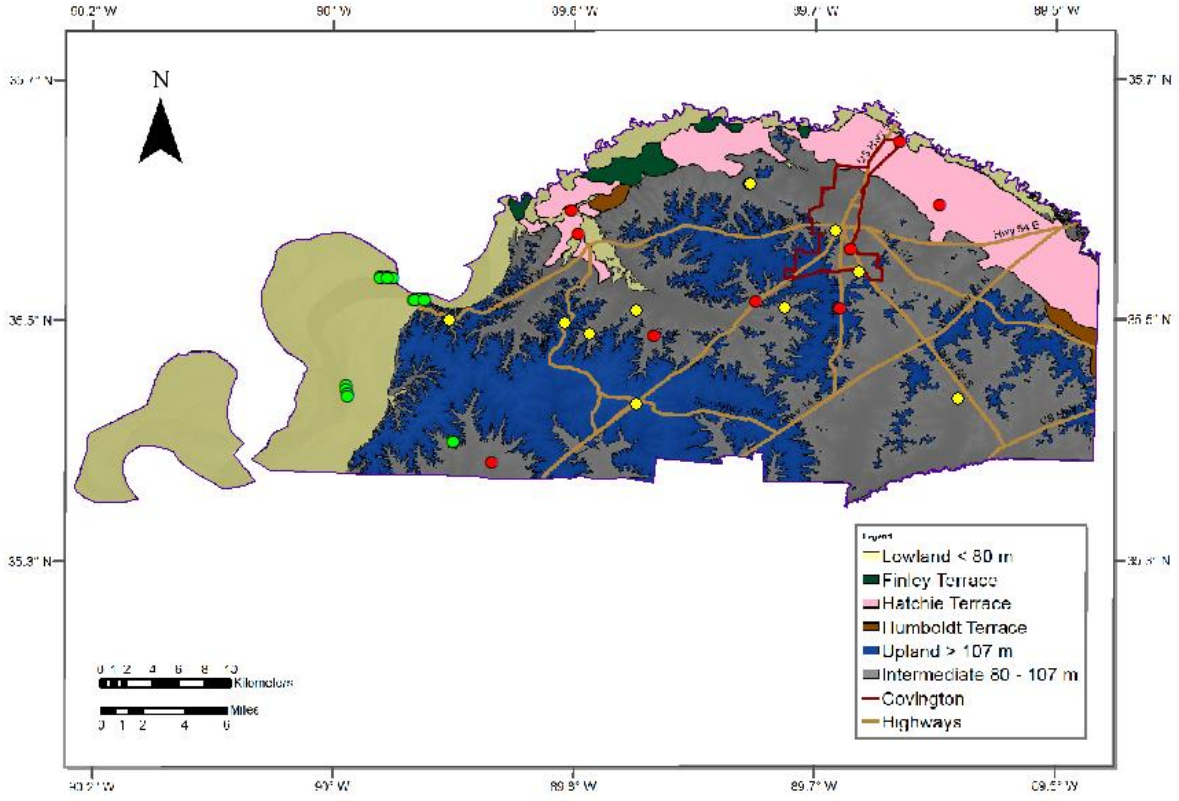

Figure 3.25. Soil boring logs location on the surface geology map.

Table 3.14. Summary of the number of borings in each geology.

Geology	Organization	USACE	TDOT	Construction Material Lab, Inc.	Total
Lowland		13	9	0	22
Intermediate		0	22	12	34
Upland		3	2	5	10

Using the same procedure that was used to find the water level at each soil boring location and project locations of Lake, Dyer, and Lauderdale counties (Cramer et al., 2019, 2020a, b), a GWL contour map to estimate the GWL for Tipton County boring logs was developed. The primary source for establishing the GWL contour map within the surface alluvial aquifer for Tipton County was the GWL contour map shown in Figure 3.26 which was developed by Schrader (2008).

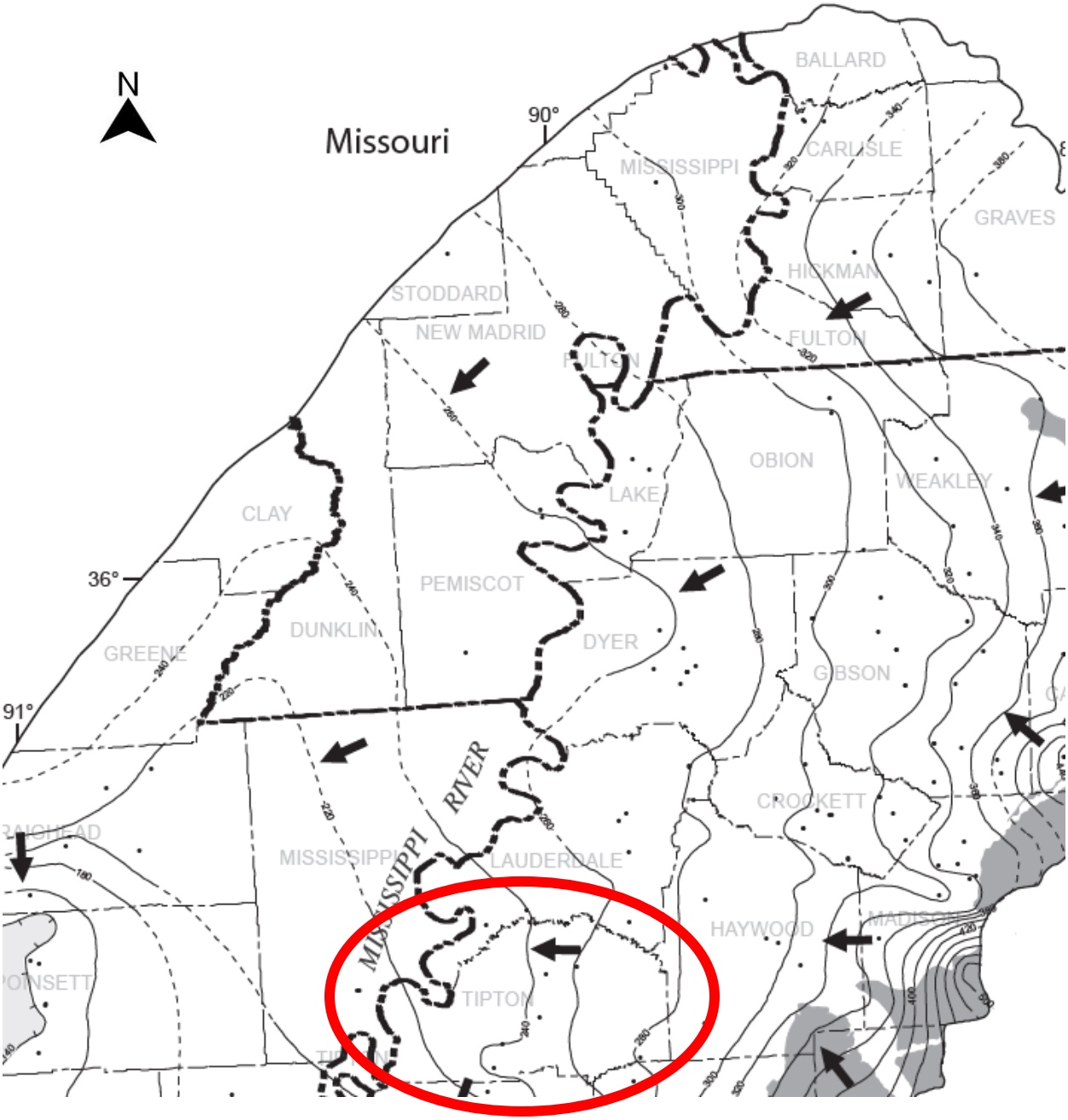

Figure 3.26. USGS groundwater level contour map (Schrader 2008).

By reviewing more reports on the GWL condition of the Mississippi embayment, and according to the studies done by Clark (2011) and Clark and Hart (2009), it has been concluded that Schrader's (2008) map is still the most updated GWL map for this area.

To establish the contour map of Tipton County, the contour lines from Lauderdale, Haywood, and Mississippi counties were interpolated and provided in Figure 15 (all contour lines are in the format of ft.-NGVD 1929). Using ArcMap, the contour lines were digitized on a shapefile boundary of Tipton County (Figure 3.27) and the contour map was developed by the IDW method. Figure 3.28 shows the GWL contour map of Tipton County that was used to develop the LPCs.

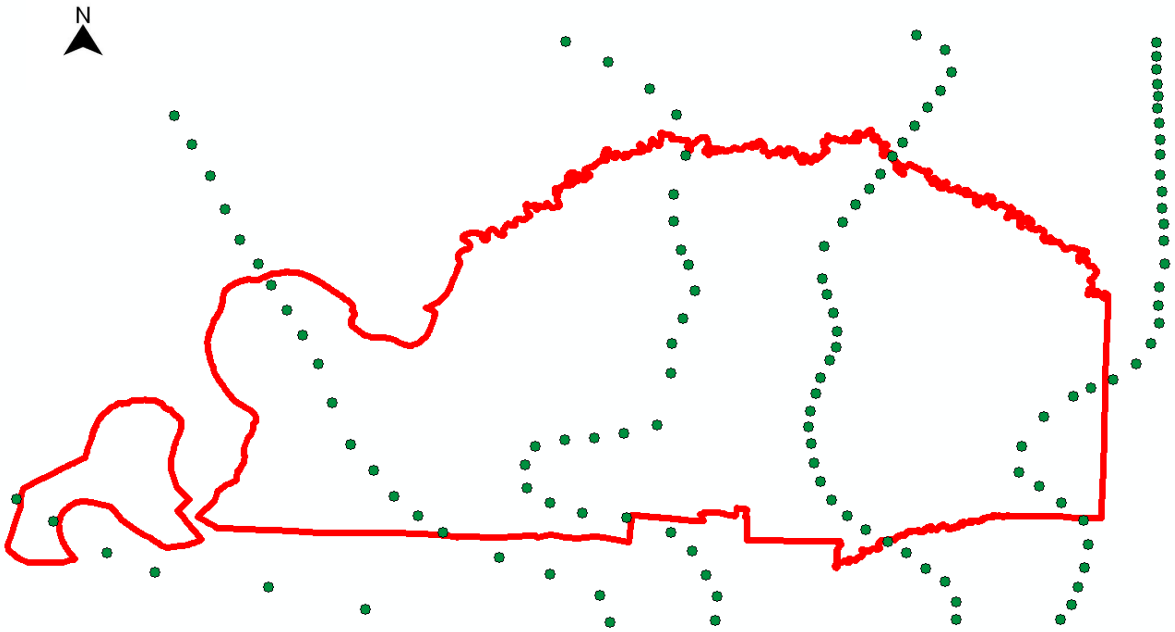

Figure 3.27. Digitized contour lines on Tipton County boundary shapefile in ArcMap.

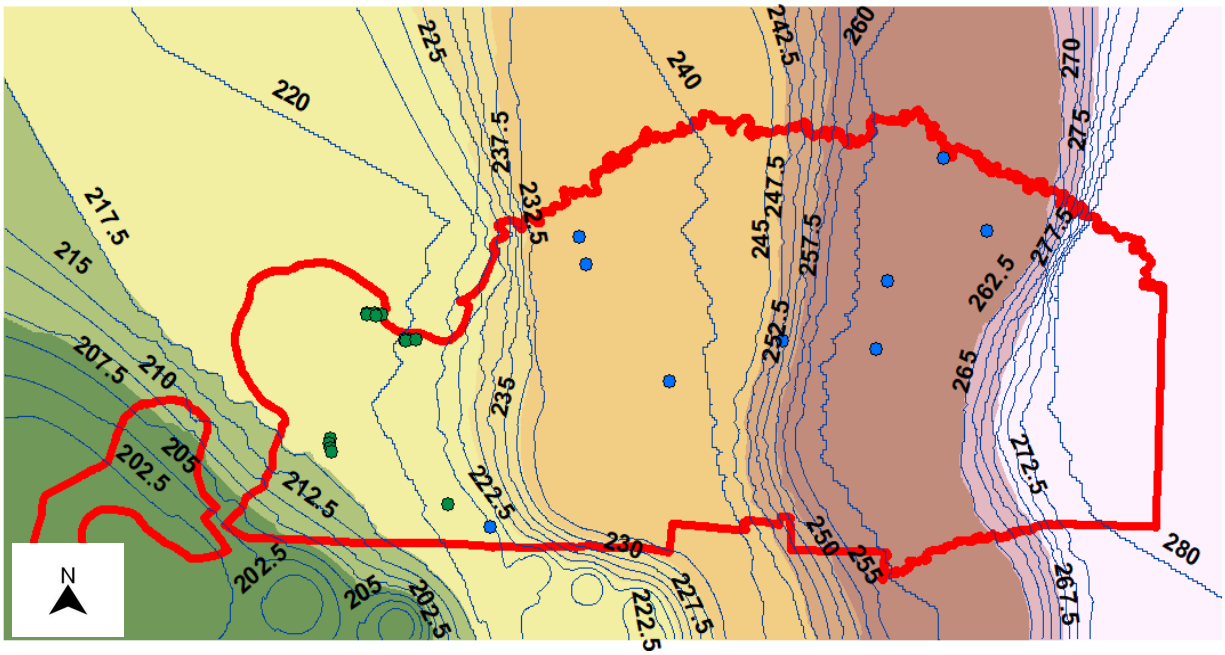

Figure 3.28. Groundwater level contour map for Tipton County.

For Lake, Dyer, and Lauderdale counties, the accuracy of the generated GWL based on Schrader's map was verified by obtaining additional data for wells within Lake, Dyer, and Lauderdale County from the USGS groundwater database (https://maps.waterdata.usgs.gov), but for Tipton County, as it is illustrated in Figure 3.29 there is only one inactive well available within Tipton County from the USGS database.

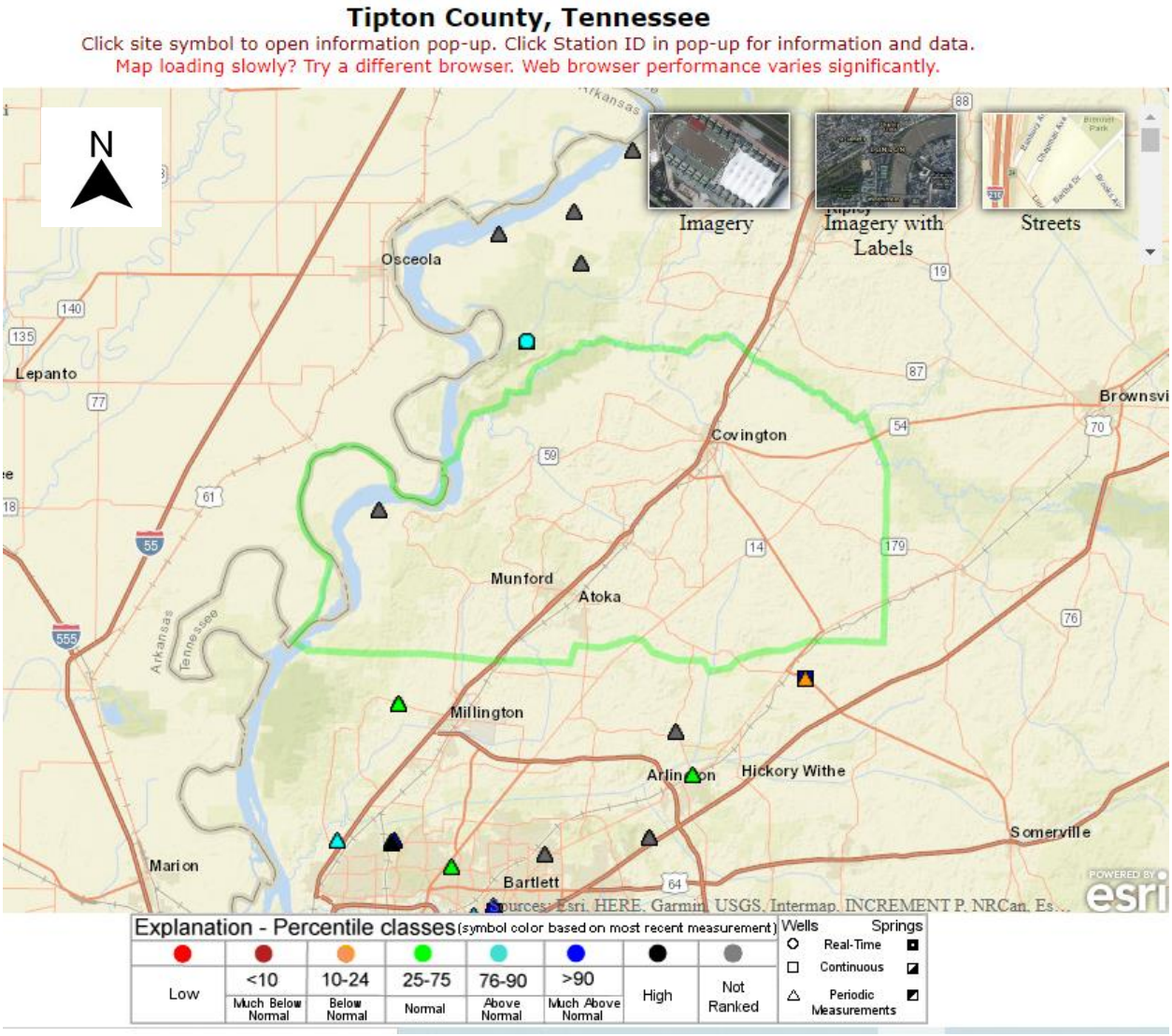

Figure 3.29. Location of the only USGS well in Tipton County.

3.2.4. Summary of Analysis of Four Western Tennessee Counties

Lake, Dyer, Lauderdale, and Tipton counties consist of three primary geologic units (Lowlands, Intermediates-terraces, and Uplands) that differ in their elevation and near-surface geology. A general description of these units is provided herein based on Cramer et al. (2018, 2019, 2020a, b, 2021, and 2022) and Saucier (1994). The Lowlands are at an elevation of < 80 m (269 ft) and consist of Holocene Mississippi River floodplain alluvium (Saucier, 1994, and

Rittenour et al., 2007). In general, the alluvium consists of surface silt and clay overbank sediment that overlies laterally accreted sand and gravel sediment deposited by the Mississippi River (Cramer et al., 2019, 2020a, b, 2021, and 2022). Saturated sand deposits are prevalent in the Mississippi River floodplain within the Lowland unit. Therefore, the Lowlands unit is the most liquefaction-prone geologic unit in west Tennessee.

Between elevations of 82 m (269 ft) and 107 m (351 ft) are the Intermediate and terrace units. Intermediate units are differentiated into river terraces of the Obion and Forked Deer rivers and areas where loess (wind-blown silt) overlies Eocene strata. The terraces have been mapped from topographically highest to lowest as the Humboldt, Hatchie, and Finley terraces (Saucier, 1987, and Rodbell, 1996). All Intermediate units are covered with Peoria loess. Except for the Finley terrace, the rest of the Intermediate surfaces have older loess units beneath the Peoria loess (Rodbell, 1996). Beneath the loess, the terrace strata consist of silt and clay overbank sediment and underlying laterally accreted sand and gravel sediment.

The Uplands unit is at elevations > 107 m (351 ft). The Uplands unit is a loess-covered high-level terrace of the ancestral Mississippi/Ohio river system (Van Arsdale et al., 2007, and Odom et al., 2020). This high-level terrace alluvium, called the Upland Complex, consists of sand and gravel that is regionally a major source of aggregate (Van Arsdale, 2012, and Lumsden et al., 2016).

Subsurface data that was collected for each county consisted of soil boring logs with Standard Penetration Test (SPT) resistance values or “N-values”, Unified Soil Classification System (USCS) classifications, and groundwater level data. Boring logs were obtained from the Memphis District of the U.S. Army Corps of Engineers (USACE), Tennessee Department of Transportation (TDOT), Tennessee Department of Economic and Community Development

(TNECD), Construction Materials Laboratory, Inc., and Joel B. Spaulding & Company, Inc. Table 3.15 provides the total number of selected boring logs within the Lowlands geologic unit of each county. A total of 419 soil boring logs were utilized for the liquefaction evaluation in this research.

Table 3.15. The total number of SPT soil borings within the lowlands of each County.

County	Total Number of Borings
Lake	34
Dyer	118
Lauderdale	153
Tipton	22
Total	**419**

Figure 3.30 shows the distribution of the selected soil boring logs within the Lowlands geologic unit of the five counties.

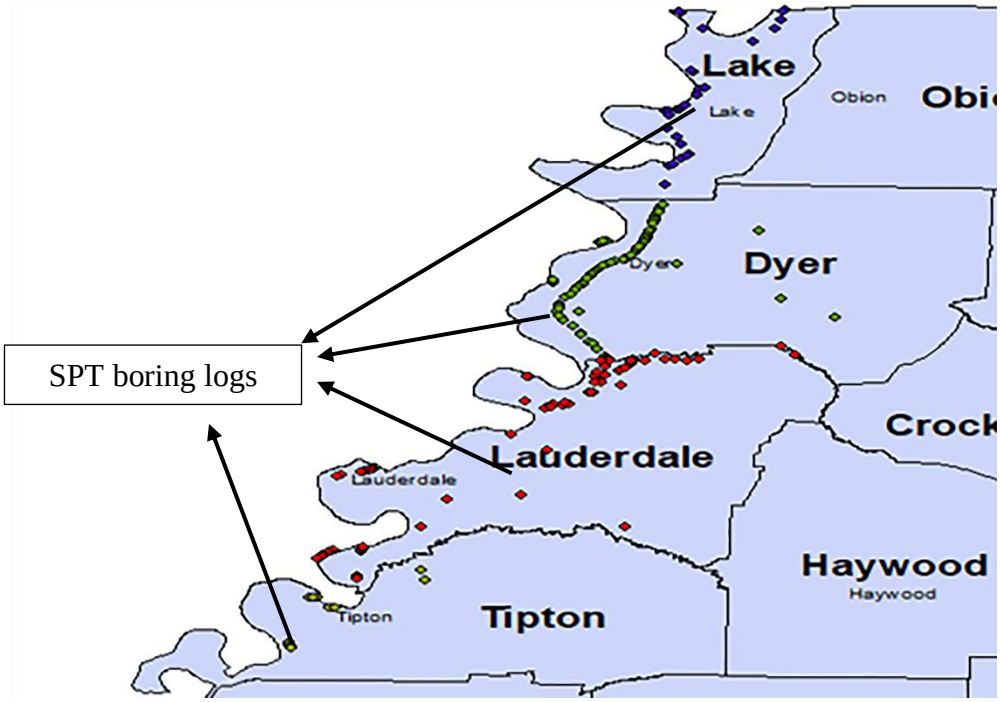

Figure 3.30. Distribution of soil borings within each County.

Many of the boring logs did not specify if the groundwater levels included in the logs were water levels encountered during drilling, immediately upon completion of drilling, or a period after

completion of drilling. Additionally, borehole cave-in depths were not included. As Christopher and Schwartz (2006) noted, due to the potential for cave-in, infiltration, and seasonal changes in groundwater levels, a borehole is not usually the best tool to estimate the long-term groundwater level conditions at a site, unless the soils are granular with minimal to no fines content (Cramer et al., 2015). Therefore, groundwater levels at the boring locations were estimated from a groundwater elevation contour map of the surface alluvium aquifer developed by Schrader (2008). Figure 3.31 shows Schrader's groundwater elevation contour map, which is based on the National Geodetic Vertical Datum (NGVD) of 1929, that extends through Lake, Dyer, Lauderdale, Tipton, and Shelby counties.

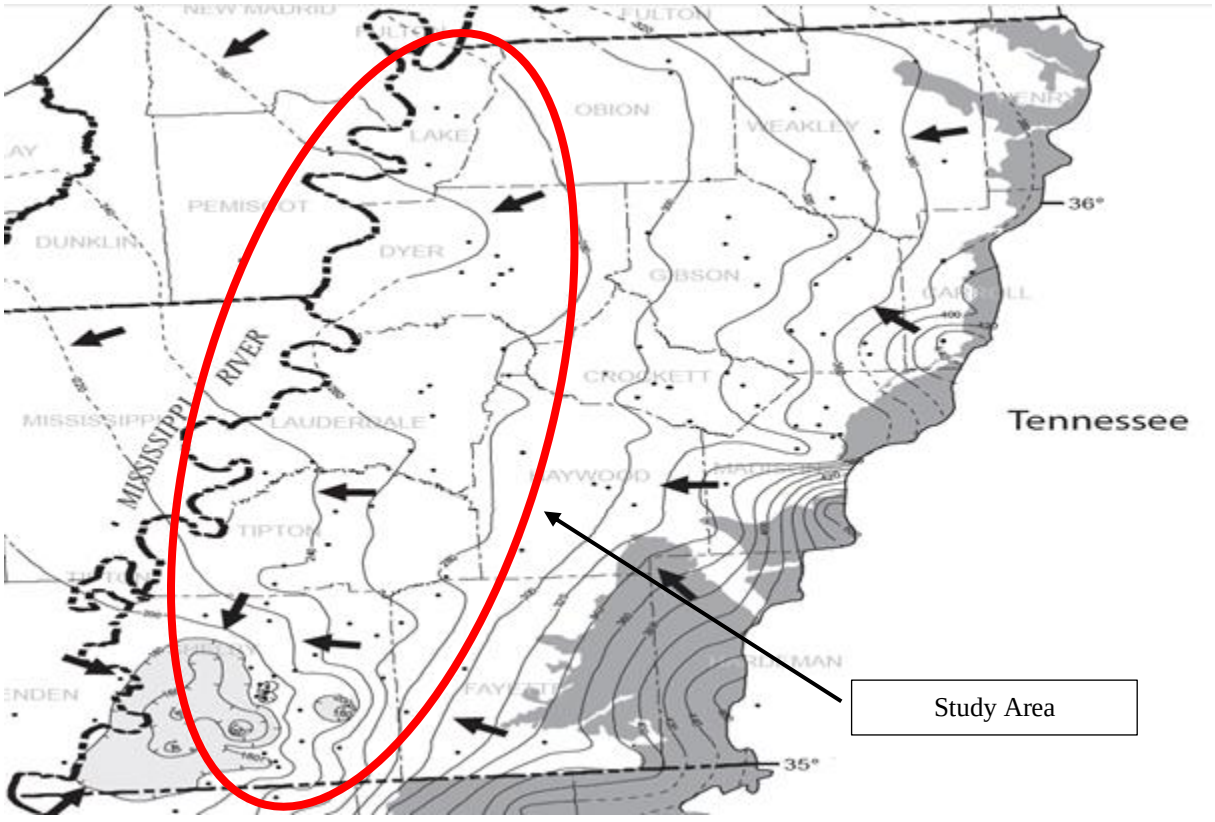

Figure 3.31. USGS groundwater level contour map (Schrader 2008) in the surface alluvium aquifer.

To establish the contour map of Lake, Dyer, Lauderdale, and Tipton counties (Cramer et al., 2019, 2020a, b, 2021, and 2022), the contour lines from Schrader's map (Figure 3.31) were interpolated. Using ArcMap, the contour lines were digitized on a shapefile boundary of five counties and the contour map was developed by the IDW method. Finally, the GWL at each soil boring location was interpolated from the contour map. To verify the accuracy of the GWL contour map that was generated based on Schrader's map in this study, additional groundwater data from wells within the area of study were obtained from the United States Geologic Survey (USGS) groundwater database (https://maps.waterdata.usgs.gov). The USGS wells were placed on the GWL contour map and the GWL at each USGS well location was interpolated. The interpolated GWL of wells from the contour map was compared with the actual measured GWL of USGS wells and the difference between the actual level of wells and the measured level of wells from the contour map was negligible.

3.3. Numerical Modeling

FLAC software was chosen to perform the liquefaction analysis in this study because of its capability of performing dynamic analysis and the flexibility of defining various soil models for various soil behaviors such as compressibility, elasticity, creep, shear strength, stiffness, partial saturation, etc. Additionally, FLAC has the capability of determining critical liquefaction-related soil properties such as excess pore water pressure, pore pressure ratio, shear stress, shear strength, and shear strain, and the capability of performing linear and non-linear site response analysis. The subsequent section goes through details of the Finite Difference Methods (FDM) that FLAC uses as numerical solutions to solve the differential equations.

3.3.1. Finite Difference Method Using FLAC

FDM is a numerical method to solve a set of differential equations representing complex material behaviors such as large displacements, large strains, linear and non-linear material behavior, failure, and total collapse with initial and boundary conditions (Itasca, 2011). In FLAC, the finite difference methods are used to replace the equations in every derivative with an algebraic expression in the form of field variables such as stress and displacement, and then explicit time marching methods are utilized to solve the algebraic expression of derivatives. Figure 3.32 shows a basic explicit calculation cycle that is performed by FLAC.

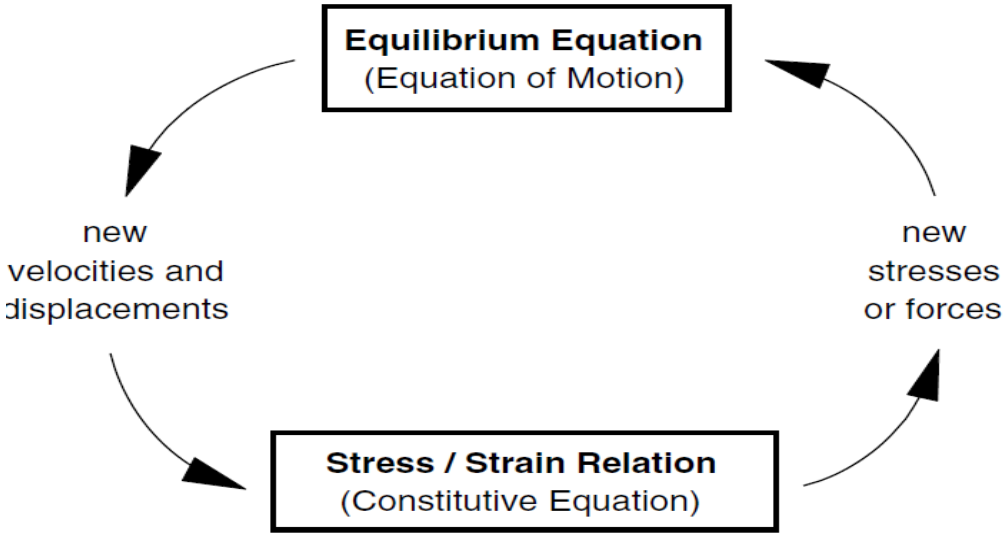

Figure 3.32. Basic explicit calculation cycle (Itasca, 2011).

Generally, finite difference methods can resolve the finite difference equations at the start of every step in an iterative solution system and displacements and strains of each grid point of the mesh are updated in every timestep. Since the materials move and deform relative to initial

boundary conditions, the mentioned procedure is known as the Lagrangian essence of the FLAC tool (Ziotopoulou, 2015).

FLAC does not simulate liquefaction directly. Instead, using the coupled dynamic-groundwater-flow calculations, FLAC monitors and analyzes the pore pressure build-up during dynamic loading of the earthquake and the resulting decrease in effective stress of the soil profile. Many alternative models try to simulate pore pressure buildup; however, they typically do not do it right because they are based on the results of specific laboratory experiments (Itasca, 2011). In a computer simulation, the stress-strain paths must be defined arbitrarily so that, based on the stress-strain paths, a robust and adequate model of pore pressure build-up with a simple formulation is derived. The computer model of pore pressure build-up must not be couched in terms that apply solely to specific laboratory tests (Itasca, 2011). FLAC has robust built-in stress-strain models which are strong and simple that account for the basic physics of pore pressure build-up and not just specific laboratory tests. In reality, cyclic loading of earthquakes has two main effects that cause liquefaction occurrence. The primary effect is the volume change of the soil skeleton that will result in strain and the secondary effect is the pore pressure build-up. It must be noted that the secondary effect of earthquake cyclic loading, which is the build-up of pore pressure, would not happen if the primary effect (volume change of the soil skeleton) does not occur and it remains constant (Itasca, 2011). FLAC models do consider both effects of cyclic loading of earthquakes and by coupling the primary effect to the secondary effect, simulates the build-up of pore pressure; consequently, liquefaction.

FLAC, as with any numerical software program, relies on the use of various models. Some of those models, such as simple and comprehensive models of liquefaction analysis that are available in FLAC to model different aspects of liquefaction, will be discussed later in this section.

Two simple built-in models of FLAC for liquefaction analysis problems include the Finn-Martin and Finn-Byrne models.

3.3.2. Finn-Martin Model

According to FLAC dynamic analysis manual (Itasca, 2011), the Finn-Martin model is extracted from Martin et al. (1975). In the Finn-Martin model, the following equation is used to relate the change in volume due to cyclic loading of an earthquake to the shear strain of the soil:

$$\Delta\varepsilon_{vd} = C_1(\gamma - C_2\varepsilon_{vd}) + \frac{C_3\varepsilon_{vd}^2}{\gamma + C_4\varepsilon_{vd}} \tag{3.14}$$

where is $\Delta\varepsilon_{vd}$ change in volume, γ is the shear strain, and C_1 to C_4 are constants such that $C_1 \cdot C_2 \cdot C_4 = C_3$

3.3.3. Finn-Byrne Model

The other built-in model of FLAC to perform liquefaction analysis is the Finn-Byre model, which is based on a relationship presented by Byrne (1991) as follows:

$$\frac{\Delta\varepsilon_{vd}}{\gamma} = C_1 \exp\left(-C_2\left(\frac{\varepsilon_{vd}}{\gamma}\right)\right) \tag{3.15}$$

where C_1 and C_2 are constants with a relationship of $C_2 = \frac{0.4}{C_1}$.

The Finn models of FLAC can be coupled with the Mohr-Coulomb soil plasticity model; however, users can modify the models. To capture the accurate mechanism based on Equations 3.14 and 3.15, the constants in each of the equations are derived from the original method proposed by Martin et al., and Byrne, respectively. For example, Byrne (1991), proposed that the constants

of Equation (3.15) can be computed from relative density, which can be estimated from field test data such as SPT by Equations (3.16) to (3.19).

$$C_1 = 7600(D_r)^{-2.5} \tag{3.16}$$

in which D_r is the relative density of soil and is calculated using an empirical relationship of:

$$D_r = 15(N_1)_{60}^{0.5} \tag{3.17}$$

Thus:

$$C_1 = 8.7(N_1)_{60}^{-1.25} \tag{3.18}$$

$$C_2 = \frac{0.4}{C_1} \tag{3.19}$$

In this study, due to the simplicity of the Finn-Byrne model, it is used for preliminary liquefaction analysis of the model. The Finn models are known as simple constitutive models because they are based on simple formulations.

3.3.4. Comprehensive FLAC Models of Liquefaction Analysis

In addition to simple formulation models of liquefaction analysis, FLAC also has some comprehensive constitutive models to conduct liquefaction analysis which are introduced here but not discussed in detail.

According to the FLAC manual (Itasca, 2011), the liquefaction analysis procedure based on the current state of practice is defined as a three-step procedure:

1. Triggering evaluation: by computing the factor of safety against liquefaction that is done by comparing the CSR to the CRR.
2. Flow slide assessment: that is carried out based on post-liquefaction strengths in liquefied zones. The post-liquefaction strength analysis can be evaluated from empirical charts such as those developed by Seed and Harder (1990) and Olson and Stark (2002).
3. Seismic displacement: in this step, displacements of the soil mass due to seismic shaking are obtained by solving the equation of motion using the Newmark approach (1965).

The comprehensive built-in FLAC models to analyze the liquefaction based on the above three steps are classified as:

- Total-Stress Synthesized Procedure
- Loosely Coupled Effective-Stress Procedure
- Fully Coupled Effective-Stress Procedure
- Fully Coupled Effective-Stress Bounding-Surface Procedure

In particular, the comprehensive constitutive soil models of FLAC for liquefaction analysis provide hysteretic loops and volume change of the model during dynamic loading. However, simple formulation models such as the Finn models of FLAC to conduct liquefaction analysis can be coupled with a simple elastic/plastic model of material behavior (such as Mohr-Coulomb) to model the liquefaction (Itasca, 2011). Additionally, the comprehensive models of FLAC for liquefaction analysis are very complicated and too hard to justify in engineering practice due to many uncertainties regarding soil properties and earthquake motions (Itasca, 2011). Therefore, the simple Finn liquefaction models are initially used with the Mohr-Coulomb soil model in this study since they can be defined based on the field test data such as SPT (which is available for the West Tennessee area) and other simple properties such as shear and elastic modulus.

The standard built-in constitutive models such as Mohr-Coulomb in FLAC do not model the liquefaction process directly. According to the FLAC manual, the standard practice approach for liquefaction analysis of earthquake loading is based on a total stress analysis in which it is assumed the soil model remains undrained at the in-situ void ratio. Basically, the liquefaction analysis in FLAC is being done based on undrained shear strength (S_u) and a relationship between SPT N-value and S_u from Terzaghi and Peck, 1967 which is provided in Table 3.16.

Table 3.16. Approximate ranges of S_u and SPT-N (Terzaghi and Peck 1967).

Consistency	SPT-N values	Undrained shear strength (C_U) (kPa)
Very soft	0 - 2	0 – 12.5
Soft	2 - 5	12.5 - 25
Medium stiff	5 - 10	25 - 50
Stiff	10 - 20	50 - 100
Very stiff	20 - 30	100 - 200
Hard	>400	>200

To perform liquefaction analysis with either the simple or comprehensive liquefaction models of FLAC, one of the main parameters that is required to be defined is damping. Damping plays an important role in both linear and non-linear methods of modeling wave transmission in layered soil profiles and dynamic soil-structure interaction. Damping is discussed in the next section.

3.3.5. Damping

To analyze the wave propagation in soil and rock due to dynamic loading and ground shaking, because of energy loss in materials, some degree of damping must be considered. Four damping models that are provided in FLAC include the Rayleigh, hysteretic, local, and artificial

damping. In the case of using plasticity soil models such as Mohr-Coulomb, the FLAC manual recommends the use of hysteretic and Rayleigh damping for dynamic analysis because they provide energy dissipation at even very low cyclic strain levels. Therefore, since the Mohr-Coulomb soil model is used in this study, a summary of both Rayleigh and hysteretic damping models is provided next.

Rayleigh damping is almost a frequency-independent damping, and it is utilized when the frequency range is restricted and the system is time-domain based (Itasca, 2011). It can be used for both linear and non-linear systems of seismic analysis in FLAC. Originally, Rayleigh damping is dependent on mass and stiffness and is defined in a format of a linear matrix as follows:

$$C = \alpha M + \beta K \tag{3.20}$$

where C is a damping matrix, M is a mass component matrix, K is the stiffness component matrix, α is the mass-proportional damping constant, and β is the stiffness proportional damping constant.

According to Bathe and Wilson (1976), the critical damping ratio at a specific angular frequency in a system with multiple degrees of freedom can be computed by:

$$\alpha + \beta\omega_i^2 = 2\omega_i\xi_i \tag{3.21}$$

where ξ_i is critical damping ratio (fraction of critical damping), and ω_i is the angular frequency of the system. For Rayleigh damping, FLAC provides some options in which users can define a critical damping ratio based only on the mass component or the stiffness component, or both mass and stiffness components. Therefore, as shown in Figure 3.33, Itasca (2011) presents three curves for the variation of normalized critical damping ratio for the different options.

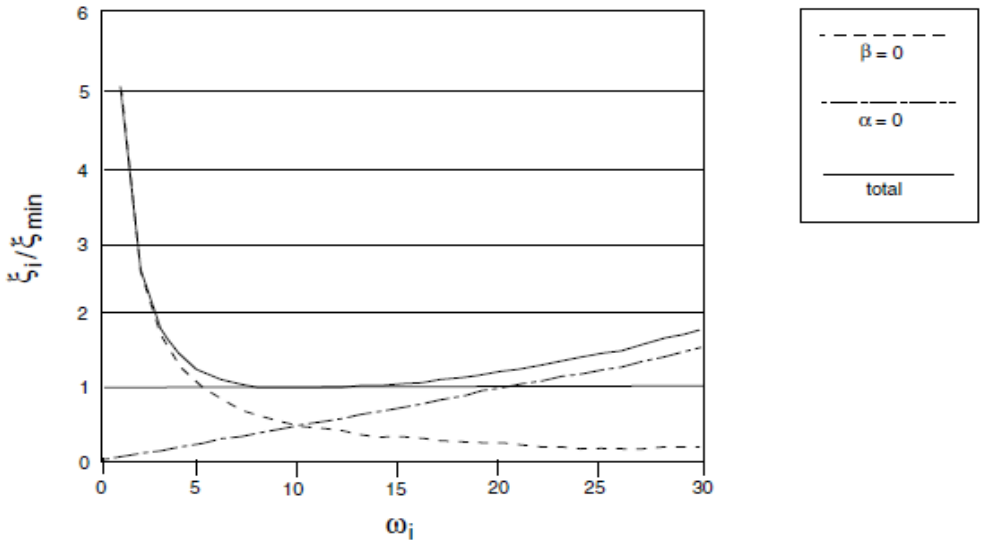

Figure 3.33. Variation of normalized critical damping ratio with angular frequency (Itasca, 2011).

Users can define appropriate damping by entering the center frequency (f_{min}) and minimum critical damping ratio (ξ_{min}) of the material using the curves shown in Figure 3.35 and the following equations.

$$\xi_{min} = (\alpha\beta)^{0.5} \tag{3.22}$$

$$\omega_{min} = (\alpha/\beta)^{0.5} \tag{3.23}$$

$$\alpha = \xi_{min} \cdot \omega_{min} \tag{3.24}$$

$$\beta = \xi_{min/}\omega_{min} \tag{3.25}$$

$$f_{min} = \omega_{min}/2\pi \tag{3.26}$$

For fully non-linear or equivalent linear analyses, hysteretic damping can be used. Hysteretic damping is time-dependent damping, not frequency-dependent. Hysteretic damping within FLAC incorporates strain-dependent modulus and damping functions. FLAC incorporates the modulus degradation curves of Seed and Idriss (1970) and Sun et al. (1988) for sand and clay, respectively. Degradation curves for sand and clay are shown in Figures 3.34 and 3.35, respectively. Based on the curves provided in Figures 3.34 and 3.35, the hysteretic damping in FLAC is formulated by:

$$\bar{\tau} = M_s\gamma \tag{3.27}$$

where M_s is the strain-dependent normalized secant modulus, γ is the shear strain, and $\bar{\tau}$ is the normalized shear stress which is:

$$\bar{\tau} = \tau/G_o \tag{3.28}$$

where G_o is the small strain shear modulus. By obtaining the secant modulus from Equation (3.27), the normalized tangent modulus (M_t) can be computed by:

$$M_t = M_s + \gamma\frac{dM_s}{d\gamma} \tag{3.29}$$

Based on the hysteretic damping formulations, the mean shear strain tensor of each cell of the model is computed before constitutive model functions are determined. A cell in FLAC is defined as an area between every four grids and it is usually a square shape except around the boundaries.

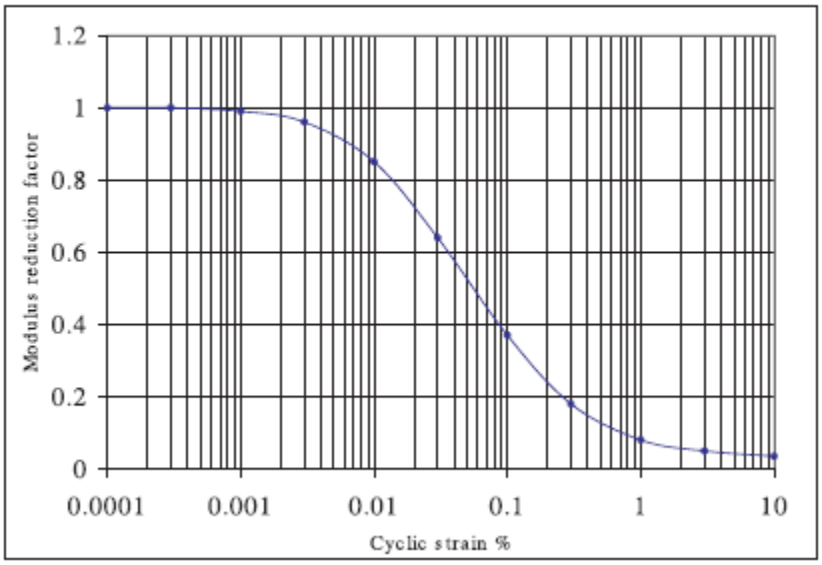

Figure 3.34. Modulus reduction curve for sand presented by Seed and Idriss, 1970 (Itasca, 2011).

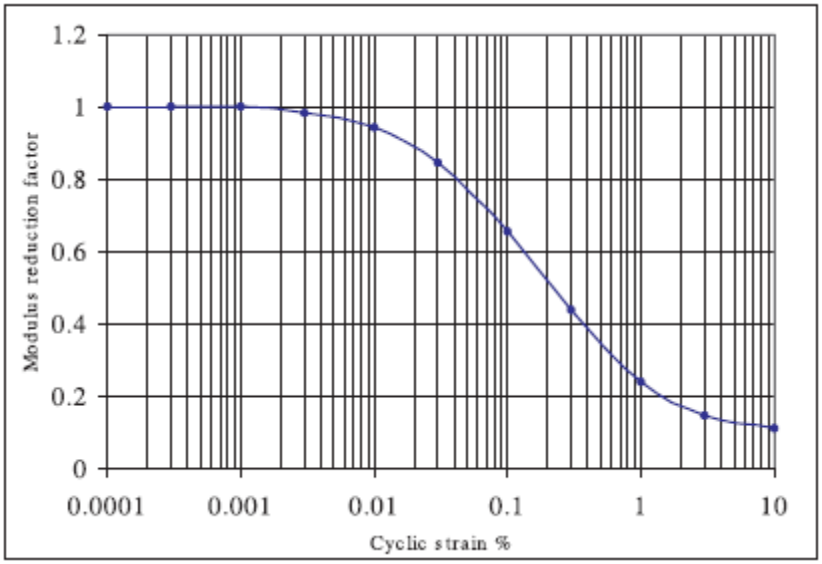

Figure 3.35. Modulus reduction curve for clay presented from Sun et al. 1988 (Itasca, 2011).

FLAC provides three options for users to define the shear modulus reduction factor with the cyclic strain of hysteretic damping. The models are summarized as default, sigmoidal, and Hardin/Drnevich models. In the default model, it is assumed that the relationship between the S-shaped curve of modulus and the log of cyclic strain is defined in a cubic equation with no slope at strains. The secant modulus of the default model is:

$$M_s = s^2(3 - 2s) \tag{3.30}$$

where

$$s = \frac{L_2 - L}{L_2 - L_1} \tag{3.31}$$

and L1 and L2 are estimated at zero slopes of strain levels and L is known as the logarithmic strain:

$$L = log_{10}(\gamma) \tag{3.32}$$

The second model to define the shear modulus reduction factor with the cyclic strain of hysteretic damping is the sigmoidal models of Sig3 and Sig4. In sigmoidal models, the curves are perfectly asymptotic, and the functions can be fitted to define well-suited modulus degradation curves. Sig3 and Sig4, respectively, are:

$$M_s = \frac{a}{1 + \exp\left(-\frac{L - x_o}{b}\right)} \tag{3.33}$$

$$M_s = y_0 + \frac{a}{1 + \exp\left(-\frac{L - x_o}{b}\right)} \tag{3.34}$$

The third model is Hardin/Drnevich. Its function is based on a relationship suggested by Hardin and Drnevich as follows:

$$M_s = \frac{1}{1 + \frac{\gamma}{\gamma_{ref}}} \tag{3.35}$$

in which $\gamma = \gamma_{ref}$ when the modulus reduction factor G/G_{max}=0.5, and it has been proved that $\gamma_{ref} = 0.06$, and $\gamma_{ref} = 0.234$ matches the curves of Figures 3.36 and 3.37, respectively.

The numerical fitting values of each of the three models of default, sigmoidal, and Hardin/Drnevich to Figures 3.36, and 3.37, are provided in Tables 3.17 and 3.18, respectively.

Table 3.17. Numerical fits value to data of Seed and Idriss for sand (Itasca, 2011).

Data set	Default	Sig3	Sig4	Hardin
Sand – upper range (Seed & Idriss 1970)	$L_1 = -3.325$ $L_2 = 0.823$	$a = 1.014$ $b = -0.4792$ $x_o = -1.249$	$a = 0.9762$ $b = -0.4393$ $x_o = -1.285$ $y_o = 0.03154$	$\gamma_{ref} = 0.06$

Table 3.18. Numerical fits to Seed and sun data for clay (Itasca, 2011).

Data set	Default	Sig3	Sig4	Hardin
Clay – upper range (Sun et al. 1988)	$L_1 = -3.156$ $L_2 = 1.904$	$a = 1.017$ $b = -0.587$ $x_o = -0.633$	$a = 0.922$ $b = -0.481$ $x_o = -0.745$ $y_o = 0.0823$	$\gamma_{ref} = 0.234$

In summary, for numerical analysis of liquefaction in this study, FLAC software is employed. FLAC can perform liquefaction analysis based on the different types of models that try to simulate pore pressure build-up in soil layers during dynamic analysis. The main categories of FLAC models that can evaluate pore pressure build-up are simple models and comprehensive models. Additionally, to investigate the behavior of soil, FLAC has built-in material models such as Mohr-Coulomb, Elastic, Hoek-Brown, etc., that can be coupled with simple pore pressure build-up FLAC for liquefaction analysis but not comprehensive models. Therefore, according to the drawbacks of comprehensive models and advantages of simple models that were discussed in this section, the simple liquefaction models (Finn) are initially used with the Mohr-Coulomb soil behavior model and hysteretic damping with a small percent of Ryleigh and hysteretic damping as well as the default shear modulus reduction option in this study.

The acceleration time histories that are obtained from ground motion databases for each earthquake in this study are at bedrock level. However, the bottom or base of the FLAC models will not be at the bedrock level and will instead consist of soil that is located above the bedrock level. The ground motion deconvolution procedure is provided in the next section.

3.3.6. Ground Motion Deconvolution Analysis for Numerical Modeling

The recorded acceleration time histories at the bedrock level must be deconvoluted to obtain the ground motion time history at the base of the FLAC model. The deconvolution process can be conducted either in FLAC or using the "SHAKE" program, which is an equivalent linear 1D wave propagation code. (Schnabel et al., 1972). SHAKE estimates the vertical wave propagation of a system of horizontal soil layers based on the layer properties such as shear modulus, density, and damping fraction, which is represented by the damping ratio. The damping fraction is an index in geotechnical engineering to measure energy dissipation during the dynamic loading of an earthquake. SHAKE solves the wave propagation equation within each horizontal layer by summing up the vertical upward and downward wave propagations.

Since the shear stress at the top layer (free field layer) must be zero, the upward and downward wave propagations of the top layer should be equal to satisfy the zero-shear stress condition (Itasca, 2011). SHAKE input and output are in terms of motion at the boundary between two layers and at the free surface instead of propagation. The motion at the boundary between two layers is the **within** motion and the motion at the free surface is known as **outcrop** motion. The within motion is the motion due to upward and downward wave propagation at the boundary between two layers and outcrop motion is the motion because of upward and downward wave propagation that occurs at a free surface. Due to zero shear stress at the free surface, it can be

concluded that the outcrop motion is twice the upward wave propagation (Itasca, 2011). Figure 3.36 illustrates a schematic analyzing the system that is performed by SHAKE as part of the deconvolution process.

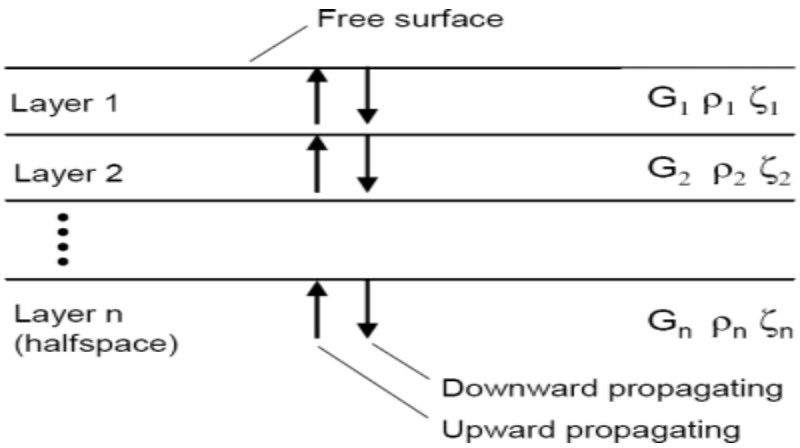

Figure 3.36. The layered system analyzed by SHAKE (layer properties are shear modulus, G, density, ρ, and damping fraction, ζ) (Itasca, 2011).

There are two types of base models in FLAC: rigid and compliant (Figure 3.37). Note that the difference between the rigid and compliant base models is that the base of the model in the rigid model is fixed while in the compliant base model the base of the model is viscous which minimizes the wave reflection to the model in dynamic analysis. Depending on the type of base, the deconvolution procedure is different in SHAKE for rigid and compliant base models. The rigid base deconvolution process is used for rigid body models with fixed base dynamic loading boundaries, and the compliant base deconvolution is applicable for rigid body models with compliant base boundaries.

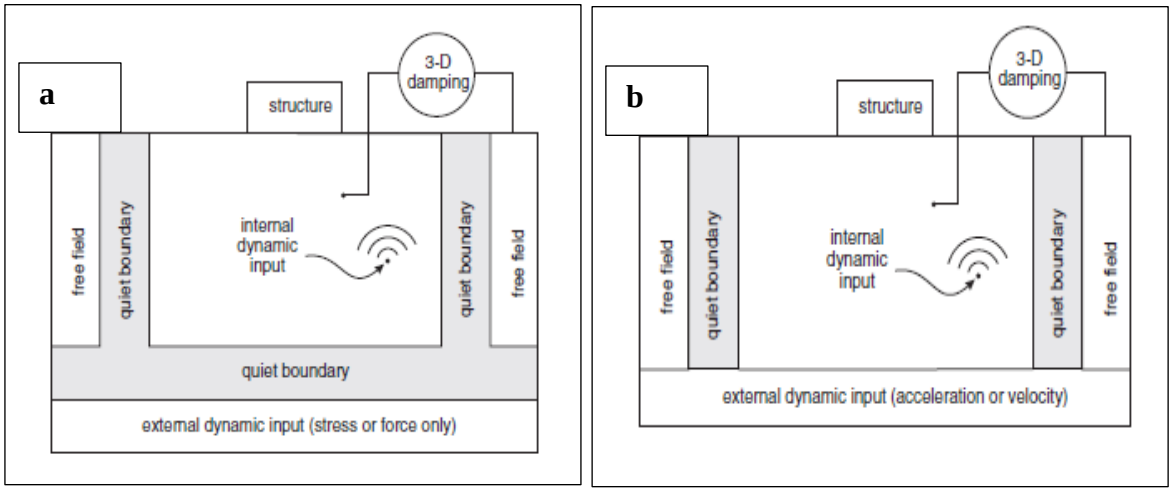

Figure 3.37. Types of dynamic loading boundary conditions available in FLAC a) compliant base and b) rigid base (Itasca, 2011).

To minimize the amount of reflection of the outward wave back into the model, FLAC recommends using quiet boundary conditions to absorb most of the energy of a reflected wave into the model. Therefore, in this study, the quiet boundary (compliant base) is used for the base of the model and compliant base deconvolution is employed in SHAKE to obtain the target motion for the FLAC model.

Figures 3.38 and 3.39 show a schematic image of how the acceleration-time history from the deconvolution procedure for a compliant base from SHAKE is incorporated at the compliant base of the FLAC model. In Figures 3.38 and 3.39, the soil structure consists of linear and non-linear elastic elements. Linear soil represents the soils with the same properties and assumes linear stress-strain behavior. Non-linear soil elements consist of soils with different properties; consequently, non-linear stress-strain behavior. To obtain the acceleration time history for the FLAC model, the upward wave propagation, which is half of the outcrop motion, is extracted from SHAKE at the top of the bedrock (point A in Figure 3.38). Since the designated motion at point A is the outcrop, therefore, the upward wave motion of the layer below point A is considered as half

of the target motion. Finally, the target motion as an input to FLAC is obtained from the upward propagation wave at point B as half of the outcrop motion (Itasca, 2011). The extracted acceleration time history from SHAKE is then converted to a velocity time history using the SeismoSignal software program (seismosoft.com) as an input motion to the FLAC model.

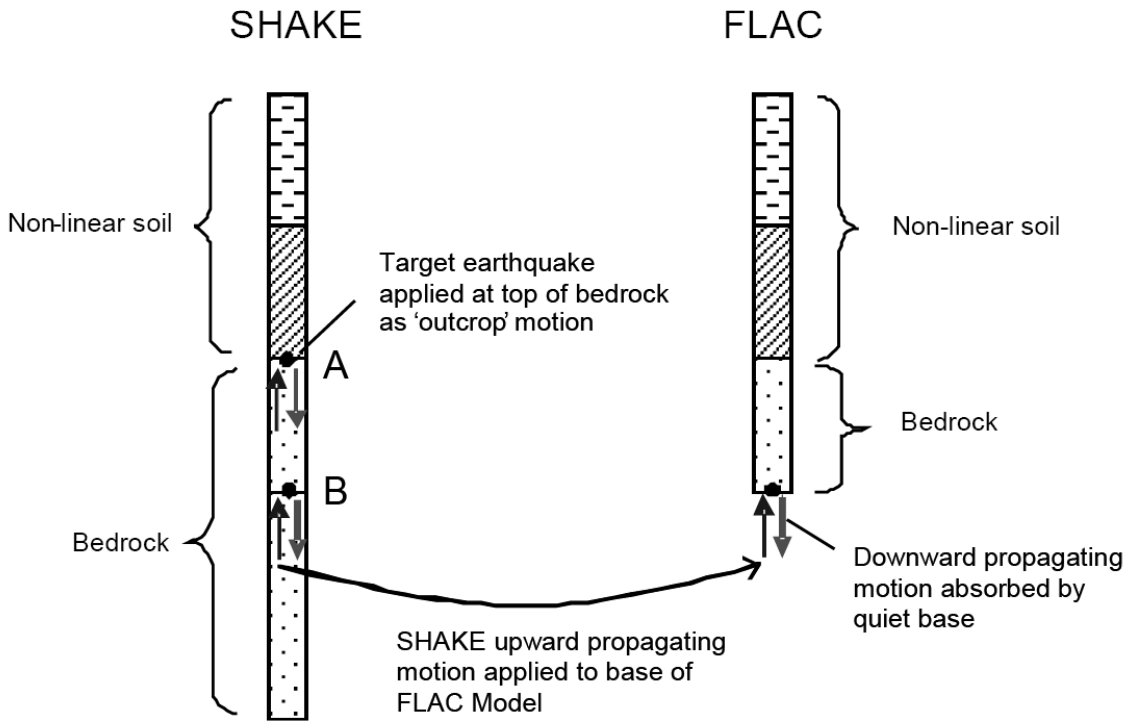

Figure 3.38. Compliant base deconvolution procedure for a typical case (Itasca, 2011).

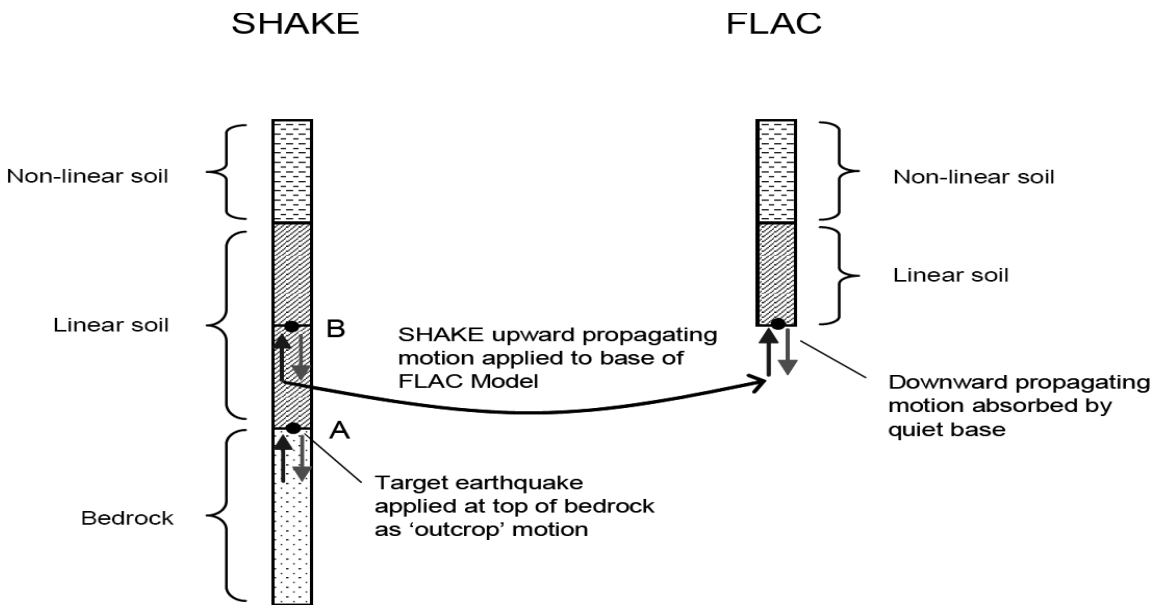

Figure 3.39. Compliant base deconvolution procedure for another typical case (Itasca, 2011).

The SHAKE program input parameters for each soil layer can either be obtained from laboratory test results or empirical charts and relationships such as modulus reduction and damping curves proposed by Vucetic and Dobry (1991) and EPRI (1993) which are shown in Figure 3.40.

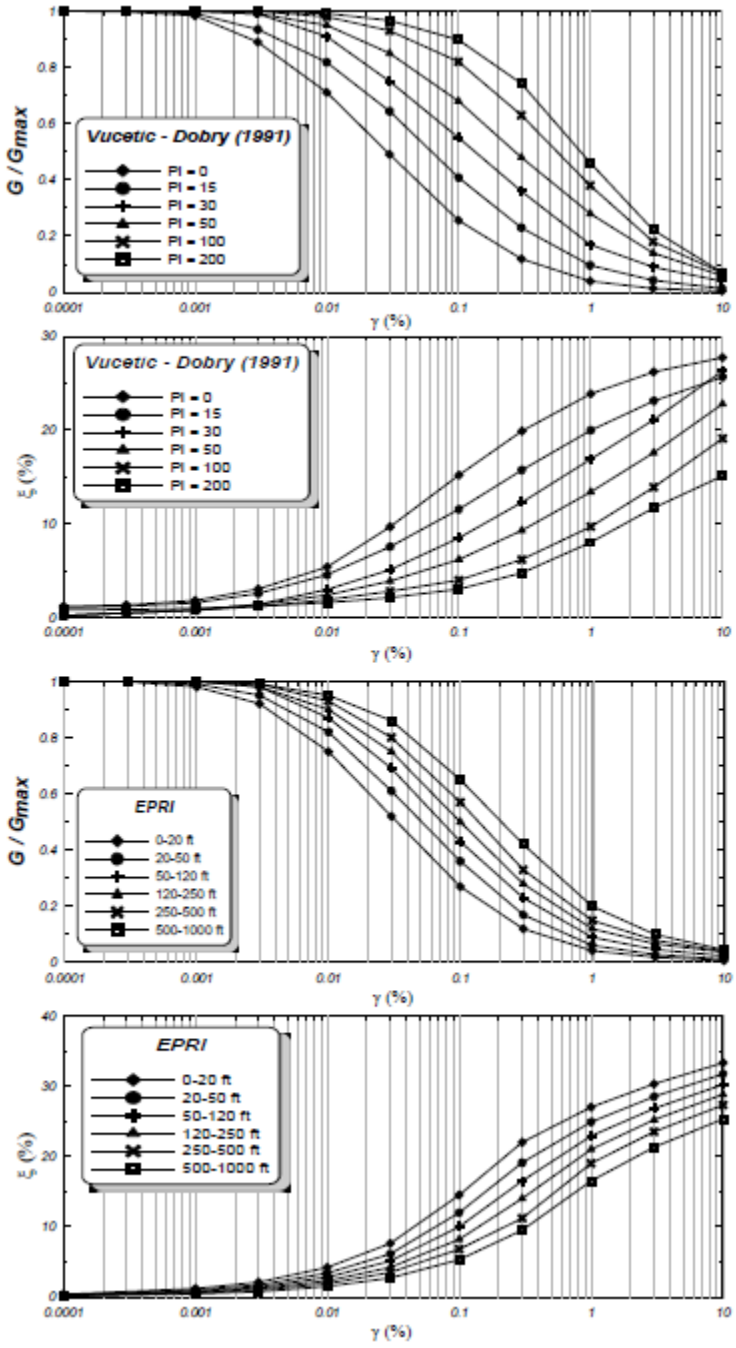

Figure 3.40. Modulus reduction and damping versus strain curves. Vucetic and Dobry (1991) curves for clay and various plasticity indices and EPRI (1993) curves for sands for various confinement depths (Itasca, 2011).

After obtaining the dynamic soil properties of each soil layer, they must be entered into the SHAKE program. To keep track of the soil properties of each soil layer in this study another

program named MCR developed by Li (2013) is coupled and used with SHAKE. MCR is a MATLAB code program that has been written to simplify the input parameters to SHAKE. It is also known as *Shake91_Input* which is an executable file. This program has the capability of defining each soil layer with specific properties separately. Figures 3.41, 3.42, and 3.43 show the environment of the MCR program.

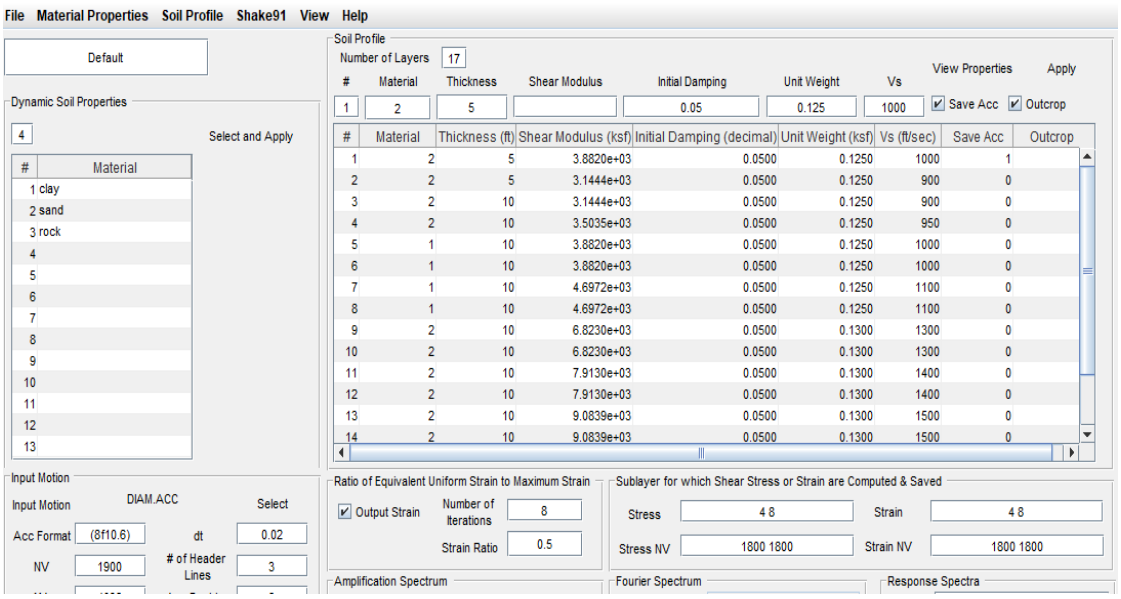

Figure 3.41. MCR program start page (Li, 2013).

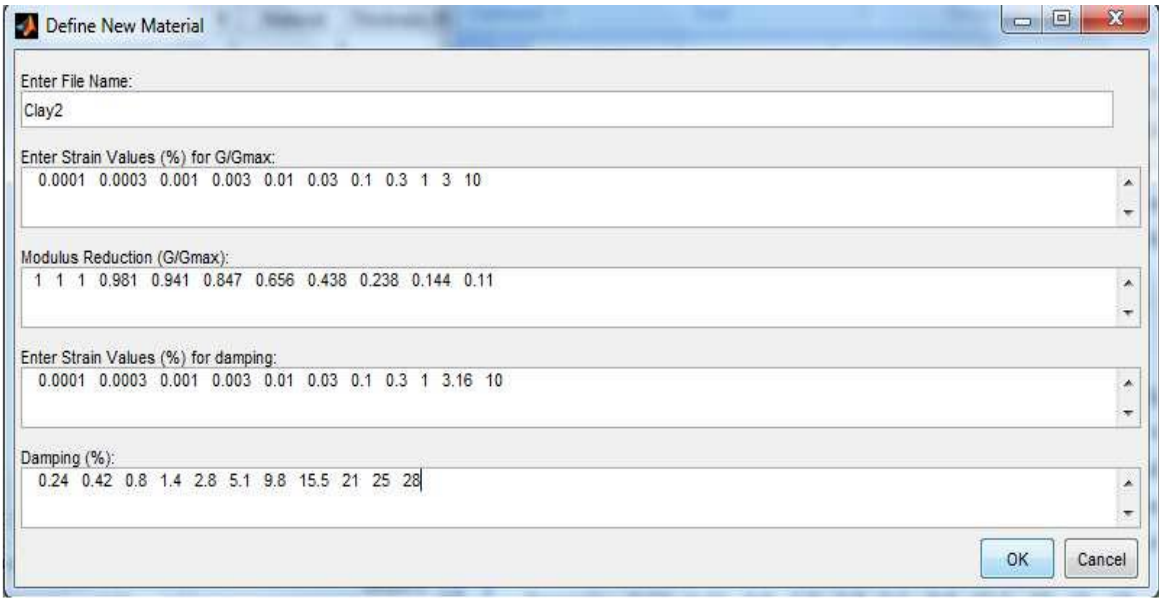

Figure 3.42. Example inputs for defining material in the MCR program (Li, 2013).

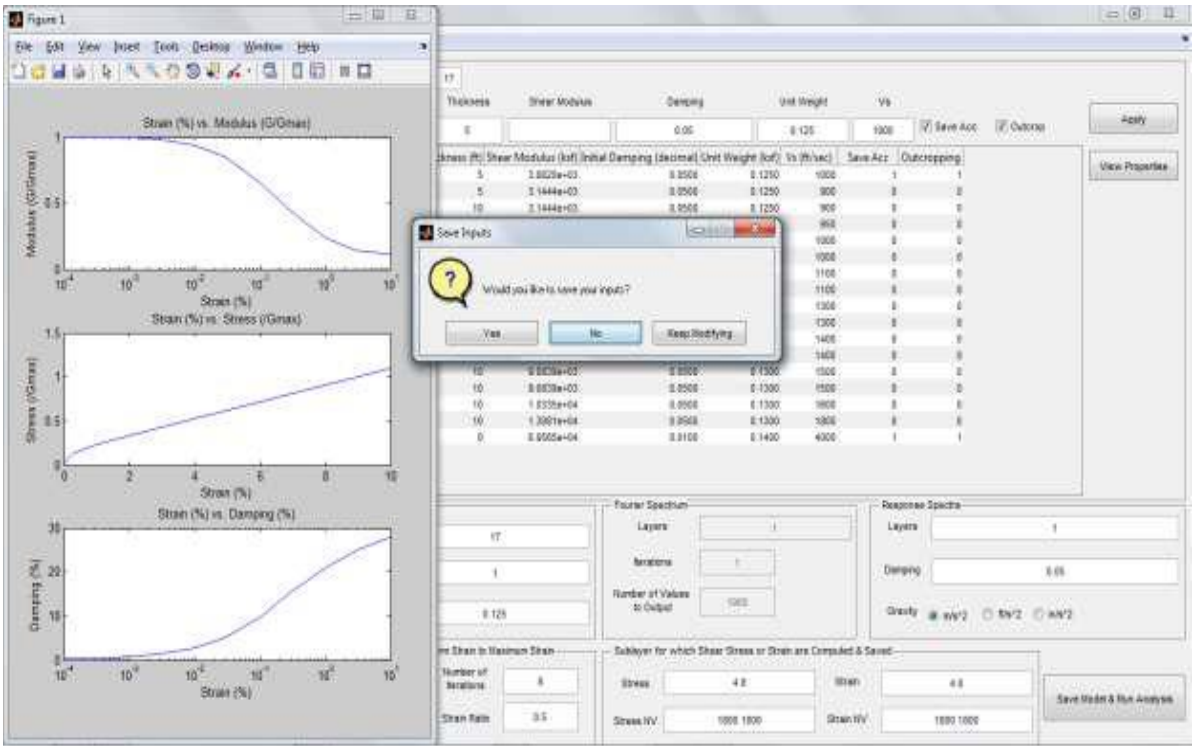

Figure 3.43. Example of produced curves by MCR program after defining material (Li, 2013).

As shown in Figure 3.43, the program plots the entered values of modulus reduction (G/G_{max}), strain values, and damping. SHAKE extracts the soil data directly from MCR.

Due to continuing residual velocity or displacement, after the motion has finished, a baseline displacement drift occurs that must be corrected (Itasca, 2011). Figure 3.44 (b) shows an example of displacement drift. Note that displacement is not zero at the end of the displacement time history of the earthquake. The baseline drifts are usually due to internal factors of the motion accelerogram such as instrument noise and background noise or external factors such as uplift at near-fault regions (Guorui and Tao, 2015). Therefore, using the FISH capability of FLAC, a FISH function of BASELINE.FIS (see Appendix B) is utilized to correct the baseline drift. The BASELINE.FIS corrects the baseline drift by adding a low-frequency sine wave to the velocity-

time history and by adjusting the sine wave parameters, the final displacement becomes zero. The schematic baseline correction procedure in FLAC is shown in Figure 3.44.

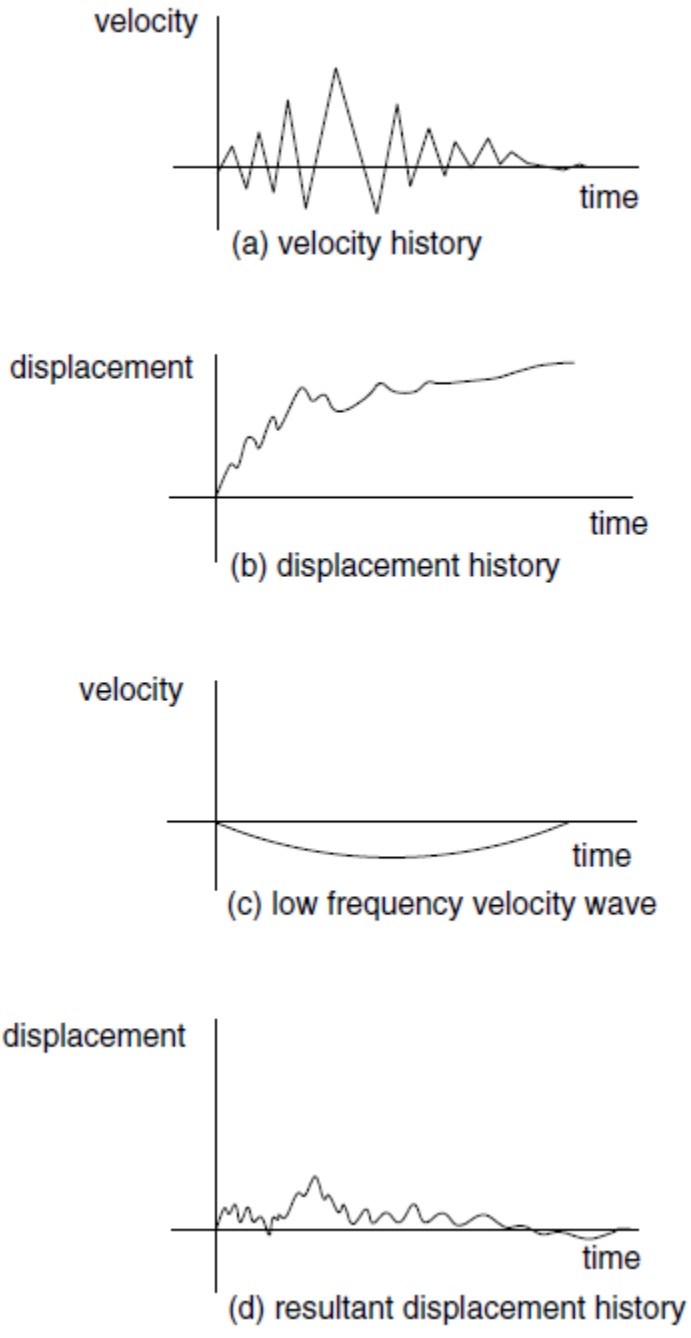

Figure 3.44. Procedure of baseline correction (Itasca, 2011).

The input motion (earthquake) in FLAC must be in a format of shear stress time history. So a baseline-corrected velocity time history is converted to a shear stress time history using Equation (3.36):

$$\sigma_s = -2(\rho C_s)V_s \tag{3.36}$$

where σ_s is the applied shear stress, ρ is the mass density of the base model soil, V_s is the input shear velocity from the velocity time history, and C_s is the speed of s-wave propagation of the base of the model and it is computed by:

$$C_s = \sqrt{G/\rho} \tag{3.37}$$

where G is the shear modulus of the soil at the base of the model.

In summary, the dynamic analysis using FLAC for this study consists of the following steps:

- Obtain the recorded acceleration time history of the earthquake(s).
- Deconvolute the earthquake in the SHAKE equivalent linear program to obtain the earthquake time history at the base of the model.
- Obtain the velocity and displacement time histories of the deconvoluted earthquake from the SeismoSignal software program to check if there is any baseline drift.
- Correct the possible baseline drift of the deconvoluted earthquake velocity time history.
- Convert the corrected velocity time history to a shear stress time history.
- Define proper time histories to monitor and record specific parameters to evaluate liquefaction.
- Run the dynamic analysis by applying the shear stress time history of the deconvoluted and base-line drift corrected earthquake at the base of the model.

3.4. Numerical Liquefaction Analysis

The overall FLAC model consists of multiple materials and behavioral models that were previously described, including the Finn models of liquefaction analysis (analysis of excess pore pressure) plus the Mohr-Coulomb strength model. This section provides a summary of analyses performed to verify the overall liquefaction analysis in the FLAC model. First, the validation of the model is tested by liquefaction analysis of the Wildlife site located in California during the Superstition Hills earthquake of 1987. The results of the numerical liquefaction analysis of the Wildlife site will then be compared with the numerical results of the liquefaction analysis of the site from a study done by Daftari, 2015.

Next, the developed numerical FLAC code will be tested by conducting a liquefaction surface manifestation analysis on four sites with different soil profiles located in New Zealand. Two of the selected sites showed liquefaction at the ground surface during both the 2010 and 2011 Canterbury Earthquakes Sequence (CES) while the other two sites did not show any evidence of liquefaction features at the ground surface during the CES. The results of numerical analysis of the New Zealand sites will be compared with site observations for verification of the FLAC model in Chapter 4 of this dissertation.

For liquefaction analysis of the Wildlife site and the New Zealand soil profiles, the geometry of the models is defined, and appropriate boundary and initial conditions are assigned. The soil properties of each layer are defined based on available data of the case history sites and the Mohr-Coulomb plasticity model is used along with the Finn-Byrne model to perform the liquefaction analysis. Initially, a static analysis is conducted before the dynamic analysis to reach the models to the state of equilibrium.

By defining new FLAC FISH functions of EXCPP.FIS, INIPP.FIS, SAVEPP.FIS, GETEXCESS.FIS, and STRAI_HIST.FIS (provided in Appendix B), the excess pore pressure ratio, which is an important factor for liquefaction analysis in numerical modeling, was obtained during the dynamic loading of the model. The excess pore pressure ratio (r_u) is defined as the ratio of pore pressure increase (Δu) to the initial effective stress (σ'_o) at each depth by the following equation:

$$r_u = \frac{\Delta u}{\sigma'_o} \tag{3.38}$$

In geotechnical earthquake engineering, soil liquefaction usually is defined as the state in which the excess pore pressure ratio becomes one and higher and this happens when the pore pressure becomes equal to or higher than the initial vertical effective stress at any specific depth.

3.4.1. Wildlife Site, California

The first study that was selected to verify the overall FLAC model and liquefaction modeling capabilities of the written FLAC code for this study is research done by Daftari, 2015. Daftari (2015) evaluated the liquefaction potential of the Wildlife site located in the Imperial Valley of California under the Superstition Hills earthquake of 1987 using FLAC and PLAXIS software programs. Daftari (2015) modeled the stratified soil profile of the Wildlife site with FLAC and by performing the dynamic analysis based on earthquake data of Superstition Hills obtained the excess pore water pressure results after 100 seconds of dynamic loading. A subsurface soil profile of the Wildlife site is shown in Figure 3.45.

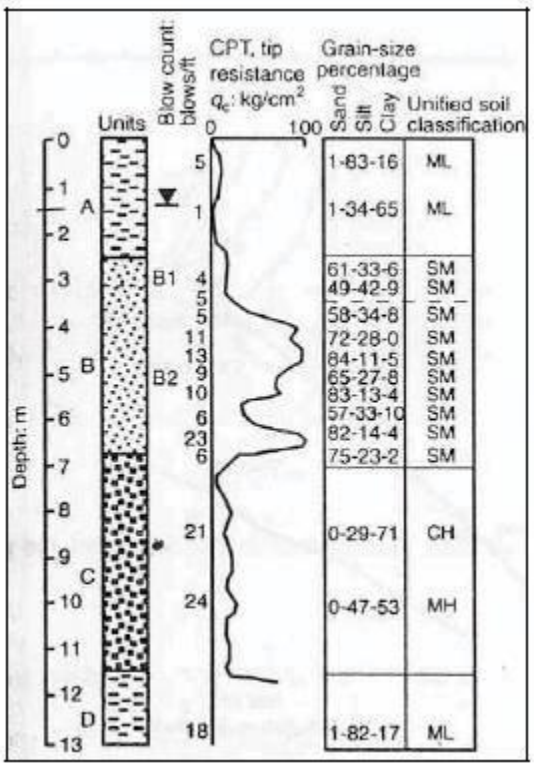

Figure 3.45. Soil profile at Wildlife site (Daftari, 2015).

In Daftari's study, the Wildlife site was modeled in FLAC to a depth of 13 meters using five soil layers with properties that are provided in Table 3.19. It must be noted that the soil properties of Layer V are utilized for the depth of 10 to 13 m, too (Daftari, 2015).

Table 3.19. Input soil parameters at the Wildlife site (Daftari, 2015).

Layer	I	II	III	IV	V
Depth (m)	0.0-1.2	1.2-2.5	2.5-3.5	3.5-6.8	6.8-10
Total Density (kg/m^3)	1600	1940	1970	1970	2000
Bulk Modulus (N/m^2)	$2.61*10^7$	$2.44*10^7$	$4.50*10^7$	$4.50*10^7$	$5.83*10^7$
Shear Modulus (N/m^2)	$1.57*10^7$	$1.47*10^7$	$2.08*10^7$	$2.08*10^7$	$2.70*10^7$
Cohesion (Pa)	$2*10^3$	$2*10^3$	-	-	-
Friction angle (°)	21.3	20.0	22.0	22.0	35.0
Dilation (°)	21.3	20.0	19.0	18.0	5.0
Porosity	0.4047	0.4431	0.4253	0.4253	0.4075

To conduct the FLAC dynamic analysis, Daftari utilized the SPT data of the Wildlife site to employ the Finn-Byrne model for liquefaction analysis as described in Chapter 2. Table 3.20 provides the SPT data and the constant values of the Finn-Byrne model for each soil layer.

Table 3.20. The input parameters of the Finn-Byrne model in FLAC (Daftari, 2015).

No	Depth (m)	SPT	D_r	C_1	C_2
I	0-1.2	6	36.74	0.93	0.43
II	1.2-2.5	6.25	37.5	0.88	0.45
III	2.5-3.5	7.65	41.48	0.68	0.58
IV	3.5-6.8	10.65	48.95	0.45	0.88
V	<6.8	10	47.43	0.49	0.81

To simulate Daftari's model, the earthquake data of Superstition Hills were obtained from the PEER ground motion database. After scaling the data to match the design response spectrum of the Wildlife site based on the power spectrum of the Superstition earthquake using the SeismoMatch program, the acceleration, velocity, and displacement time histories were developed in the SeismoSignal program as shown in Figure 3.46.

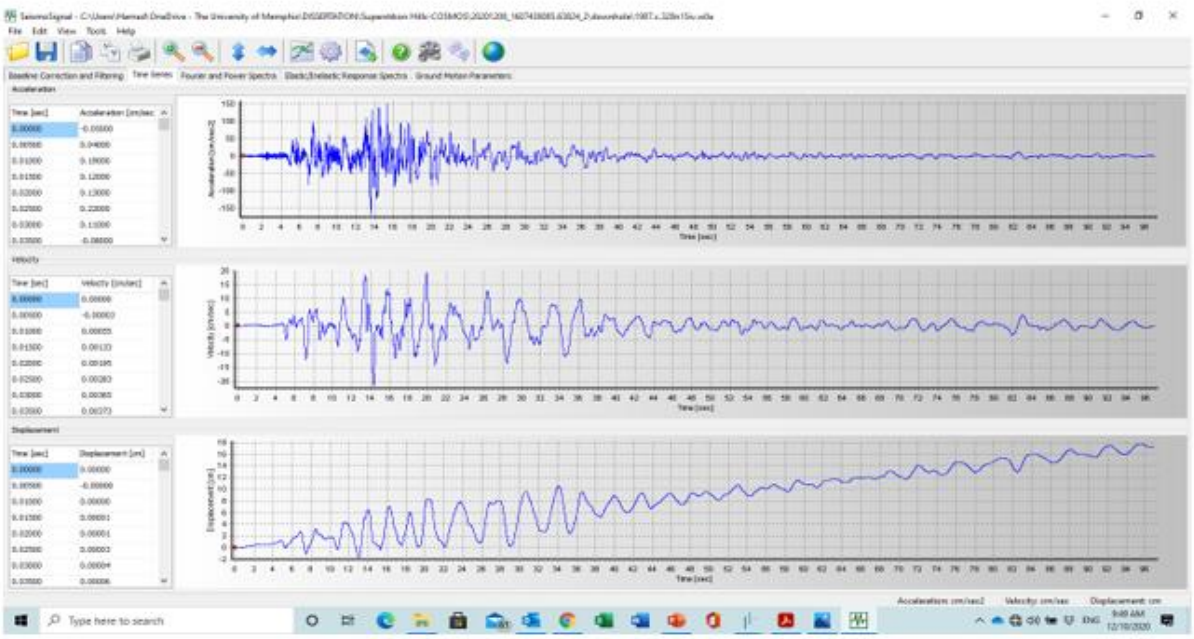

Figure 3.46. Acceleration, velocity, and displacement time histories of Superstition Hills recorded at Wildlife site.

From Figure 3.46 it can be seen that the displacement time history of the target earthquake has a baseline drift of 17.09 cm at the 97th second that had to be corrected. Therefore, using the FISH capability of FLAC, a FISH function of BASELINE.FIS was utilized to correct the baseline drift as is illustrated in Figure 3.47.

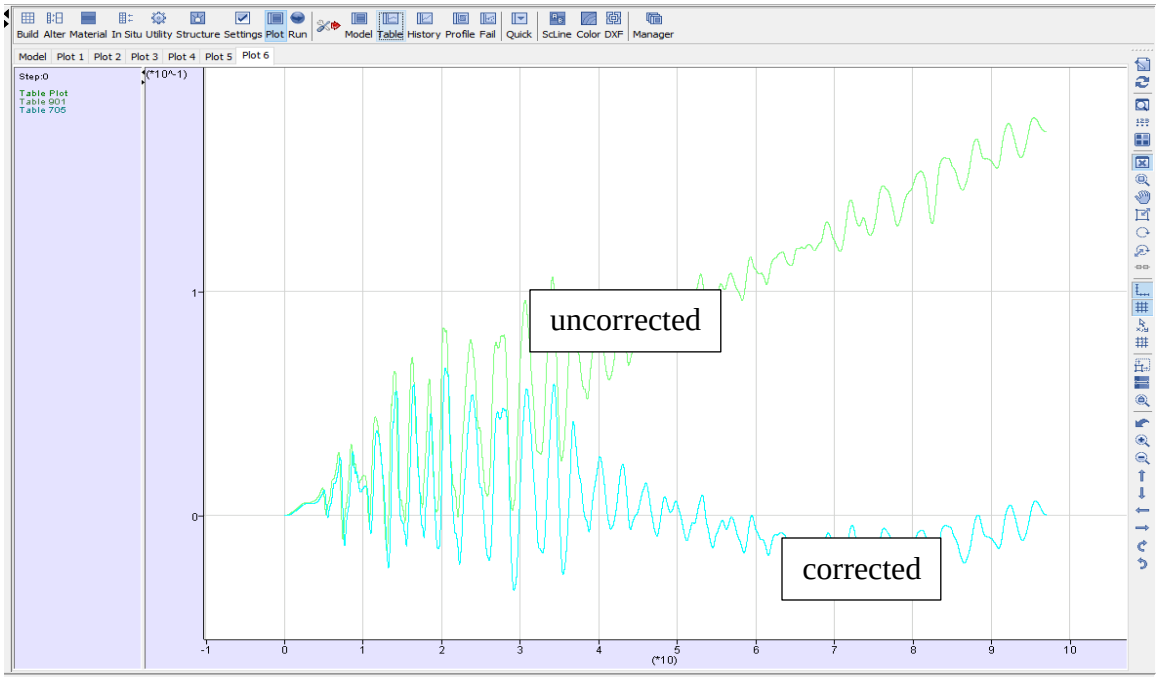

Figure 3.47. Baseline corrected displacement time history of the Superstition Hills earthquake.

After correction of the baseline drift of the displacement time history, by getting a derivative of the displacement time history, the velocity time history of the target motion for use as input motion data for dynamic analysis of FLAC was obtained as shown in Figure 3.48.

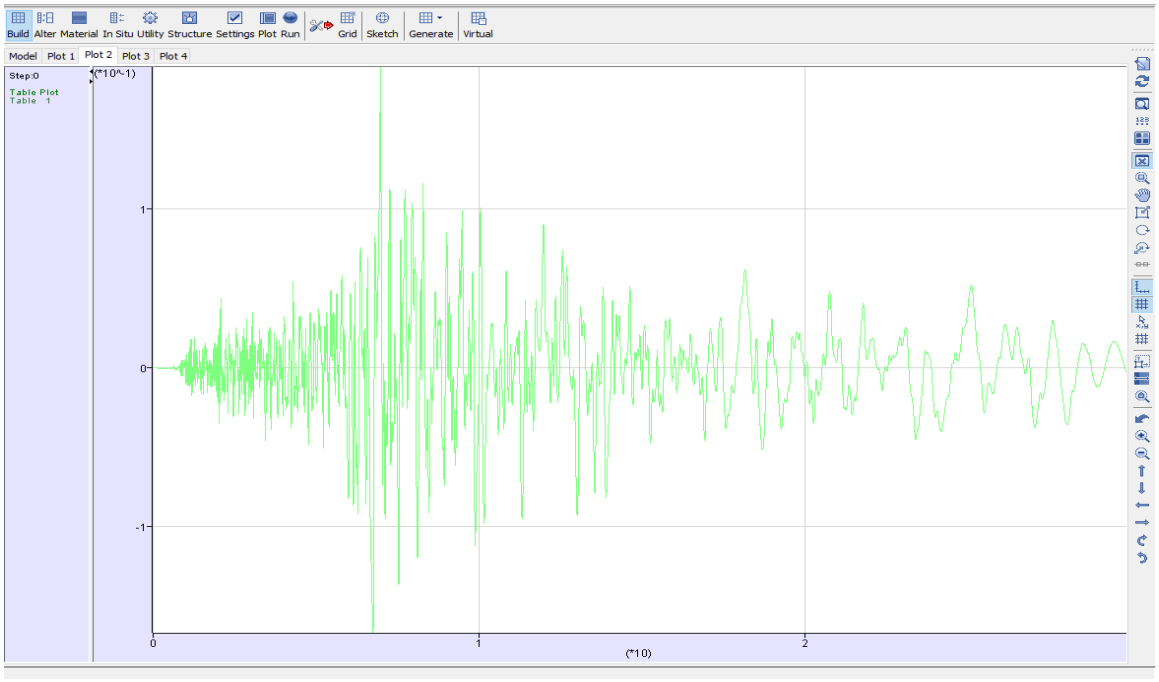

Figure 3.48. Input velocity time history of Superstition earthquake in FLAC.

Figure 3.49 shows the initiated Wildlife site model in FLAC with the five soil layers. The model mesh size is one meter per side and the overall model size is 13m×35m. To calculate the appropriate mesh size of a FLAC model, the maximum frequency of each earthquake must be obtained from the Fourier power spectrum and applied in the following equation.

$$f = \frac{V_s}{\lambda} = \frac{V_s}{10\Delta L} \tag{3.39}$$

where V_s is the shear wave velocity of the base of the model, f is the maximum frequency, λ is the wavelength with the highest frequency, and ΔL is the largest zone dimension for the model. The mesh size obtained from Equation (3.39) is the optimum mesh size.

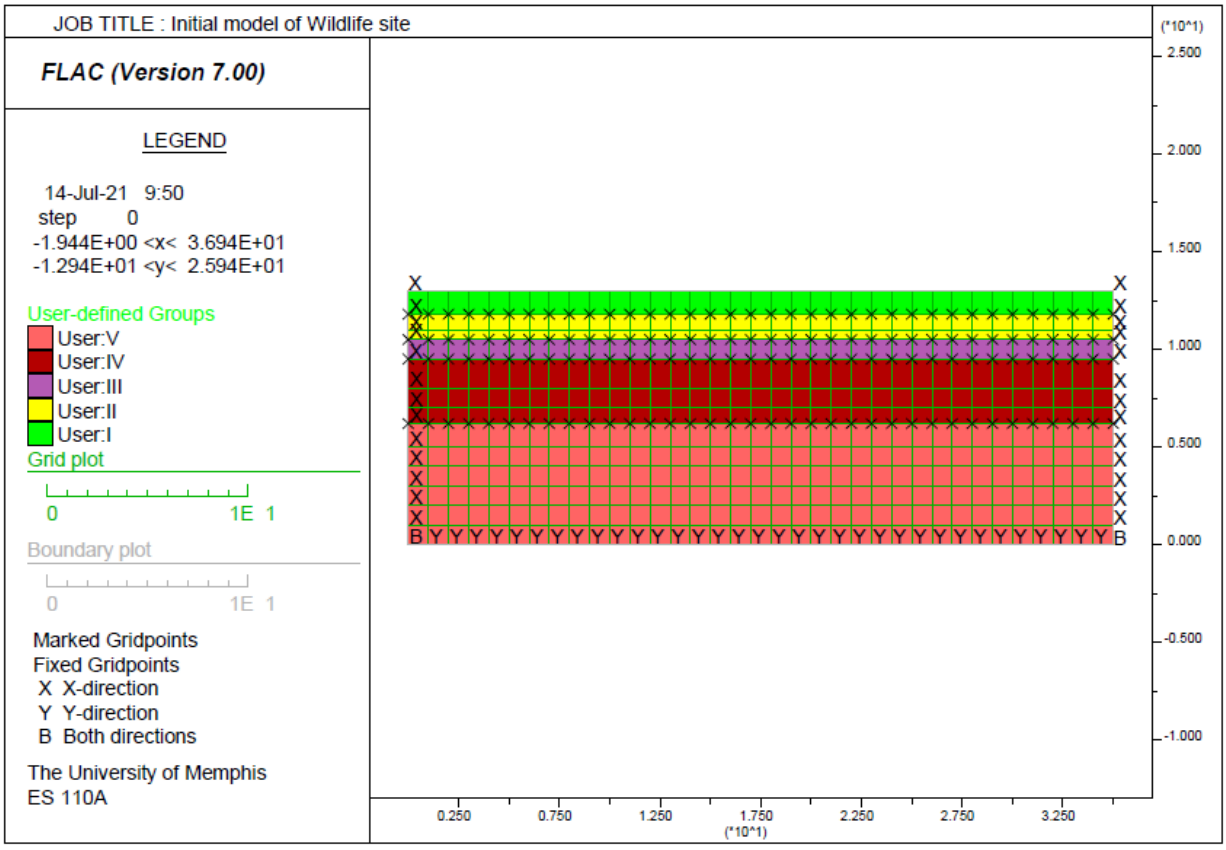

Figure 3.49. Initial model of the Wildlife site in FLAC (different colors represent different soils).

3.4.2. New Zealand Soil Profiles Analysis

The CES of 2010-2011 liquefied many parts of Christchurch, New Zealand, and impacted 60,000 buildings and properties (Rhodes, 2017). The observations from different sites in Christchurch reveal that at some sites, liquefaction was manifested at the ground surface while at other sites although liquefaction occurred in deeper layers, due to the existence of non-liquefiable layers on top of liquefiable layers in the soil profile, there was no evidence of liquefaction surface manifestation. From a study done by Rhodes (2017), four different soil profiles were selected for this study consisting of two sites that showed liquefaction surface manifestation and two sites that did not show liquefaction surface manifestation. The liquefied soil profiles were denoted as

YES/YES (YY1 and YY2), and the non-liquefied soil profiles were named as NO/NO (NN1 and NN2) models. Therefore, in this study, the numerical analysis has been done on **two** YY soil profiles and **two** NN soil profiles shown in Figures 3.50 and 3.51, respectively.

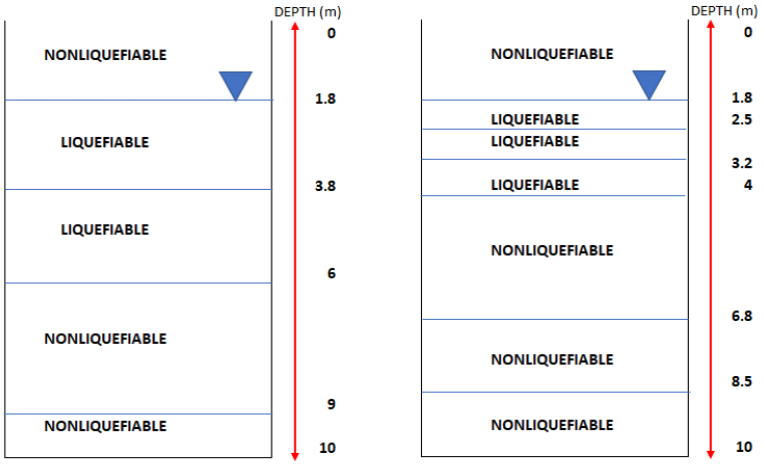

Figure 3.50. YY1 and YY2 soil profiles.

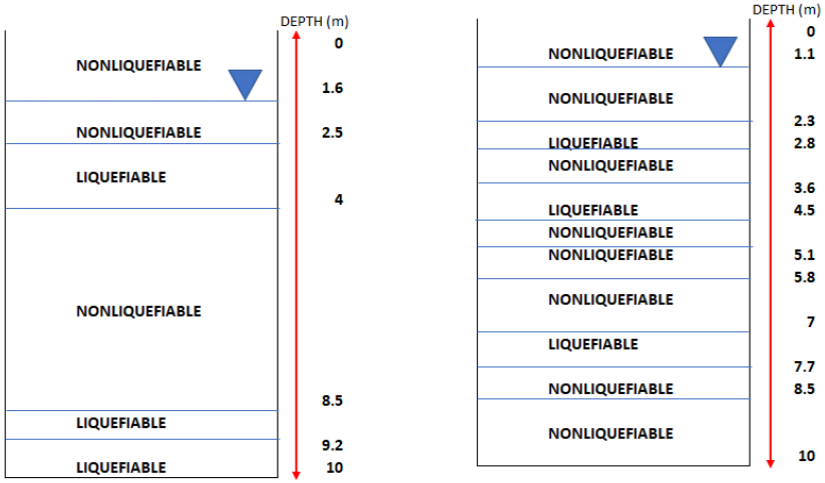

Figure 3.51. NN1 and NN2 soil profiles.

In the above figures, a liquefiable layer was identified as a layer that has liquefaction potential, i.e., loose saturated sandy soil identified (Rhodes, 2017).

The YY1 soil profile has five different soil layers. Throughout the five soil layers, to a depth of 10 meters, there are two loose sand layers with a total thickness of 4.2 m known as the critical zone (the zone with a high probability of liquefaction) below a 1.8 m thick, non-liquefiable soil crust.

The YY2 model has seven layers consisting of 2.2 m thick liquefiable soil layers (critical zone) right below a 1.8 m unsaturated soil layer on top of the soil profile. The rest of the layers below the critical zone are not considered as critical layers (layers with a high probability of liquefaction) due to their higher SPT value, however they are not considered as non-liquefiable layers either.

The NN1 soil profile, which did not show liquefaction at the ground surface, has six different soil layers. From top to bottom, the first 2.5 m consists of two layers of non-liquefiable soil on top of a 1.5 m critical layer followed by a very thick (4.5 m) non-liquefiable layer and two thin liquefiable layers at the very bottom of the soil profile.

The NN2 soil profile consists of eleven soil layers. The NN2 model has three liquefiable layers denoted as critical layers at different depths through the 10 m soil profile. The thickest liquefiable layer has a thickness of 0.9 m and the thinnest liquefiable layer is 0.5 m thick. There are non-liquefiable soils on top of all three liquefiable soil layers.

The properties of each soil layer have either been directly measured or calculated using empirical equations (Rhodes, 2017). Tables 3.21 and 3.22 provide the soil properties of the YY1 and NN2 soil profiles. Tables 3.23 and 3.24 provide the soil properties of the YY2 and NN1 soil profiles.

Table 3.21. soil properties of the YY1 model.

LYER No.	Depth (m)	SPT value for clean sand	Fines content %	unit weight KN/m^3	E KPa	Shear modulus KPa	Poisson's ratio	Permeability m/s
1	0 - 1.8	23	13	18	38004	14617	0.3	0.000004
2	1.8 - 3.8	10	3	19	5704	2194	0.3	0.000004
3	3.8 - 6	12	3	19	11404	4386	0.3	0.0001
4	6 - 9	17	3	19	30404	11694	0.3	0.0002
5	9 - 10	23	3	19	38004	14617	0.3	0.0003

Table 3.22. soil properties of the NN2 model.

LYER No.	Depth (m)	SPT value for clean sand	Fines content %	unit weight KN/m^3	E KPa	Shear modulus KPa	Poisson's ratio	Permeability m/s
1	0 - 1.1	23	16	18	38004	14616.92	0.3	0.0001
2	1.1 - 2.3	>50	58	19	50000	19231	0.3	0.0000001
3	2.3 - 2.8	10	22.5	19	5704	2194	0.3	0.000004
4	2.8 - 3.6	>50	58	19	50000	19231	0.3	0.0000001
5	3.6 - 4.5	10	21	19	5704	2194	0.3	0.000004
6	4.5 - 5.1	>50	58	19	50000	19231	0.3	0.0000001
7	5.1 - 5.8	13	13	19	17104	6578	0.3	0.0001
8	5.8 - -7	>50	58	19	50000	19231	0.3	0.0000001
9	7 - 7.7	10	21	19	7604	2925	0.3	0.000004
10	7.7 - 8.5	>50	58	19	50000	19231	0.3	0.0000001
11	8.5 - 10	17	9	19	30404	11694	0.3	0.0001

Table 3.23. soil properties of the YY2 model.

LYER No.	Depth (m)	SPT value for clean sand	Fines content %	unit weight KN/m^3	E KPa	Shear modulus KPa	Poisson's ratio	Permeability m/s
1	0 - 1.8	23	26	18	38004	14617	0.3	4E-6
2	1.8 - 2.5	11	26	19	7604	2925	0.3	4E-6
3	2.5- 3.2	13	26	19	13304	5117	0.3	4E-6
4	3.2 - 4	17	8	19	30404	11694	0.3	1E-4
5	4 – 6.8	19	13	19	32304	12425	0.3	2E-4
6	6.8 -8.5	135	21	19	34204	13155	0.3	3E-4
7	8.5-10	140	23	19	38004	14617	0.3	3E-4

Table 3.24. soil properties of the NN1 model.

LYER No.	Depth (m)	SPT value for clean sand	Fines content %	unit weight KN/m^3	E KPa	Shear modulus KPa	Poisson's ratio	Permeability m/s
1	0 - 1.6	23	26	18	38004	14617	0.3	4E-6
2	1.6 - 2.5	>50	58	19	50000	19231	0.3	1E-7
3	2.5 - 2.4	10	13	19	5704	2194	0.3	1E-4
4	4 – 8.5	>50	58	19	50000	19231	0.3	1E-7
5	8.5 –9.2	12	12	19	11404	4386	0.3	1E-4
6	9.2-10	10	26	19	50000	19231	0.3	4E-6

All of the New Zealand soil profiles were initiated in FLAC using the simple plasticity soil model of Mohr-Coulomb. The size of the YY and NN sites for this analysis is 25m×10m with a mesh size of 80×32 that was computed using the maximum frequency of the earthquake and Equation 3.39. The initial models of the YY1, YY2, NN1, and NN2 soil profiles are shown in Figures 3.52, 3.53, 3.54, and 3.55, respectively.

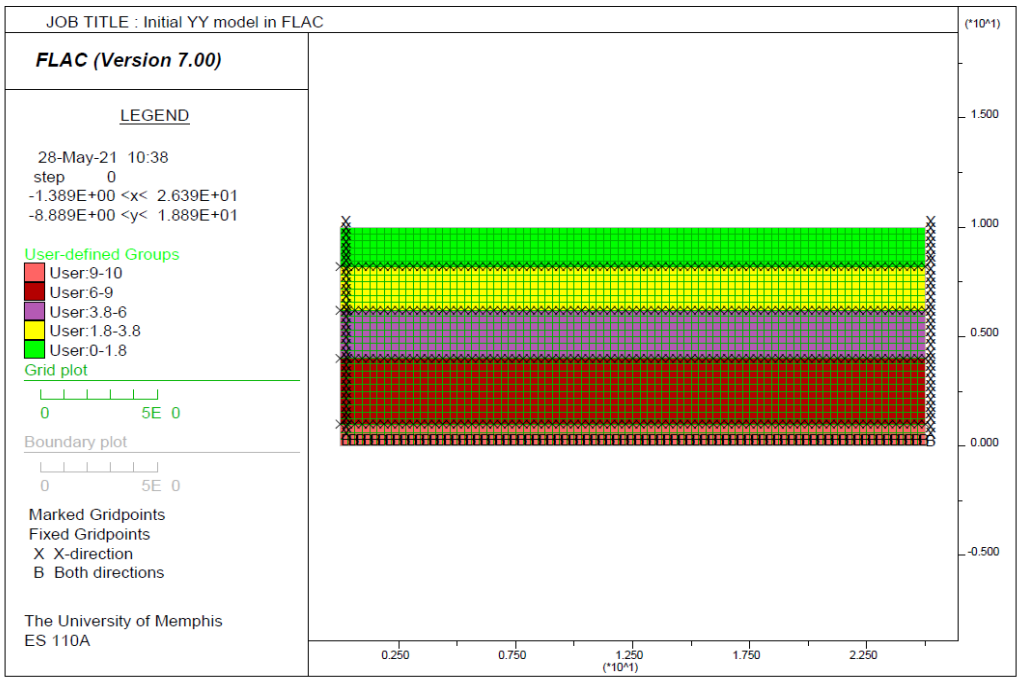

Figure 3.52. Initial YY1 model in FLAC (different colors represent different soils).

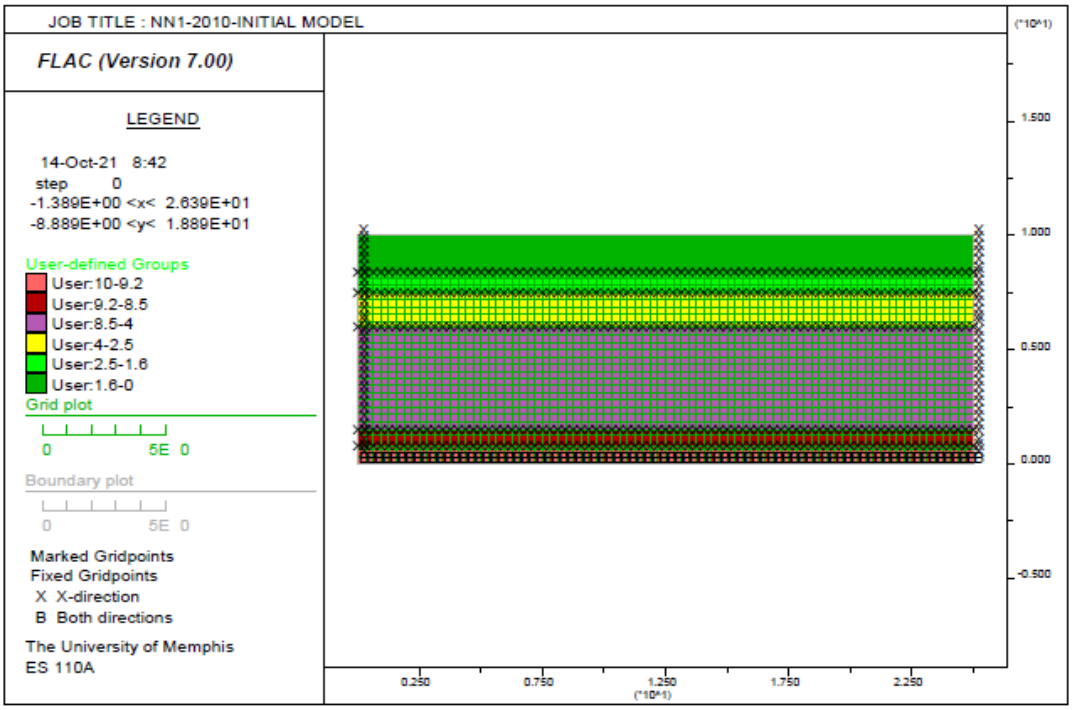

Figure 3.53. Initial YY2 model in FLAC (different colors represent different soils).

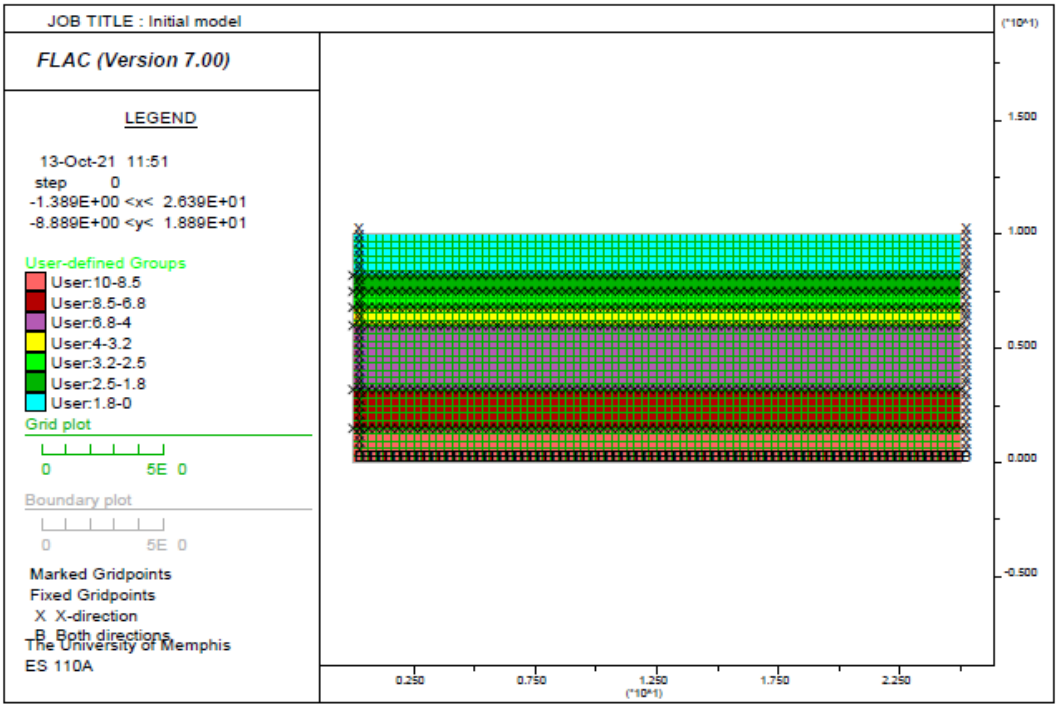

Figure 3.54. Initial NN1 model in FLAC (different colors represent different soils).

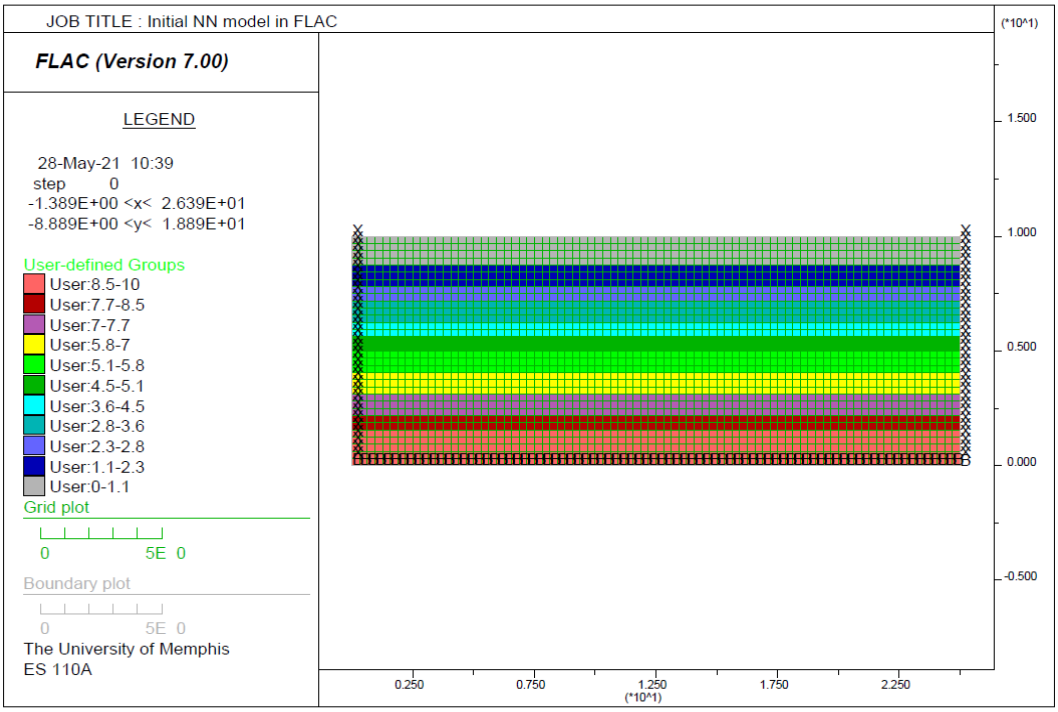

Figure 3.55. Initial NN2 model in FLAC (different colors represent different soils).

In this study, the dynamic analysis of the YY and NN models was conducted for the M_w 7.1 Darfield earthquake (2010) and the M_w 6.3 Christ Church earthquake (2011) of New Zealand. On September 4, 2010, a strong earthquake with a large magnitude of 7.1 shook Canterbury, New Zealand. The depth of the earthquake was 10 km, and the peak acceleration was 1780.8 mm/sec^2 (0.1816g). The CES earthquake of 2011 occurred on February 21, 2011, with a magnitude of 6.3, a depth of 5 km. The PGA of this earthquake was 1821 mm/sec^2 (0.1857g). The ground motion recorded acceleration time histories of the CES of 2010-2011 were obtained from the Geological Hazard Information for New Zealand (GeoNet) database. For each of the 2010 and 2011 earthquakes, the acceleration time histories were recorded at different stations. For this study, both the 2010 and 2011 recorded data from Christchurch Canterbury Aero Club (CACS) were utilized. Figures 3.56 and 3.57 show the acceleration time histories of the 2010 and 2011 earthquakes, respectively.

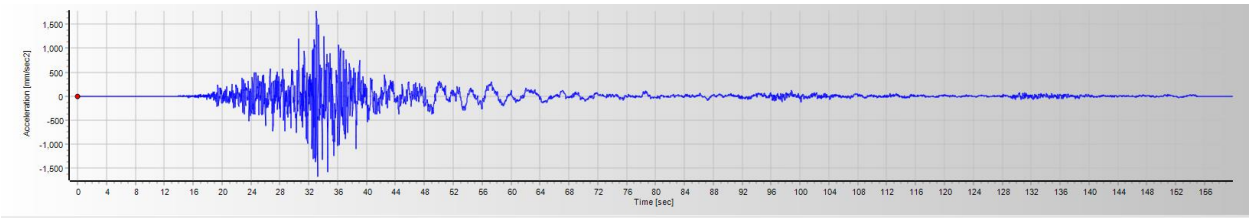

Figure 3.56. Acceleration time history of New Zealand 2010 earthquake.

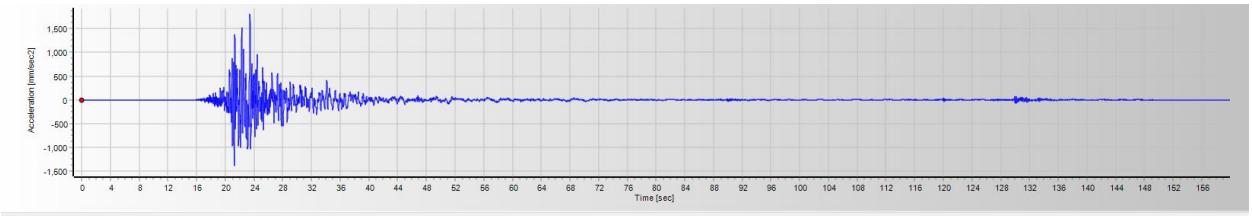

Figure 3.57. Acceleration time history of New Zealand 2011 earthquake.

In this study, the dynamic input was applied in FLAC in the format of velocity time histories. However, the velocity time histories of dynamic input cannot be applied along with the boundary conditions of the model, therefore, the velocity time histories must first be converted to stresses using Equation (3.36) and then applied along the boundaries. The velocity-time histories of the deconvoluted earthquakes of 2010 and 2011 are shown in Figures 3.58 and 3.59, respectively.

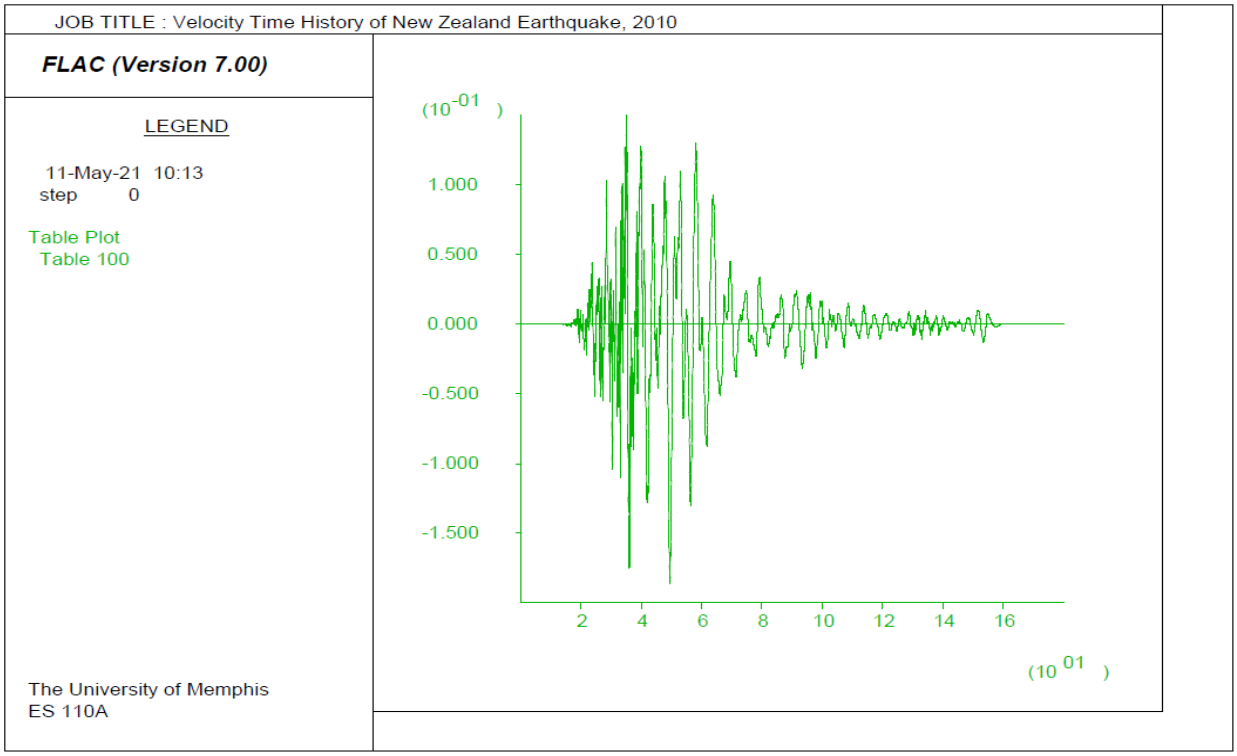

Figure 3.58. Velocity time history of deconvoluted New Zealand 2010 earthquake.

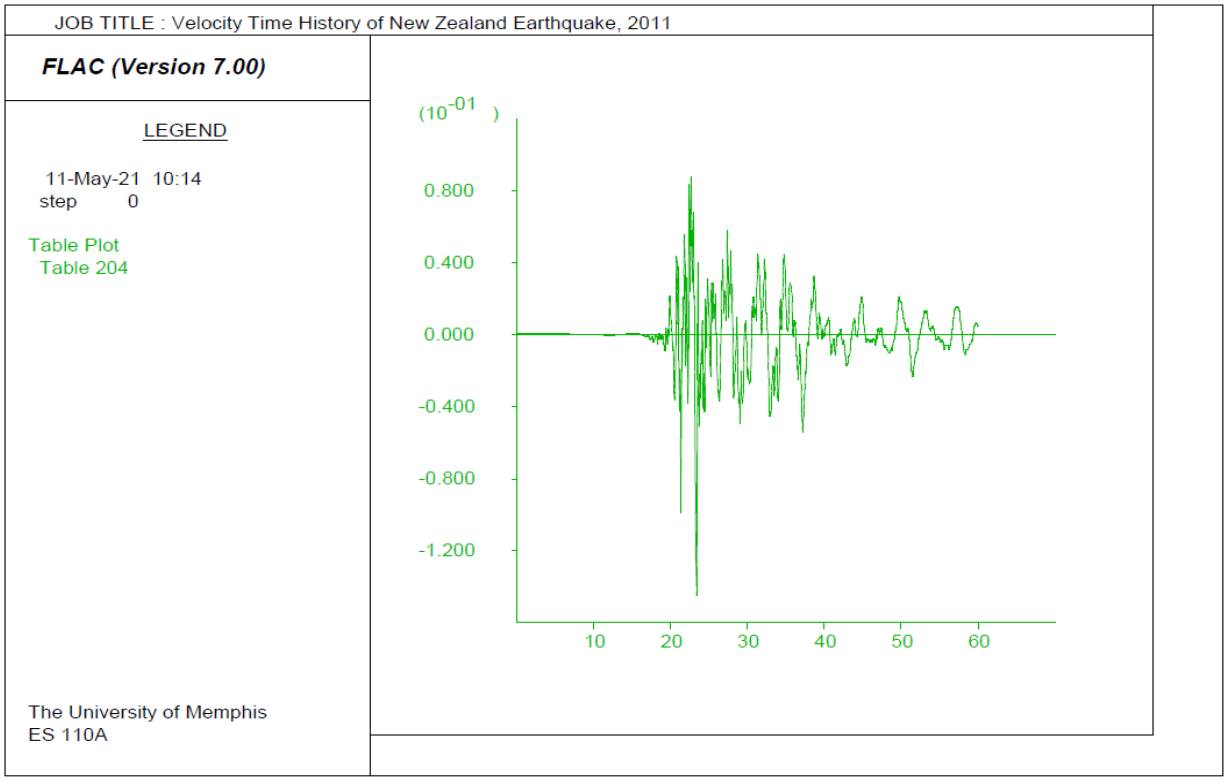

Figure 3.59. Velocity time history of deconvoluted New Zealand 2011 earthquake.

The dynamic analysis of the 2010 earthquake was applied to the YY and NN models for 160 seconds, and the dynamic analysis of the 2011 earthquake was applied to the models for 70 seconds. The Finn-Byrne model is utilized in this study to conduct liquefaction analysis. To analyze the liquefaction occurrence in the models, the appropriate FISH functions were defined to monitor and calculate the pore pressure ratio in different layers of the soil profiles during the dynamic analysis.

3.5. Sensitivity Analysis

This presents the methodology of the sensitivity analysis of liquefaction surface manifestation to the thickness and shear strength of upper non-liquefiable soil layers.

Additionally, the shear strength/stress in different soil layers of the New Zealand soil profiles due to the earthquakes of 2010 and 2011 is analyzed to investigate the impact of shear strength/stress on liquefaction surface manifestation occurrence. For all New Zealand soil models, shear strength and shear stress in each soil layer are obtained based on Mohr-Coulomb failure criteria as well as the results of dynamic analysis of the models. As presented in the previous sections, the simple Finn-Byrne liquefaction model is initially used with the Mohr-Coulomb soil model. These models can be defined based on field test data such as SPT (which is available for the West Tennessee area) and other simple properties such as the shear and elastic moduli of the soil. For all models, after dynamic analysis, the shear strength and shear stress are interpolated from the contour maps and then summarized to explain the liquefaction behavior of each soil model. The results are provided in Chapter 4 of this dissertation.

3.5.1. Sensitivity Analysis of Liquefaction Surface Manifestation to the Thickness of Soil Layers

In this series of analyses, the sensitivity of liquefaction surface manifestation occurrence to the thickness of liquefiable and non-liquefiable soil layers has been studied and will be discussed in the following sections.

3.5.1.1. YY1 Soil Profile

In this set of analyses, the liquefaction surface manifestation sensitivity of the YY1 model has been evaluated by changing the thickness of the upper non-liquefiable layer. For the YY1 model, the liquefiable layers have not been changed in this sensitivity analysis, and all properties were kept the same since the purpose was to evaluate the liquefaction potential sensitivity of these

layers to the thickness of the upper non-liquefiable layer. In the new YY1 soil profile analysis, the thickness of the upper non-liquefiable layer has been increased to 4.8 m while in the original profile it was 1.8 m which could not stop the liquefaction surface manifestation occurrence. The total depth of the soil profile was kept the same at 10 m by reducing the thickness of the bottom non-liquefiable layers to keep it comparable with the original model. By keeping the total depth at 10m, the same mesh size and deconvoluted earthquake time histories were utilized for the sensitivity analysis. Figure 3.60 shows a schematic of the new soil profile of YY1 with each layers' thickness.

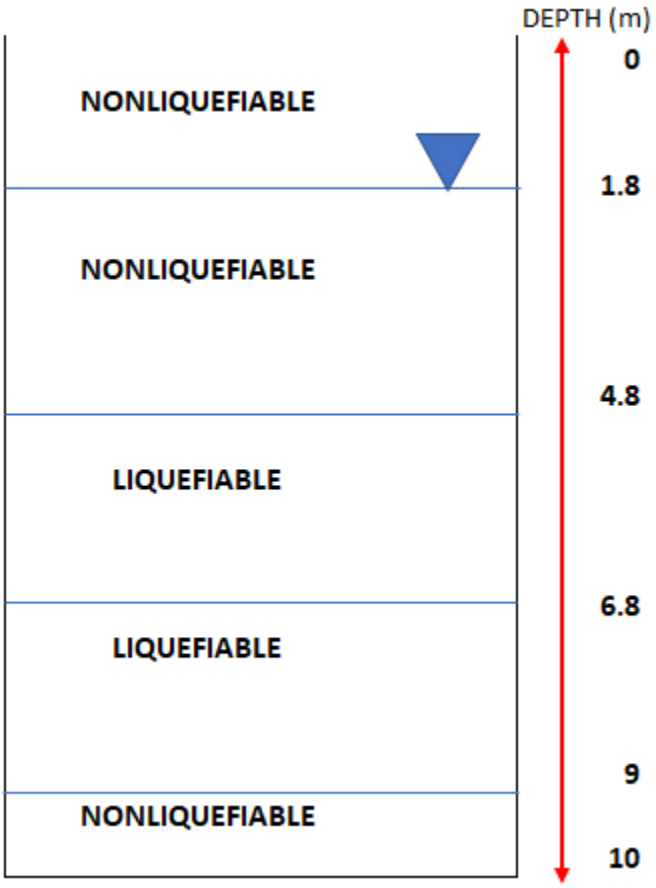

Figure 3.60. Schematic new soil profile of YY1 with layers' thickness.

Additionally, Table 3.25 provides a comparison between the thickness of different layers in the original YY1 and the new YY1 for soil layer thickness sensitivity analysis.

Table 3.25. Layers thickness of YY1 model for thickness sensitivity analysis (NL stands for Non-liquefiable and L stands for Liquefiable).

YY1-Original		YY1-Thickness Changed	
Layer Type	Thickness	Layer Type	Thickness
NL	1.8	NL	1.8
L	2	NL	3
L	2.2	L	2
NL	3	L	2.2
NL	1	NL	1

3.5.1.2. YY2 Soil Profile

The second model is the YY2 soil profile. In the new YY2 model, the thickness of the upper non-liquefiable layer increases to 3.3 m from 1.8 m in the original YY2. Figure 3.61 shows the new YY2 soil profile and Table 3.26 provides the change in thickness of layers from the original to the new YY2.

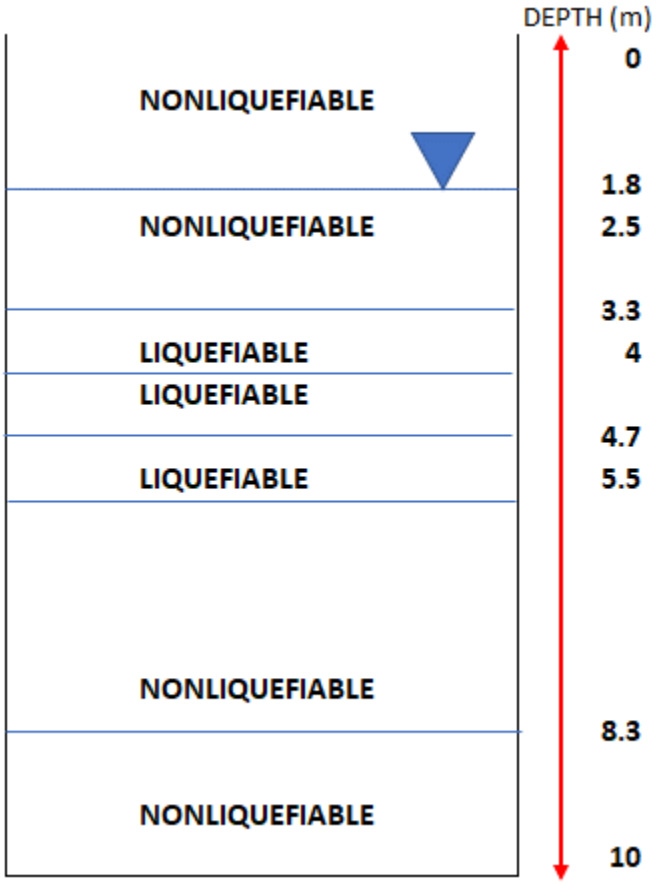

Figure 3.61. Schematic new soil profile of YY2 with layers' thickness.

Table 3.26. Layers thickness of YY2 model for thickness sensitivity analysis (NL stands for Non-liquefiable and L stands for Liquefiable).

YY2-Original		YY2-Thickness changed	
Layer Type	Thickness	Layer Type	Thickness
NL	1.8	NL	1.8
L	0.7	NL	1.5
L	0.7	L	0.7
L	0.8	L	0.7
NL	2.8	L	0.8
NL	1.7	NL	2.8
NL	1.5	NL	1.7

3.5.1.3. NN1 Soil Profile

Unlike the original YY1 and YY2 soil profiles, which showed liquefaction at the ground surface in both the 2010 and 2011 New Zealand earthquakes, the NN1 soil profile did not show any evidence of liquefaction at the ground surface in either the 2010 or 2011 earthquakes. In the thickness sensitivity analysis of the NN1 model, by decreasing the thickness of the upper non-liquefiable layer and keeping the thickness of the liquefiable layers the same as in the original NN1 profile, one could evaluate the impact of the thickness on liquefaction surface manifestation. In the new NN1 model, the thickness of the upper non-liquefiable layer was decreased to 1.6 m while in the original model it was 2.5 m. The overall profile was kept at 10 m. Figure 3.62 shows the new NN1 soil profile and Table 3.27 provides the differences in thicknesses between the original and new NN1 model.

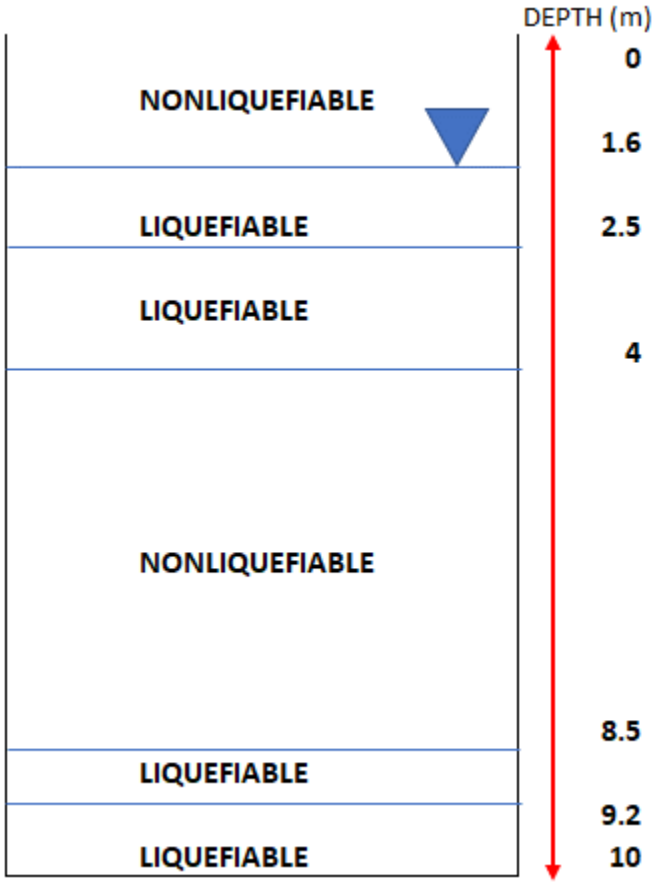

Figure 3.62. Schematic new soil profile of NN1 with layers' thickness.

Table 3.27. Layers thickness of NN1 model for thickness sensitivity analysis.

NN1-Original		NN1-Thickness changed	
Layer Type	Thickness	Layer Type	Thickness
NL	1.6	NL	1.6
NL	0.9	L	0.9
L	1.5	L	1.5
NL	4.5	NL	4.5
L	0.7	L	0.7
L	0.8	L	0.8

3.5.2. Sensitivity Analysis of Liquefaction Surface Manifestation to The Shear Strength of Soil Layers

The second sensitivity analysis that was performed as part of this research is shear strength sensitivity analysis. In this analysis, by keeping the same thickness of soil profiles as the original

New Zealand soil profiles, the sensitivity of the liquefaction surface manifestation potential of liquefiable soil layers to the shear strength of upper non-liquefiable soil crust is evaluated. The details of the shear strength sensitivity analysis for each of the New Zealand soil profiles are provided in the following sections.

3.5.2.1. YY1 Soil Profile

The original soil profile of the YY1 model consists of a 1.8 m, unsaturated, non-liquefiable layer underlain by two liquefiable soil layers (critical zone) with a total thickness of 4.2 m. This model showed liquefaction at the ground surface in both the 2010 and 2011 CES because the developed shear stress in the critical zone was higher than the shear strength of the upper non-liquefiable layers (see Figure 3.63). In the new analysis, the thickness of the critical zone and the upper non-liquefiable layer were retained, and by increasing the shear strength of the upper non-liquefiable layer, the dynamic analysis under both the 2010 and 2011 earthquakes was conducted. The shear strength/stress of different soil layers of the YY1 models for the 2010 and 2011 earthquakes are provided and compared between the original and new YY1 models in Tables 3.28 and 3.29. In this analysis, the shear strength of the upper non-liquefiable layer was increased from 134.63 kPa to 196 kPa. The target shear strength of 196 kPa was selected based on the shear stresses in the liquefiable layers of the original YY1 soil profile. The intent was to make the shear strength of the upper non-liquefiable crust equal to or higher than the shear stress of the underlying critical zone, in both the 2010 and 2011 numerical dynamic analyses.

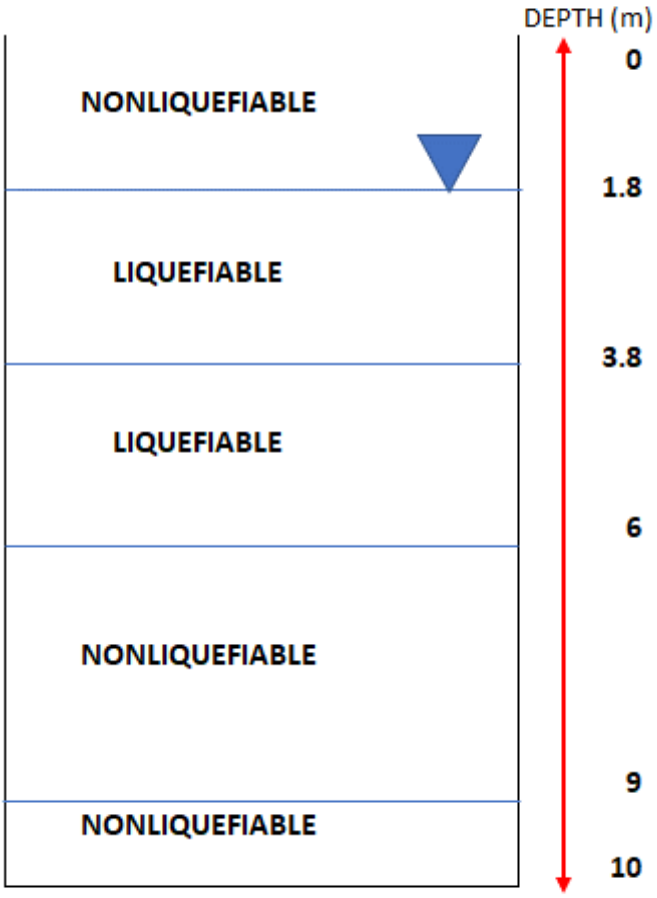

Figure 3.63. Schematic soil profile of YY1 with layers' thickness for shear strength sensitivity analysis.

Table 3.28. Shear strength or stress of different soil layers of YY1 model for shear strength sensitivity analysis for 2010 earthquake (units are kPa) (red numbers are shear stress and black numbers are shear strength).

Layer Essence	Thickness	Shear strength or Shear stress-original	Shear strength or Shear stress-new
NL	1.8	134.63	196
L	2	196	196
L	2.2	196	196
NL	3	166	165.69
NL	1	205	204.88

Table 3.29. Shear strength or stress of different soil layers of YY1 model for shear strength sensitivity analysis for 2011 earthquake (units are kPa) (red numbers are shear stress and black numbers are shear strength).

Layer Essence	Thickness	Shear strength or Shear stress-original	Shear strength or Shear stress-new
NL	1.8	134.63	196
L	2	172	172
L	2.2	172	122
NL	3	166	165.69
NL	1	205	204.88

3.5.2.2. YY2 Soil Profile

Like the YY1 model, for the YY2 model, by increasing the shear strength of the upper non-liquefiable crust, the sensitivity of the profile to the shear strength was analyzed. Figure 3.64 shows the formation of the YY2 soil profile.

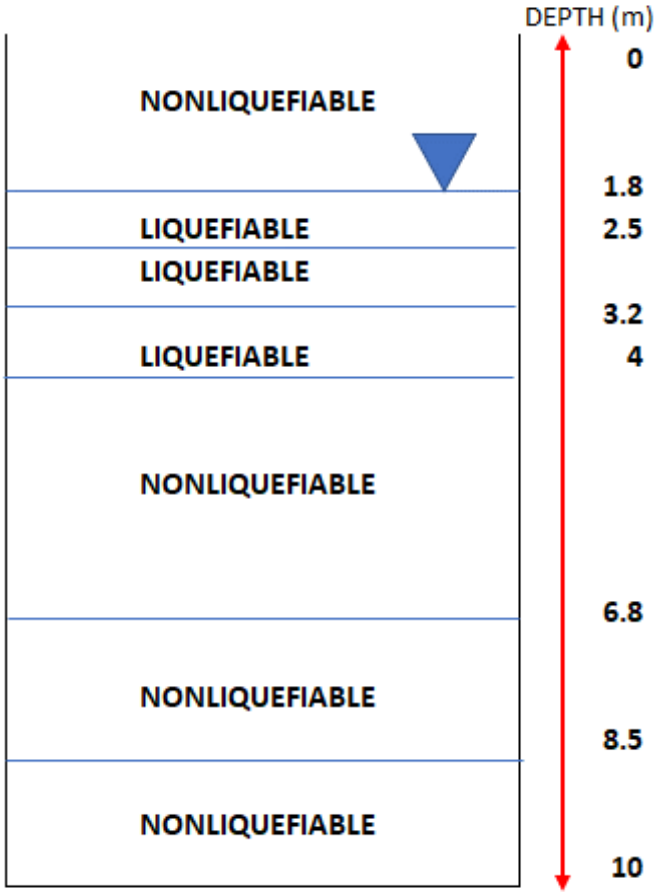

Figure 3.64. Schematic soil profile of YY2 with layers' thickness for shear strength sensitivity analysis.

Tables 3.30 and 3.31 provide the shear strength/stress for the original as well as the new YY2 for both the 2010 and 2011 earthquakes. In this analysis, the shear strength of the upper non-liquefiable layer was increased from 134 kPa to 196 kPa. Like the YY1 model, for the YY2 model the goal was to make the shear strength of the upper non-liquefiable crust equal to or higher than the shear stress of the underlying critical zone, in both the 2010 and 2011 numerical dynamic analyses.

Table 3.30. Shear strength/stress of different soil layers of YY2 model for shear strength sensitivity analysis for 2010 earthquake (units are kPa) (red numbers are shear stress and black numbers are shear strength).

Layer Essence	Thickness	Shear strength or Shear stress-original	Shear strength or Shear stress-new
NL	1.8	134	196.00
L	0.7	147	147
L	0.7	147	147
L	0.8	147	147
NL	2.8	158.65	158.65
NL	1.7	179.90	179.90
NL	1.5	203.30	203.30

Table 3.31. Shear strength/stress of different soil layers of YY2 model for shear strength sensitivity analysis for 2011 earthquake (units are kPa) (red numbers are shear stress and black numbers are shear strength).

Layer Essence	Thickness	Shear strength or Shear stress-original	Shear strength or Shear stress-new
NL	1.8	98.00	196.00
L	0.7	122	122
L	0.7	122	122
L	0.8	122	98
NL	2.8	158.65	158.65
NL	1.7	179.90	179.90
NL	1.5	203.30	203.30

3.5.2.3. NN1 Soil Profile

The NN1 soil profile is shown in Figure 3.65 with layer thickness and essence. This soil profile did not show any liquefaction at the ground surface during the 2010 and 2011 CES earthquakes of New Zealand. In the shear strength sensitivity analysis of the NN1 soil profile, by changing the shear strength as provided in Tables 3.32 and 3.33 for the 2010 and 2011 earthquakes, the liquefaction surface manifestation was investigated. Unlike the YY models, for the NN1 model, the shear strength of the upper non-liquefiable layer was decreased to 98 kPa to check if decreasing the shear strength of the upper non-liquefiable layer can cause liquefaction surface

manifestation from liquefied soils of liquefiable layers. The target shear strength of 98 kPa was selected based on the shear stresses in the liquefiable layers of the original NN1 soil profile.

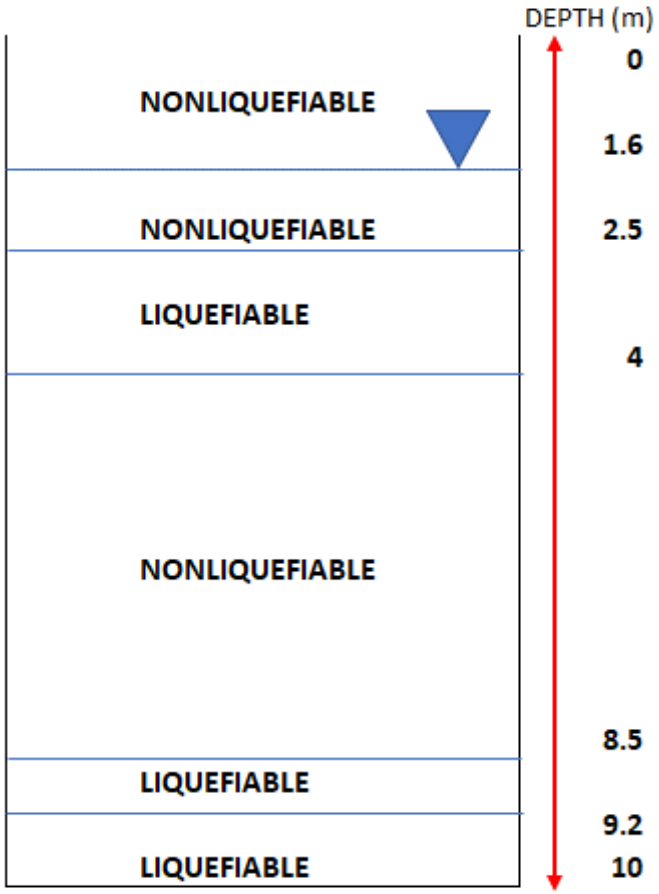

Figure 3.65. Schematic soil profile of NN1 with layers' thickness for shear strength sensitivity analysis.

Table 3.32. Shear strength/stress of different soil layers of YY1 model for shear strength sensitivity analysis for 2010 earthquake (units are kPa) (red numbers are shear stress and black numbers are shear strength).

Layer Essence	Thickness	Shear strength or Shear stress-original	Shear strength or Shear stress-new
NL	1.6	132.84	98.00
NL	0.9	147.58	98.00
L	1.5	98	147-196
NL	4.5	178.54	178.54
L	0.7	96.78	96.78
L	0.8	71.74	71.74

Table 3.33. Shear strength/stress of different soil layers of YY1 model for shear strength sensitivity analysis for 2011 earthquake (units are kPa) (red numbers are shear stress and black numbers are shear strength).

Layer Essence	Thickness	Shear strength or Shear stress-original	Shear strength or Shear stress-new
NL	1.6	132.84	98.00
NL	0.9	147.58	98.00
L	1.5	49.00	147
NL	4.5	178.54	178.54
L	0.7	96.78	96.78
L	0.8	71.74	71.74

3.6. Shear Strength and Thickness Correlation to Adjust LPI_{ISH} Framework

The last analysis of this research is finding a relationship between soil layer thickness, shear strength, and occurrence of liquefaction surface manifestation based on the 18 analyses that were conducted and described in this chapter on the New Zealand soil profiles YY1, YY2, NN1, and a partial analysis of NN2. Figure 3.66 shows the schematic path to find the correlation between soil layer thickness, soil layer shear strength, and liquefaction surface manifestation occurrence.

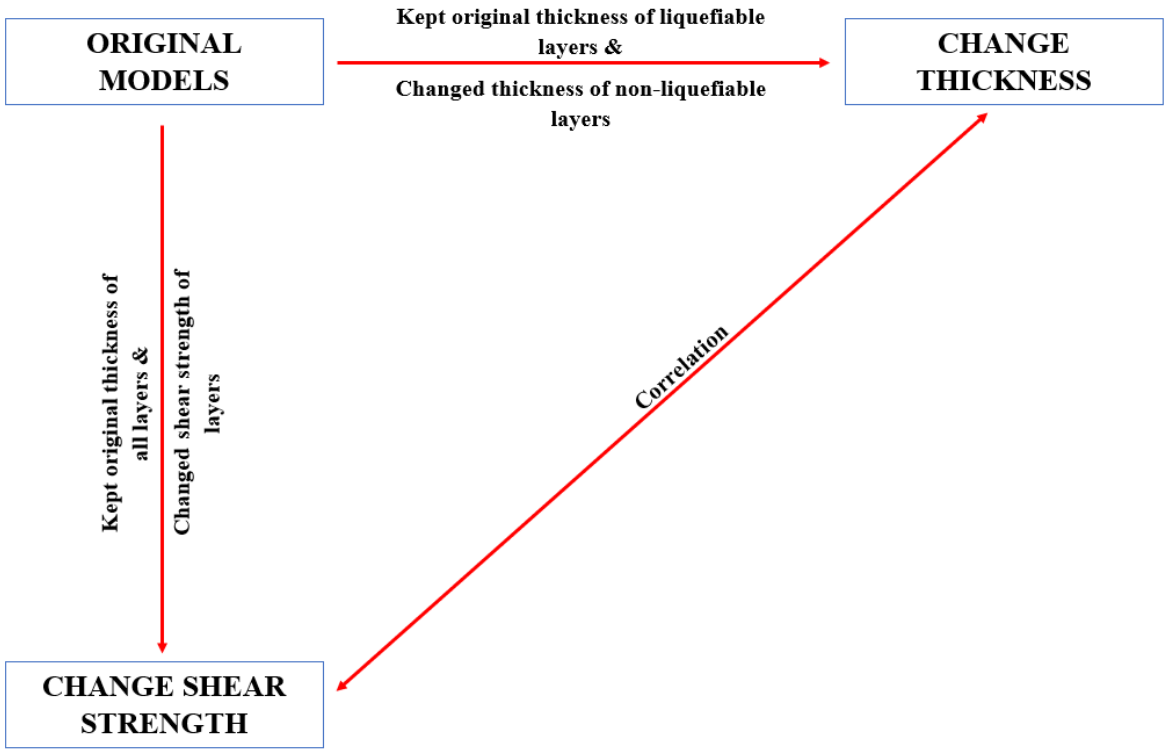

Figure 3.66. Flowchart of correlation between thickness, shear strength, and liquefaction surface manifestation.

To find the relationship, a series of statistical analyses were done to extract the strongest relationship between the three parameters. For this study, to find the relationship between more than two parameters (three parameters), the results of all the analyses were defined in a matrix form in MATLAB and, using the CORR and PARTIALCORR functions of MATLAB, the conditions that lead to the adjustment of the LPI_{ISH} framework based on the correlation between thickness, shear strength, and liquefaction surface manifestation is obtained.

In statistics, the correlation between two variables is defined as the magnitude of the linear association between the variables and is presented by the correlation coefficient. In this study, since the number of variables is three (more than two) the basic definition of correlation must be extended to three variables.

For the two-variables case, the correlation range is between 0 to 1 with 0 indicating the weakest consistency and 1 representing the strongest consistency, i.e., strong agreement. The correlation coefficient (r) is obtained by equation (3.40):

$$r = \frac{\sum(x_i - \bar{x})(y_i - \bar{y})}{\sqrt{\sum(x_i - \bar{x})^2 \sum(y_i - \bar{y})^2}} \tag{3.40}$$

where, x_i are the values of the x-variable in a sample, $\bar{x}$ is the mean of the values of the x-variable, y_i are the values of the y-variable in a sample, and $\bar{y}$ is the mean of the values of the y-variable.

Since, for this study, there are three variables of thickness, shear strength, and liquefaction surface manifestation occurrence, the above equation is not appropriate. Thus, the method of Multiple Correlation was employed to find the correlation between three variables. In multiple correlation methodology with variables x, y, and z, the correlation coefficient is computed using the following equation.

$$r_{x,y,z} = \sqrt{\frac{r_{xz}^2 + r_{yz}^2 - 2r_{xz}r_{yz}r_{xy}}{1 - r_{xy}^2}} \tag{3.41}$$

where r_{xz}, r_{yz}, r_{xy} are correlations between every two variables. Here x and y are thickness and shear strength, respectively, and they are independent variables while z is liquefaction surface manifestation and is the dependent variable.

As provided in the previous sections of this chapter, a total of 18 different analyses were done as follows:

- Three models of YY1, YY2, and NN1.
- Three different analyses of the original models, thickness sensitivity analysis, and shear strength sensitivity analysis.

- Two earthquake scenarios of CES 2010 and 2011 for each of the models in the original, thickness sensitivity and shear strength sensitivity analyses.

The NN2 soil profile of New Zealand has been excluded from the correlation analysis because, for the NN2 model, in a 10 m soil profile, there are 11 soil layers in a very stratified formation of liquefiable and non-liquefiable soil layers with very thin layers, which makes it so difficult to perform sensitivity analysis on this model, specifically soil layers thickness sensitivity analysis. The results of the correlation analysis are provided in Chapter 4.

CHAPTER 4. RESULTS

Chapter 4 of this dissertation provides the results of the liquefaction hazard analysis of West Tennessee followed by the results of the numerical analysis of the Wildlife, CA, site and the New Zealand soil profiles. Later in this chapter, the results of the sensitivity analysis of thickness and shear strength will be provided, followed by the detailed correlation analysis of shear strength and soil layer thickness.

4.1. LPI and LPI_{ISH} Based Results of West Tennessee

As discussed in Chapter 3, in this study LPCs were developed using the three-step procedure utilized by Rix and Romero-Hudock (2006) and Cramer et al. (Cramer et al., 2008, 2019, 2020a, b, 2021, and 2022). Then, by employing the obtained factor of safety for each boring log, the liquefaction potential indices of LPI and LPI_{ISH} at each soil boring location were computed for four western Tennessee counties of Lake, Dyer, Lauderdale, and Tipton.

Lake County consists of only lowland surficial geologic units; the other counties have lowland, intermediate, and upland geologic units. Since the number of soil boring logs was insufficient in the intermediate and upland geologic units, the data from the intermediate and upland geologic units were combined and a single LPC was developed for non-lowlands (intermediate and upland) in each county.

To develop the LPCs, the LPI and LPI_{ISH} were determined at each boring location for peak ground acceleration (PGA) values of 0.1, 0.2, 0.3, 0.4, 0.5, 0.6, 0.7, 0.8, 0.9, and 1.0g and earthquake magnitudes (M_w) of 5, 5.5, 6, 6.5, 7, 7.5, and 8 (Cramer et al., 2019, 2020a, b, 2021, and 2022). Thus, LPI and LPI_{ISH} are determined for each of 70 possible combinations of PGA and M_w (i.e., 70 earthquake scenarios). After the determination of LPI and LPI_{ISH} at each boring

location, the distribution of the number of soil boring locations (frequency) of a given range of LPI and LPI_{ISH} values was determined for every individual combination of PGA and M_w for the Lowlands and non-lowlands geologic units of each of the West Tennessee counties by creating a MATLAB code.

4.1.1. Lake County

As mentioned in previously, the geologic unit for the entire Lake County is lowlands. Thus, the LPCs had to be developed for only one geologic unit. The LPCs for Lake County were developed based on both the LPI and LPI_{ISH} methods as shown in Figure 4.1. The LPI-based LPC of Lake County shows a significantly higher probability of liquefaction than the LPI_{ISH}-based LPC, especially for stronger earthquake scenarios. For the PGA/MSF range of 0 to 0.4 both curves are almost equal; however, from PGA/MSF 0.4 to 1.2, the LPI-based LPC gradually goes higher than LPI_{ISH}-based LPC, reaching a maximum difference of 45% for the strongest earthquake scenario (PGA/MSF of 1.2).

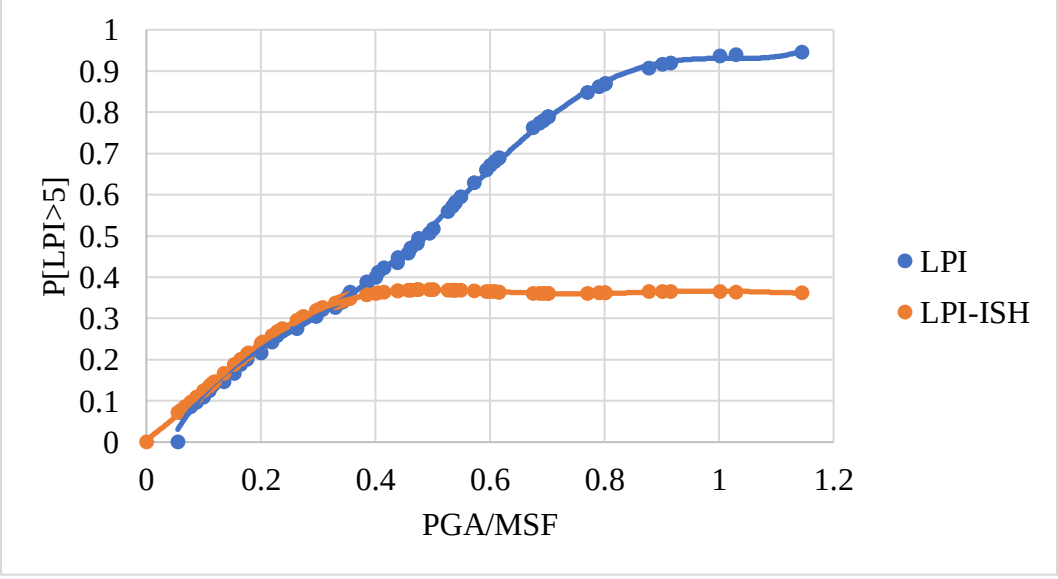

Figure 4.1. LPI and LPI_{ISH}-based LPCs of Lake County.

As noted in Chapter 3, for Lake County, LPCs were developed based on SPT N-values and V_s data. A comparison of the LPCs based on N-values and V_s profiles is presented next. However, the comparison is only for the LPI-based method. Figure 4.2, which shows a comparison between the N-value LPC and the V_s LPC at P[LPI>5] (LPI of 5 is the threshold value for liquefaction surface manifestation occurrence), indicates that V_s profile data yields higher probabilities of exceeding an LPI of 5.

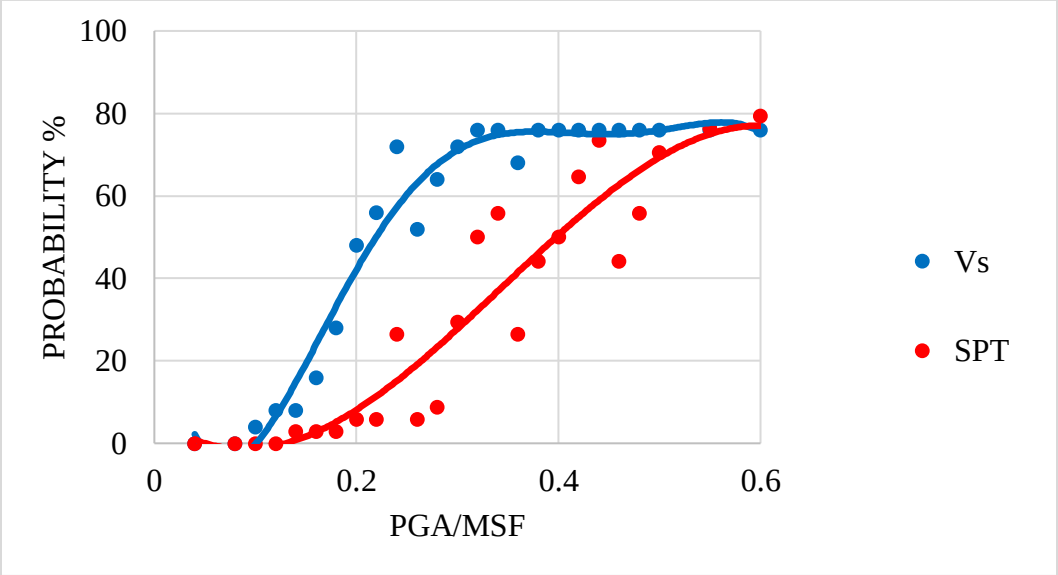

Figure 4.2. Comparison of obtained LPCs based on SPT data and shear wave velocity profiles for LPI>5.

It should be noted that the soil boring locations representing the N-values used for the LPCs in Figure 4.2 are different from the V_s profile locations. Therefore, to better compare LPCs between data obtained with N-values and V_s profiles, I analyzed data included in the Pezeshk et al. (1998) study, which includes both N-value data and V_s profile data obtained at the same locations at ten sites in west Tennessee. The results of this analysis are presented in the Dyer County Seismic and Liquefaction Hazard Analysis report (Cramer et al., 2020a).

4.1.2. Dyer County

The surficial geology of Dyer County consists of lowland, intermediate, and upland geologic units. Most boring data within Dyer County are located in the lowlands and insufficient boring data is available from the intermediate and upland areas to develop LPCs. Therefore, the boring data from the intermediate and uplands geologic units were combined to represent the non-lowland parts of Dyer County. Thus, LPCs were developed for lowland and non-lowland parts of Dyer County.

For the lowland part of Dyer County, an initial LPC was developed based on the LPI method and using data from 118 SPT borings. Figure 4.3 provides the LPC for the probability of exceeding an LPI of 5 denoted as P[LPI>5]. As shown in Figure 4.3, LPC is plotted as a probability range ([0,1]) of exceeding the target LPI value versus the PGA/MSF.

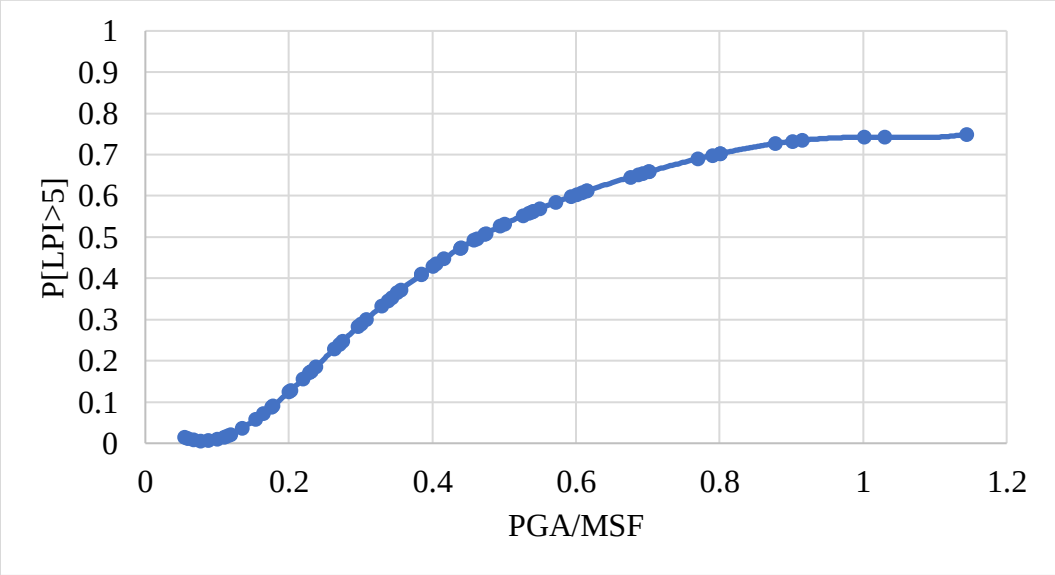

Figure 4.3. Lowland LPI-based LPC of Dyer County.

The non-lowland LPI-LPC of Dyer County was developed based on a combination of 22 SPT borings from the intermediate geologic unit and 2 SPT borings from the upland geologic unit.

Therefore, the non-lowland LPC is based on 24 SPT borings. Figure 4.4 shows the non-lowland LPC of Dyer County for P[LPI>5].

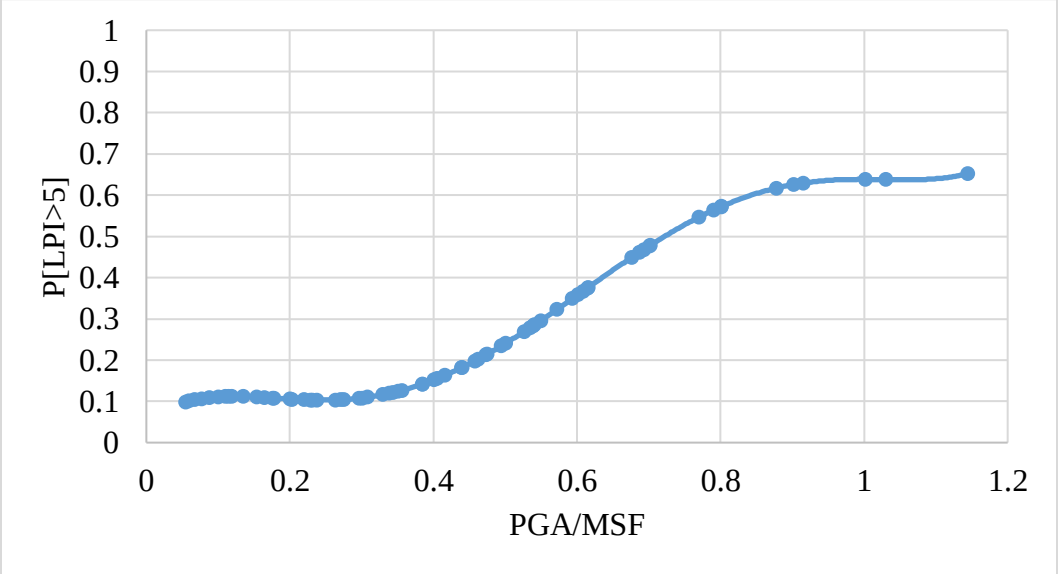

Figure 4.4. Non-lowland LPI-based LPC of Dyer County.

The above figure shows an unusually high probability of liquefaction for P[LPI>5] for typical non-lowland subsurface conditions, which are less prone to liquefaction than the lowlands. Based on a further evaluation of the Dyer County non-lowland SPT data, the geometric mean of N_{160cs} is 17 while the liquefaction threshold value of N_{160cs} is less than or equal to 30. N_{160cs} is the equivalent clean sand standard penetration resistance that is used in the evaluation of liquefaction potential based on the simplified method. Additionally, the geometric mean of the soil fines content of the 24 non-lowland borings is 6.6% while the liquefaction threshold value of fines content is less than or equal to 35%. Therefore, since the geometric mean of both N_{160cs} and the fines content of the non-lowland soil boring data are less than the threshold values for these parameters, the probability of liquefaction for P[LPI>5] is unusually high for non-lowland areas of Dyer County. Additional soil borings data may lower the probability of liquefaction.

Using Maurer's framework based on LPI_{ISH}, another set of LPCs for both lowland and non-lowland parts of Dyer County was developed. Figures 4.5 and 4.6 illustrate the LPCs obtained based on SPT boring data for lowland and non-lowland areas, respectively.

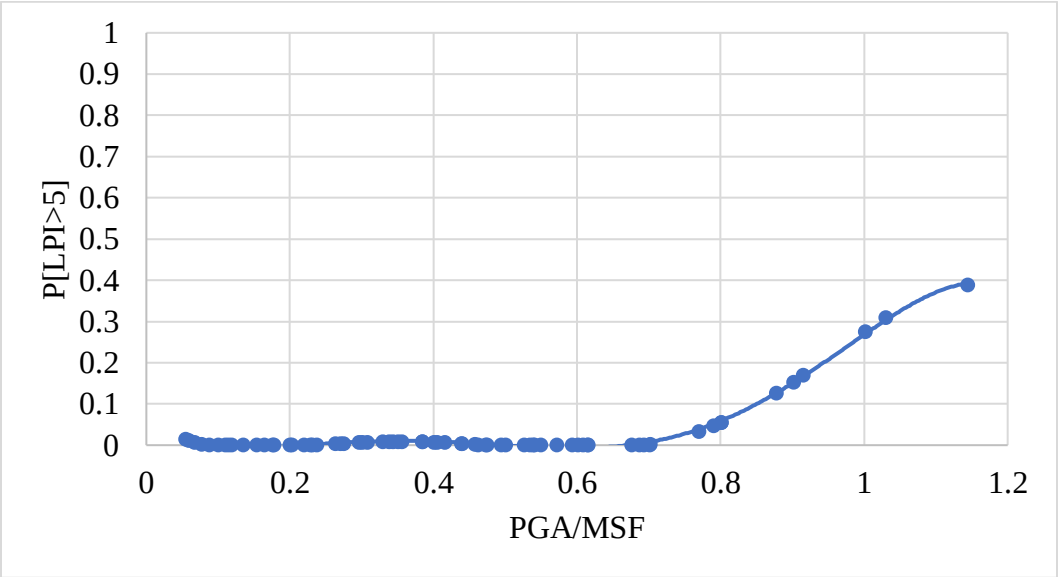

Figure 4.5. Lowland LPI_{ISH}-based LPC of Dyer County.

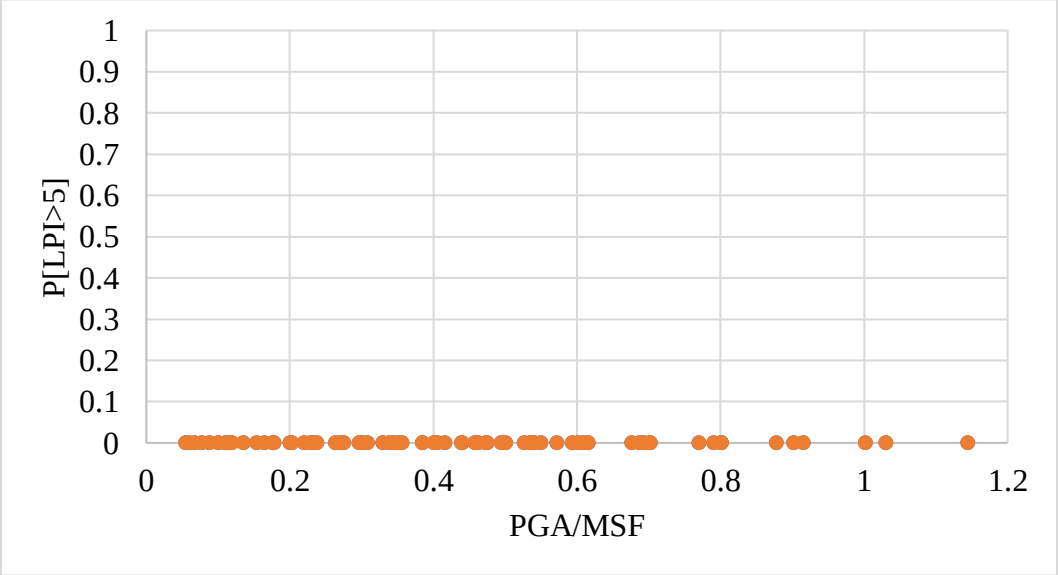

Figure 4.6. Non-lowland LPI_{ISH}-based LPC of Dyer County.

Figures 4.7 and 4.8, which show a comparison of LPI and LPI_{ISH}-based LPCs for lowland and non-lowland areas of Dyer County for P[LPI>5], indicate that the probability of liquefaction provided by the LPCs based on the LPI_{ISH} framework is significantly lower than the probability of

liquefaction provided by the LPCs based on the LPI framework, especially at higher ratios of PGA/MSF. The maximum difference is about 45% in lowlands and 35% in non-lowlands.

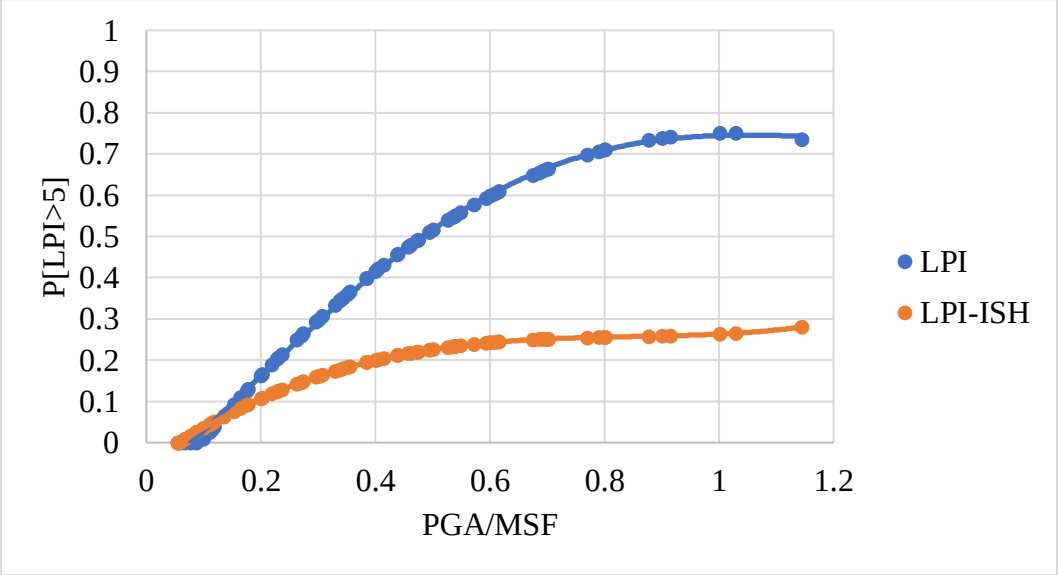

Figure 4.7. Comparison of LPI- and LPI_{ISH}-based lowland LPCs for P[LPI>5].

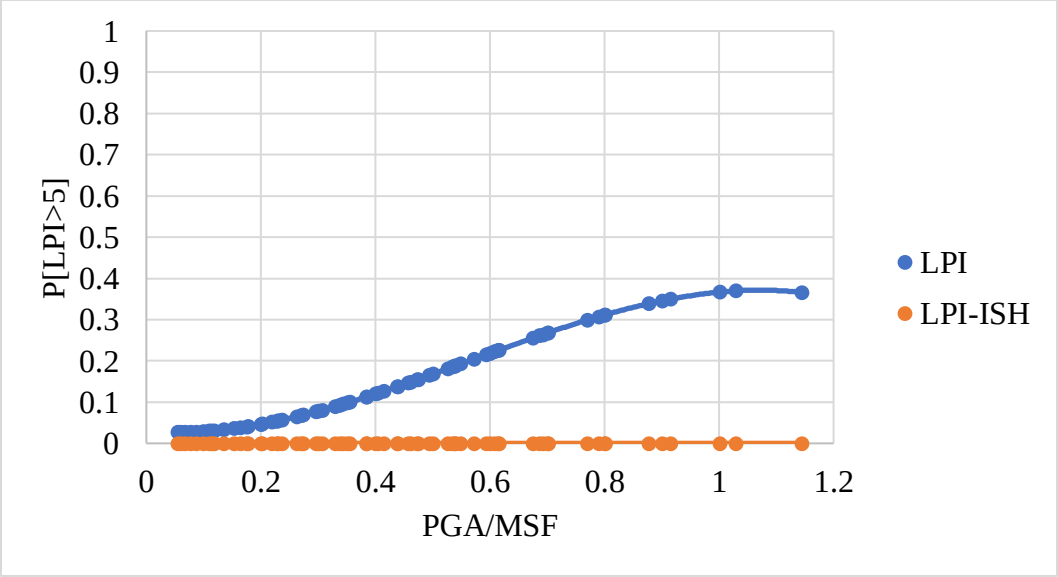

Figure 4.8. Comparison of LPI- and LPI_{ISH}-based non-lowland LPCs for P[LPI>5].

In summary, for both the lowland and the non-lowland areas of Dyer County, the probability of liquefaction provided by the LPCs based on the LPI_{ISH} framework are lower than the LPCs based on the LPI framework, especially at higher ratios of PGA/MSF.

4.1.3. Lauderdale County

For Lauderdale County, the LPCs were initially developed based on the LPI approach in which it is assumed that all liquefiable layers equally contribute to the surficial manifestation of liquefaction without considering the impact of the non-liquefiable cap on liquefiable layers. LPI-based LPCs were generated for three surface geology units of lowland, intermediate, and upland. For the lowland part of Lauderdale County, LPCs were developed based on SPT data of 153 soil borings while for the intermediate and upland regions the number of utilized soil borings data were 47 and 9, respectively. Figures 4.9, 4.10, and 4.11 show the LPCs for lowland, intermediate, and upland areas of the probability of exceeding LPI of 5 versus the ratio of PGA over MSF.

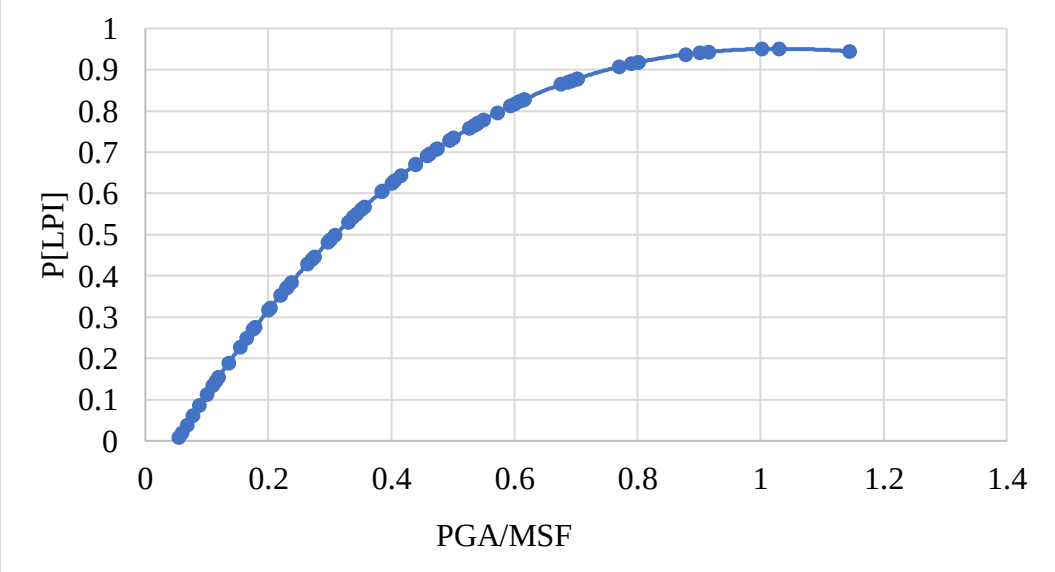

Figure 4.9. LPI-based lowland LPC from SPT data.

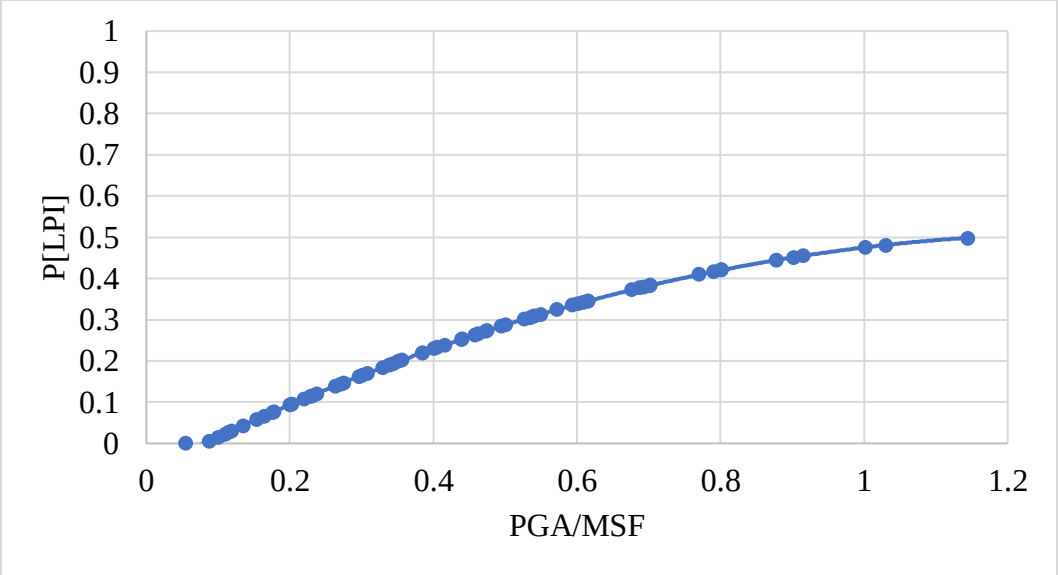

Figure 4.10. LPI-based intermediate LPC from SPT data.

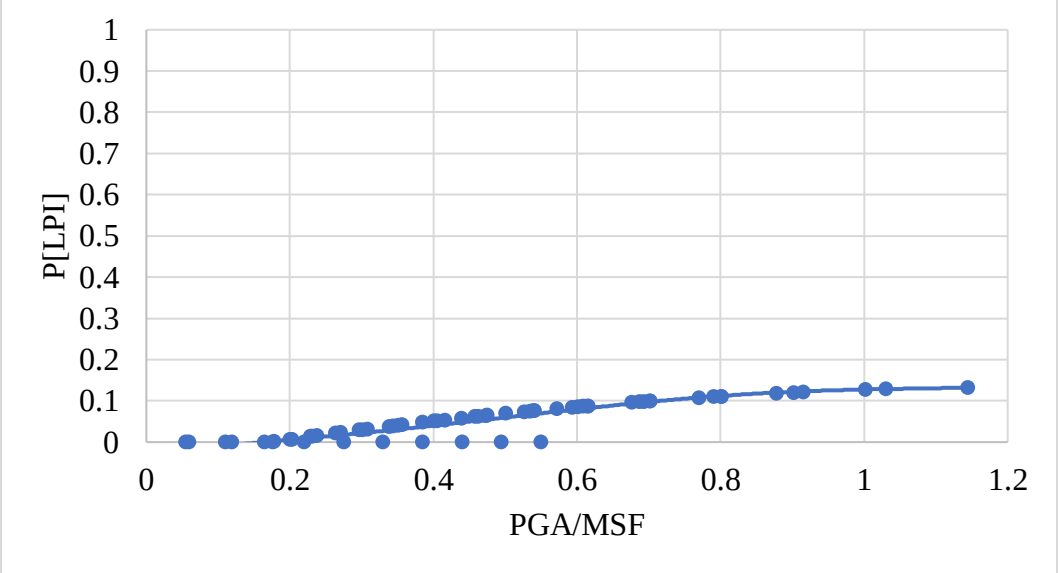

Figure 4.11. LPI-based upland LPC from SPT data.

As was expected, the lowland LPC is significantly higher than the intermediate and upland LPCs. Table 4.1 provides the maximum probability of exceeding LPI>5 for each geologic unit that was observed from the LPCs at the highest ratio of PGA/MSF.

Table 4.1. The maximum probability of exceeding LPI>5 and LPI>15 at each geologic unit.

The maximum probability of exceeding	Lowland	Intermediate	Upland
P[LPI>5]	0.94 (94%)	0.49 (49%)	0.13 (13%)

For Dyer County, due to a lack of enough soil boring data within the intermediate and upland, the LPCs were developed for the lowland and non-lowland, which was the combination of the intermediate and upland. For Lauderdale County, also, the boring log data of intermediate (47 borings) and upland (9 borings) were combined to develop the LPCs for the non-lowland parts of the county as it is shown in Figure 4.12. The maximum probability of exceeding LPI>5 at the highest ratio of PGA /MSF for the non-lowland area is 0.43 (43%). Therefore, compared to the intermediate only, the probability decreases and, compared to the upland only, the probability of liquefaction occurrence increases when the soil boring data of intermediate and upland are combined.

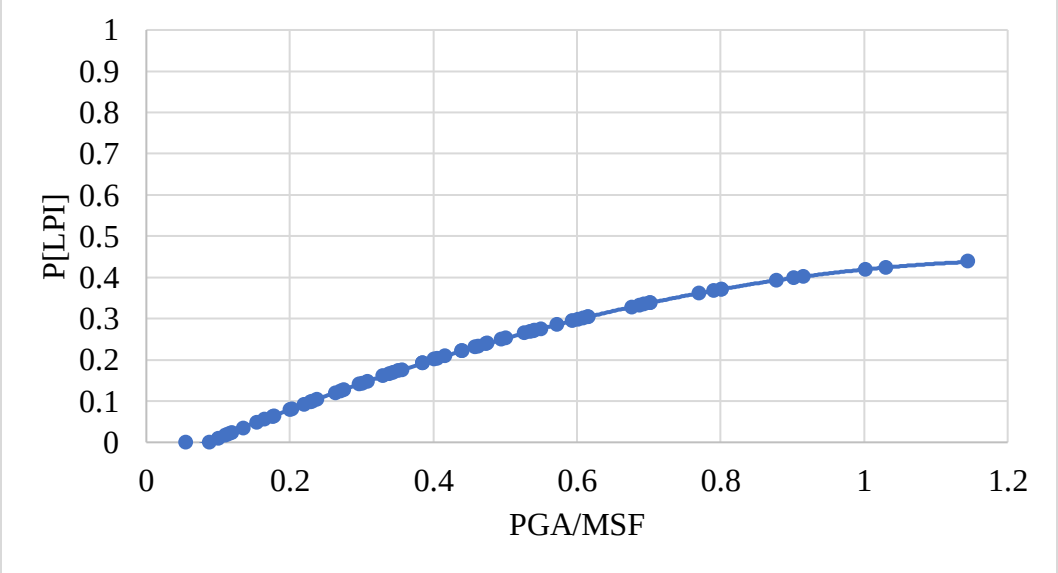

Figure 4.12. LPI-based non-Lowland LPC from SPT data.

In addition to the LPI-based method of developing LPCs, LPI_{ISH} was utilized to develop LPCs in which the influence of non-liquefiable crust thickness on the surface manifestation of

liquefaction is considered. The LPI_{ISH}-based LPCs were generated for both lowland and non-lowland parts of Lauderdale County; they are shown in Figures 4.13 and 4.14, respectively.

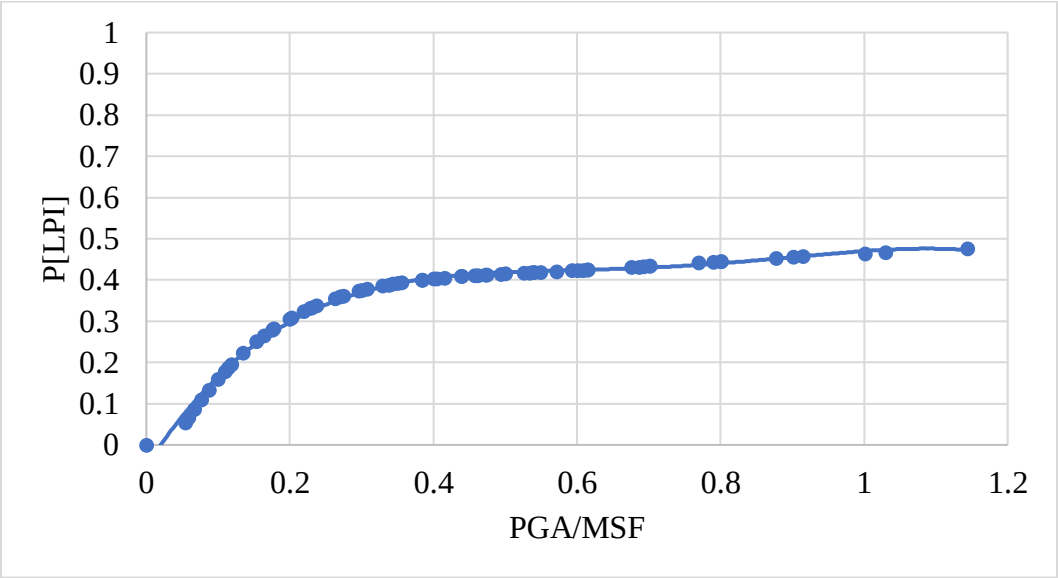

Figure 4.13. LPI_{ISH}-based LPC of lowland from SPT data.

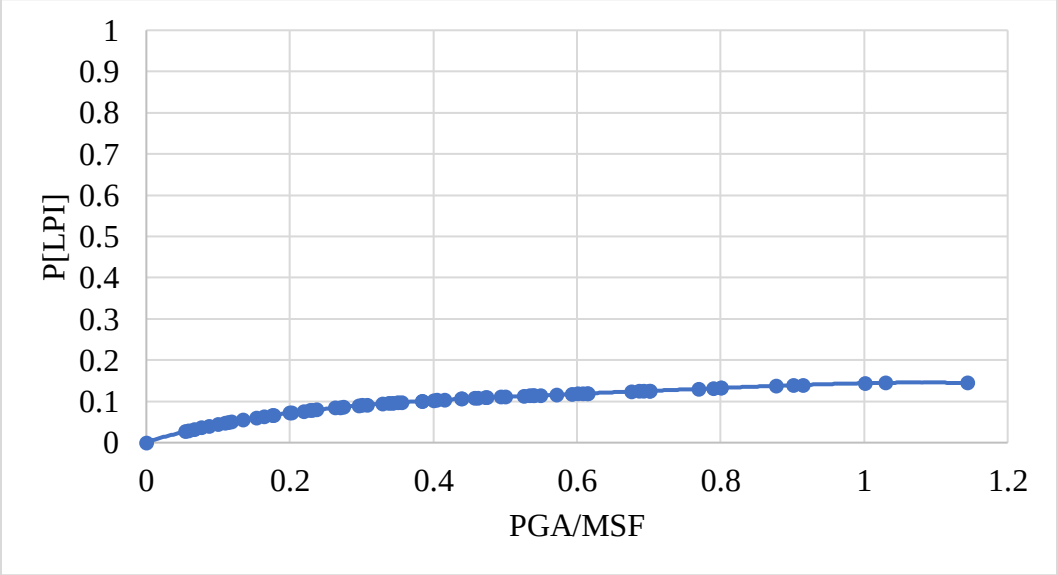

Figure 4.14. LPI_{ISH}-based LPC of non-Lowland from SPT data.

Similar to the previous counties, the lowland LPI_{ISH}-based LPC shows a higher trend than the non-lowland LPI_{ISH}-based LPC.

For the lowland and non-lowland areas of Lauderdale County, the obtained LPCs from different methods for the probability of exceeding the threshold value of (P[LPI, LPI_{ISH}>5]) are compared in this section. Figures 4.15 provides a comparison of LPI- and LPI_{ISH}-based lowland LPCs.

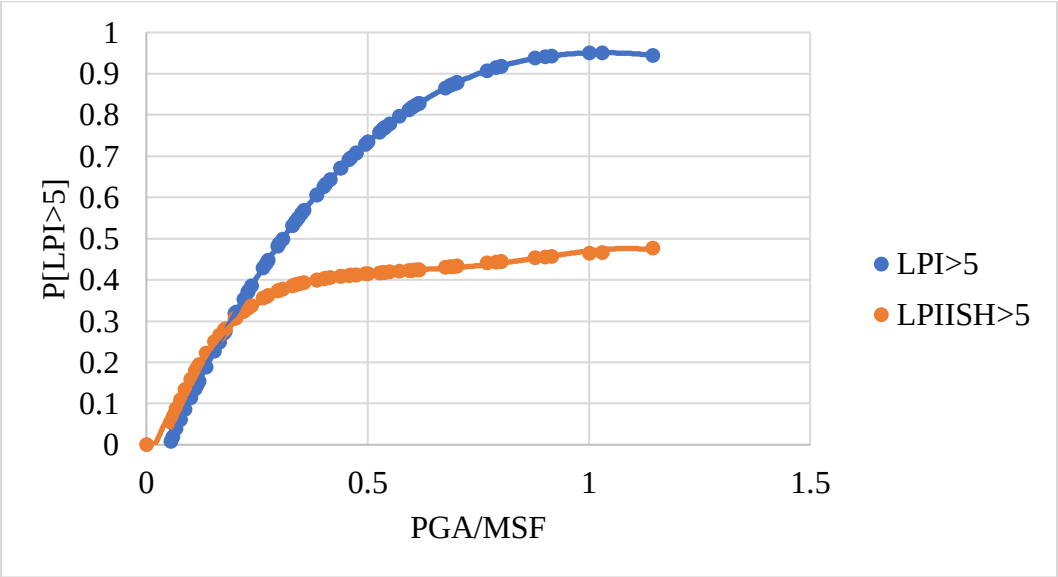

Figure 4.15. LPI- and LPI_{ISH}-based lowland LPCs for P[LPI>5].

Figure 4.15 indicated that the LPI_{ISH}-based LPC is significantly lower than the LPI-based LPC, especially for PGA/MSF ratios of higher than 0.25 (i.e., stronger earthquake scenarios) and the maximum difference is about 45% for PGA/MSF in the range of 0.6 to 1.2.

For the non-lowland parts of the county, the comparison between LPI and LPI_{ISH}-based LPCs is shown in Figure 4.16. Similar to the results of the lowland areas, for the non-lowland areas the LPI_{ISH}-based LPC shows lower probabilities than the LPC from the LPI method. However, the amount of difference between the LPCs of the two frameworks is less for the non-lowlands than the lowlands.

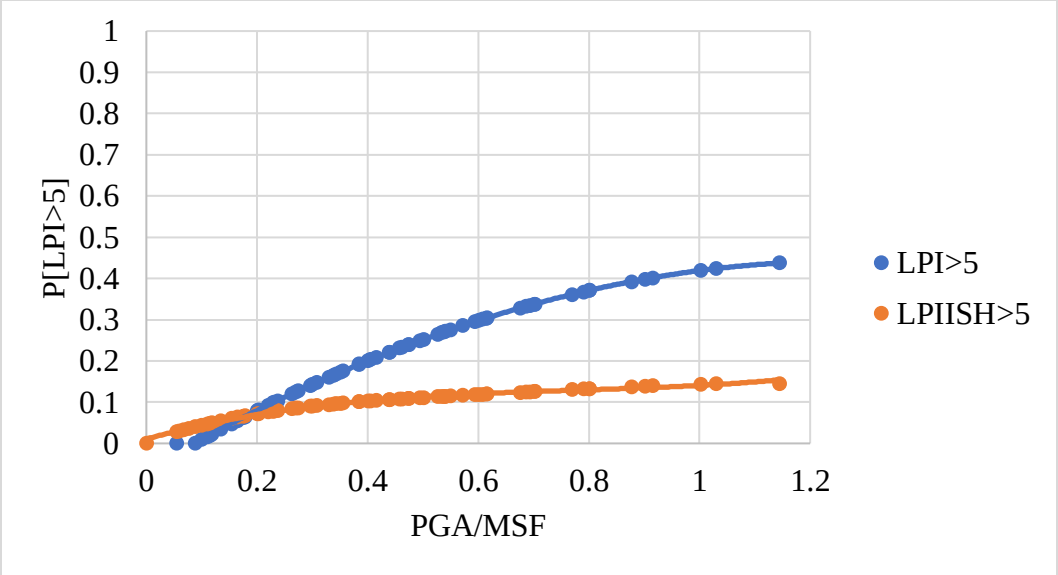

Figure 4.16. LPI- and LPI_{ISH}-based non-lowland LPCs for P[LPI>5].

Figure 4.16 showed that both LPCs have a similar probability in the range of 0 to 0.2 PGA/MSF while for PGA/MSF, higher than 0.2, the LPI-based LPC reaches 45% probability for a PGA/MSF of 1.2 while the LPI_{ISH} LPC is showing a probability of 15%.

4.1.4. Tipton County

Initially, the LPI-based LPCs were generated for three surficial geologic units of lowland, intermediate, and upland separately. The total number of SPT soil borings that were utilized to develop the LPI-based LPCs of lowland, intermediate, and upland are 22, 27, and 10, respectively. Figures 4.17, 4.18, and 4.19 show the LPCs for lowland, intermediate, and upland of the probability of exceeding LPI of 5 versus the ratio of PGA over MSF.

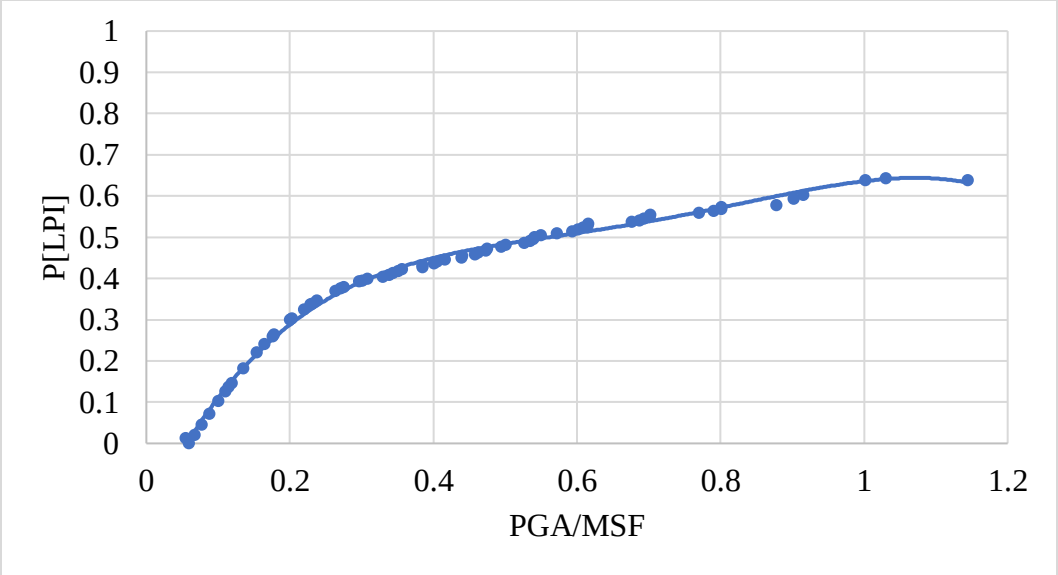

Figure 4.17. LPI-based lowland LPCs from SPT data.

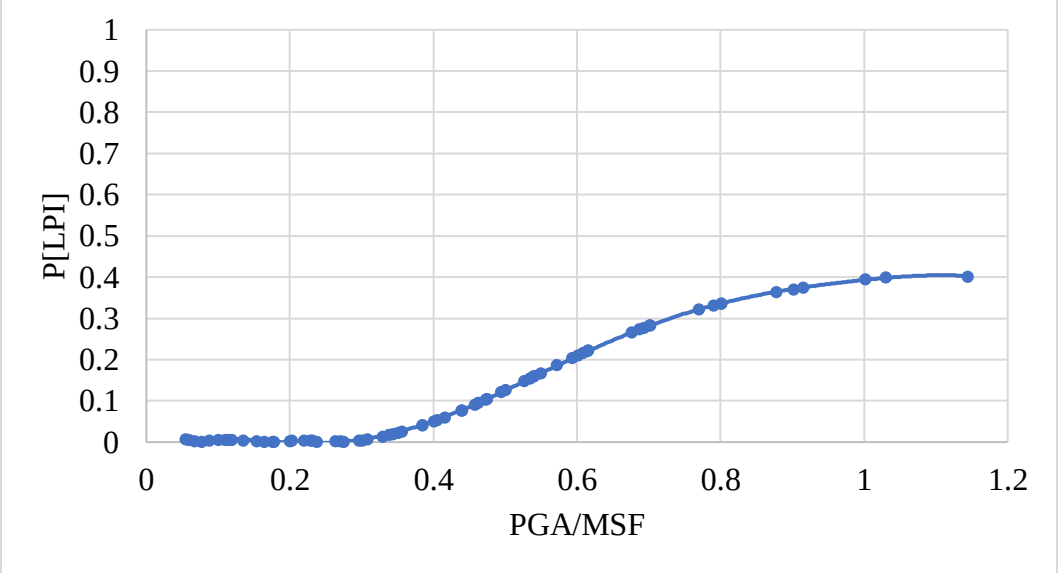

Figure 4.18. LPI-based intermediate LPCs from SPT data.

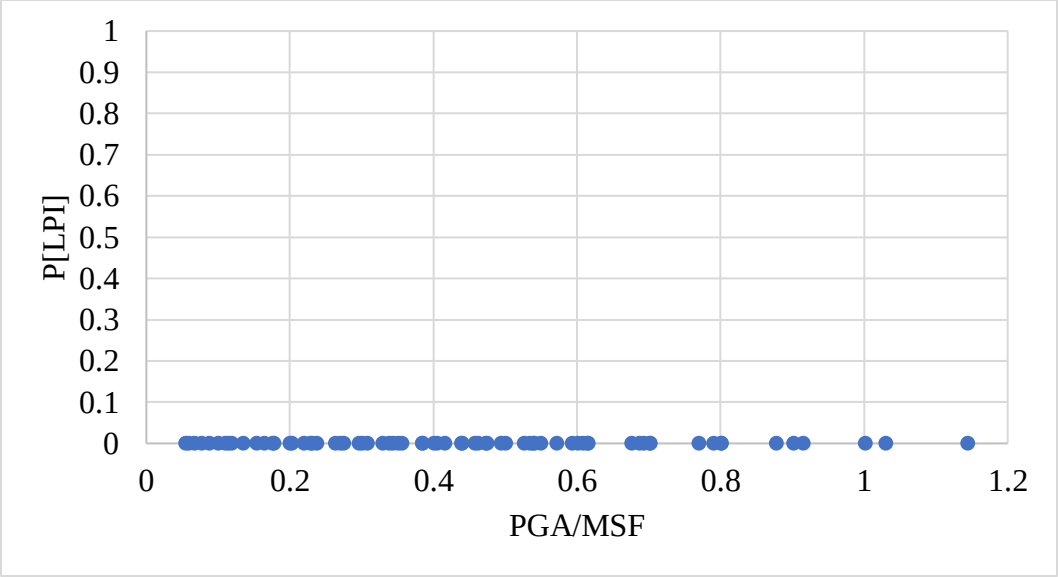

Figure 4.19. LPI-based upland LPCs from SPT data.

In Figures 4.17 to 4.19, the lowland LPCs are showing the highest probability of liquefaction because lowlands are the most susceptible geologic units to liquefaction. The uplands show a zero percent probability of liquefaction for the entire range of PGA/MSF for LPI>5. Table 4.2 provides the maximum probability of exceeding LPI>5 for each geologic unit that was obtained from the LPCs at the highest ratio of PGA/MSF.

Table 4.2. The maximum probability of exceeding LPI>5 and LPI>15 at each geologic unit.

The maximum probability of exceeding	Lowland	Intermediate	Upland
P[LPI>5]	0.64 (64%)	0.40 (40%)	0.0 (0%)

Like Dyer and Lauderdale counties, for Tipton County there is a lack of enough soil borings in the intermediate and upland areas. Therefore, by combining the boring logs of intermediate and upland, another set of LPCs was generated for the non-lowland part of Tipton County. The SPT boring log data of intermediate and upland were combined and a new LPC for non-lowlands was developed as shown in Figure 4.20. The maximum probability of exceeding LPI>5 at the highest ratio of PGA/MSF for the non-lowland is 0.49 (49%). Thus, compared to the intermediate and

upland, by combining their data the probability increases because the upland LPCs are completely zero percent.

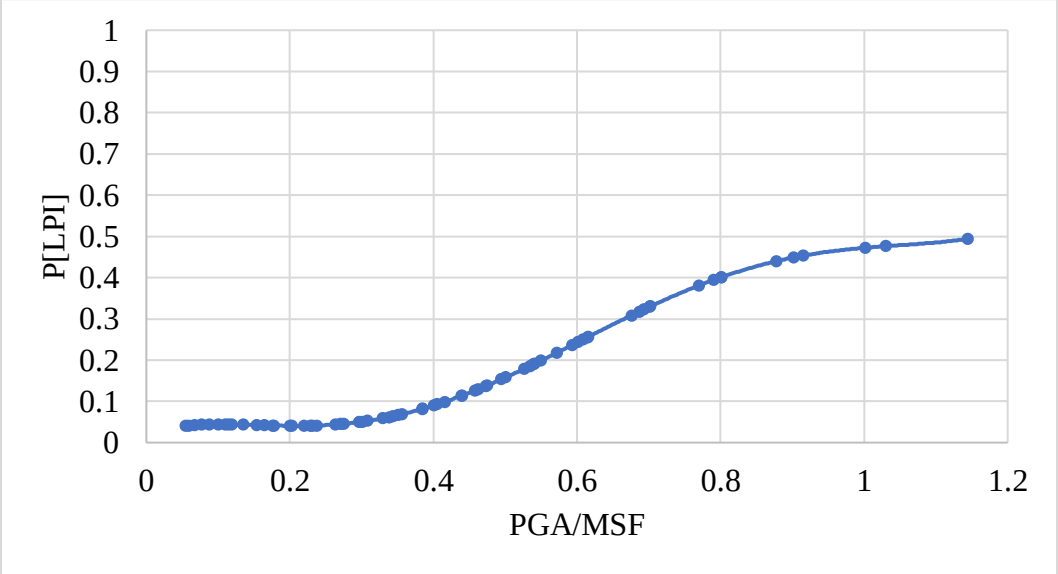

Figure 4.20. LPI-based non-Lowland LPCs from SPT data.

Additional LPCs for Tipton County were developed based on Maurer's framework (LPI_{ISH}). Due to having only 10 soil boring logs within the uplands of Tipton County, the LPI_{ISH}-based LPCs were generated for lowlands and non-lowlands. Figures 4.21 and 4.22 show the lowland and non-lowland LPCs, respectively.

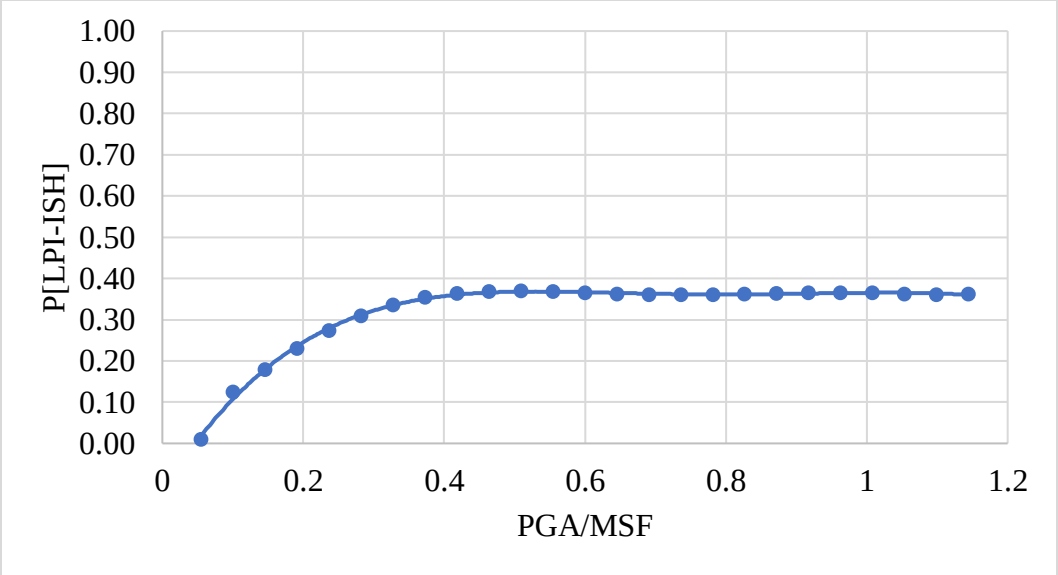

Figure 4.21. LPI_{ISH}-based LPC of lowland from SPT data.

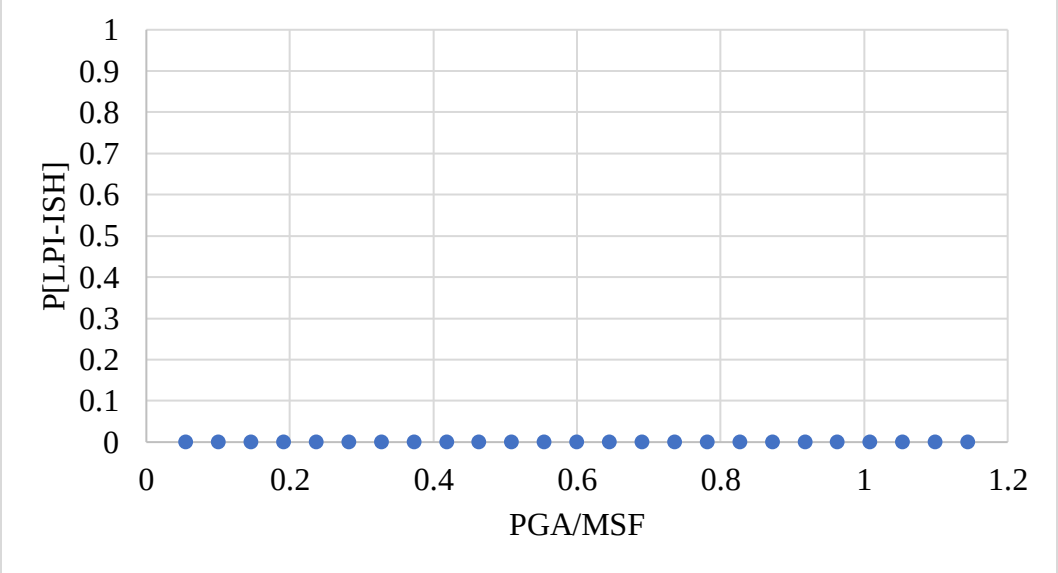

Figure 4.22. LPI_{ISH}-based LPC of non-Lowland from SPT data.

For the lowlands, the LPI_{ISH}-based LPCs reach a maximum liquefaction probability of 36%. However, the non-liquefiable layer impact is higher on non-lowlands LPI_{ISH}-based LPCs that the LPCs show a zero percent probability of liquefaction for all 70 earthquake scenarios.

The LPI- and LPI_{ISH}-based LPCs of lowlands and non-lowlands for $P[LPI\text{-}LPI_{ISH}>5]$ are compared in this section. Figures 4.23 illustrates a comparison of LPCs for lowland areas of Tipton

County. Figure 4.23 indicates that the probability of liquefaction provided by the LPC based on the LPI_{ISH} framework is significantly lower than the probability of liquefaction provided by the LPC based on the LPI framework, especially at higher ratios of PGA/MSF. The maximum difference is about 28%. Figure 4.24 compares the LPI and LPI_{ISH} based LPCs in the non-lowland areas of Tipton County. Figure 4.24 shows that the probability of liquefaction provided by the LPC based on the LPI_{ISH} framework is lower than the LPC based on the LPI framework, especially at higher ratios of PGA/MSF. The maximum difference is about ~50%.

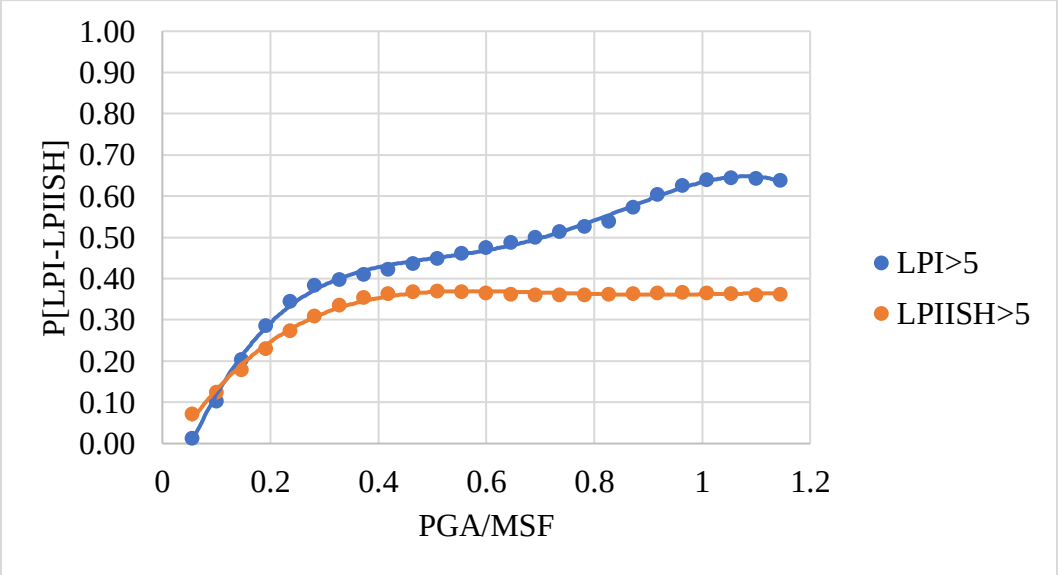

Figure 4.23. LPI- and LPI_{ISH}-based lowland LPCs for P[LPI>5].

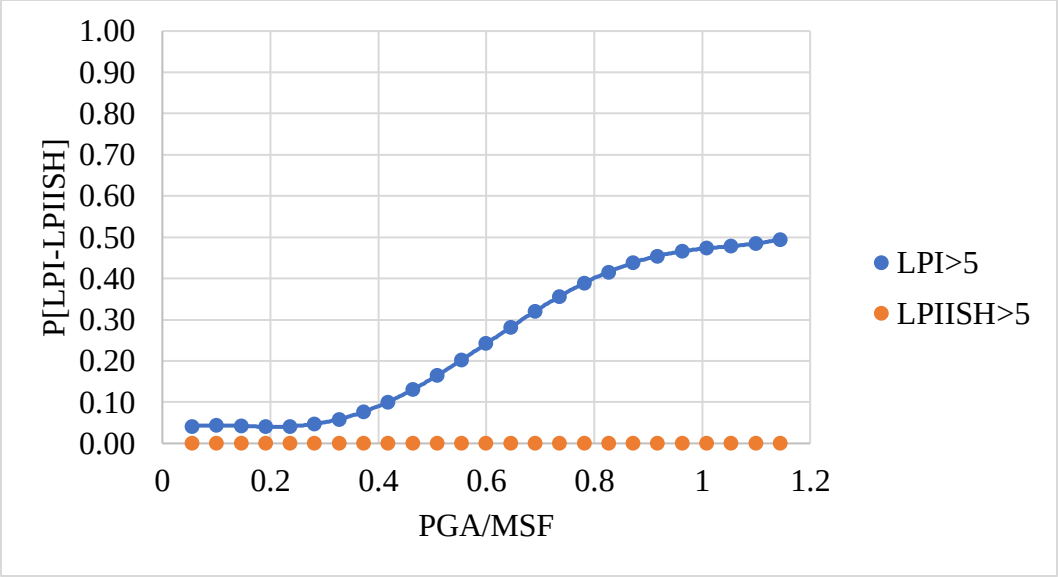

Figure 4.24. LPI- and LPI_{ISH}-based non-lowland LPCs for P[LPI>5].

As mentioned previously, the effect of upper non-liquefiable soil layers on the surface manifestation of liquefiable soil layers is the most notable difference between the LPI and LPI_{ISH} methods. LPI does not consider the impact of non-liquefiable soil layers while LPI_{ISH} considers it. Thus, considering the impact of non-liquefiable layers causes the LPI_{ISH}-based LPCs to show a lower liquefaction probability than LPI-based LPCs. Also, it should be noted that the weighting function in the LPI and LPI_{ISH} equations (Dyer County Seismic and Liquefaction Hazard Maps, Cramer et al., 2020a) are different, which causes different weights to be assigned the liquefiable layers; consequently, different LPI and LPI_{ISH} values are obtained for the same soil layer. For a better understanding of the reason for the differences between the LPI and LPI_{ISH}-based LPCs, especially for lowlands, I conducted more detailed analyses of the soil boring logs of the lowland areas of Tipton County as far as percentage and depth of liquefiable and non-liquefiable layers that are presented herein.

Each of the 22 soil boring profiles of the lowland region was divided into 2 ft increments to the depth of 66 ft; therefore, a total of 726 layers were used in this study where 18% percent of

layers are liquefiable (saturated loose sand with less than 35% fines) and 82% of layers are non-liquefiable layers. Thus, most soil layers are non-liquefiable as shown in Figure 4.25.

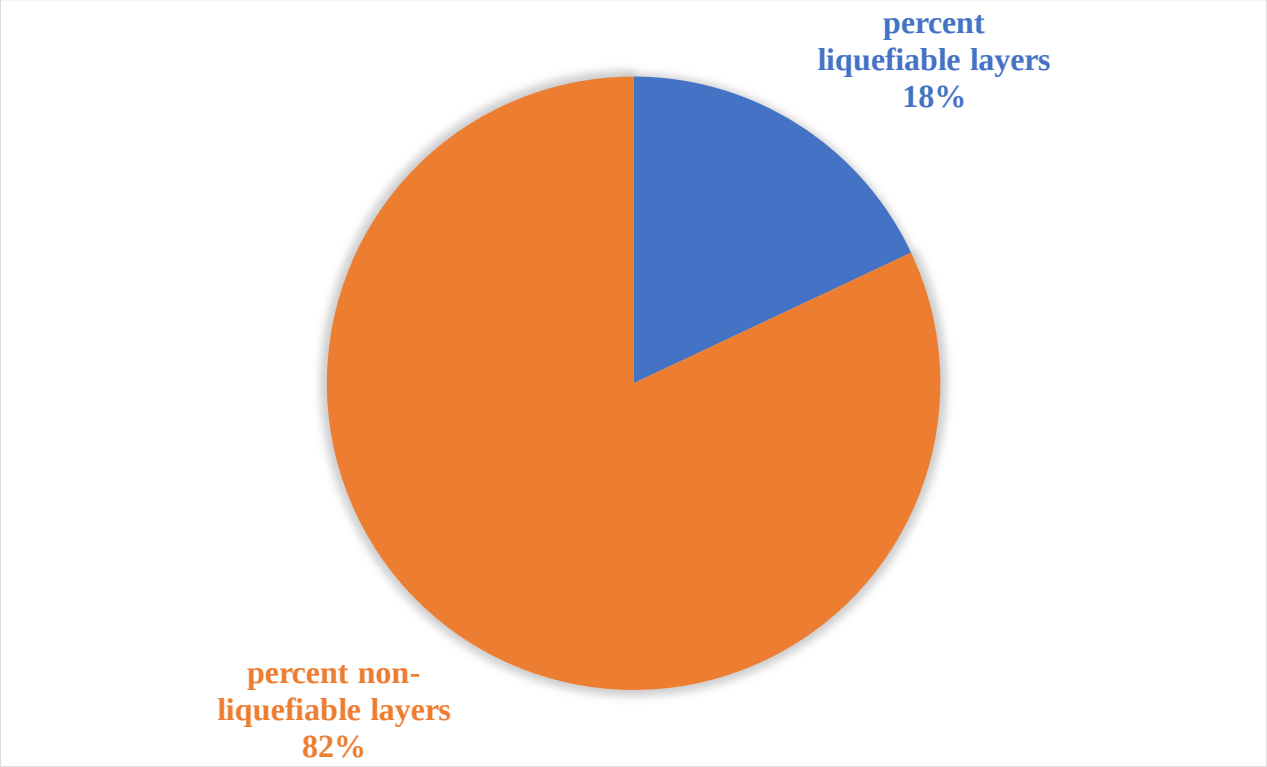

Figure 4.25. Percent liquefiable and non-liquefiable layers.

Both methods give more weight to shallower liquefiable layers than deeper layers; however, in the LPI_{ISH} method the weighting function is based on a power-law, and in the LPI method, the weighting function is linear (details are provided in the Dyer County study, Cramer et al., 2020a). Figure 4.26 shows the distribution of liquefiable and non-liquefiable layers of 22 lowland soil borings within the various depths to the first 10 meters. Most of the layers of the first 10 meters of soil borings are non-liquefiable. Therefore, since most of the soil layers from 0 to 10 m in depth are non-liquefiable, by considering the impact of non-liquefiable layers on the liquefaction potential of liquefiable layers in the LPI_{ISH} method, the probability of liquefaction

surface manifestation decreases and the LPI_{ISH} based LPCs show lower probability surface manifestation of liquefaction than LPI-based LPCs.

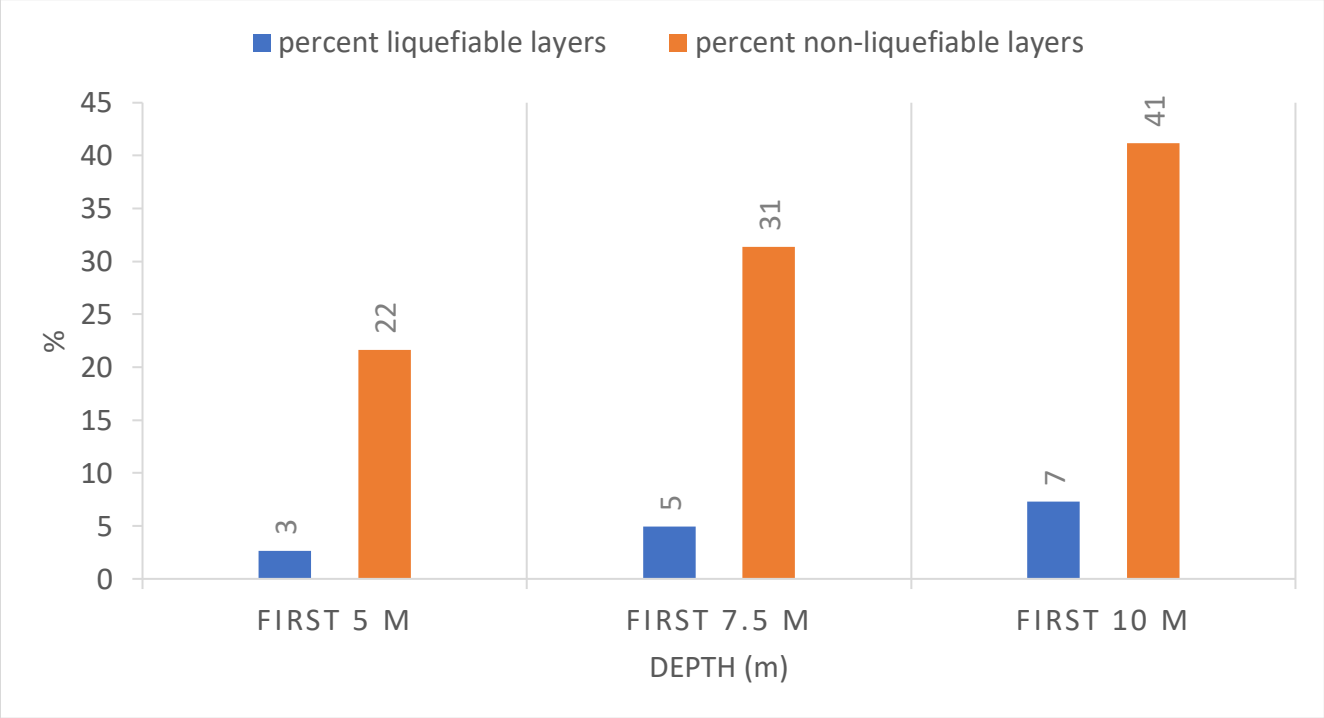

Figure 4.26. distribution of liquefiable and non-liquefiable layers along 20 meters depth.

4.1.5. Summary of Results of Liquefaction Hazard Analysis of All five Western Tennessee Counties as a Single Area

Figure 4.27 shows the LPI-based LPC for P[LPI>5] for the Lowlands geologic unit of all five West Tennessee counties. LPCs are developed from the distribution of P[LPI>5] with the ratio of PGA/MSF that is obtained for each of the 70 earthquake scenarios. As shown in Figure 4.27, LPC is plotted as a probability range ([0,1]) (i.e., 0% to 100% probability) of exceeding LPI of 5 versus the ratio of PGA over MSF. The arrows in Figure 4.27 show this ratio of 0.5 for P[LPI>5] of 0.6 for the earthquake scenario of PGA of 0.5 and M_w of 7.5, which is shown in the histogram of Figure 4.28. The LPC in Figure 4.27 provides the probability that liquefaction surface manifestation can occur based on Iwasaki's threshold of 5. The probability increases with an increase in PGA/MSF and reaches a maximum probability of ~0.9 (90%) at PGA/MSF of ~1.2, which represents the most intense earthquake scenario of this study.

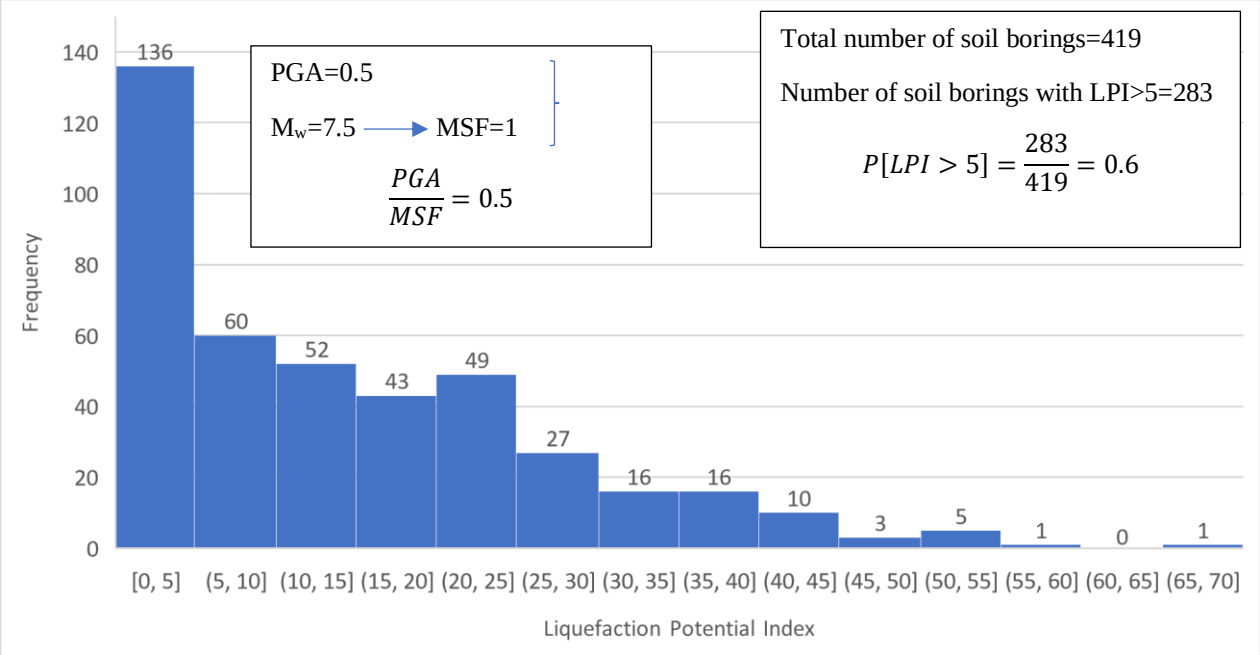

Figure 4.27. Histogram of LPI computed from SPT data for PGA=0.5 and M_w=7.5.

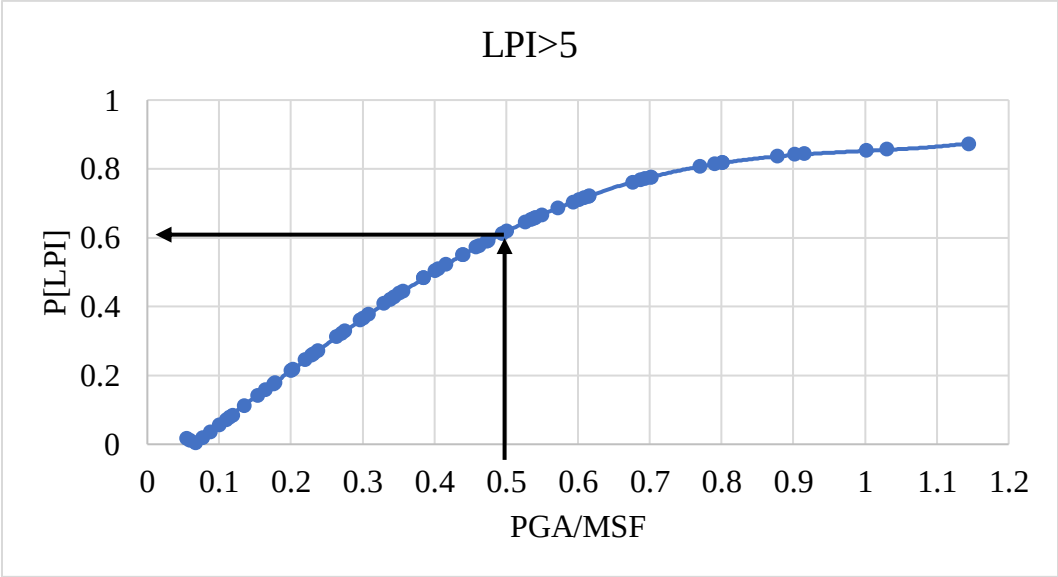

Figure 4.28. LPI based LPC.

Using Maurer's framework and based on the LPI_{ISH} method (Maurer et al., 2015), the LPI_{ISH}-based LPC for $P[LPI_{ISH}>5]$ shown in Figure 4.29 was developed based on the same procedure used to generate the LPI-based LPC for the Lowlands geologic unit of all five West Tennessee counties. The LPI_{ISH}-based LPC reaches a maximum probability of ~0.42 (42%) at PGA/MSF of ~1.2.

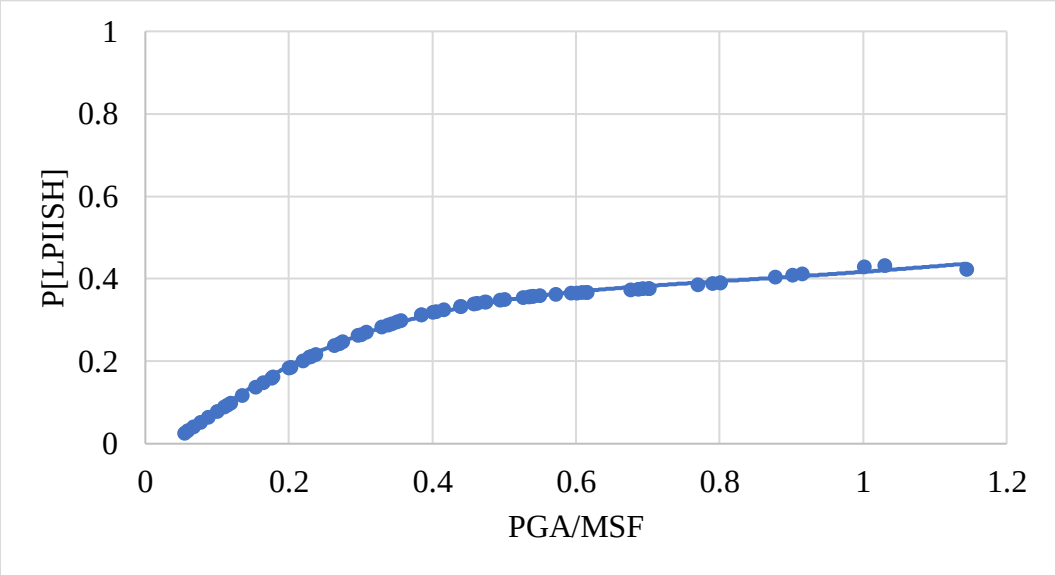

Figure. 4.29. LPI_{ISH}-based LPC.

Figure 4.30 provides a comparison of the LPI- and LPI_{ISH}-based LPCs for $P[LPI\text{-}LPI_{ISH}>5]$. Figure 4.30 indicates that the probability of liquefaction surface manifestation provided by the LPI_{ISH} method is significantly lower than the probability of liquefaction surface manifestation provided by the LPC based on the LPI framework, especially at higher ratios of PGA/MSF, i.e., more intense earthquake scenarios. The maximum difference between the two LPCs is about 45% for $P[LPI\text{-}LPI_{ISH}>5]$.

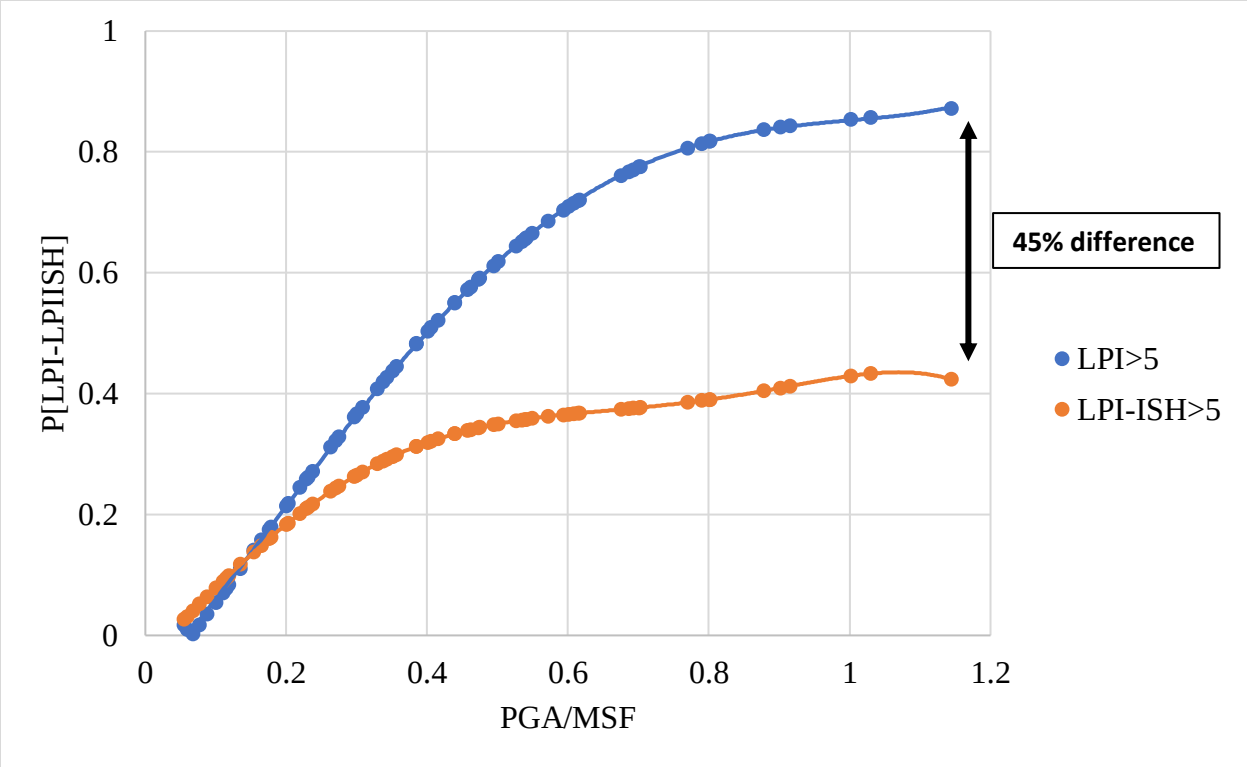

Figure 4.30. Comparison of LPI- and LPI_{ISH}-based lowland LPCs for P[LPI- LPI_{ISH} >5].

Two primary reasons that the LPI-based LPC predicts a higher probability of liquefaction surface manifestation than the LPI_{ISH}-based LPC are proposed herein. First, the LPI_{ISH} method includes the impact of non-liquefiable layers on liquefaction surface manifestation by incorporating a limiting non-liquefiable layer thickness whereby surficial manifestation is not expected to puncture through the non-liquefiable layer regardless of the thickness of the underlying liquefiable layer. The LPI does not consider the impact of non-liquefiable soil layers. Second, LPI_{ISH} incorporates a power-law depth weighting function that provides for shallower liquefiable layers to contribute more to surficial manifestation than deeper layers. The results of a more detailed investigation of the reasons for the difference between LPI and LPI_{ISH}-based LPCs are presented next.

Each of the 419 soil boring profiles was divided into 0.6 m (2 ft) increments to the maximum depth of 20 m (66 ft). Therefore, a total of 13,827 soil layers were used in this study. Figure 4.31 presents that 31% of the soil layers are liquefiable (saturated loose sand with less than 35% fines and $(N_1)_{60CS}$ values less than 30) and 69% of the layers are non-liquefiable. Thus, a majority of the soil layers are non-liquefiable. The LPI_{ISH} method incorporates a limiting non-liquefiable layer thickness whereby surficial manifestation is not expected regardless of the thickness of the underlying liquefiable layer and LPI does not. Therefore, it can be expected that the probability of liquefaction surface manifestation provided by the LPC based on the LPI_{ISH} method is lower than the LPC based on the LPI procedure as shown in Figure 4.30.

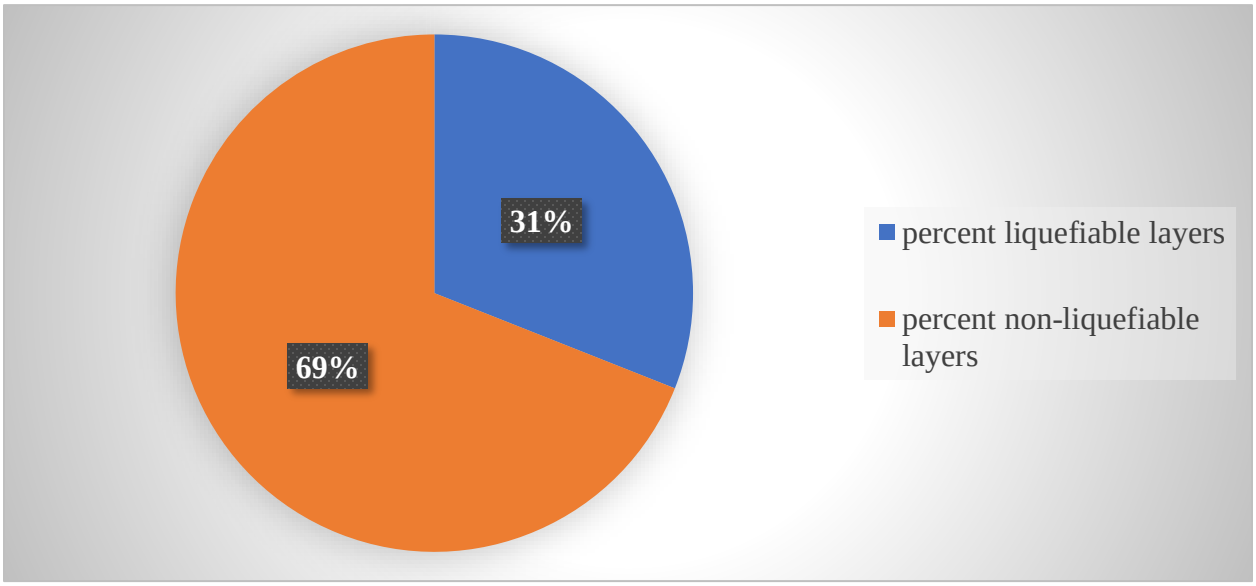

Figure 4.31. Percent liquefiable and non-liquefiable layers.

Both methods provide for shallower liquefiable soil layers to contribute more to the surficial manifestation of liquefaction than deeper layers. However, in the LPI_{ISH} method, the weighting function shown in Figure 2 is based on a power-law distribution, and in the LPI method, the weighting function is linear. Therefore, in the LPI_{ISH} method, shallower liquefiable layers

contribute more to liquefaction surface manifestation than deeper layers compared to the LPI method. Figure 4.32 shows the distribution of liquefiable and non-liquefiable layers with the depth of the 13,827 soil layers analyzed within the 419 soil borings. Most of the 0.6 m (2 ft) incremental soil layers within the first 10 m (~33 ft) of the soil borings are non-liquefiable and most of the liquefiable layers are located between depths of 10 to 20 meters. Therefore, since most of the soil layers from 0 to 10 m (~33 ft) depth are non-liquefiable, by considering the impact of non-liquefiable layers on liquefaction potential in the LPI_{ISH} method, the probability of liquefaction surface manifestation decreases, and the LPI_{ISH}-based LPC shows a lower probability of liquefaction surface manifestation than the LPI-based LPC. Additionally, because most of the liquefiable layers are located between depths of 10 to 20 meters (33 to 66 ft), and since in the LPI_{ISH} method, shallower liquefiable layers contribute more to liquefaction surface manifestation than deeper layers compared to the LPI method, the probability of liquefaction surface manifestation decreases and the LPI_{ISH}-based LPCs show lower probability of surface manifestation of liquefaction than LPI-based LPCs.

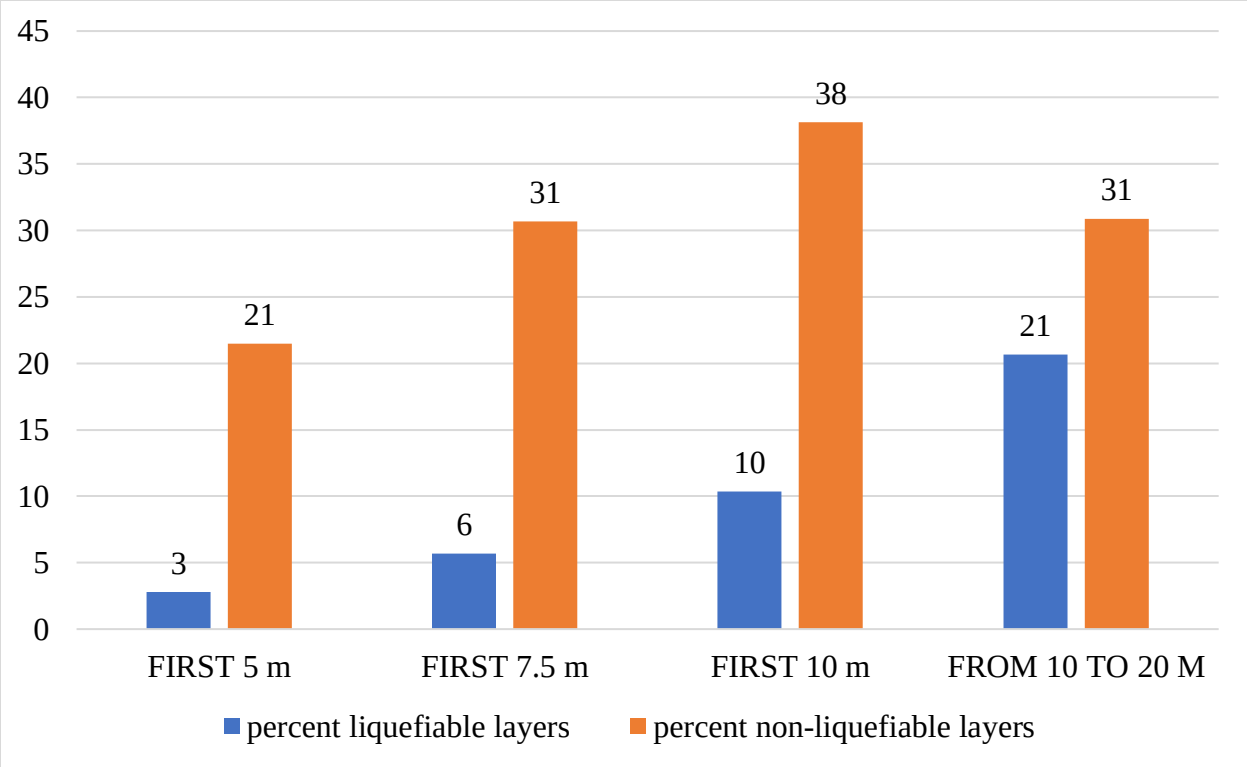

Figure 4.32. Distribution of liquefiable and non-liquefiable layers along 20 meters depth.

Figure 4.30 showed that the difference between the LPI- and LPI_{ISH}-based LPCs increases with an increase in PGA/MSF, i.e., an increase in earthquake intensity. The MSF is the same for both LPI and LPI_{ISH} methods and is determined by Equations (2) and (3). Therefore, the impact of PGA on the difference between LPI- and LPI_{ISH} -based LPCs can be evaluated by determining the consistency between the calculated LPI and LPI_{ISH} values at each of the 419 soil boring log locations for various PGAs.

The final value of LPI and LPI_{ISH}, respectively, at each soil boring location to develop the LPCs are computed from the summation of the severity times weighting function at each 0.6 m (2 ft) increment soil layer to a depth of 20 m (66 ft).

The purpose of the consistency assessment between LPI and LPI_{ISH} values at each soil boring location for different PGAs is to evaluate the impact of earthquake intensity provided by various PGAs on the difference in LPCs between the two methods shown in Figure 4.30.

Table 4.3 and Figure 4.33 provide the consistency, i.e., correlation coefficient, between LPI-based and LPI_{ISH}-based P[LPI>5] values from Figure 4.30 for various PGAs. The consistency range is between 0 to 1 with 0 indicating the weakest consistency and 1 representing the strongest consistency, i.e., strong agreement. The correlation coefficient (r) is obtained by equation (4.1):

$$r = \frac{\sum(x_i - \bar{x})(y_i - \bar{y})}{\sqrt{\sum(x_i - \bar{x})^2 \sum(y_i - \bar{y})^2}} \tag{4.1}$$

where *i* represents each boring location from location 1 to 419, x_i is LPI at boring location *i* as provided by equation (10), $\bar{x}$ is the mean of the severity times the weighting function of all 33 soil layers at boring location *i* in the LPI method, y_i is LPI_{ISH} at boring location *i* as provided by Equation (11), $\bar{y}$ is the mean of the severity times the weighting function of all 33 soil layers at boring location *i* in the LPI_{ISH} method. Table 4.3 and Figure 4.33 provide *r* values for a range of PGAs studied. Table 4.3 indicates that the consistency between LPI and LPI_{ISH} values is higher for lower ranges of PGA and decreases as the PGA increases. Therefore, the lower the PGA the better the agreement between the LPI and LPI_{ISH} methods. However, the change in consistency variation between PGA values is negligible from PGA of 0.5 to PGA of 1.0 as can be seen in Figure 4.33. Therefore, at PGA values greater than 0.5, the difference between LPI and LPI_{ISH} methods is most likely the result of the two primary differences previously proposed between the two methods, which are (1) The LPI_{ISH} method includes the impact of non-liquefiable layers on liquefaction surface manifestation by incorporating a limiting non-liquefiable layer cap thickness whereby surficial manifestation is not expected to puncture through the non-liquefiable layer regardless of the thickness of the underlying liquefiable layer while LPI does not consider the

impact of non-liquefiable soil layers. (2) LPI_{ISH} incorporates a power-law depth weighting function that provides for shallower liquefiable layers to contribute more to surficial manifestation than deeper layers.

Table 4.3. Consistency between LPI and LPI_{ISH} at various PGAs.

PGA	Consistency between LPI and LPI_{ISH} values (r, correlation coefficient)
0.1	0.9155
0.2	0.8061
0.3	0.7309
0.4	0.7076
0.5	0.6965
0.6	0.6941
0.7	0.6925
0.8	0.6898
0.9	0.6895
1	0.6891

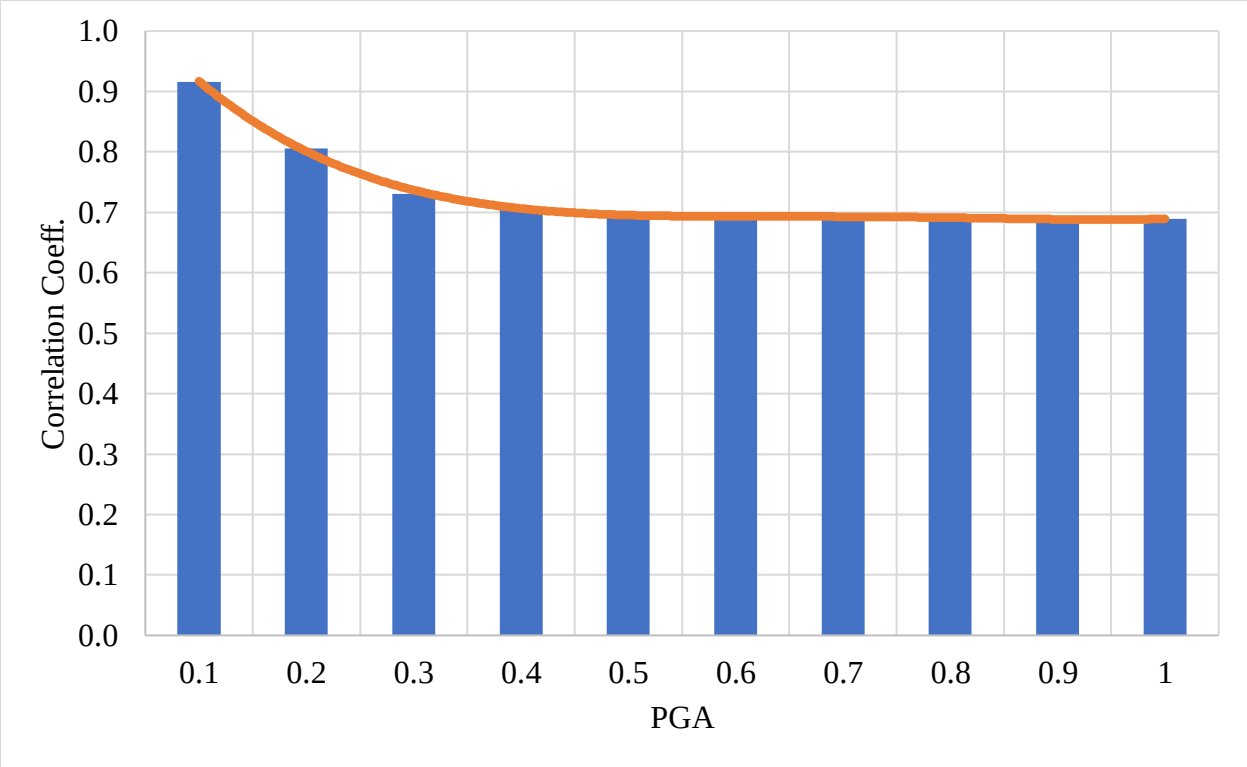

Figure 4.33. Consistency curve between LPI and LPI_{ISH} at various PGAs.

4.2. Liquefaction Hazard Mapping of West Tennessee Based on LPI and LPI_{ISH}

As part of a five-year seismic and liquefaction hazard mapping project for five western Tennessee counties of Lake, Dyer, Lauderdale, Tipton, and Madison that began in 2017 under a Disaster Resilience Competition grant from the U.S. Department of Housing and Urban Development to the State of Tennessee (HUD project), both LPI and LPI_{ISH} approaches were utilized to develop liquefaction hazard maps. It has been observed that the liquefaction hazard maps obtained from the LPI and LPI_{ISH} methods are significantly different. The LPI_{ISH}-based liquefaction hazard maps show a lower probability of liquefaction than the LPI-based liquefaction hazard maps. The inconsistency between the LPI- and LPI_{ISH}-based liquefaction hazard maps is because of the key differences between the two frameworks, especially the impact of non-

liquefiable layers on the surficial manifestation of liquefaction that is considered in the LPI_{ISH} but not the LPI procedure.

Regional liquefaction hazard maps have been developed by various researchers (Holzer, 2012; Cramer et al., 2008, 2019, 2020a, b) for preliminary assessment of liquefaction hazards. Initially, geological and geotechnical research led to the development of these maps (Power and Holzer 1996). Usually, liquefaction hazard mapping is developed based on surficial geology maps; these types of maps cannot predict the severity of the liquefaction probability of a region.

Two common types of hazard maps are probabilistic- and deterministic-based hazard maps. These maps are designed to give the general public as well as land-use planners, utilities, and lifeline owners a better tool to assess their risk from earthquake damage. Figures 4.34 and 4.35 show the probabilistic liquefaction hazard maps for the probability of exceedance in 50 years based on LPI and LPI_{ISH} methods, respectively, for Dyer County. The LPI-based map for the lowlands shows a probability of exceedance in 50 years based on LPI>5 on the order of 0.3 to 0.7 whereas the LPI_{ISH}-based map shows a lower probability of ~0.2 for the lowlands. On the other hand, for the non-lowlands that are less susceptible to liquefaction, the difference between LPI and LPI_{ISH}-based hazard maps is lower than in the lowlands. For the non-lowlands, LPI-based maps show a probability of up to 0.1 while the LPI_{ISH} map shows a zero probability of liquefaction.

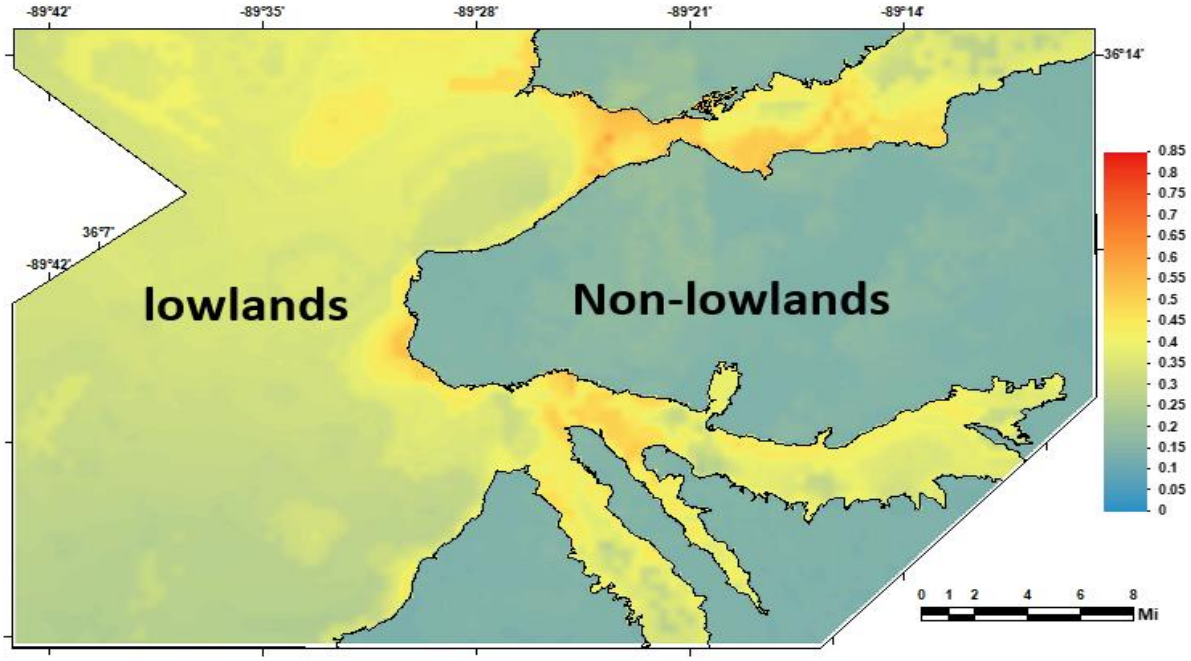

Figure 4.34. Dyer County probabilistic liquefaction hazard maps for the probability of exceedance in 50 years based on LPI>5 (Cramer et al., 2020a).

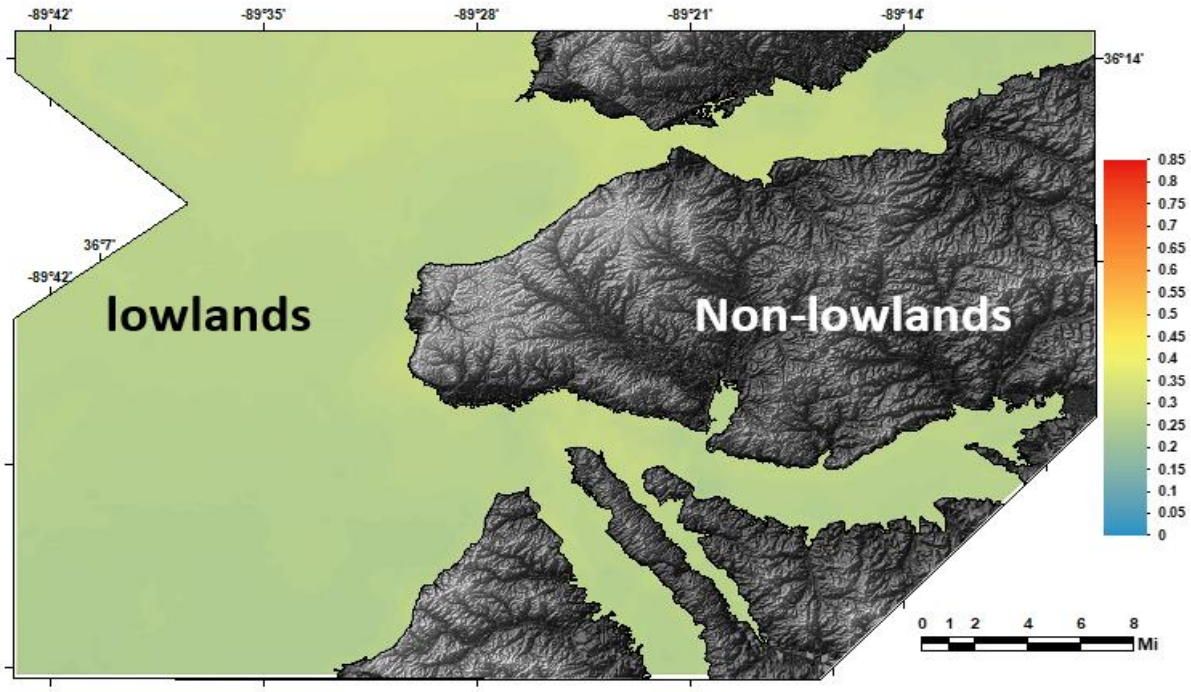

Figure 4.35. Dyer County probabilistic liquefaction hazard maps for the probability of exceedance in 50 years based on LPI_{ISH}>5 (Cramer et al., 2020a).

An example of deterministic liquefaction hazard maps for an earthquake scenario that includes the New Madrid Reelfoot thrust (the central segment of New Madrid Seismic Zone) with

a magnitude of 7.7 based on LPI and LPI_{ISH} is provided in Figures 4.36 and 4.37, respectively. For the lowlands, the LPI-based map shows the probability of liquefaction surface manifestation in a range of 0.3 to 0.7 while the LPI_{ISH}-based map shows the probability of 0.1-0.2 for the lowlands. For the non-lowlands, the probabilities from LPI- and LPI_{ISH}-based are 0.2 and 0.0, respectively.

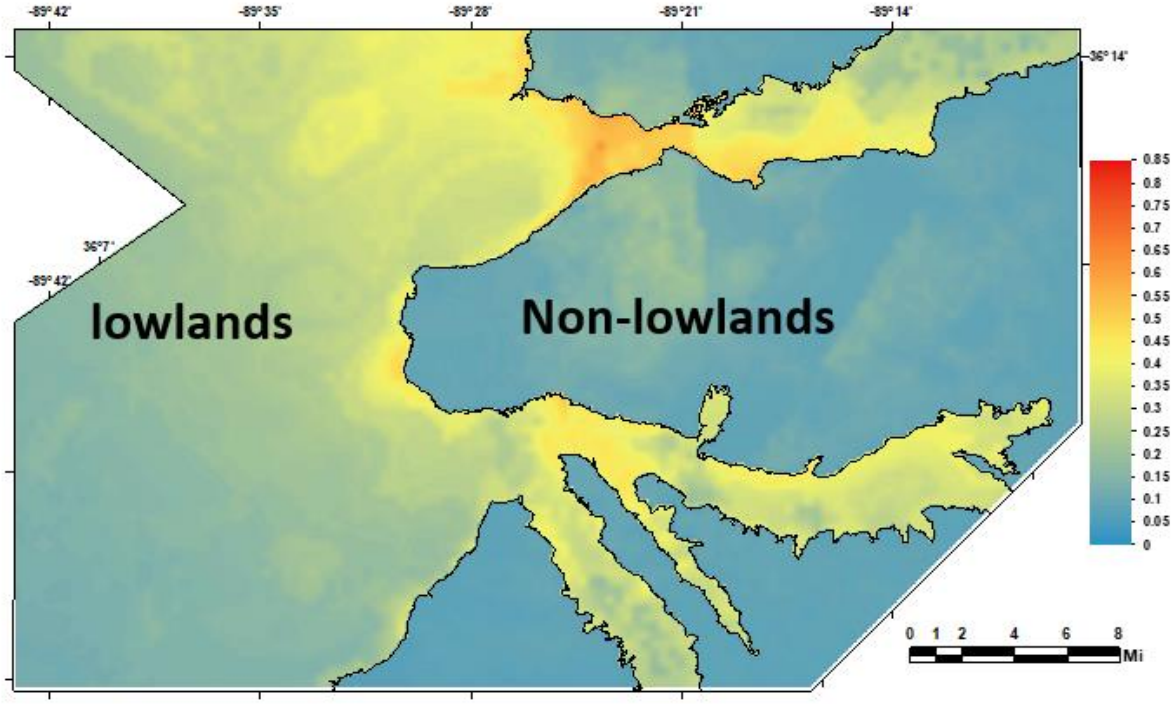

Figure 4.36. Dyer County deterministic liquefaction hazard maps based on an earthquake scenario of New Madrid Reelfoot thrust (the central segment of New Madrid Seismic Zone) with a magnitude of 7.7 for LPI>5 (Cramer et al., 2020a).

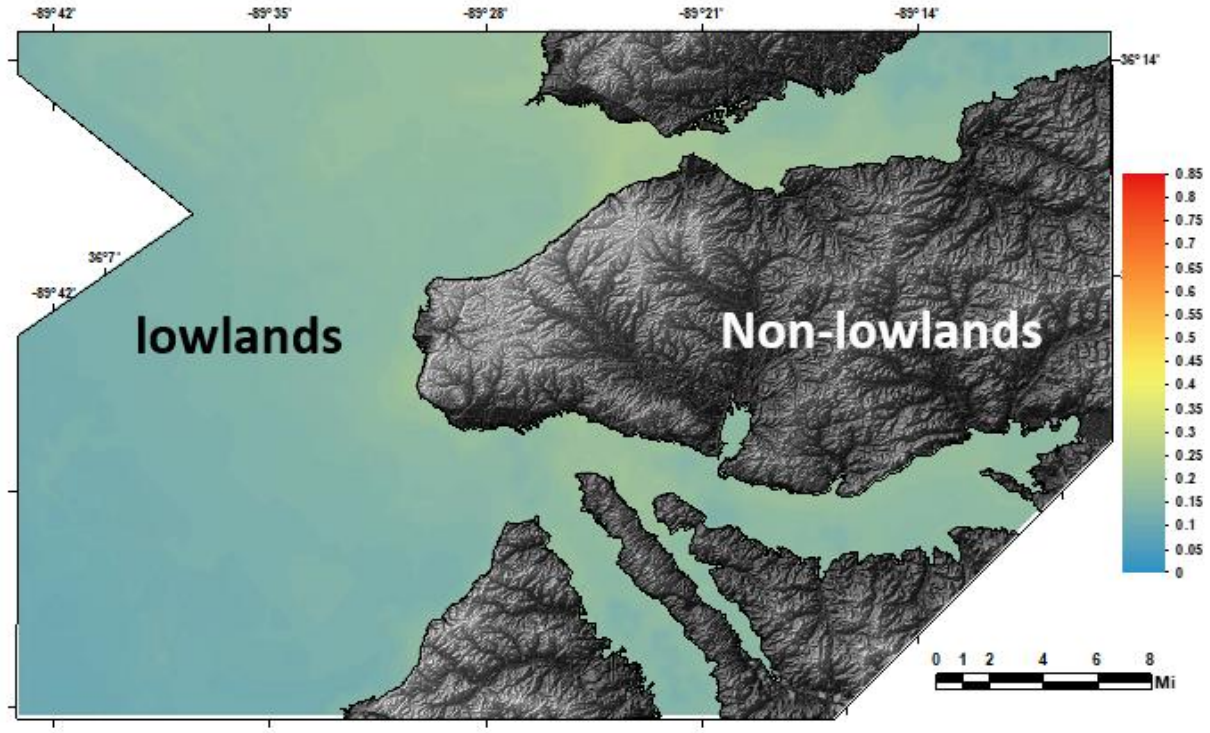

Figure 4.37. Dyer County deterministic liquefaction hazard maps based on an earthquake scenario of New Madrid Reelfoot thrust (the central segment of New Madrid Seismic Zone) with a magnitude of 7.7 for LPI_{ISH}>5 (Cramer et al., 2020a).

For Lauderdale County, the LPI-based liquefaction hazard maps also illustrate higher liquefaction probability than the LPI_{ISH}-based hazard maps for both probabilistic and deterministic type maps. Figures 4.38 and 4.39 show probabilistic liquefaction hazard maps for the probability of exceedance in 50 years based on the LPI and LPI_{ISH} approaches, respectively. For lowlands, the LPI-based map shows a liquefaction probability of 0.5 while the LPI_{ISH} map reaches a maximum 0.4 probability of liquefaction. For non-lowlands, the LPI-based map shows a probability of up to 0.2, and the LPI_{ISH}-based map shows a probability of less than 0.1.

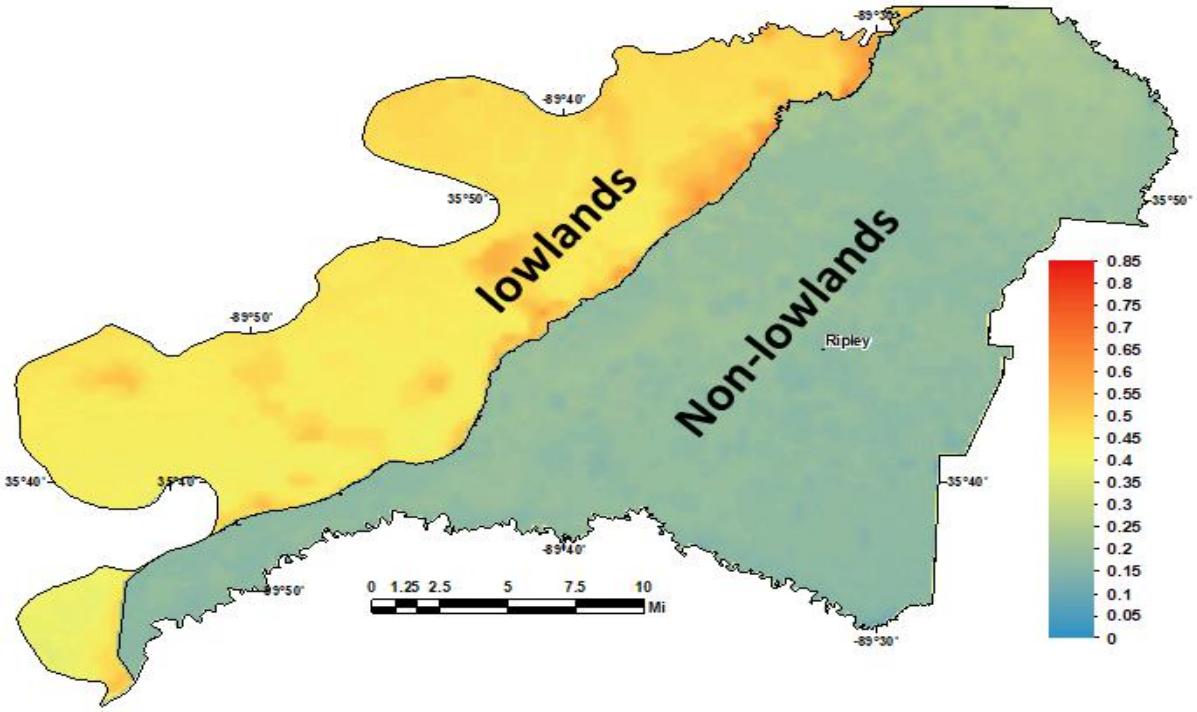

Figure 4.38. Lauderdale County probabilistic liquefaction hazard maps for the probability of exceedance in 50 years based on LPI>5 (Cramer et al., 2020b).

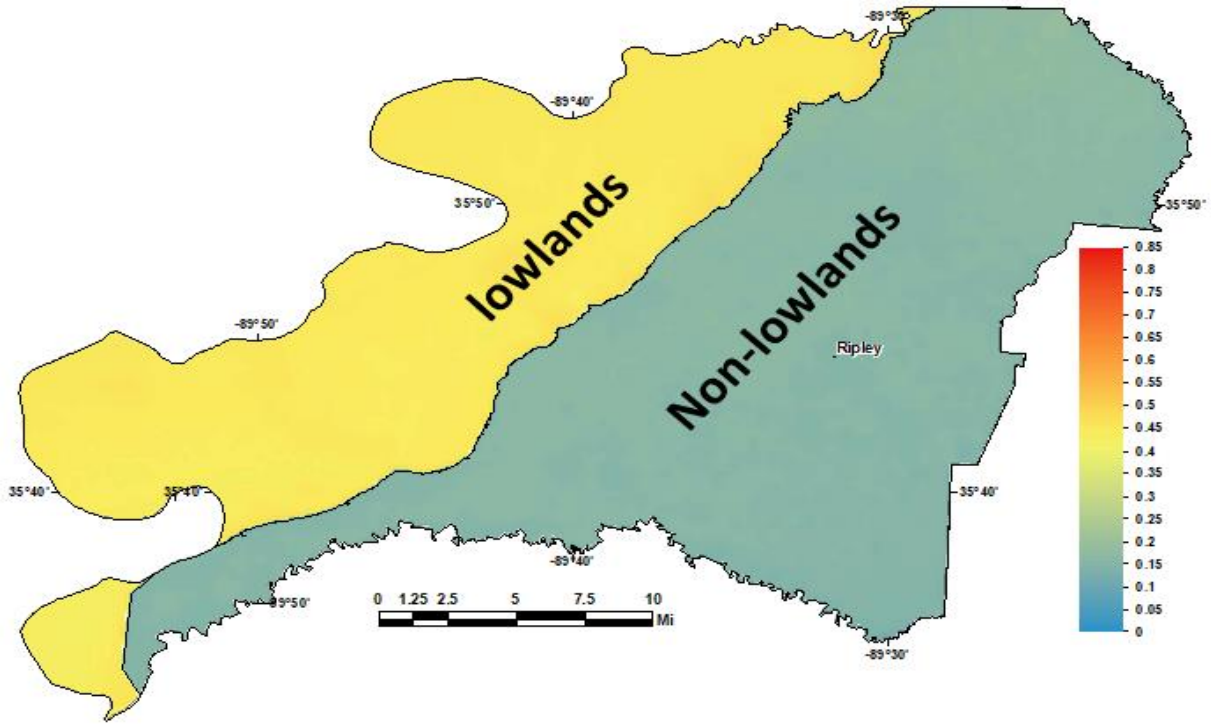

Figure 4.39. Lauderdale County probabilistic liquefaction hazard maps for the probability of exceedance in 50 years based on LPI_{ISH}>5 (Cramer et al., 2020b).

The LPI and LPI_{ISH}-based deterministic liquefaction hazard maps of Lauderdale County for the 7.7 earthquake scenario of the New Madrid Reelfoot thrust are provided in Figures 4.40 and 4.41, respectively. For the lowlands, the LPI-based map shows a probability of liquefaction from 0.4 to 0.8 while the LPI_{ISH} map reaches a maximum of 0.4 probability of liquefaction. For the non-lowlands, the LPI-based map shows a probability up to 0.25, and the LPI_{ISH}-based map shows a probability of less than 0.1.

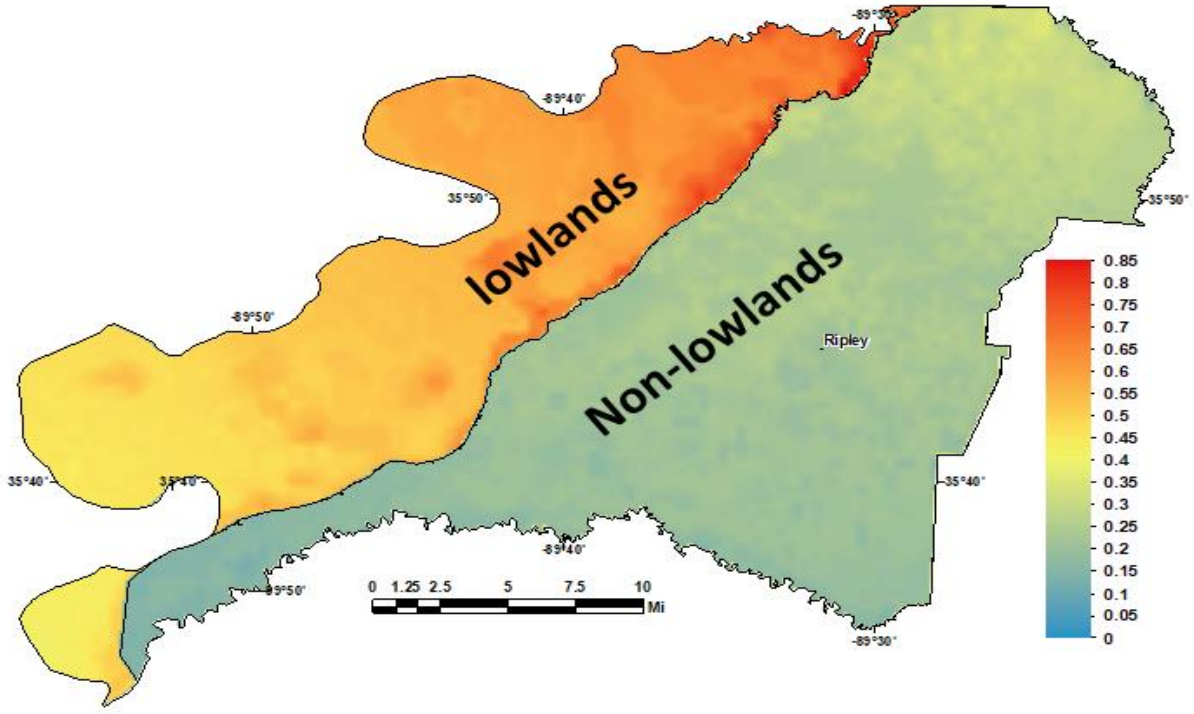

Figure 4.40. Lauderdale County deterministic liquefaction hazard maps based on an earthquake scenario of New Madrid Reelfoot thrust (the central segment of New Madrid Seismic Zone) with a magnitude of 7.7 for LPI>5 (Cramer et al., 2020b).

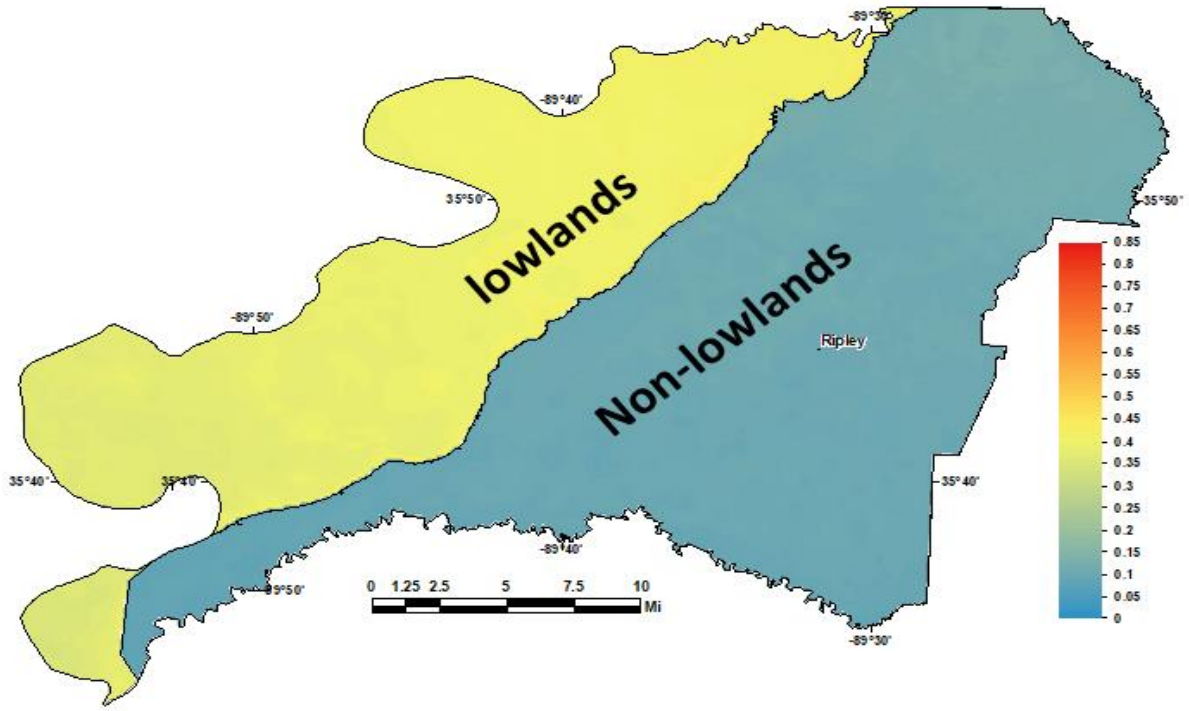

Figure 4.41. Lauderdale County deterministic liquefaction hazard maps based on an earthquake scenario of New Madrid Reelfoot thrust (the central segment of New Madrid Seismic Zone) with a magnitude of 7.7 for LPI_{ISH}>5 (Cramer et al., 2020b).

At the time of writing this dissertation and as a part of the HUD project, the liquefaction hazard maps were developed for all five counties of Lake, Dyer, Lauderdale, Tipton, and Madison as part of the HUD project. For all five counties of the HUD project, it was observed that the LPI method predicts significantly higher liquefaction probability than the LPI_{ISH} method. The effect of upper non-liquefiable soil layers on the surface manifestation of liquefiable soil layers is the most notable difference between the LPI and LPI_{ISH} methods. LPI does not consider the impact of non-liquefiable soil layers while LPI_{ISH} considers it. Thus, considering the impact of non-liquefiable layers causes lower liquefaction surface manifestation probability. Section 2.2.2 provides three key differences between the LPI_{ISH} and LPI methods that contribute to the LPI method predicting higher liquefaction probability than the LPI_{ISH} method. Further information regarding liquefaction

hazard analysis and results of the HUD project can be found in Cramer et al. (2019, 2020a, b, 2021, and 2022).

4.3. Results of Numerical Liquefaction Analysis

This section provides and discusses the results of numerical liquefaction analysis including analysis of the Wildlife, California, and New Zealand sites, and sensitivity analysis of models to the thickness and shear strength of upper surficial non-liquefiable layers. The numerical analyses are conducted in two phases: mechanical (static) and dynamic analyses. First, the mechanical analysis was done for the models to reach the state of equilibrium under gravity stresses (with the flow and dynamic options of FLAC deactivated) and then the dynamic loading is applied to the models to evaluate the occurrence of liquefaction.

4.3.1. Wildlife Site, California

In Figure 4.42, the results of the pore pressure contour map were compared with the results of Daftari's study to confirm the calculations of Phase I, mechanical. As shown in Figure 4.42, the obtained pore pressure in different layers of the model from this study agrees with the results of Daftari (2015).

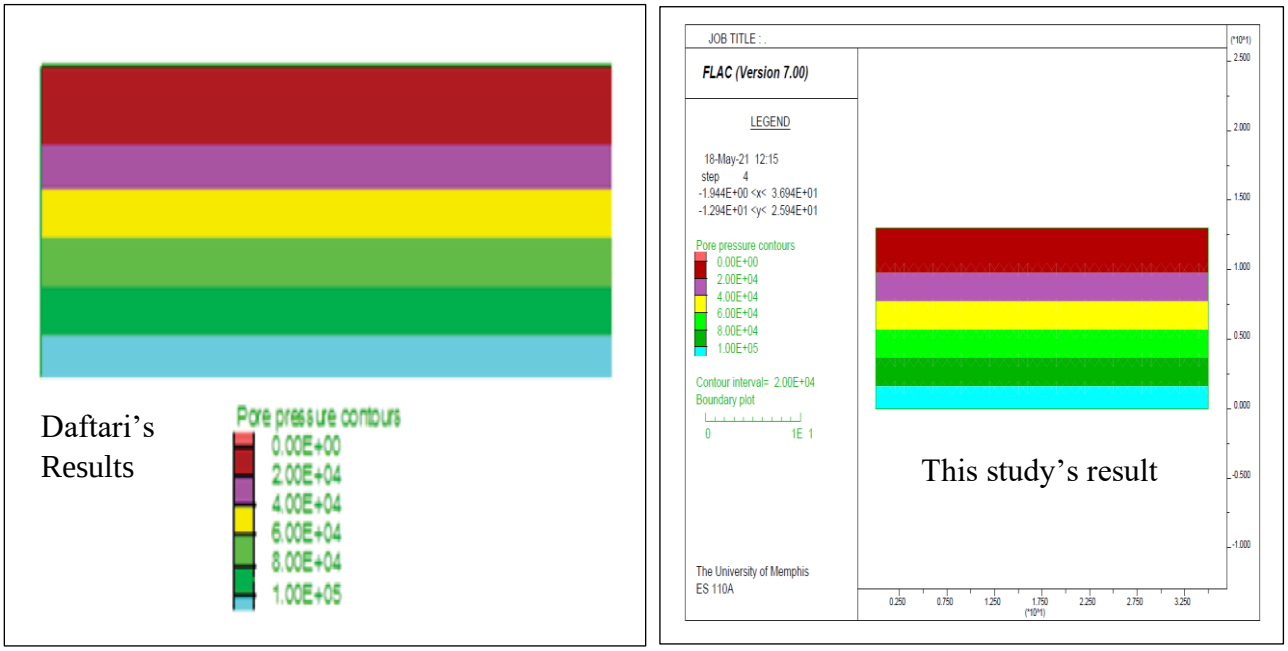

Figure 4.42. Comparison of pore pressure contour maps developed in this analysis and Daftari's analysis before the Superstition Hills earthquake (unit of pore pressure is Pa).

For dynamic analysis of the Wildlife site, the baseline-corrected velocity time history shown in Figure 3.48 had to be converted to a shear stress time history. The obtained shear stress time history was applied at the base of the model as an input motion. The damping model was not provided in Daftari's analysis, therefore in this analysis, the hysteretic damping procedure with default values of L1=-3.156, and L2=1.904 was utilized, and to avoid low-level oscillation, a small value of 0.2% stiffness proportional Rayleigh damping was combined with the hysteretic damping.

In Daftari's study only the displacement vector map, velocity vector map, as well as excess pore water pressure at five depths were provided. Therefore, the results of the dynamic analysis of this study were compared and confirmed with the displacement vector map of the Superstition Hills earthquake and excess pore water pressure at two depths. Figure 4.43a is the plot of displacement vectors from the Superstition Hills earthquake from Daftari's study and Figure 4.43b is the plot of displacement vectors after the dynamic analysis of FLAC in this study. As can be seen, the results agree with high resolution and the insignificant difference could be due to different

initial and boundary conditions of the simulations. Because the initial and boundary conditions of Daftari's study were not provided, those were assumed for the new simulation based on the FLAC manual recommendations. For the boundary conditions, the sides were considered fixed in both directions, and the base of the model was considered compliant. For the dynamic analysis of the Wildlife site, the flow option for flow fluid was activated and saturation was considered 0% for the dry zone (above the groundwater) and 100% for the soil layers below the groundwater level. All displacements and velocities were forced to zero before running the dynamic analysis. The dynamic analysis of the model was run for 200 seconds.

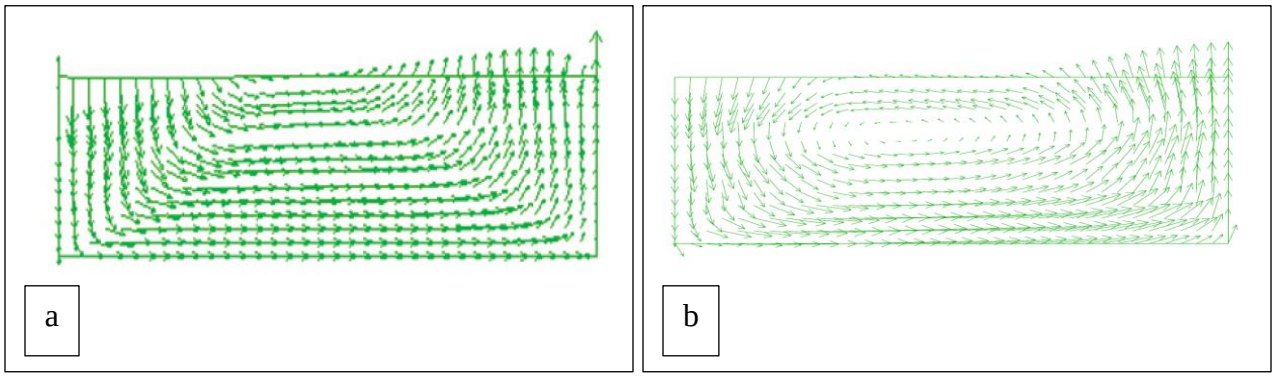

Figure 4.43. Comparison of the model of displacement vectors developed in this analysis and Daftari's analysis after the Superstition Hills earthquake (a) Daftari's study (b) this study.

Figure 4.44 illustrates the depth of installed piezometers P1 to P6 at the Wildlife site and Figure 4.45 shows the obtained excess pore pressures of P1, P2, P3, and P5 from Daftari's dynamic analysis.

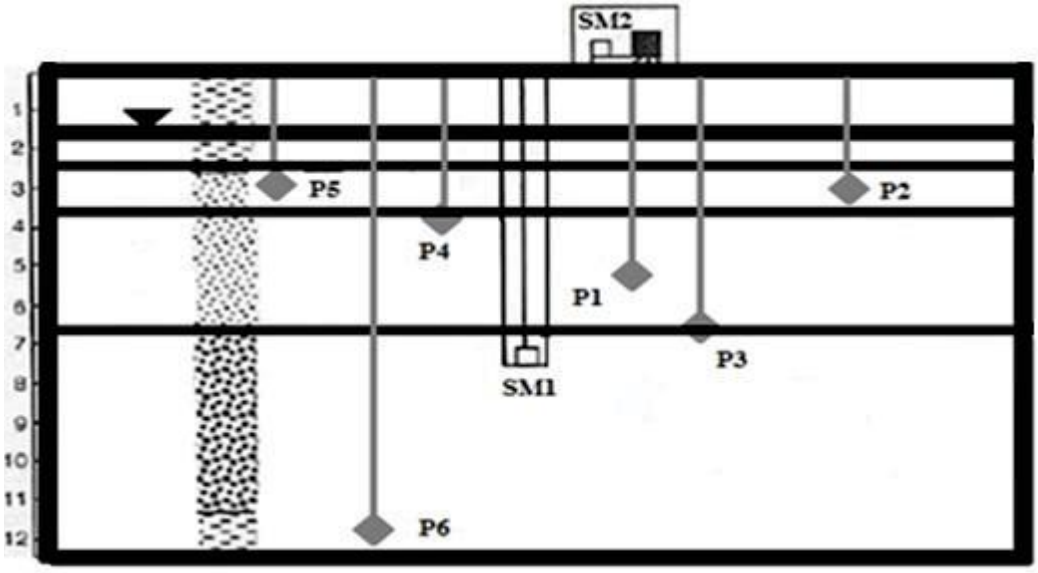

Figure 4.44. Location of piezometers at the Wildlife site (Daftari 2015).

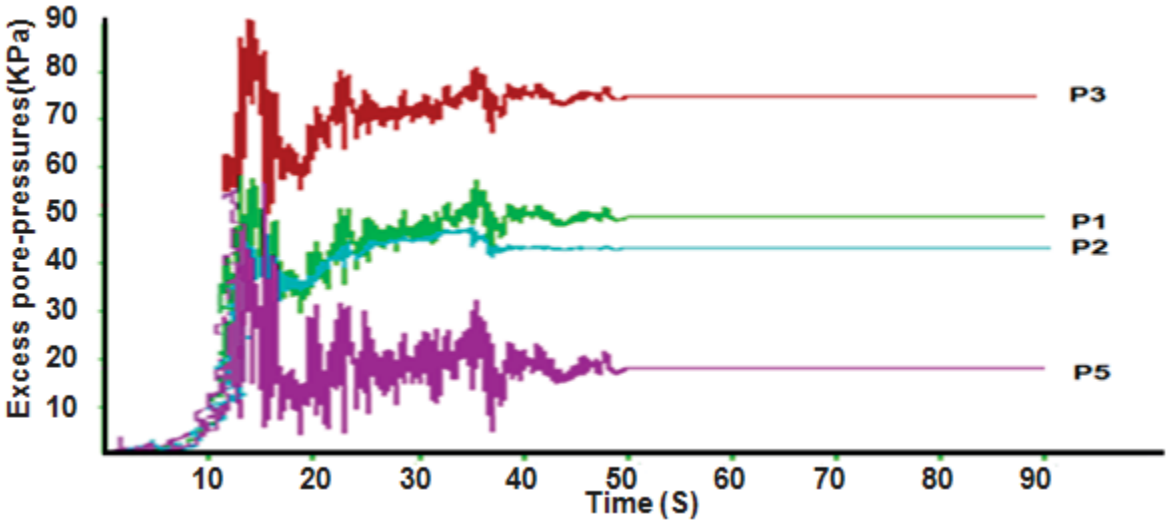

Figure 4.45 Calculated excess pore pressure at the Wildlife site at different piezometer depths (Daftari, 2015).

The results of excess pore water pressure of P3 and P5 from dynamic analysis of the Wildlife site in this study are provided in Figures 4.46 and 4.47. The maximum obtained excess pore pressure at P1 in this study is 65 KPa and the calculated excess pore pressure at P3 in Daftari's study is 70 KPa. According to a study done by Davis and Berrill (2001), the actual measured pore pressure at P3 from the Superstition Hills earthquake was 63 KPa, which is in good agreement

with 65 KPa obtained in this study. For P5, this study shows the maximum excess pore pressure of 49 kPa (Figure 4.47) while Daftari's excess pore pressure at P5 is 30 KPa and the measured pore pressure at P5 was reported as 50 KPa (Davis and Berrill, 2001). The obtained pore pressure at P5 in this study is different than Daftari's result, and that could be due to the different mish size as well as different version of Flac software. However, the obtained pore pressure at P3 and P5 in this study has a strong consistency with the actual measured pore pressure at P3 and P5. It can be concluded that the excess pore water pressure results obtained in this study are in general agreement with the actual measurements of pore pressure at specific piezometers from the Superstition Hills earthquake.

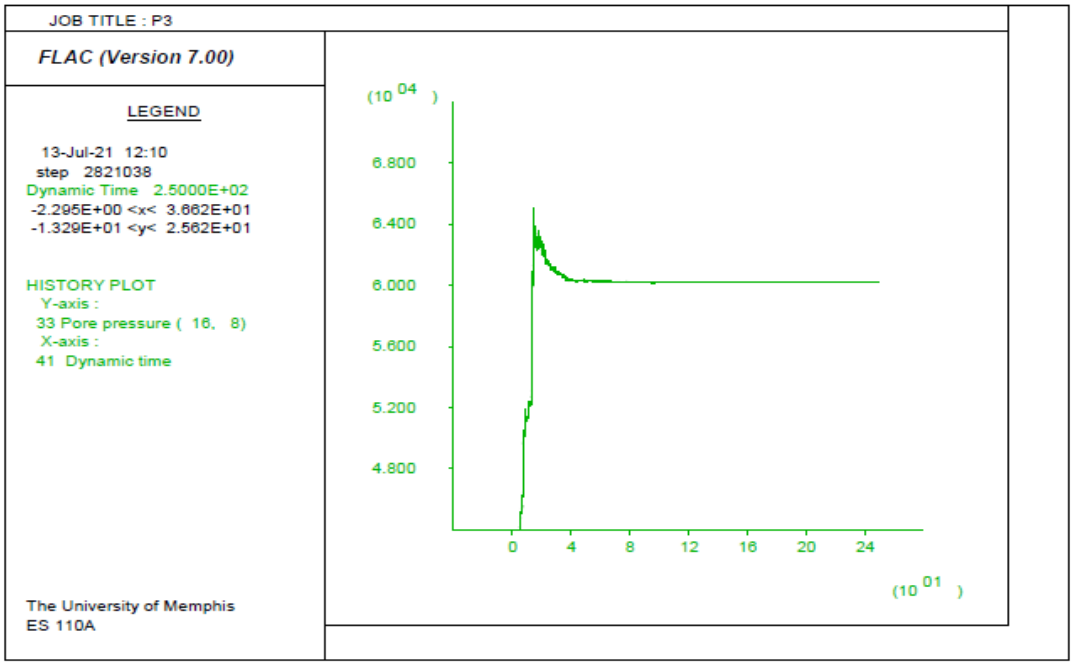

Figure 4.46. Obtained excess pore pressure at the depth of P3 from FLAC analysis of wildlife site in this study to verify results (vertical axis is pore pressure in Pa, and the horizontal axis is time in second).

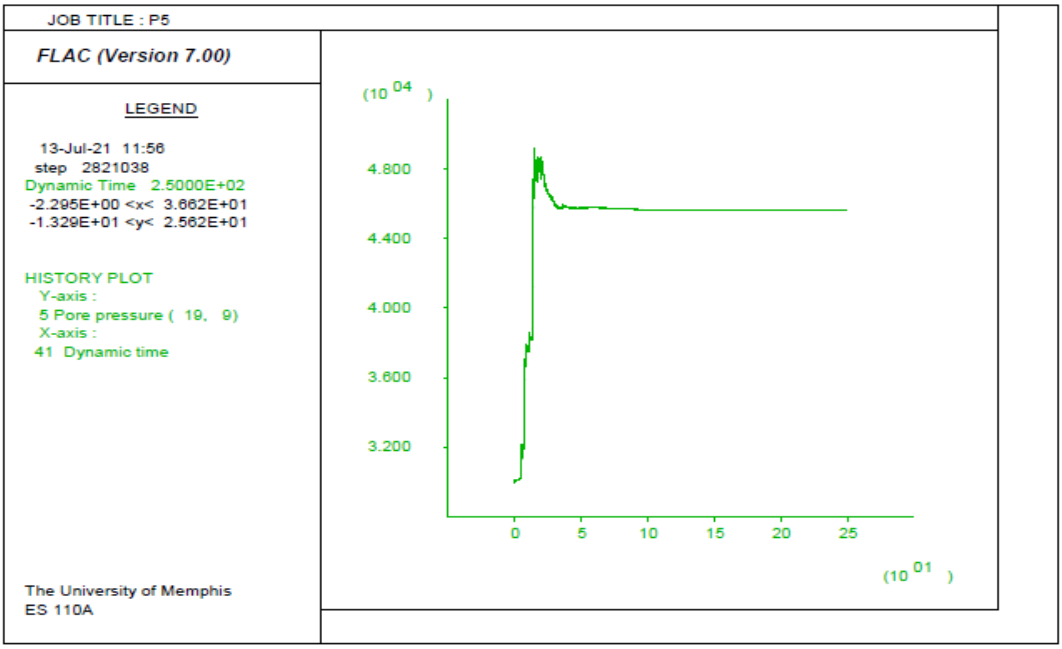

Figure 4.47. Obtained excess pore pressure at the depth of P5 from FLAC analysis of wildlife site in this study to verify results (vertical axis is pore pressure in Pa, and the horizontal axis is time in second).

The excess pore pressure ratio contour map of the Wildlife site profile obtained from the FLAC analysis is shown in Figure 4.48. According to the results of the contour maps, the maximum excess pore pressure ratio, i.e., Equation (3.38), due to dynamic loading exceeds one and reaches 1.5 in some layers near the ground surface, but mostly the excess pore pressure is in the range of 0.25-0.5 in the soil profile. Liquefaction is triggered when the excess pore pressure ratio is 1 or greater.

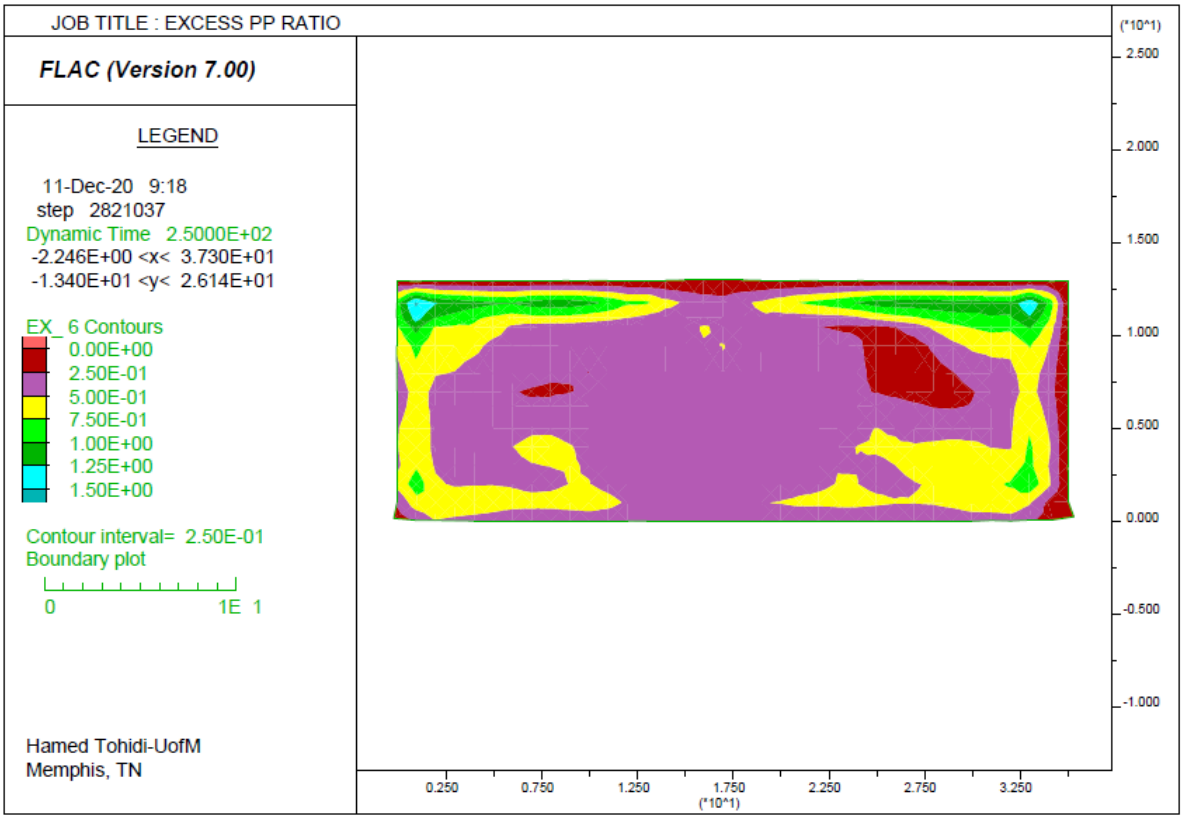

Figure 4.48. Excess pore-pressure ratio contours of the model from FLAC.

From the re-analysis of the Wildlife site, the liquefaction occurrence in any soil layer can be captured based on the distribution of excess pore-pressure ratio. Also, by comparing the obtained excess pore pressure from the dynamic analysis of the Wildlife site in this analysis with the actual measurement of excess pore pressure of the installed piezometers at the Wildlife site from the Superstition earthquake, it can be concluded that the numerical analysis of this study based on Finn models coupled with Mohr-Coulomb material behavior model to perform liquefaction analysis provides reliable results.

In the following section, the developed numerical model to assess the liquefaction surface manifestation potential of a soil profile will be verified by analysis of the soil profiles, which in

reality displayed and did not display liquefaction surface manifestation during the Canterbury earthquakes of 2010 and 2011.

4.3.2. New Zealand Soil Profiles

4.3.2.1. Results of Dynamic Analysis of YY Models

Due to the presence of a thick liquefiable soil layer (critical zone) near the ground surface in the YY1 model at a depth of 1.8 m to 6 m in Figure 3.50, this model showed liquefaction on the ground surface in both the 2010 and 2011 earthquakes (Rhodes, 2017). In the numerical analysis of the YY1 model in this study and based on analysis of excess pore water pressure as well as displacement vectors and pore pressure ratio, it has been found that the liquefaction surface manifestation occurs in the YY1 model in both 2010 and 2011 FLAC dynamic analysis. Figure 4.49 shows the excess pore pressure evolution in the critical zone of the YY1 model during the dynamic analysis of the 2010 earthquake. The development of excess pore pressure causes a significant decrease in effective stress; consequently, liquefaction occurs. Additionally, Figure 4.49 shows the dissipation of excess pore pressure in the critical zone which is known as the post-liquefaction behavior of the soil.

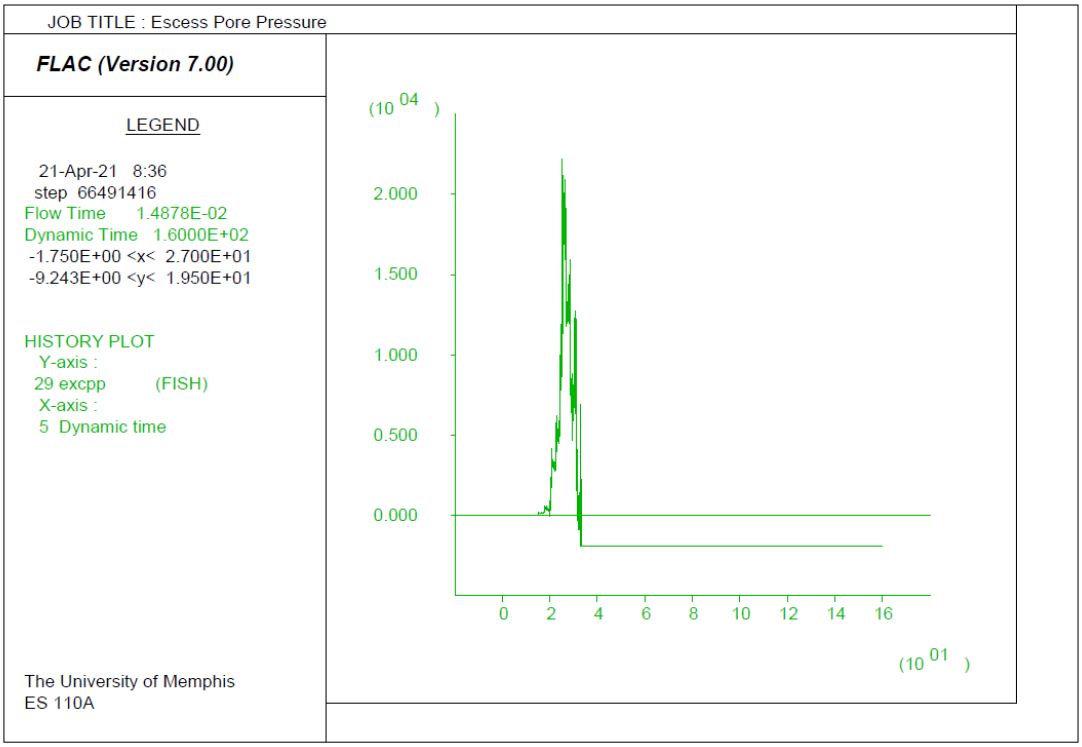

Figure 4.49. Excess pore pressure evolution in the critical zone of the YY model during the dynamic analysis of the 2010 earthquake (the vertical axis is pore pressure in Pa, and the horizontal axis is time in seconds).

Figure 4.50 shows the pore pressure ratio contour map of the YY1 model after the dynamic analysis of the 2010 earthquake. As the initial effective stress goes to zero in the critical zone and the pore pressure ratio becomes one, liquefaction develops in the critical zone. In the soil layers below the critical zone, the pore pressure ratio reaches 0.5, which shows the decrease in the effective stress and increase in excess pore pressure but, due to the high density of these layers (based on SPT N-values), liquefaction did not occur. The non-liquefiable soil layer, which is the very top unsaturated layer above the critical zone, does not show any evidence of liquefaction and the pore pressure ratio is completely zero in this layer. This proves that liquefaction did not occur in the layer; however, in the critical zone of the soil profile, liquefaction occurrence can be concluded since the pore pressure ratio exceeds one. Because the critical zone is thick and the upper non-liquefiable layer is not thick enough, the shear stress

in the critical zone overcomes the shear strength of the top non-liquefiable layer and liquefaction surface manifestation occurs. Figure 4.51 shows the displacement vectors (movement of soil) in the critical zone where the upward pore pressure was able to break through the non-liquefiable layer and push the liquefied soils to the ground surface.

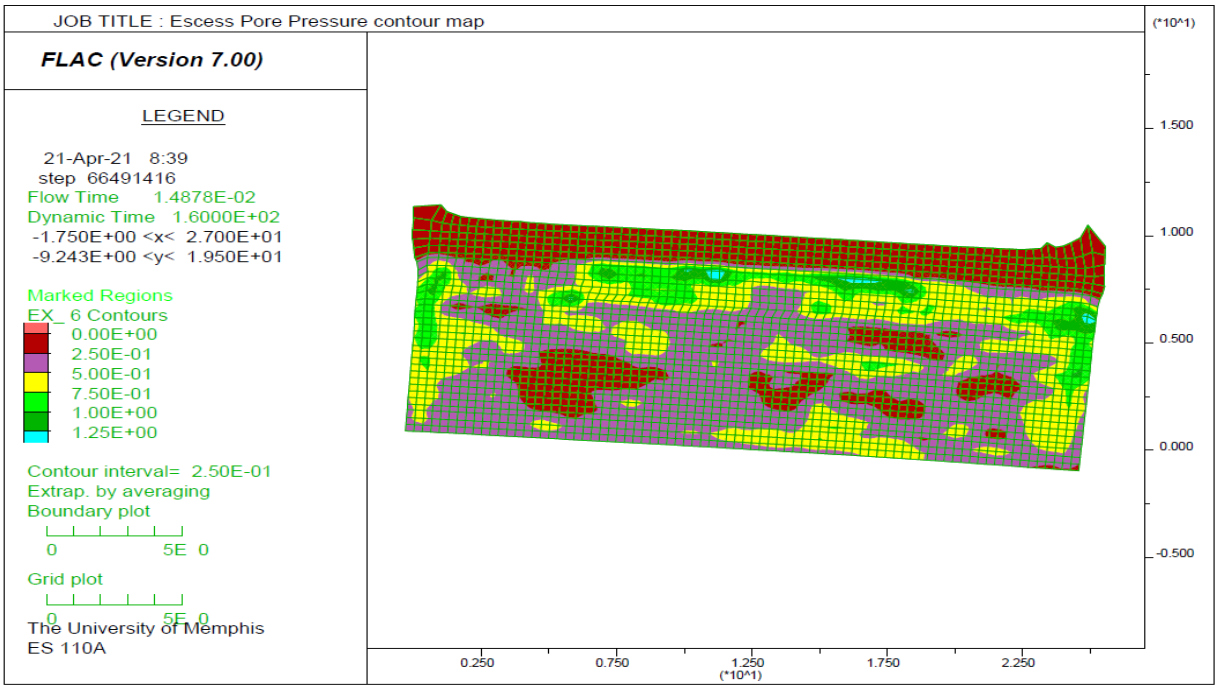

Figure 4.50. Pore pressure ratio contour map of the YY1 model after the dynamic analysis of the 2010 earthquake.

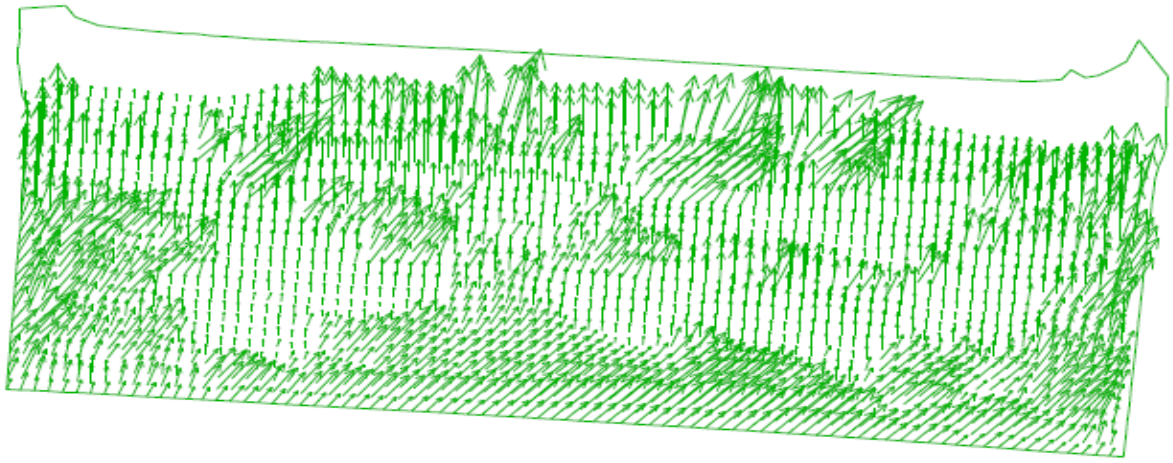

Figure 4.51. displacement vectors of the YY1 model due to liquefaction.

The results of the numerical analysis of CES 2011 on the YY1 model also confirm liquefaction surface manifestation. Figure 4.52 shows the excess pore pressure evolution in the critical zone located at a depth of 1.8 m to 6 m of the YY1 model during the dynamic analysis of the 2011 earthquake. Additionally, Figure 4.53 indicates the pore pressure ratio of one in the critical zone that has occurred due to zero effective stress. Since the 2011 earthquake duration and PGA is less than in 2010, the pore pressure ratio in layers below the critical zone is mostly zero. The results of displacement vectors in the YY1 model in Figure 4.54 illustrate the movement of soil particles from the critical zone to the ground surface. The movement of liquefied soils of the critical zone to the ground surface occurs because the shear stress of liquefied layer becomes higher than the shear strength of the upper non-liquefiable layer.

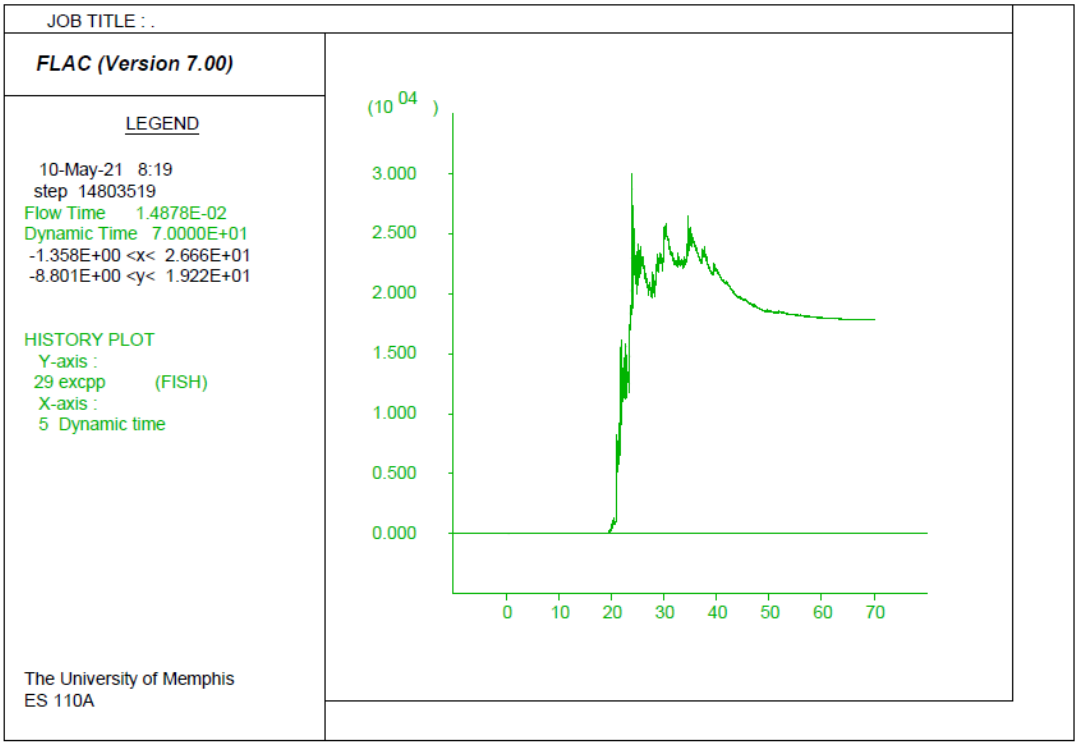

Figure 4.52. excess pore pressure evolution in the critical zone of the YY1 model during the dynamic analysis of the 2011 earthquake (vertical axis is pore pressure in Pa, and the horizontal axis is time in second).

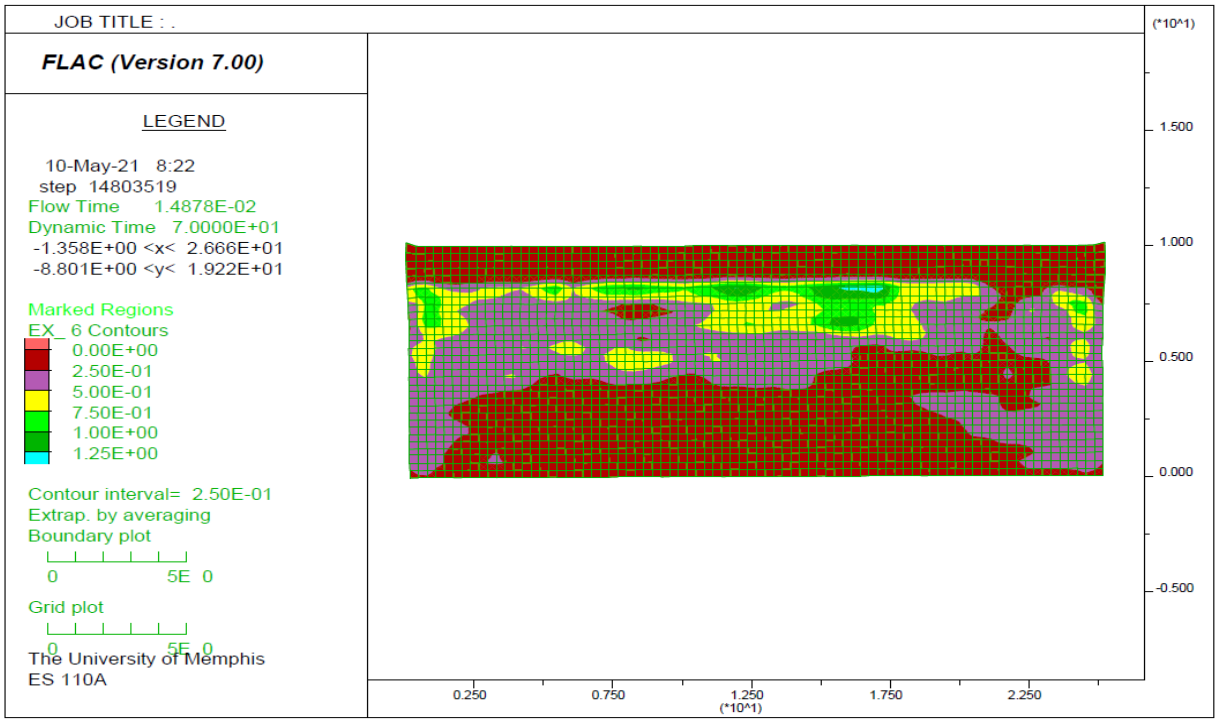

Figure 4.53. Pore pressure ratio contour map of the YY1 model after the dynamic analysis of the 2011 earthquake.

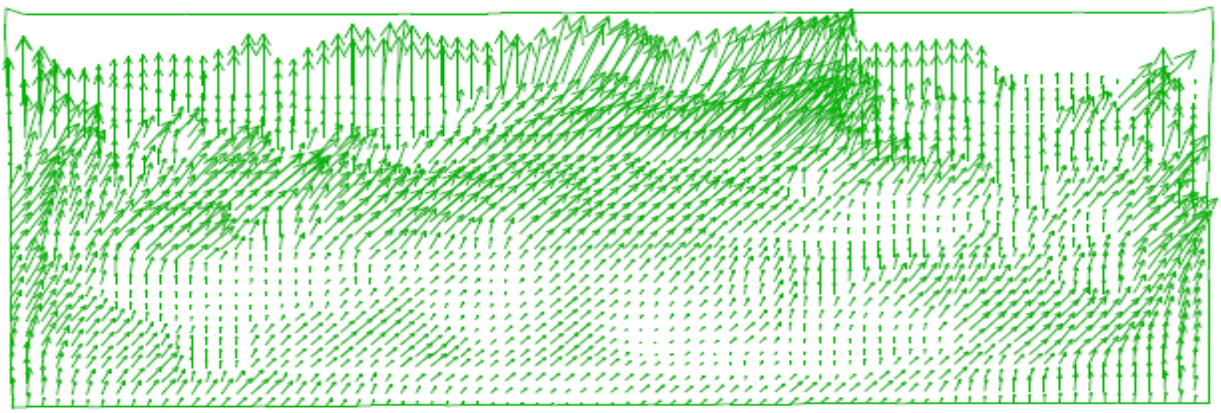

Figure 4.54. Displacement vectors of the YY1 model due to liquefaction after the dynamic analysis of the 2011 earthquake.

Table 4.4 provides a comparison between the developed shear stress in liquefiable soil layers due to the dynamic loading of earthquakes with the shear strength of the non-liquefiable soil layers (shear stresses are computed only for liquefiable layers).

Table 4.4. Shear stress/strength of the YY1 model (red numbers are shear stress in liquefiable layers and green numbers are shear strength in non-liquefiable soil layers).

YY1	
Shear stress or Shear strength 2010 (KPa)	**Shear stress or Shear strength 2011 (KPa)**
134.63	134.63
50 196	50 172
60 196	60 172
165.69	165.69
204.88	204.88

In the above table, the developed shear stress in liquefiable soil layers due to both the 2010 and 2011 earthquakes is greater than the shear strength of the upper non-liquefiable soil layer. Thus, this analysis explains the occurrence of liquefaction surface manifestation due to the upward movement of liquefied soil layers, i.e., since the shear stress in liquefiable soil layers is higher than the shear strength of the upper non-liquefiable soil layer, the liquefied soil can break through the non-liquefiable soil layer and manifest at the ground surface. Additionally, by looking at Figure 4.54, it can be seen that some downward movement of liquefied soils to the lower non-liquefiable soil layer occurred since its shear strength is less than the shear stress in the liquefiable soil layers.

The results of the dynamic analysis of the YY2 soil profiles are provided in this section. For the 2010 earthquake, the pore pressure ratio contour map of YY2 vividly shows liquefaction occurrence in the critical zone of the model (see Figure 4.55). Since the critical zone is a thick continuous zone with three liquefiable soil layers, due to the excess pore pressure as a result of liquefaction in the critical zone, the upward seepage moves the liquefied soil particles on the

critical zone to the ground surface by breaking the thin upper non-liquefiable layer. Thus, the liquefaction surface manifestation occurs as can be seen in the displacement vector map shown in Figure 4.56.

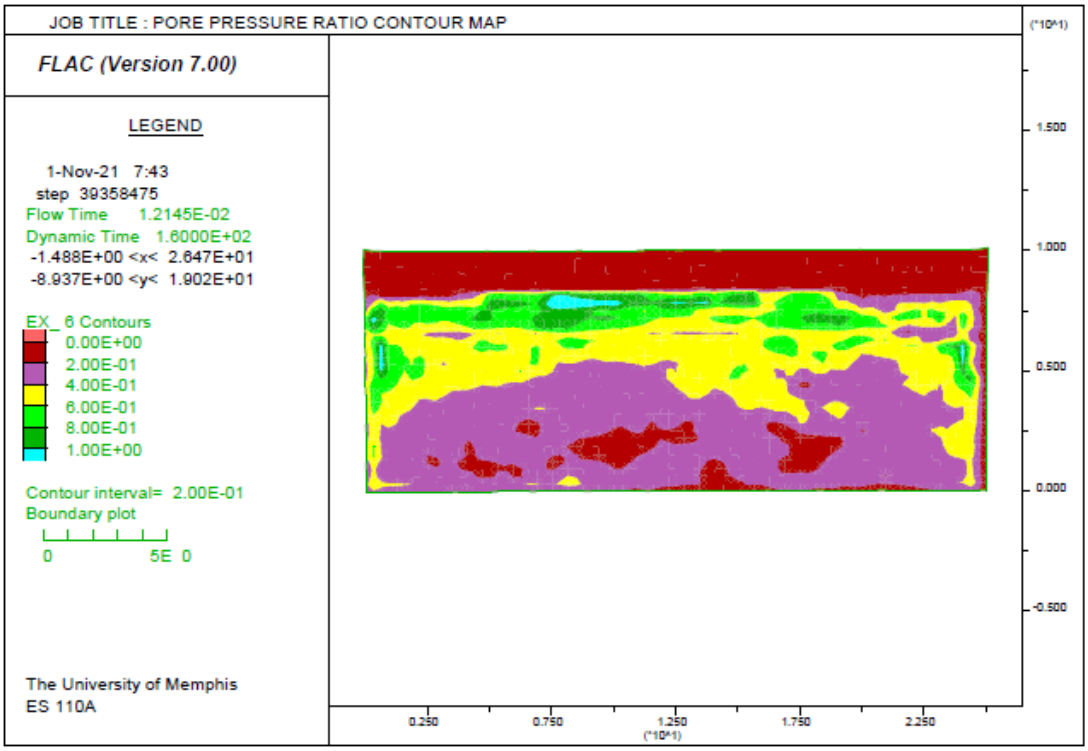

Figure 4.55. Pore pressure ratio contour map of the YY2 model after the dynamic analysis of the 2010 earthquake.

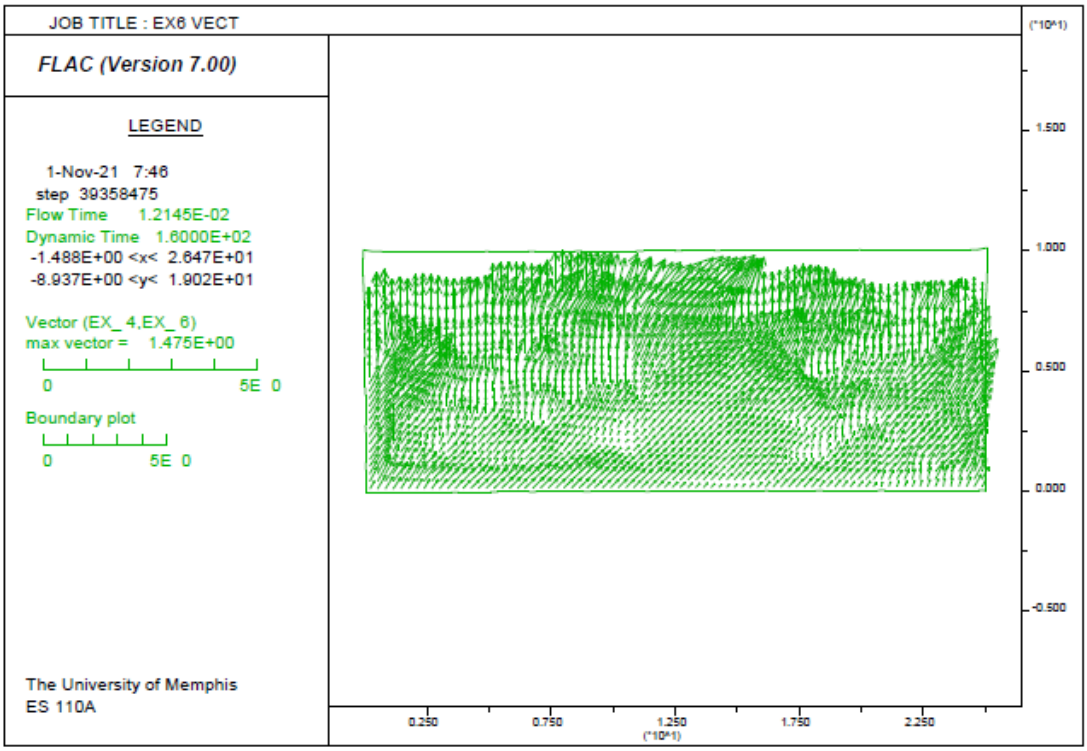

Figure 4.56. Displacement vectors of the YY2 model due to liquefaction after the dynamic analysis of the 2010 earthquake.

The 2011 earthquake also liquefies the soil profile and causes liquefaction surface manifestation. Figure 4.57 shows a pore pressure ratio of one or more in the critical zone of the soil profiles. Additionally, Figure 4.58 illustrates the movement of soil particles of the critical zone to the ground surface through the upper non-liquefiable layer due to excess pore water pressure and upward seepage. The reason that the upward seepage can push the liquefied soils to the ground surface is that the shear stress in the critical zone as a result of earthquake shaking is stronger than the shear strength of the upper non-liquefiable layer and liquefied soils can break through the upper non-liquefiable layer and progress to the ground surface.

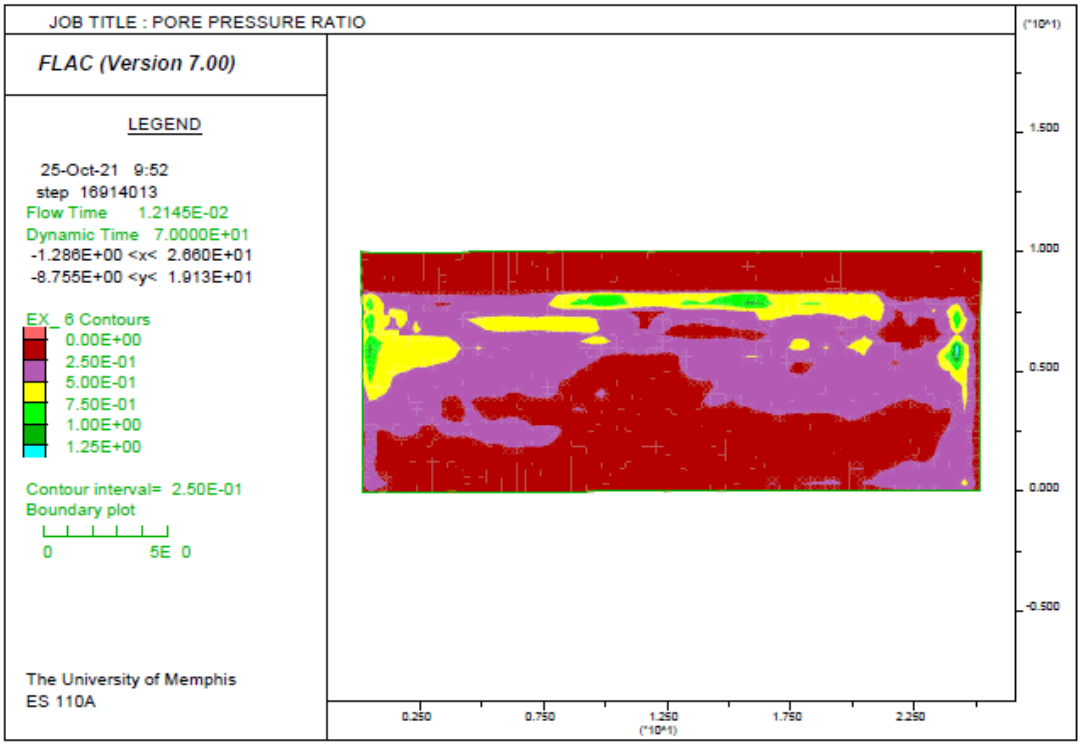

Figure 4.57. Pore pressure ratio contour map of the YY2 model after the dynamic analysis of the 2011 earthquake.

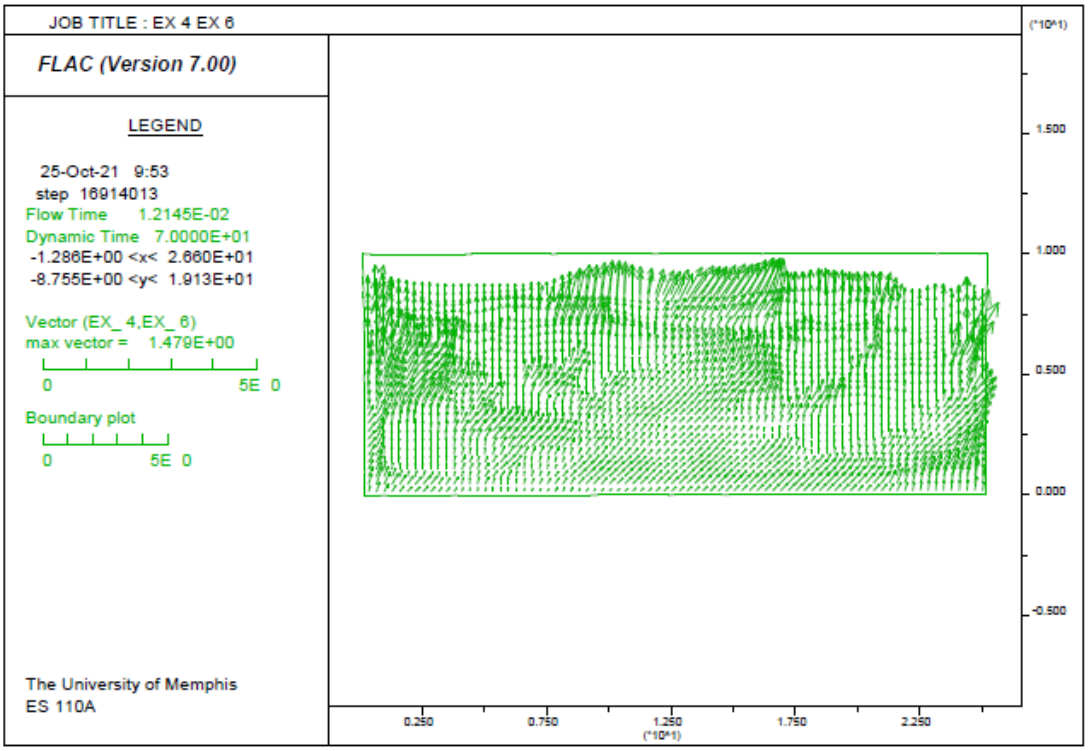

Figure 4.58. Displacement vectors of the YY2 model due to liquefaction after the dynamic analysis of the 2011 earthquake.

The results of shear stress and shear strength analysis of the YY2 soil profiles are provided in Table 4.5. Both the 2010 and 2011 CES earthquakes apply shear stress in liquefiable soil layers more than the shear strength of upper and lower non-liquefiable soil layers. Therefore, the upward movement of liquefied soils to the ground surface, as well as some downward and lateral movement of liquefied soils occurs as shown in Figure 4.58.

Table 4.5. Shear stress/strength of the YY2 model (red numbers are shear stress in liquefiable layers and green numbers are shear strength in non-liquefiable soil layers).

YY2	
Shear stress or Shear strength 2010 (KPa)	**Shear stress or Shear strength 2011 (KPa)**
98	98
55 147	55 122
65 147	65 122
80 147	80 122
158.65	158.65
179.90	179.90
203.30	203.30

4.3.2.2. Results of Dynamic Analysis of NN Models

The results of the 2010 dynamic analysis of the NN1 soil profile do not show any liquefaction surface manifestation, which agrees with the actual site observations. Although Figure 4.59 does not show any movement of liquefied soils to the ground surface, Figure 4.60, the pore pressure ratio contour map, clearly shows the occurrence of liquefaction ($r \geq 1$) in the only liquefiable soil layer below a thick non-liquefiable crust. But, since the thickness of the critical layer is much less than the upper non-liquefiable crust, the shear stress in the critical layer is not strong enough to overcome the shear strength of the upper crust; however, the lateral spread due to liquefaction in the critical layer can be seen in Figure 4.59.

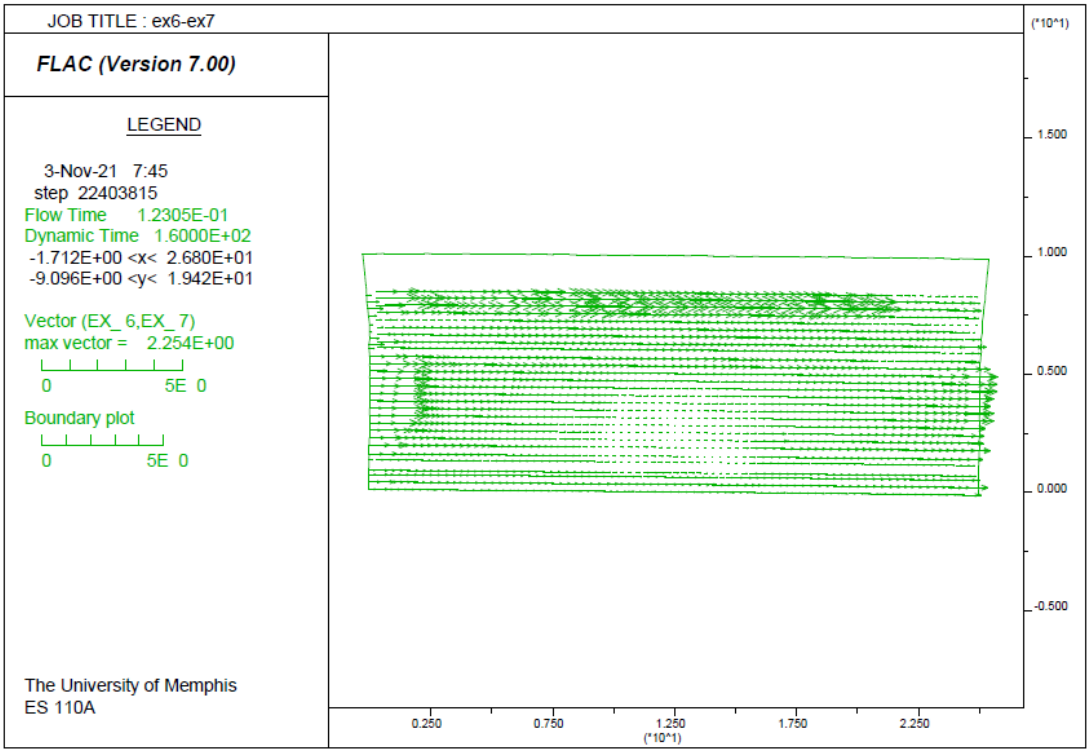

Figure 4.59. Displacement vectors of the NN1 model due to liquefaction.

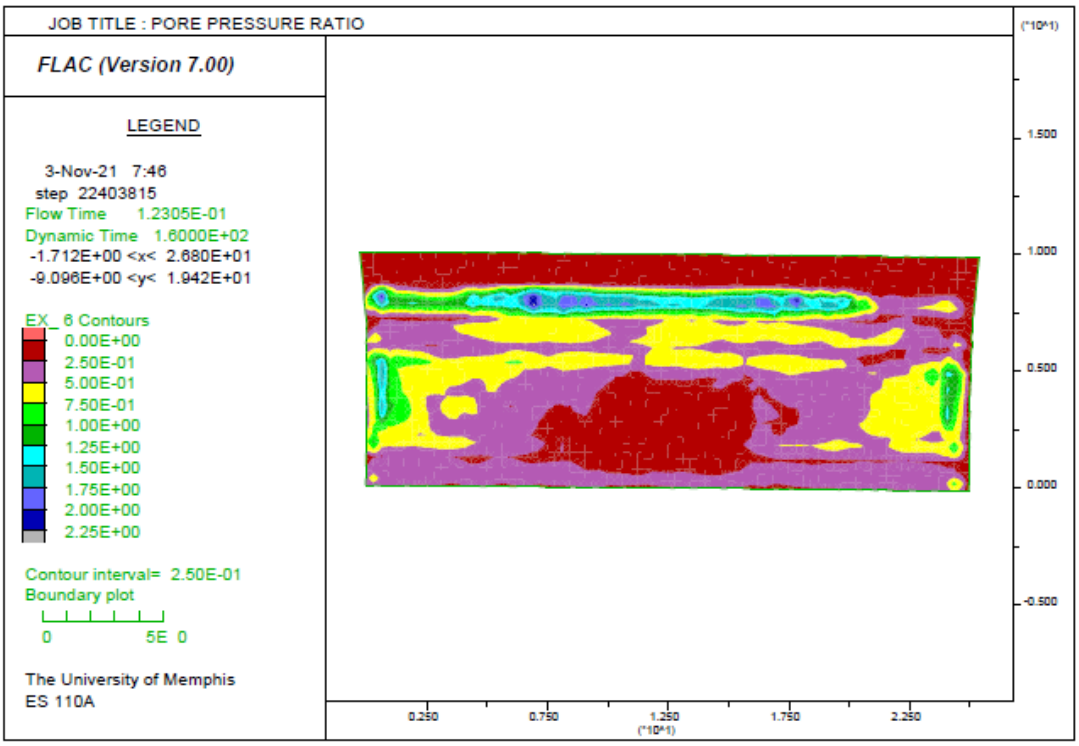

Figure 4.60. Pore pressure ratio contour map of the NN1 model after the dynamic analysis of the 2010 earthquake.

The second FLAC dynamic analysis of the NN1 model was conducted by applying the CES 2011 earthquake to the soil profile. Figure 4.61 shows the pore pressure ratio contour map, which is in the range of liquefaction occurrence (≥1) in the liquefiable layers. The pore pressure ratio in some of the non-liquefiable layers is more than zero but in most of the non-liquefiable layers it is zero. Additionally, although the liquefaction occurs in the liquefiable soil layers, Figure 4.62 shows no movement of liquefied soils through the non-liquefiable layers to the ground surface. Since the shear stress of liquefaction in the liquefiable layers is not more than the shear strength of the non-liquefiable layers, lateral spread occurs as a result of liquefaction in liquefiable soil layers.

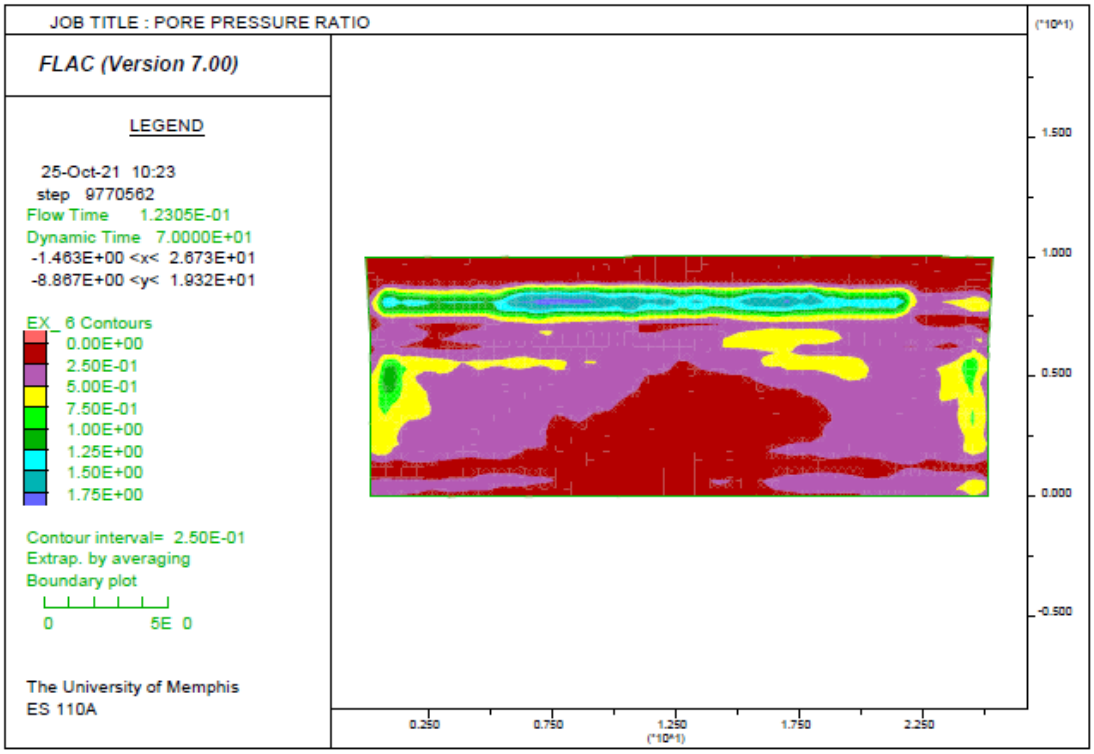

Figure 4.61. Pore pressure ratio contour map of the NN1 model after the dynamic analysis of the 2011 earthquake.

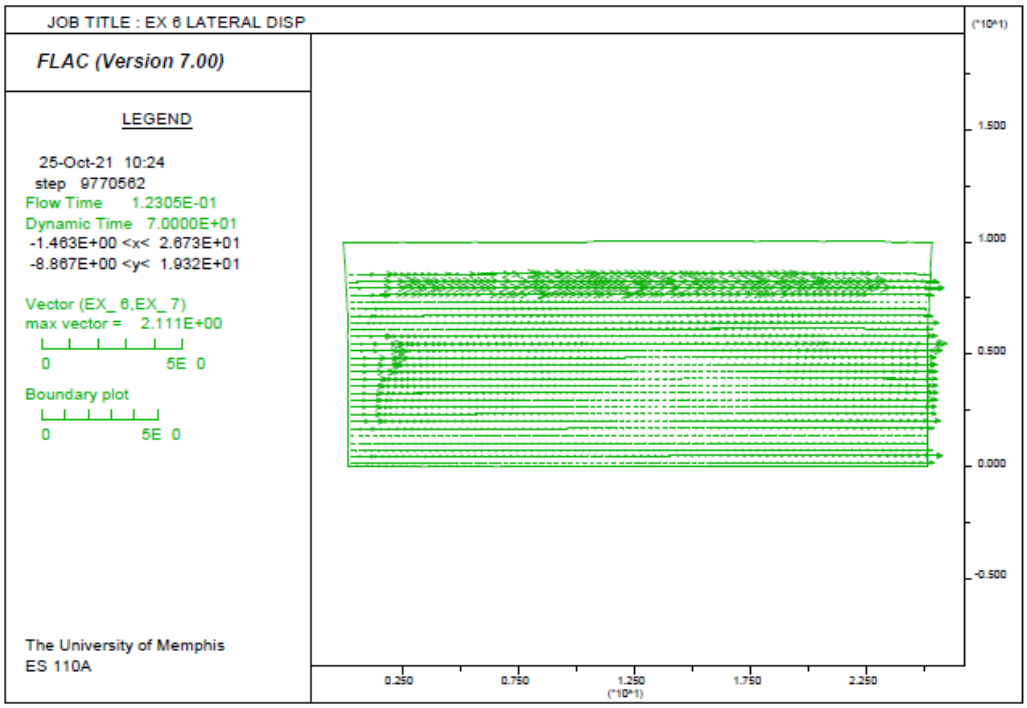

Figure 4.62. displacement vectors of the NN1 model due to liquefaction.

The NN sites did not show liquefaction surface manifestation during either the CES 2010 earthquake or 2011 earthquake (Rhode, 2017).

Table 4.6 highlights the shear stresses of liquefiable soil layers of NN1 as well as the shear strength of non-liquefiable soil layers of the NN1 soil profile. The shear stress in the shallowest liquefiable soil layer of NN1 due to the 2010 and 2011 earthquakes is much less than the shear strength of the upper two non-liquefiable soil layers. Therefore, it is unlikely that the liquefied soils of the shallowest liquefiable soil layer can overcome the shear strength of the upper non-liquefiable layers and go all the way up to the ground surface. For the bottom two liquefiable soil layers of the NN1 soil profile, it can be seen that the shear stresses are weaker than the shear strength of the very thick upper non-liquefiable layer; consequently, no upward movement of liquefied soils occurs.

Table 4.6. Shear stress/strength of the NN1 model (red numbers are shear stress in liquefiable layers and green numbers are shear strength in non-liquefiable soil layers).

NN1	
Shear stress or Shear strength 2010 (KPa)	**Shear stress or Shear strength 2011 (KPa)**
132.84	132.84
147.58	147.58
50 98.00	50 49
178.54	178.54
96.78	96.78
71.74	71.74

As shown in Figure 3.51, the NN2 soil profile has eleven layers including both liquefiable and non-liquefiable soil layers. The results of the numerical analysis of this site do not show any liquefaction surface manifestation. However, liquefaction occurred in the liquefiable soil layers of the NN2 site during both the 2010 and 2011 earthquakes. Due to the presence of many non-liquefiable layers above the liquefiable layers, as well as the low pressure of the thin liquefiable layers, their shear stress is not strong enough to overcome the shear strength of the non-liquefiable layers and move to the ground surface. Thus, there is no evidence of liquefaction surface manifestation.

Figures 4.63, 4.64, and 4.65 summarize the FLAC dynamic analysis of the 2010 earthquake on the NN2 model. Figure 4.63 shows the pore pressure ratio contour map in different layers of the NN2 soil profile. Figure 4.63 indicates the pore pressure ratio of one in the liquefiable soil layers and a pore pressure ratio of 0 to 0.5 in the non-liquefiable soil layers. Thus, from the pore pressure ratio ≥ 1 in the liquefiable layers, liquefaction occurrence can be concluded in these layers.

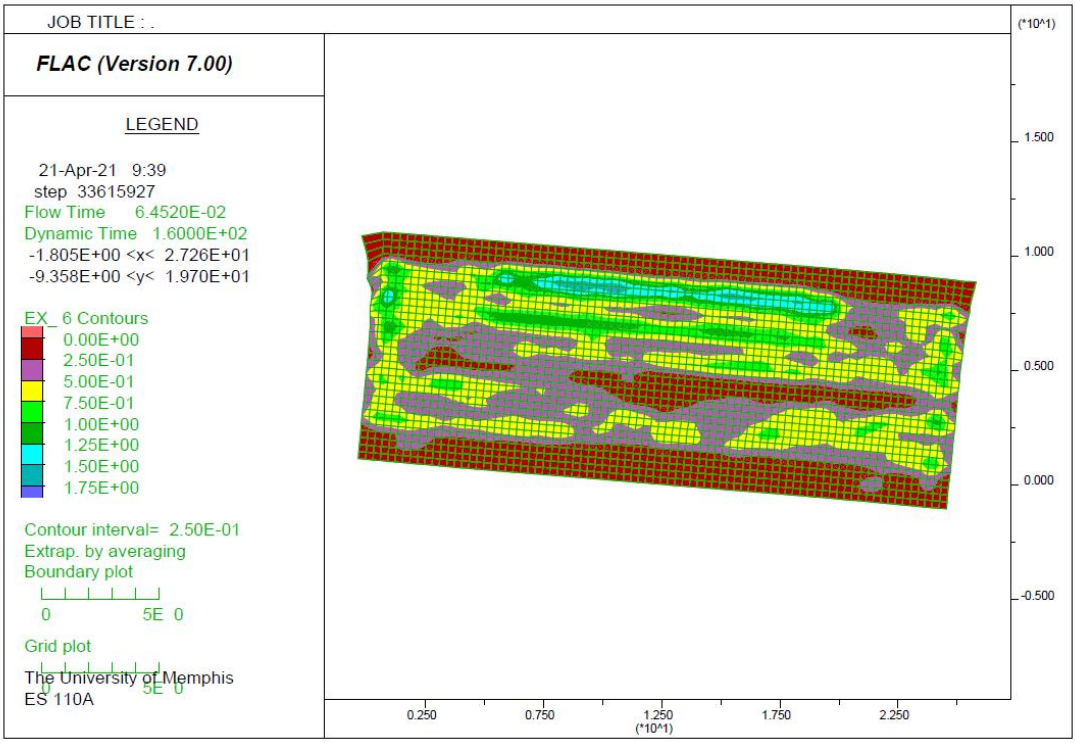

Figure 4.63. Pore pressure ratio contour map of the NN2 model after the dynamic analysis of the 2010 earthquake.

Figure 4.64 shows the displacement vectors of soil layers of the NN2 model during the 2010 earthquake. The liquefaction and consequent lateral spread occurrence are obvious in the liquefiable soil layers, but there is no evidence of movement (displacement vectors) to the ground surface. Since the upward soil movement from the liquefiable soil layers is not able to break the upper non-liquefiable soil layers and push the liquefied soils to the ground surface, lateral spread occurs horizontally as a result of liquefaction in the liquefiable soil layers.

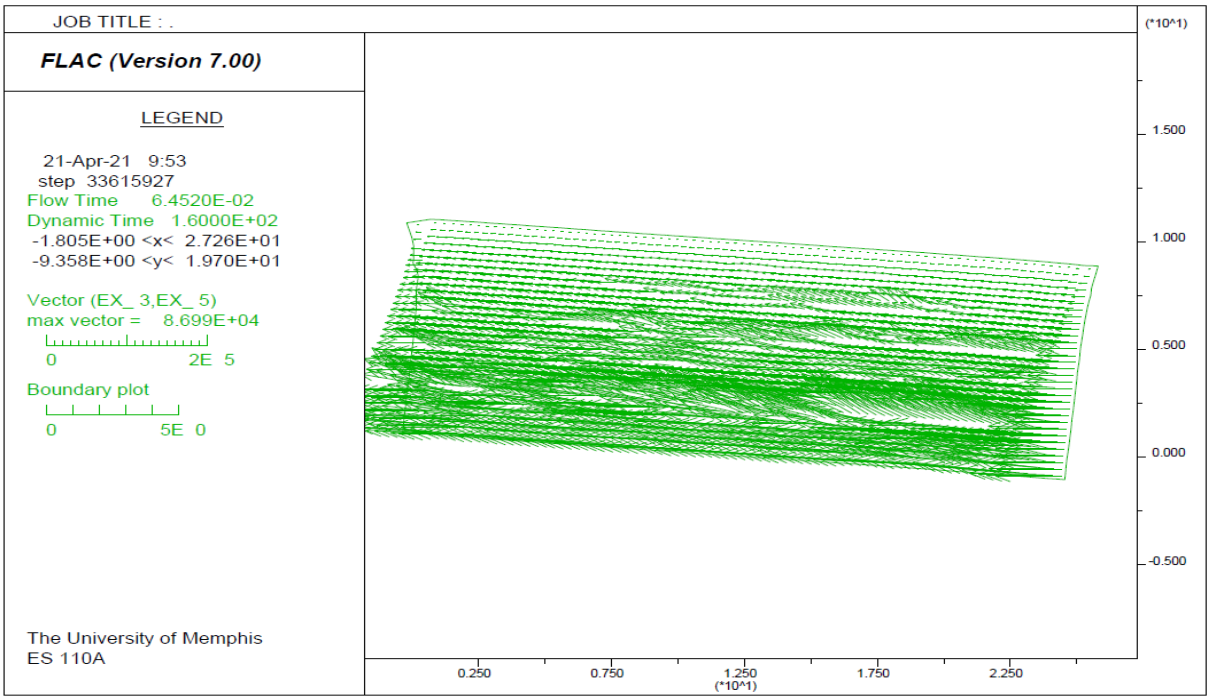

Figure 4.64. Displacement vectors of the NN2 model after the earthquake of 2010.

Figure 4.65 shows the excess pore pressure development in the topmost liquefiable soil layer and by comparing the excess pore pressure value of this layer with the initial effective stress at this layer, it can be concluded that the numbers are equal, which means liquefaction occurred in this layer. But because this layer is very thin and the upper non-liquefiable layer is thick, the upward seepage cannot push the soils through the upper non-liquefiable layers and manifest liquefaction at the ground surface.

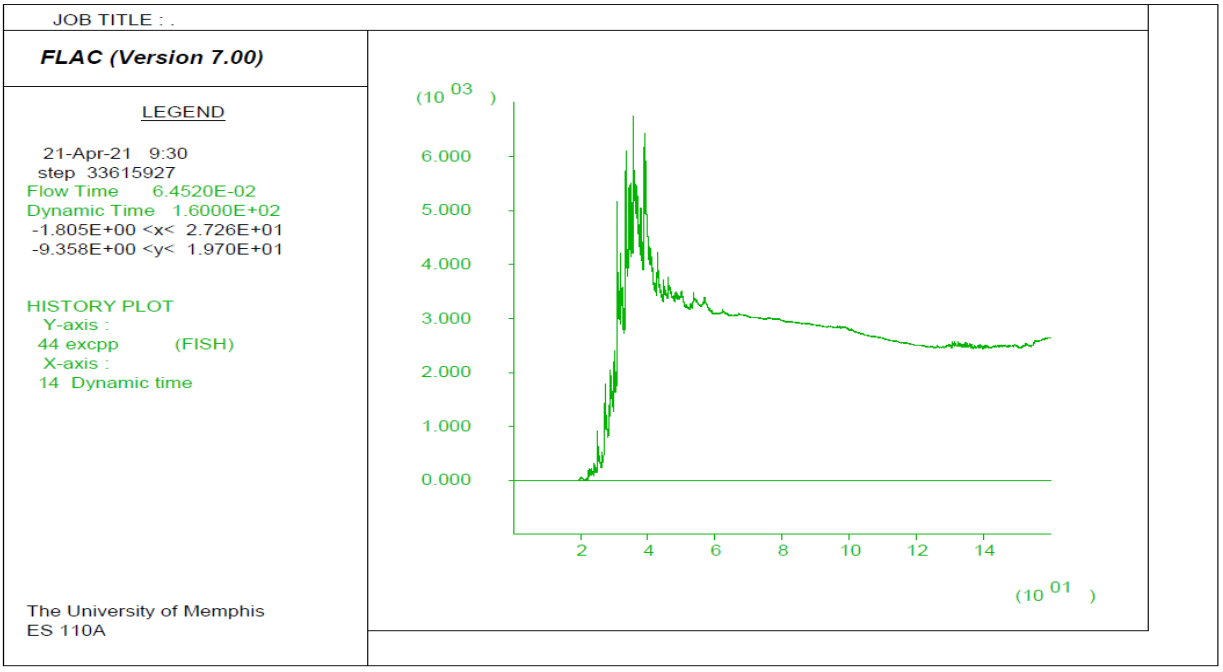

Figure 4.65. Excess pore pressure development in the most top liquefiable soil layer of the NN2 model (vertical axis is pore pressure in Pa, and the horizontal axis is time in second).

The second FLAC dynamic analysis of the NN2 model was conducted by applying the CES 2011 earthquake to the soil profile. Figure 4.66 shows the pore pressure ratio contour map, which is in the range of liquefaction occurrence ($r \geq 1$) in the liquefiable layers. The pore pressure ratio in some of the non-liquefiable layers is more than zero but in most of the non-liquefiable layers it is zero. Additionally, although liquefaction occurs in the liquefiable soil layers, Figure 4.67 shows no movement of liquefied soils through the non-liquefiable layers to the ground surface. Since the shear stress of liquefaction in the liquefiable layers is not more than the shear strength of the non-liquefiable layers, lateral spread occurs as a result of liquefaction in the liquefiable soil layers.

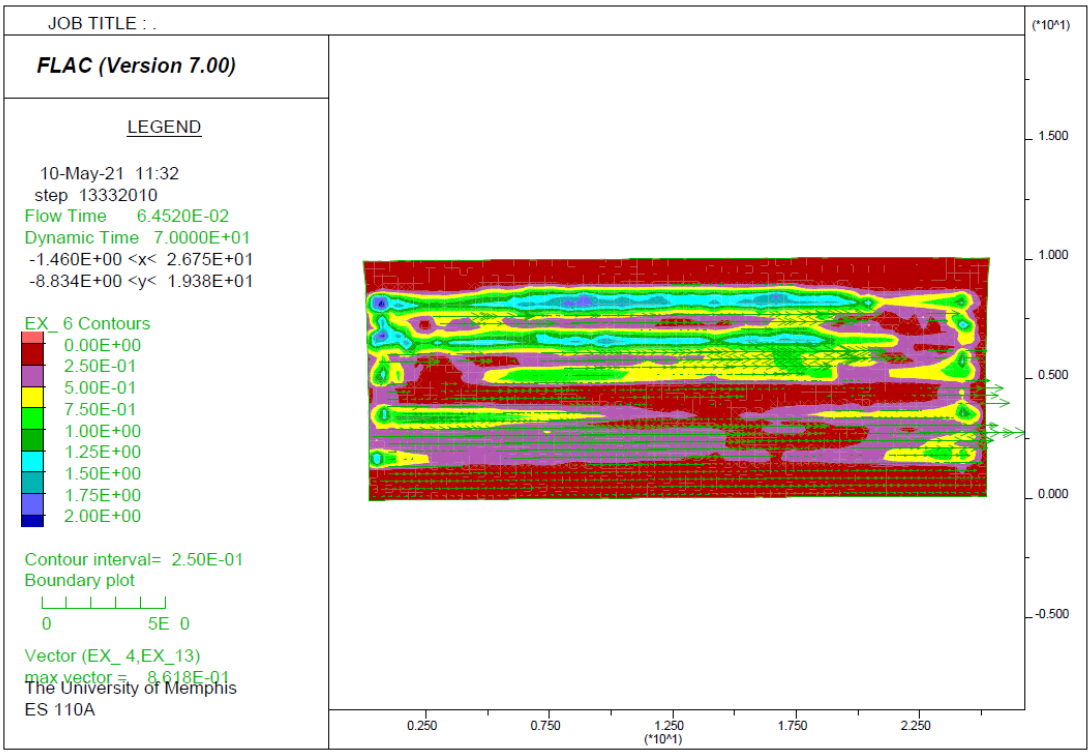

Figure 4.66. Pore pressure ratio contour map of the NN2 model after the dynamic analysis of the 2011 earthquake.

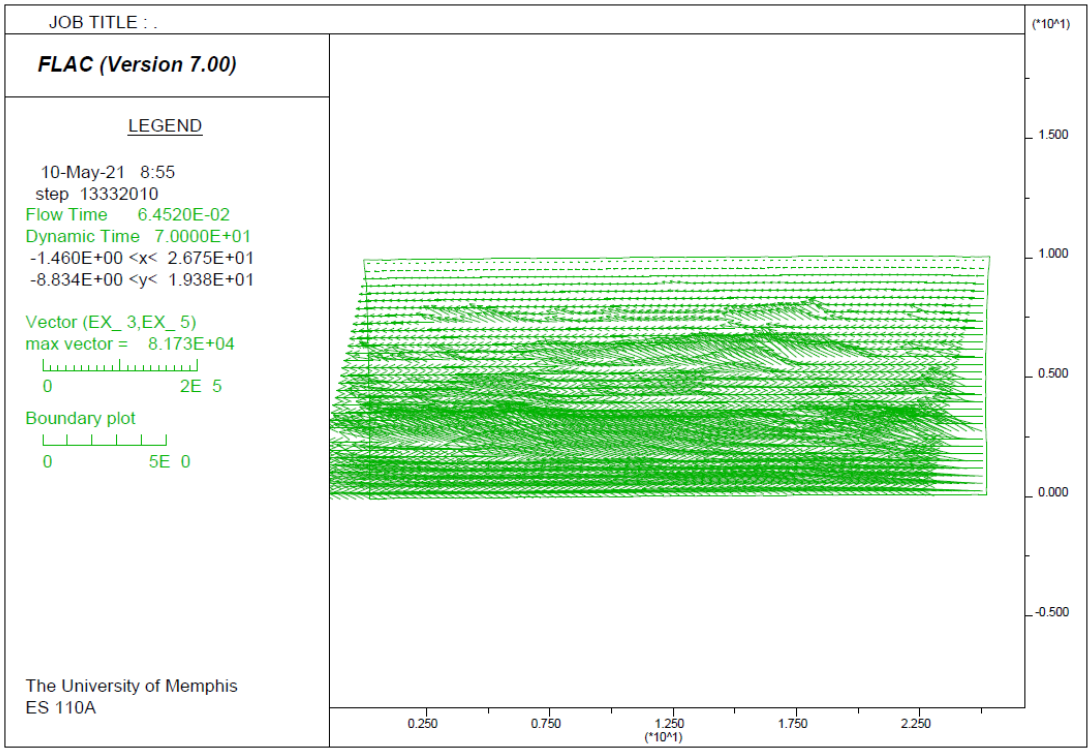

Figure 4.67. Displacement vectors of the NN2 model after the earthquake of 2011.

Table 4.7 provides the shear stress and shear strength of different soil layers of the NN2 model after dynamic analysis of the 2010 and 2011 earthquakes. It is obvious that, unlike in the other models (YY1, YY2, and NN1), the trend of shear stress in the liquefiable layer and shear strength in the upper non-liquefiable layers has an inconsistency. One of the main reasons that may explain the inconsistency of shear stress and shear strength of the NN2 soil profile is the presence of 11 very thin soil layers in a 10 m deep soil profile, which may cause FLAC to not capture the right value of shear strength and shear stress in these thin layers. Therefore, for the rest of the analyses of this study, the NN2 soil profile is excluded.

Table 4.7. Shear stress/strength of the NN2 model (red numbers are shear stress in liquefiable layers and green numbers are shear strength in non-liquefiable soil layers).

NN2	
Shear stress or Shear strength 2010 (kPa)	**Shear stress or Shear strength 2011 (kPa)**
128.18	128.18
144.28	144.28
50 196.00	50 98.00
156.30	156.30
50 98.00	50 98.00
168.26	168.26
101.25	101.25
179.58	179.58
50 196.00	50 98.00
191.05	191.05
171.87	171.87

4.3.2.3. LPI and LPI_{ISH} Analyses of New Zealand Soil Profiles

For both the YY and NN models, by employing the simplified method of Seed and Idriss (1971), the factor of safety at each soil layer was estimated. After computing the FS at each soil layer based on the simplified procedure, the LPI and LPI_{ISH} were calculated based on Equations 1

and 2, respectively. Table 4.8 provides the obtained LPI and LPI_{ISH} results for the 2010 and 2011 earthquakes for each of the four soil profiles of YY1, YY2, NN1, and NN2. The values in Table 4.8 were obtained for the first 10 m of the soil profile and the integral limit in Equations 1 and 2 were considered from 0 to 10. Depth of 10 to 20 meter were considered non-liquefiable in all four models.

Table 4.8. Computed LPI and LPI_{ISH} for YY and NN models based on the earthquake of 2010 and 2011.

	LPI				LPI_{ISH}			
	YY1	**YY2**	**NN1**	**NN2**	**YY1**	**YY2**	**NN1**	**NN2**
2010	7.6	1.1	6.5	6.5	4.4	0	4.9	4.1
2011	2.7	0	4.2	1.9	0.3	0	2.1	0

According to Iwasaki (1978-1982) and Maurer (2015), for both LPI>5 and LPI_{ISH}>5, liquefaction surface manifestation is expected. Therefore, according to Table 4.8, the LPI-based predictions for the 2010 earthquake are not in agreement with what was observed during the earthquakes except for YY1. Even though the NN profiles did not show any liquefaction surface manifestation, the LPI predicts it. On the other hand, the calculated LPI_{ISH} values for both the YY and NN sites based on the 2010 earthquake are less than 5, which agrees with no liquefaction surface manifestation at the NN sites, but it underpredicts the liquefaction surface manifestation potential of the YY sites.

The LPI and LPI_{ISH} analyses were also performed on the YY and NN sites based on the New Zealand earthquake of 2011 as shown in Table 4.8. According to this analysis, neither the LPI nor LPI_{ISH} methods predicts the liquefaction surface manifestation for the YY soil profiles, which shows those inconsistency between the methods and site observations. However, both methods predict no probability of liquefaction surface manifestation for the NN sites, which is consistent with site observations.

From the provided results in this section, it has been observed that the LPI- and LPI_{ISH}-based liquefaction predictions are not consistent with site observations. Both the LPI and LPI_{ISH} approaches showed some significant over/under predictions because neither method includes the impact of shear strength and thickness of non-liquefiable soil layers on the surface manifestation of liquefaction. This is the basis for this study, which evaluates the impact of shear strength and thickness of non-liquefiable soil layers and suggests an adjusted LPI_{ISH} procedure.

4.3.2.4. Summary

By investigating the details of the YY models, it is clear that there are common properties in both YY soil profiles as follows:

- For both models, the liquefiable (critical) layer/zone is right below the unsaturated layer of 1.8m thickness.
- For both models, there is only one non-liquefiable layer which is an unsaturated layer on top of the liquefiable zone.
- For both models, the thickness of the liquefiable zone is more than the upper non-liquefiable layer (see Table 4.9).

Table 4.9. Thickness of liquefiable (critical layer) and upper non-liquefiable layers in YY1 and YY2.

	CRITICAL	NON-LIQ
YY1	4.2 m	1.8 m
YY2	2.2 m	1.8 m

- Both models show liquefaction at the ground surface for both the 2010 and 2011 earthquakes.

- Since the thickness of the liquefiable zone in YY1 is more than in YY2 and the upper non-liquefiable layer thickness is 1.8m for both models, it can be concluded that the potential of liquefaction surface manifestation of YY1 is more than for YY2.

The common properties of both NN models that make them non-liquefiable are:

- In both NN models, the thickness of the critical layer/zone is less than in the YY models.
- For almost all critical layers/zones of the NN models, the upper non-liquefiable layer(s) is thicker (Table 4.10).

Table 4.10. Thickness of liquefiable (critical layer) and upper non-liquefiable layers in NN1 and NN2.

	CRITICAL	NON-LIQ
NN1	1.5 m	2.5 m
	1.5 m	4.5 m
NN2	0.5 m	2.3 m
	0.9 m	0.8 m
	0.7 m	2.5 m

- For both NN models, there is more than one non-liquefiable layer on top of the critical layer/zone.

The following conclusions can be made based on the results of the YY and NN model analyses:

- The shallower the critical layer/zone, the higher the probability of liquefaction surface manifestation.
- If the critical zone is shallow and thicker than the upper non-liquefiable layer, the probability of liquefaction surface manifestation is high.
- If the upper non-liquefiable layer is thicker than the lower critical zone, the probability of liquefaction surface manifestation is low.
- The thicker the critical layer/zone in liquefiable soil profiles, the higher the potential for liquefaction at the ground surface.

So, according to the above bullet points, the approach in the next section will be to evaluate the sensitivity of the liquefaction surface manifestation potential of each soil profile to the thickness and shear strength of the upper non-liquefiable soil layers, accordingly.

4.4. Sensitivity Analysis of Liquefaction Surface Manifestation to the Thickness of Upper Non-liquefiable Soil Layers

Section 3.5.1.1 provides the methodology for the sensitivity analysis of liquefaction surface manifestation occurrence to the thickness of liquefiable and non-liquefiable soil layers. The results of that analysis.

4.4.1. YY1

Section 3.5.1.1 provided the details of the methodology of assessing the liquefaction surface manifestation sensitivity of the YY1 model by changing the thickness of the upper non-liquefiable layer. The liquefiable layers have not been changed in this sensitivity analysis, and all properties were kept the same. Table 4.11 summarizes the thickness of different soil layers in the new YY1 model and the original YY1 model.

Table 4.11. Thickness of different soil layers in the new YY1 model and the original YY1 model (red numbers are liquefiable layers and green numbers are non-liquefiable soil layers).

YY1	
Original Thicknesses (m)	**New Thicknesses (m)**
1.8	1.8
2	3.8
2.2	2
3	2.2
1	1

By performing the dynamic analysis on the new YY1 model of Figure 3.60 under both the 2010 and 2011 CES earthquakes, it has been revealed that the thickness of the upper non-liquefiable soil layer has a significant impact on the liquefaction surface manifestation occurrence. Figures 4.68 and 4.69 show the displacement vector maps of soil particles of the critical zone due to the dynamic loading of the 2010 and 2011 earthquakes respectively for the new YY1 model. According to Figures 4.68 and 4.69, the movement of soil particles in the critical zone is obvious, but due to the high thickness of the upper non-liquefiable soil layer, the liquefied soil of the critical zone does not show liquefaction at the ground surface.

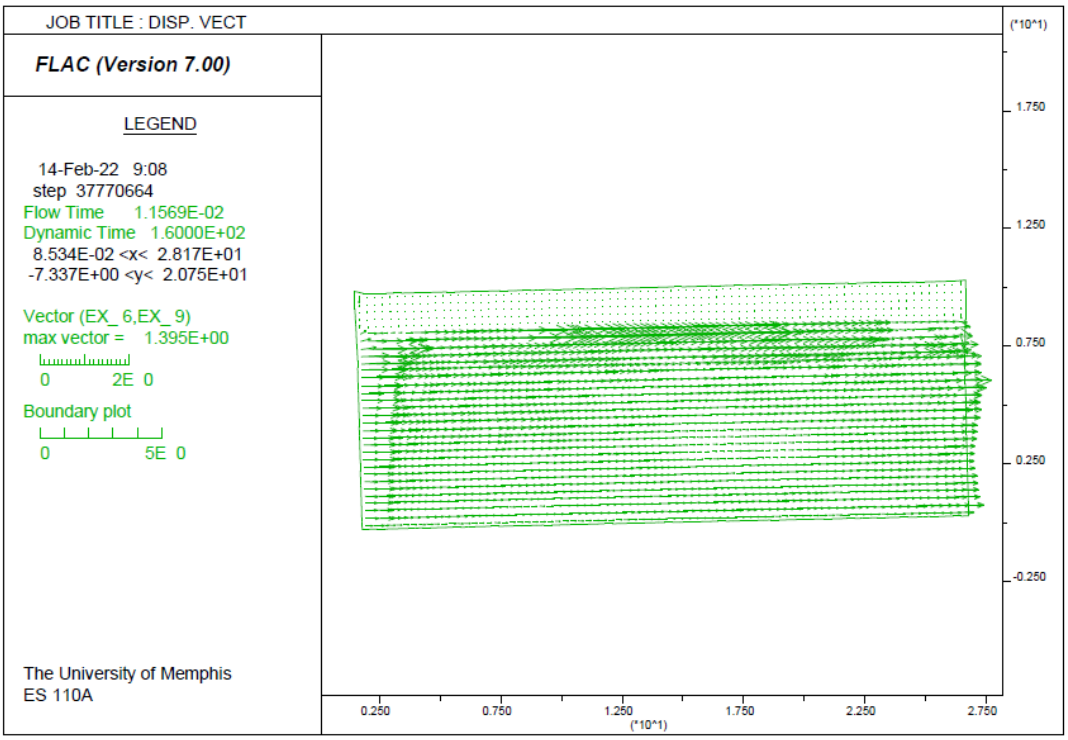

Figure 4.68. Displacement vector maps of soil particles of the critical zone due to dynamic loading of 2010.

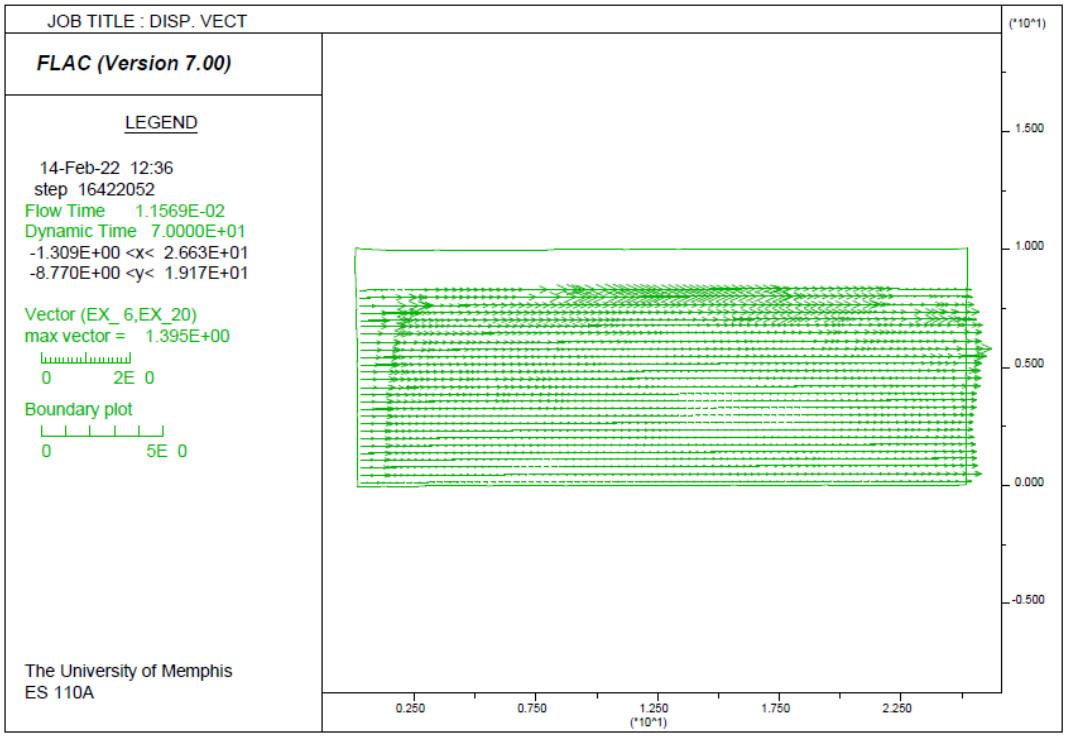

Figure 4.69. Displacement vector maps of soil particles of the critical zone due to dynamic loading of 2011.

Additionally, the pore pressure ratio contour maps of 2010 and 2011 for the new YY1 model are shown in Figures 4.70 and 4.71. Referring to these figures, liquefaction occurrence in the critical zone of the YY1 model is confirmed since the pore pressure ratio is one or higher in the critical zone.

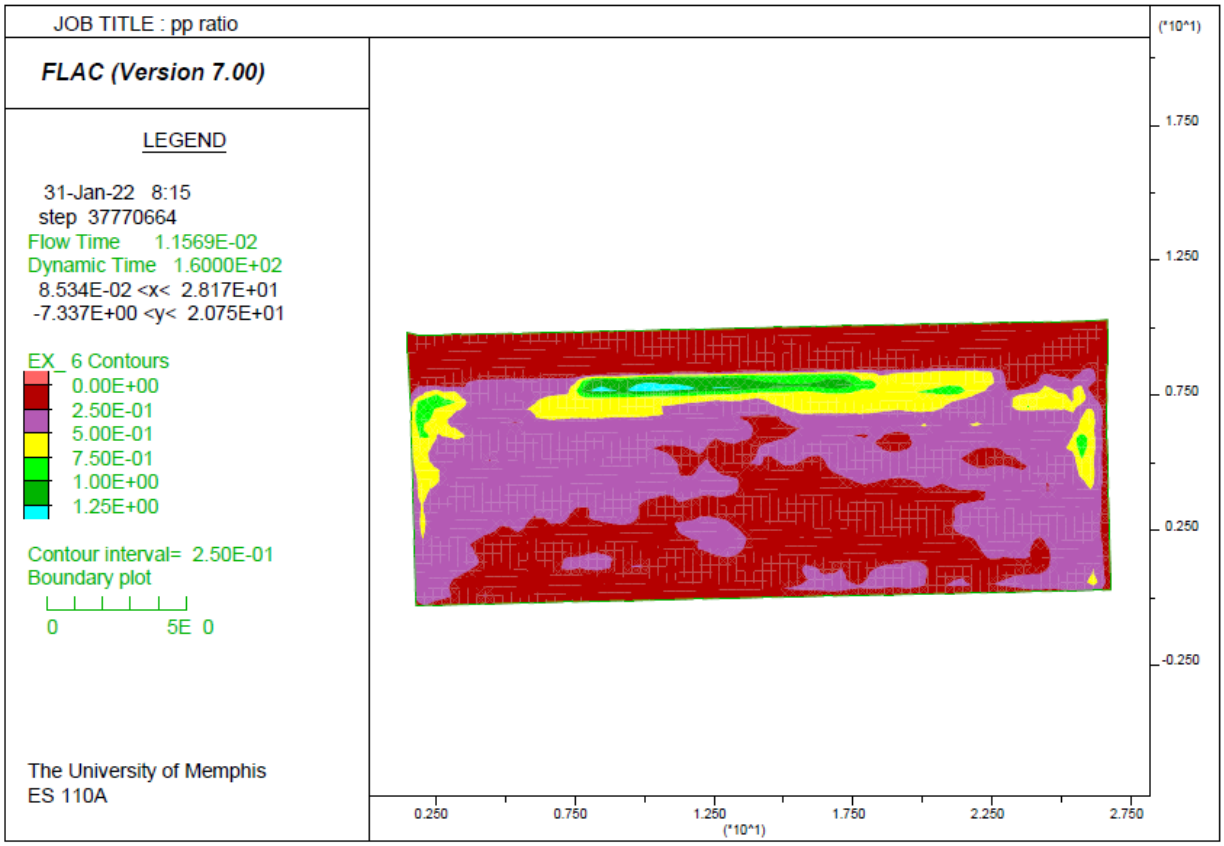

Figure 4.70. Pore pressure ratio contour maps of 2010.

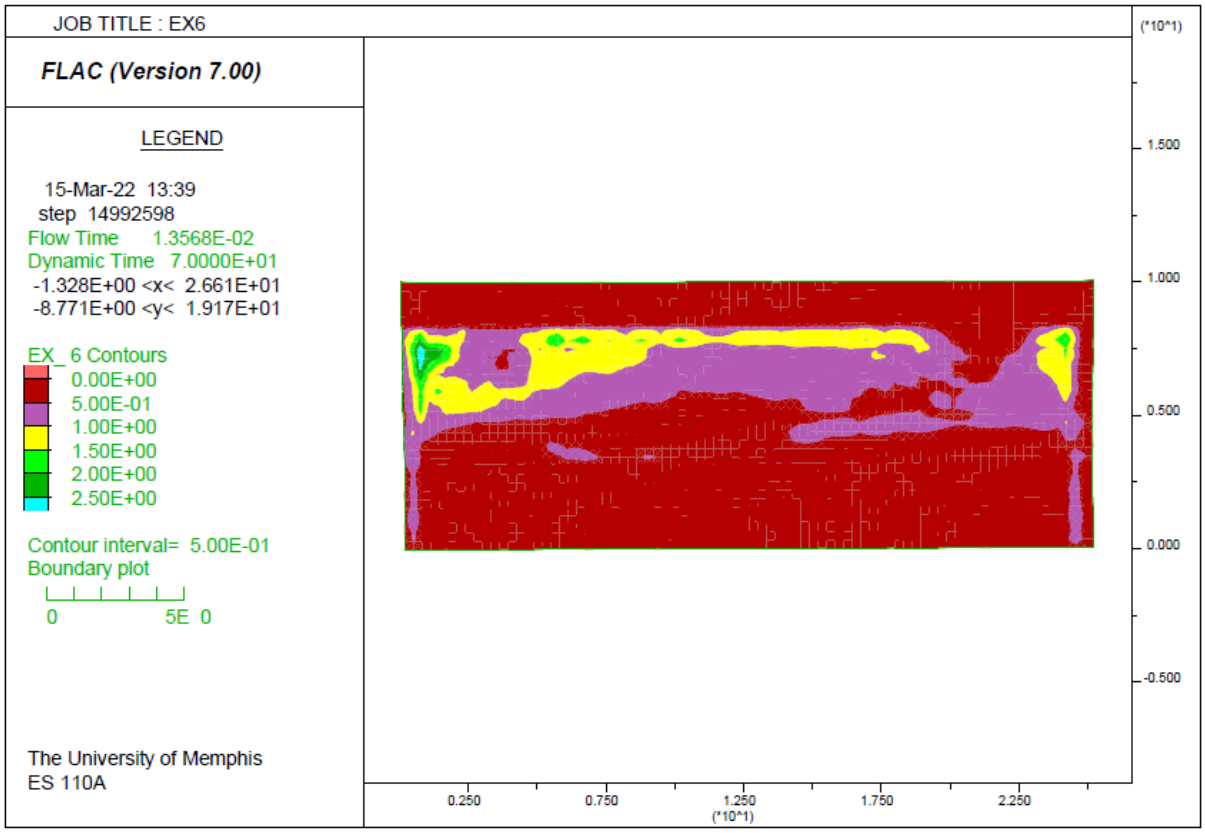

Figure 4.71. Pore pressure ratio contour maps of 2011.

4.4.2. YY2

Like the YY1 soil profile, a sensitivity analysis of the thickness of the upper non-liquefiable layer has been done for the YY2 soil profile in Figure 3.62 and the results are provided and discussed in this section. Also, Table 4.12 provides the thickness of the different soil layers in the new and original YY2 models.

Table 4.12. Thickness of different soil layers in the new YY2 model and the original YY2 model (red numbers are liquefiable layers and green numbers are non-liquefiable soil layers).

YY2	
Original Thicknesses (m)	**New Thicknesses (m)**
1.8	1.8
0.7	1.5
0.7	0.7
0.8	0.7
2.8	0.8
1.7	2.8
1.5	1.7

The non-occurrence of liquefaction surface manifestation in the new YY2 soil profile can also be concluded by looking at the displacement vector maps. Figures 4.72 and 4.73 show the displacement vector maps of the YY2 model for the 2010 and 2011 earthquakes, respectively. In both displacement vector maps, there is no movement of liquefied soil to the ground surface.

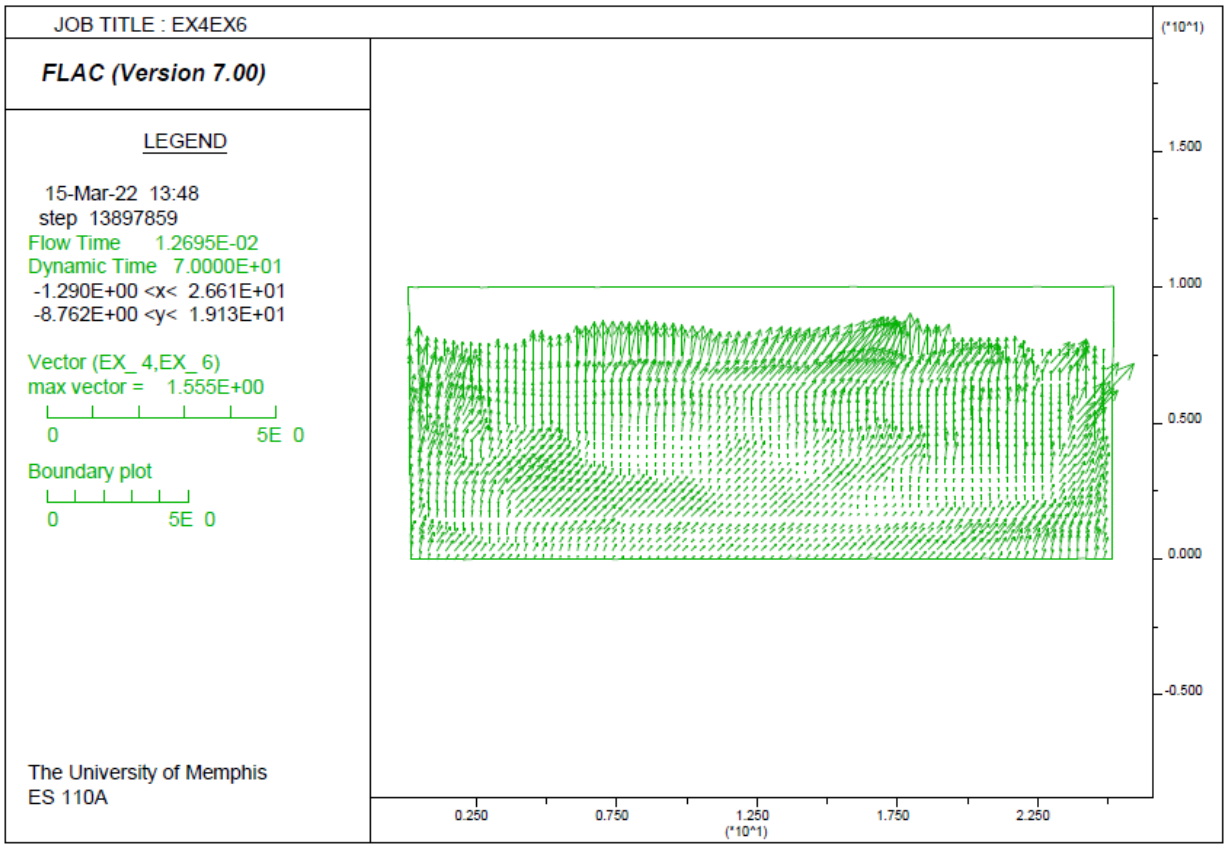

Figure 4.72. Displacement vector maps of soil particles of the critical zone due to dynamic loading of 2010.

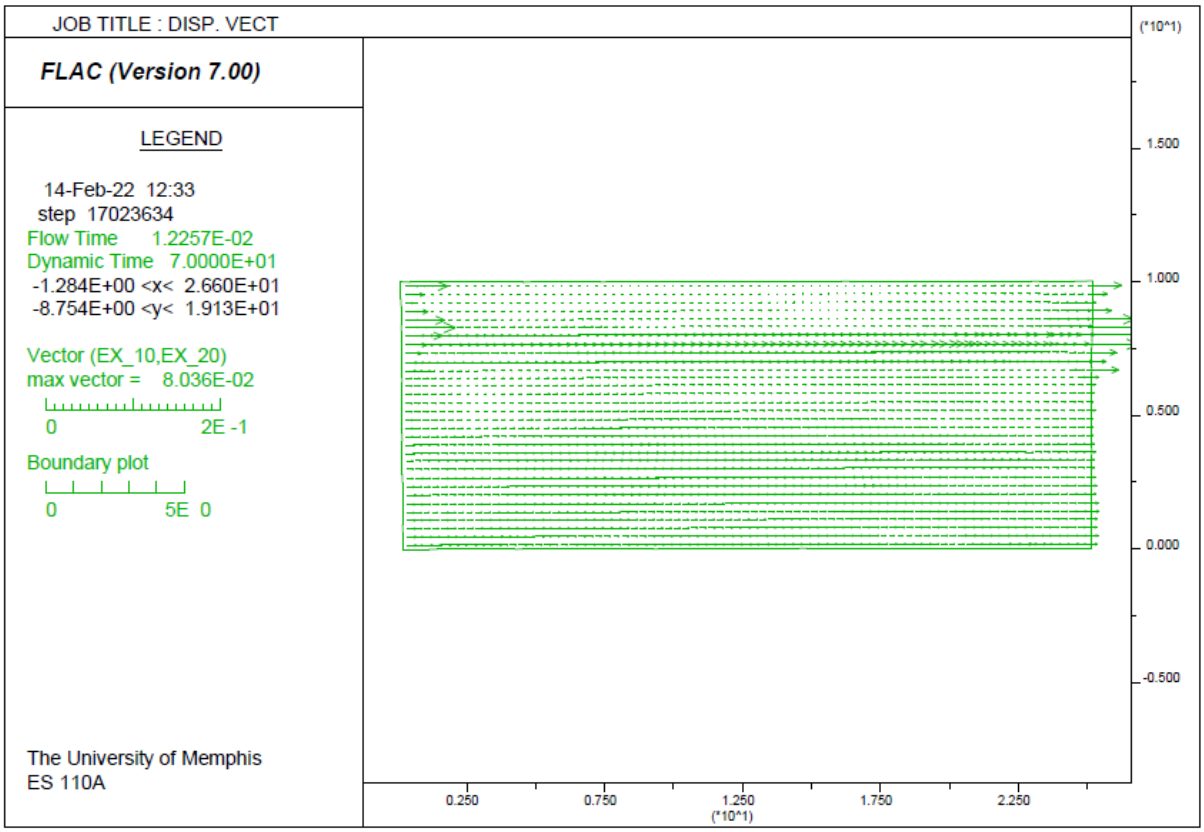

Figure 4.73. Displacement vector maps of soil particles of the critical zone due to dynamic loading of 2011.

To investigate the occurrence of liquefaction in the liquefiable soil layers, the pore pressure ratio contour map of the YY2 model is shown in Figures 4.74 and 4.75 after dynamic analysis of 2010 and 2011, respectively. It can be seen that the pore pressure ratio is in the range of one or higher for the liquefiable layers, which means that excess pore pressure has been developed in these layers.

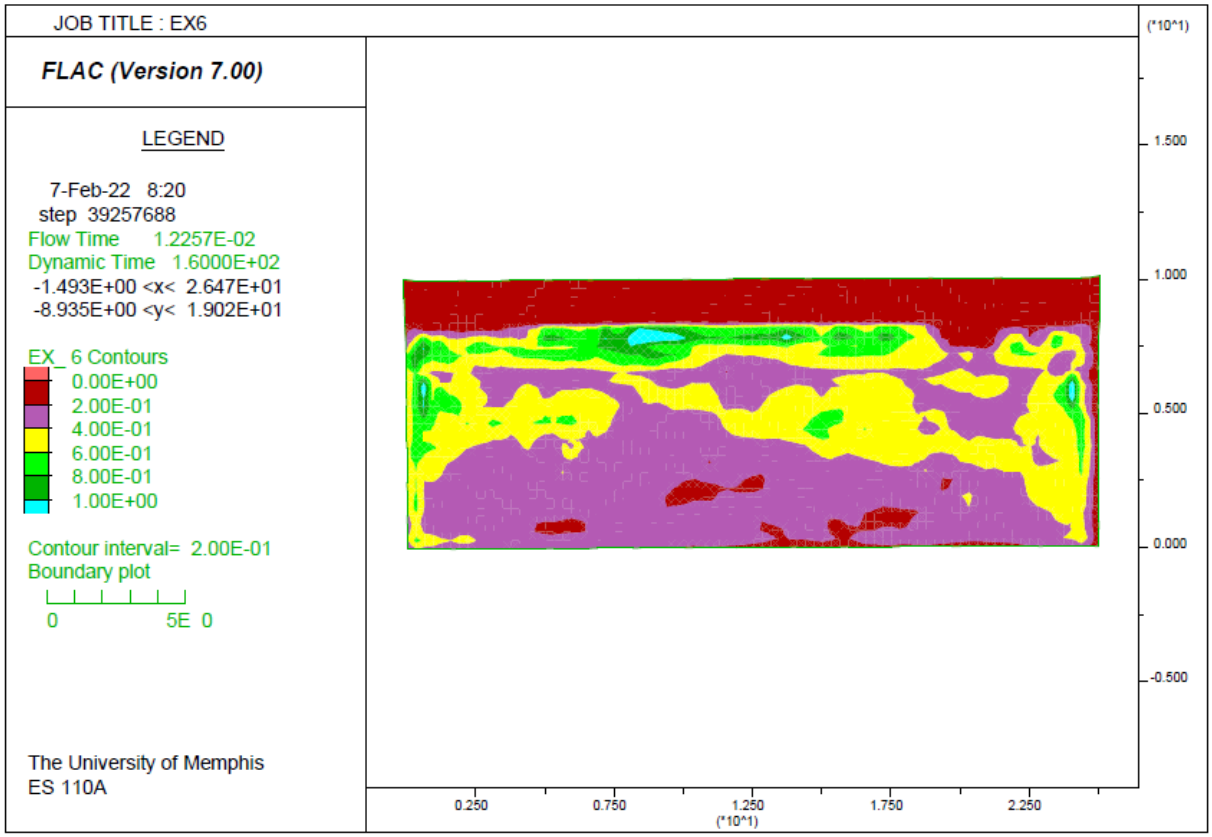

Figure 4.74. Pore pressure ratio contour maps of 2010.

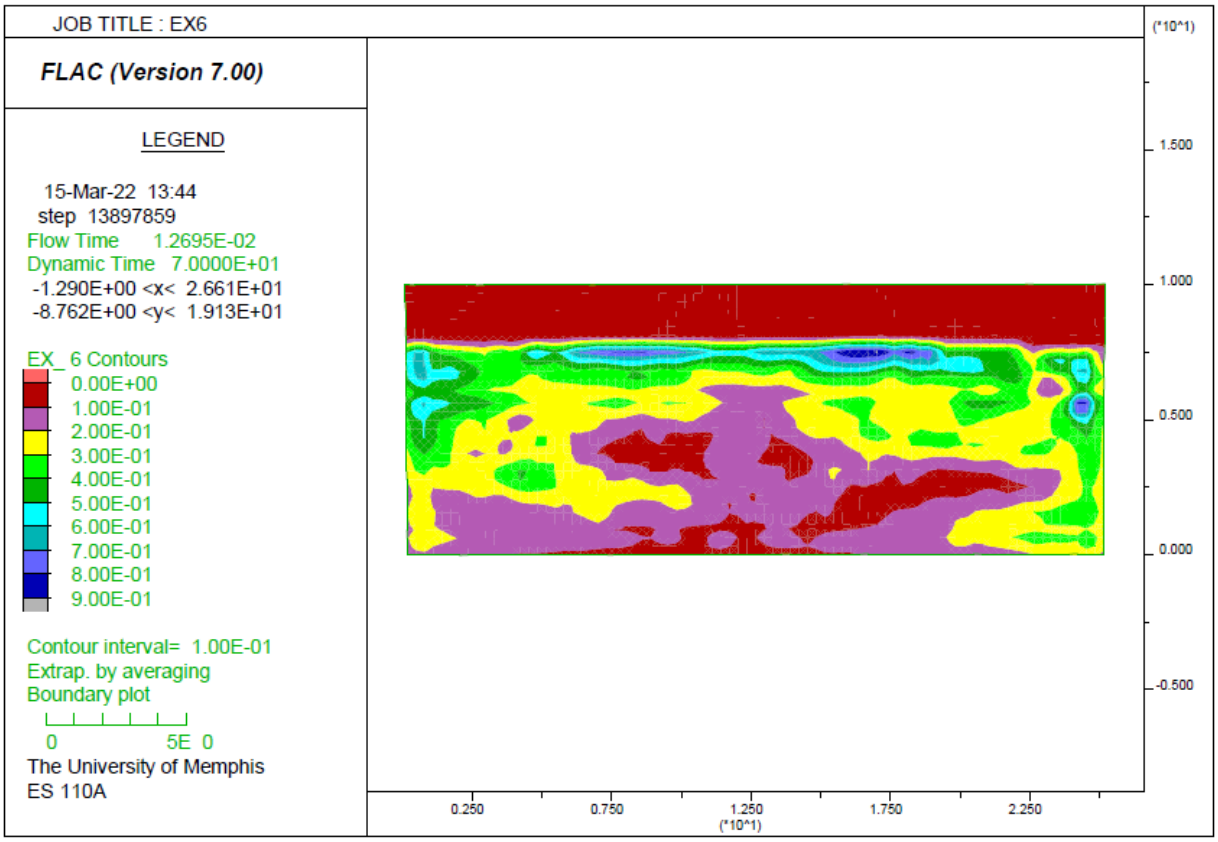

Figure 4.75. Pore pressure ratio contour maps of 2011.

4.4.3. NN1

By performing the dynamic analysis using the 2010 and 2011 CES time histories on the new NN1 model shown in Figure 3.62, it can be observed that liquefaction has occurred on the ground surface due to decreasing thickness of the upper non-liquefiable layer. The thickness of different soil layers in the original and new NN1 model is provided in Table 4.13.

Table 4.13. Thickness of different soil layers in the new NN1 model and the original NN1 model (red numbers are liquefiable layers and green numbers are non-liquefiable soil layers).

NN1	
Original Thicknesses (m)	**New Thicknesses**
1.6	1.6
0.9	0.9
1.5	1.5
4.5	4.5
0.7	0.7
0.8	0.8

The displacement vector maps of the new NN1 soil profile are shown in Figures 4.76 and 4.77 for the earthquakes of 2010 and 2011, respectively. The movement of liquefied soil particles to the ground surface is clear in the new NN1 soil profile during both the 2010 and 2011 earthquakes.

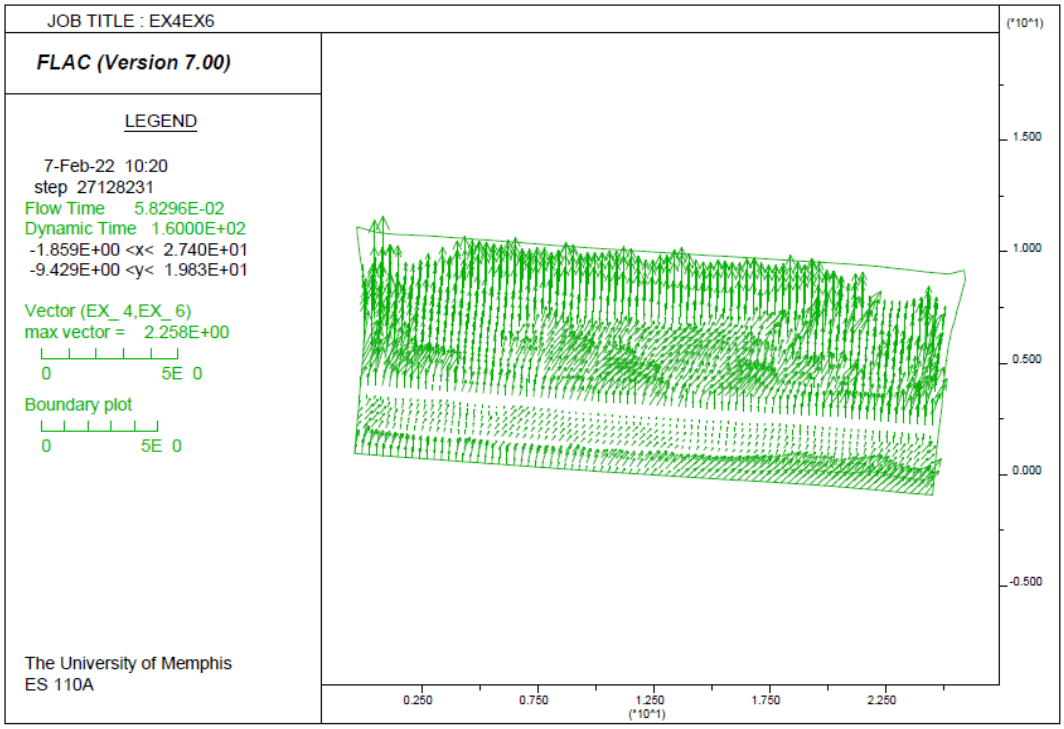

Figure 4.76. Displacement vector maps of soil particles of the critical zone due to dynamic loading of 2010.

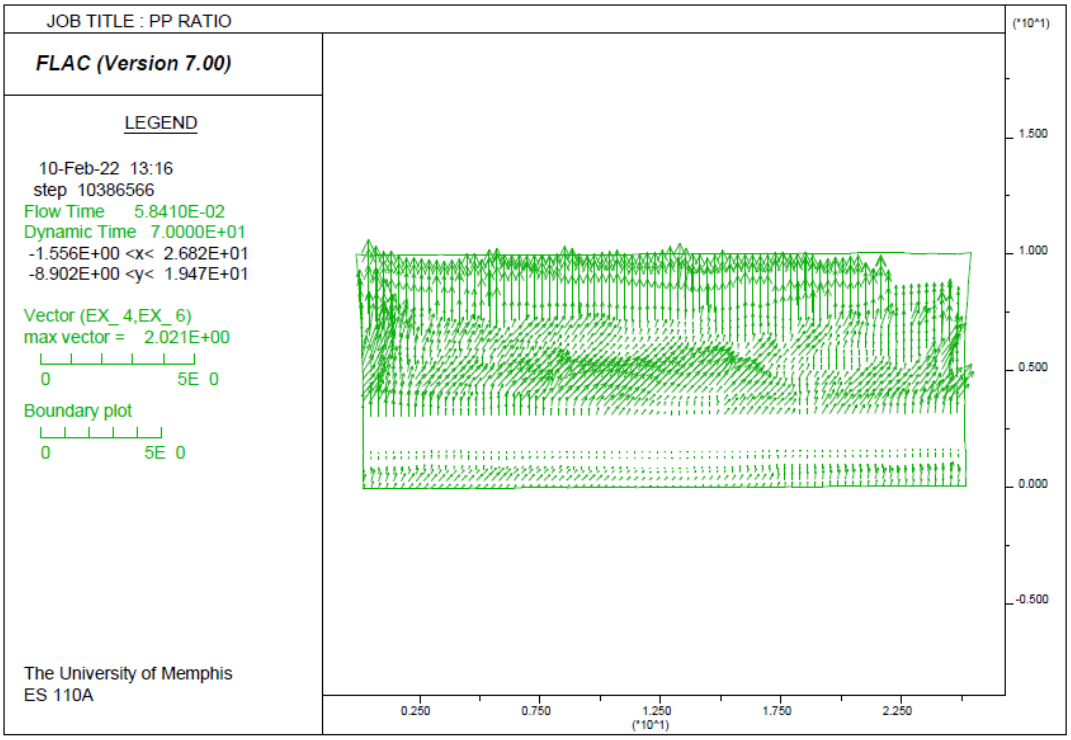

Figure 4.77. Displacement vector maps of soil particles of the critical zone due to dynamic loading of 2010.

On the other hand, pore pressure ratio contour maps of the new NN1 model, shown in Figures 4.78 and 4.79 for both the 2010 and 2011 earthquakes, show a ratio of one or higher in the liquefiable soil layers, which supports the occurrence of liquefaction in those layers.

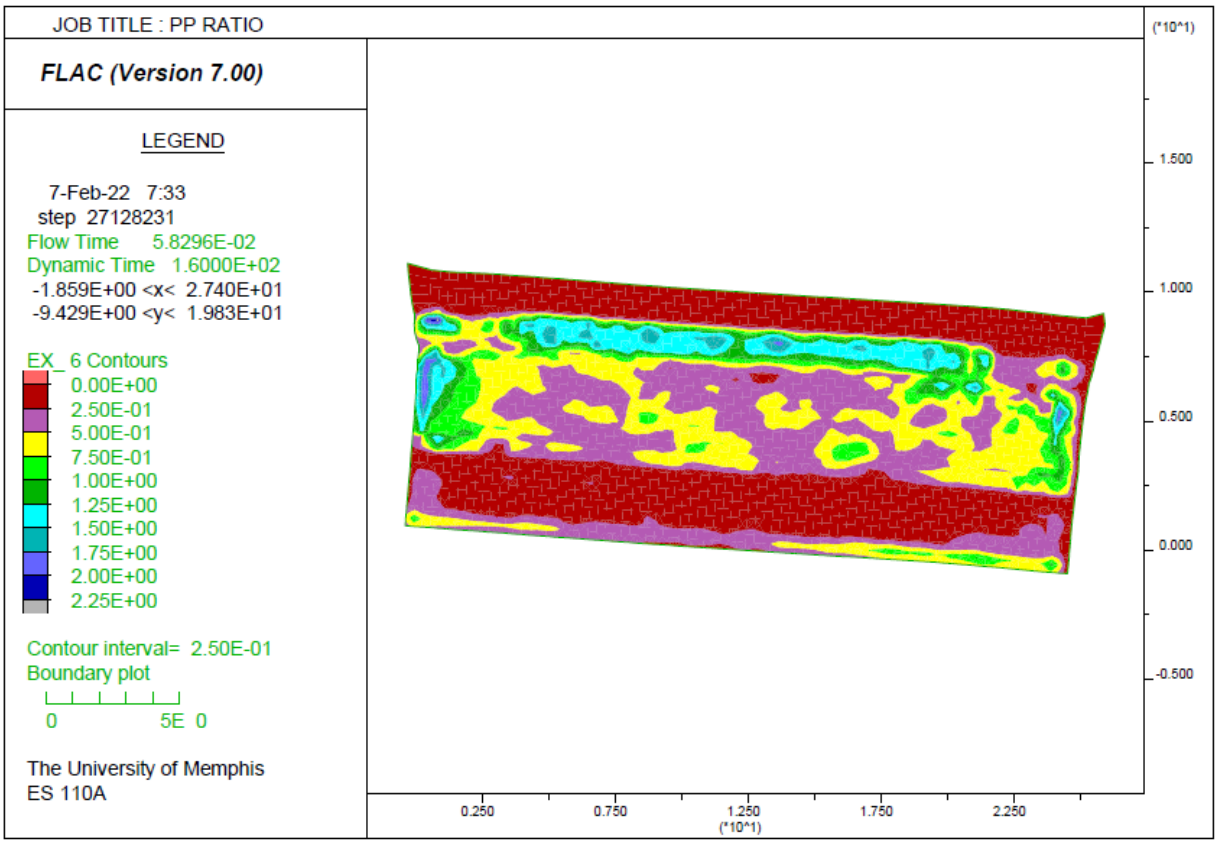

Figure 4.78. Pore pressure ratio contour maps of 2010.

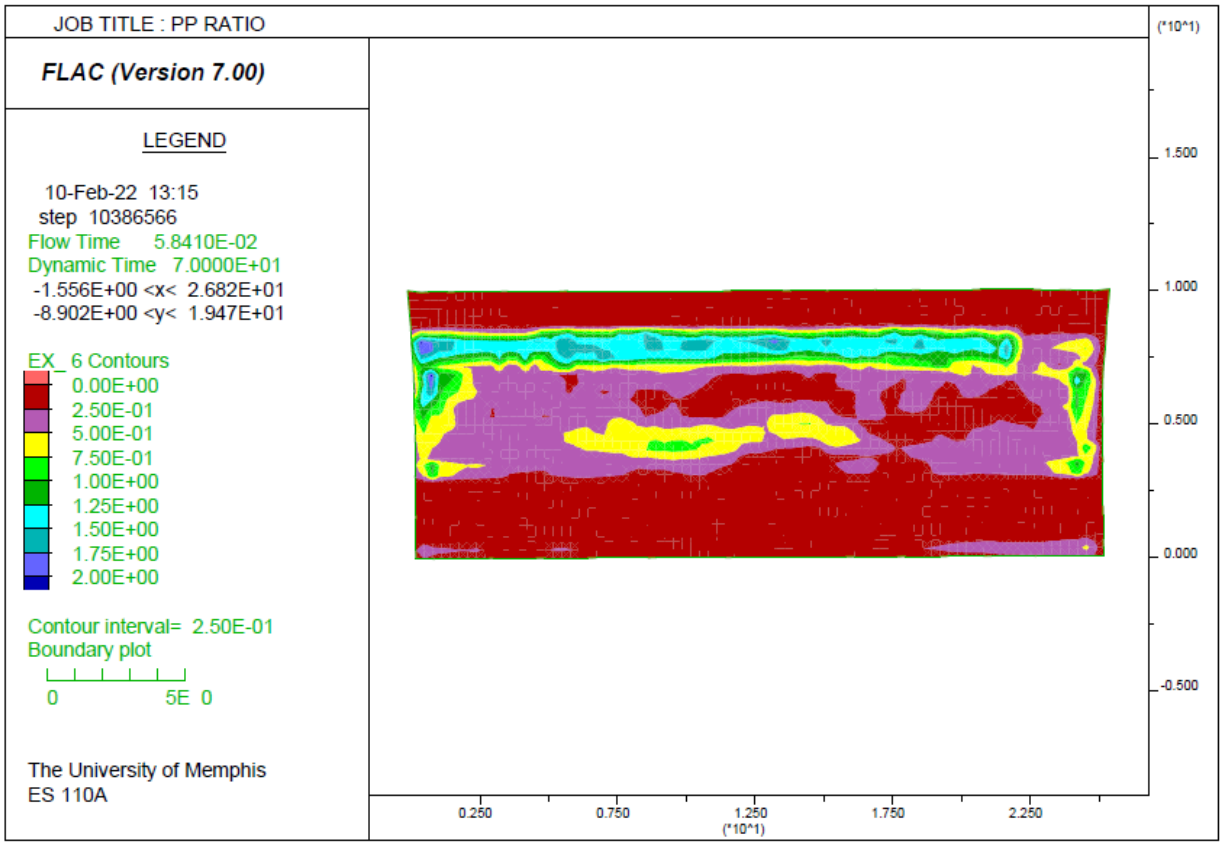

Figure 4.79. Pore pressure ratio contour maps of 2011.

4.4.4. Summary

By looking at the results that were provided in this section, it can be concluded that the thickness of different soil layers plays an important role in the occurrence of liquefaction surface manifestation in a soil profile. Increasing or decreasing the thickness of the upper non-liquefiable soil layers in different soil profiles can stop the occurrence of liquefaction at the ground surface or cause the occurrence of liquefaction at the ground surface. As shown in this section, by increasing the thickness of the upper non-liquefiable in the YY1 and YY2 models (which displayed liquefaction at the ground surface during earthquakes 2010 and 2011 in New Zealand), no liquefaction was observed at the ground surface in the numerical analysis. Furthermore, by decreasing the thickness of the upper non-liquefiable layer in the NN1 model (which did not

display liquefaction at the ground surface during earthquakes in 2010 and 2011 in New Zealand), liquefaction surface manifestation occurred.

4.5. Sensitivity Analysis of Liquefaction Surface Manifestation to the Shear Strength of Upper Non-liquefiable Soil Layers

The second sensitivity analysis that was done as part of this research is shear strength sensitivity analysis. Section 3.5.2 provided the methodology used in this study. By keeping the same thickness of soil layers as in the original New Zealand soil profiles but changing the shear strength of the non-liquefiable layers, one can evaluate the sensitivity of liquefaction surface manifestation potential to the shear strength of the upper non-liquefiable soil crust. The results of the shear strength sensitivity analysis for each soil profile are provided in the following sections.

4.5.1. YY1

The original soil profile of the YY1 model shown in Figure 4.80 consists of a 1.8m unsaturated non-liquefiable layer underlain by two liquefiable soil layers (critical zone) with a total thickness of 4.2m. This model showed liquefaction at the ground surface in both the 2010 and 2011 CES because the developed shear stress in the critical zone was higher than the shear strength of the upper non-liquefiable crust. In the new analysis, the shear strength of the non-liquefiable layer was increased, and a new dynamic analysis was conducted under both the 2010 and 2011 earthquakes. Table 4.14 summarizes the shear strength and stress of the original model as well as the obtained shear strength and stress of the new analysis (shear stresses are computed only for liquefiable layers) Additionally, Figures 4.81 and 4.82 show the displacement vector maps of the YY1 soil profile for the 2010 and 2011 earthquakes, respectively.

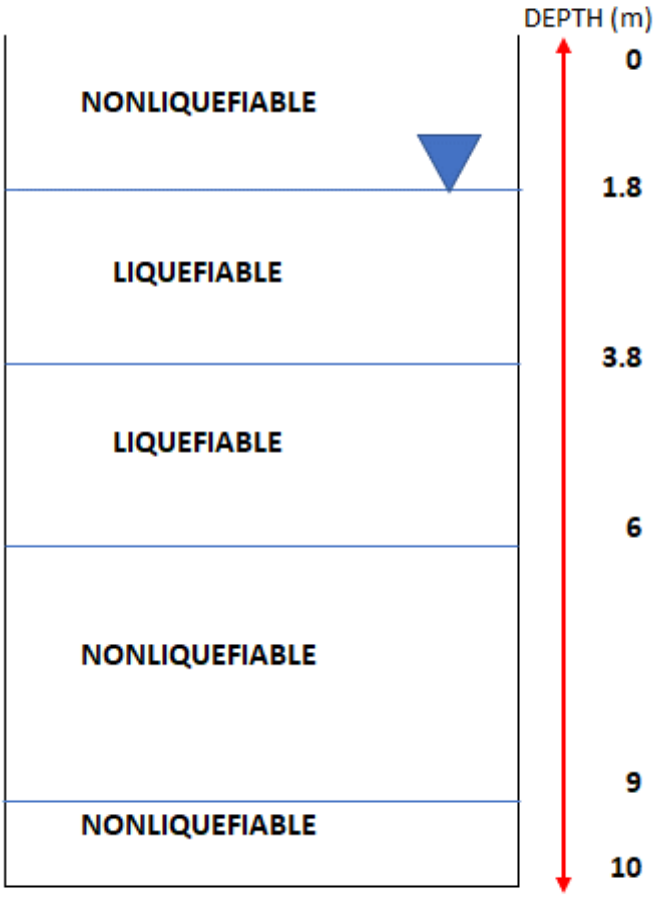

Figure 4.80. Schematic YY1 soil profile to perform shear strength sensitivity analysis.

Table 4.14. Shear stress/strength of YY1 model (green numbers are shear strength and red numbers are shear stress).

Layer Essence	Thickness	Original Shear strength or Shear stress	New Shear strength or Shear stress
NL	1.8	134.63	196
L	2	50 172	50 172
L	2.2	50 172	50 172
NL	3	166	166
NL	1	205	205
		Liquefaction surface manifestation	NO Liquefaction surface manifestation

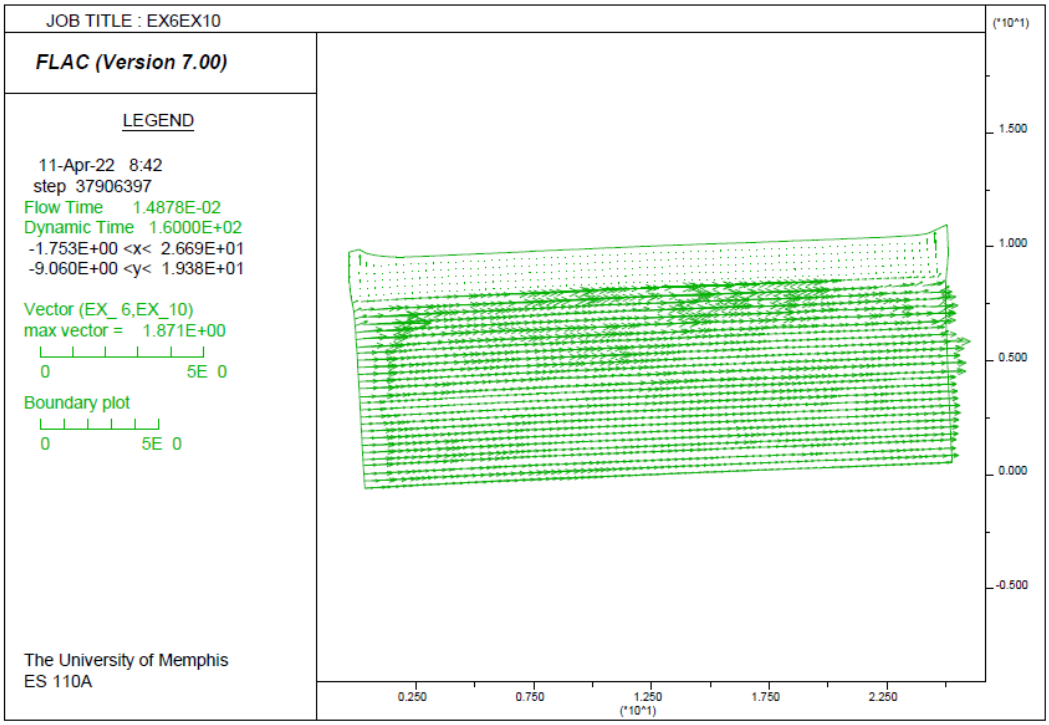

Figure 4.81. Displacement vector maps of soil particles of the critical zone due to dynamic loading of 2010 in the shear strength sensitivity analysis.

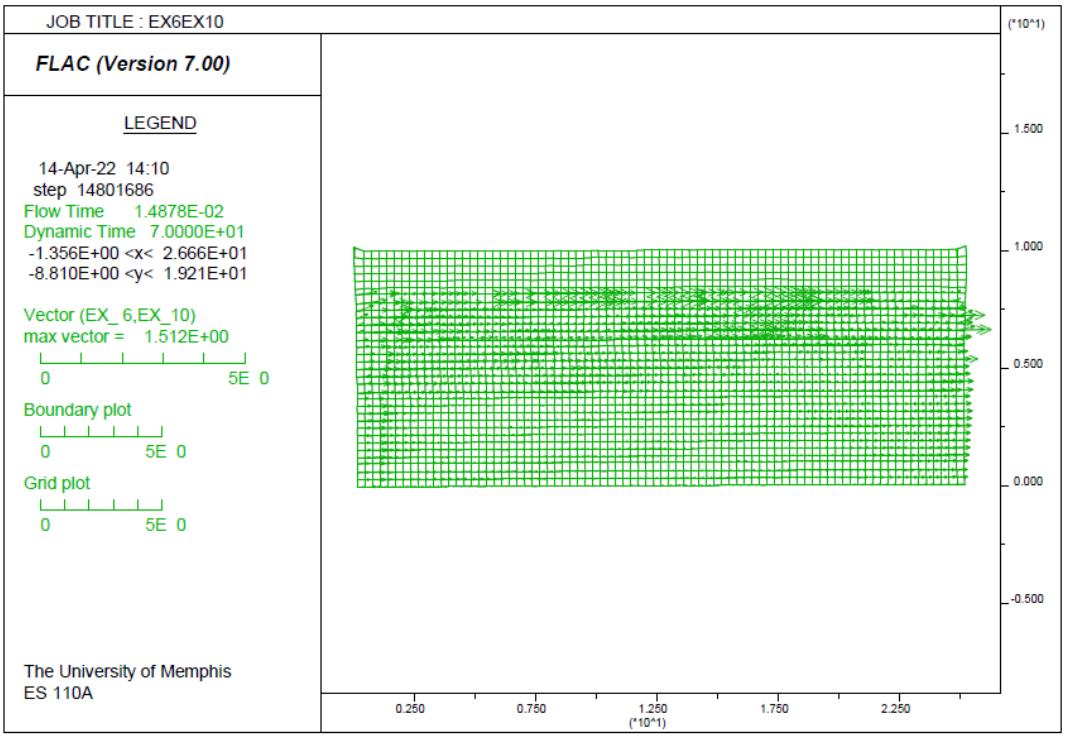

Figure 4.82. Displacement vector maps of soil particles of the critical zone due to dynamic loading of 2011 in the shear strength sensitivity analysis.

By increasing the shear strength of the upper non-liquefiable layer from 134 kPa to 196 kPa, and even though the thickness of the upper layer is less than that of the underlying liquefiable soil layers, the liquefied soil particles are not able to move to the ground surface. The occurrence of liquefaction in the critical zone for the 2010 and 2011 earthquakes can be observed in the pore pressure ratio contour maps (Figures 4.83 and 4.84), which show a pore pressure ratio of one or higher in the critical zone.

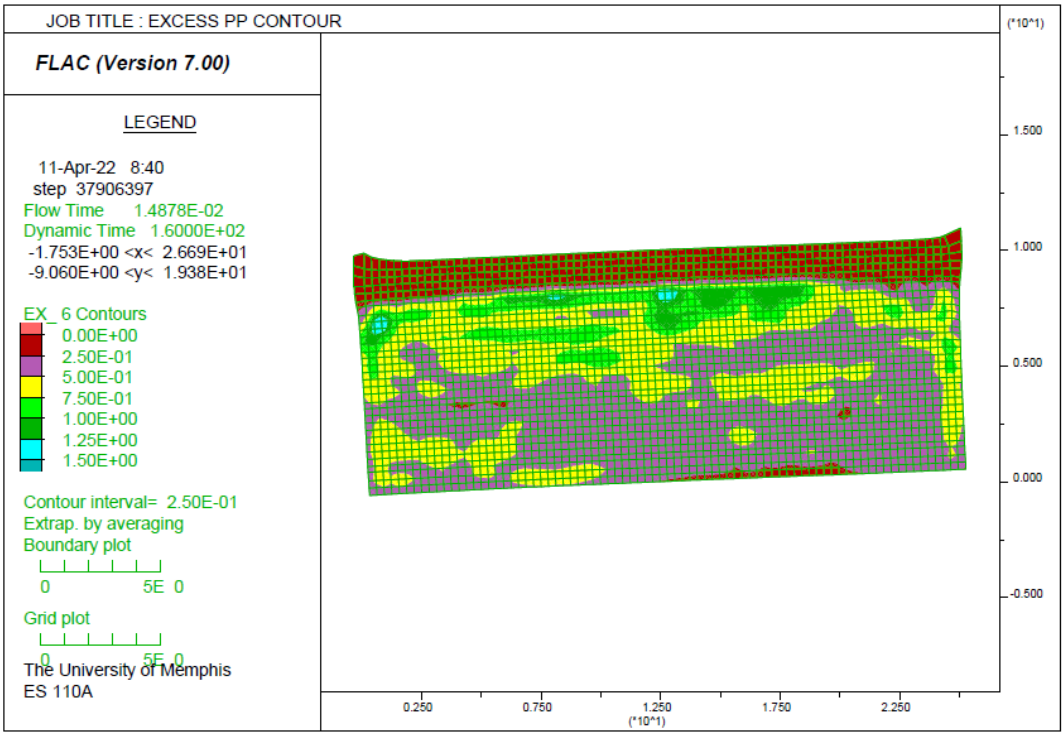

Figure 4.83. Pore pressure ratio contour maps of 2010.

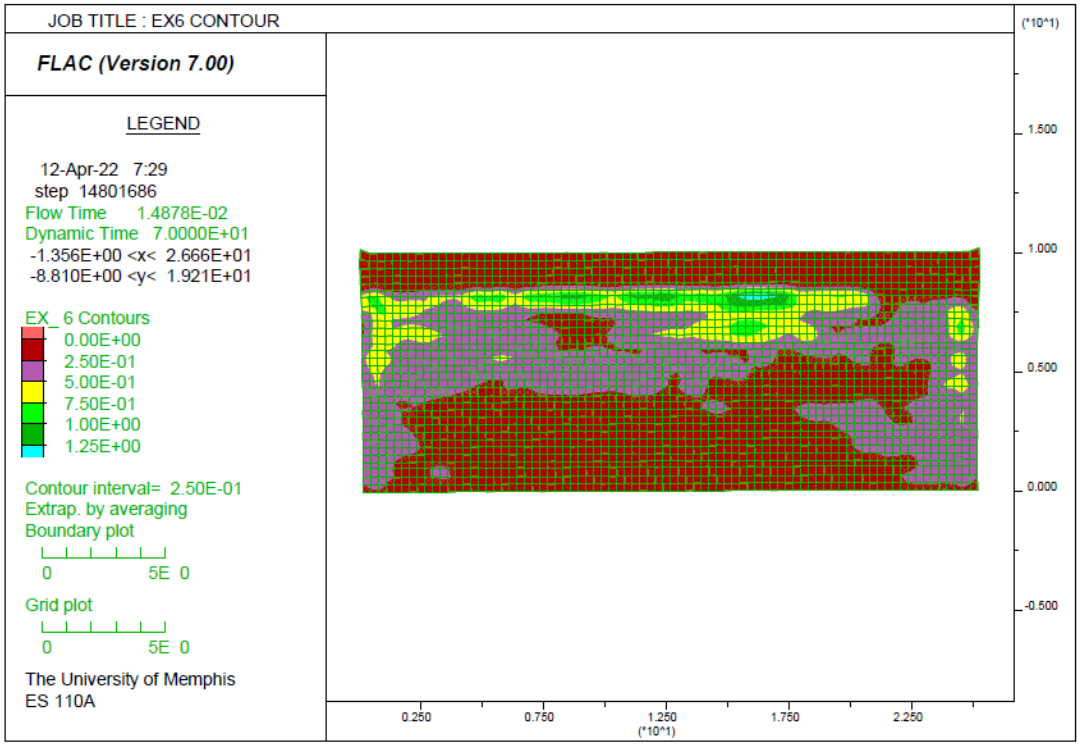

Figure 4.84. Pore pressure ratio contour maps of 2011.

4.5.2. YY2

For the YY2 model, the shear strength of the very top non-liquefiable layer was increased to evaluate the impact of shear strength on liquefaction surface manifestation potential. Figure 4.85 shows the formation of the YY2 soil profile.

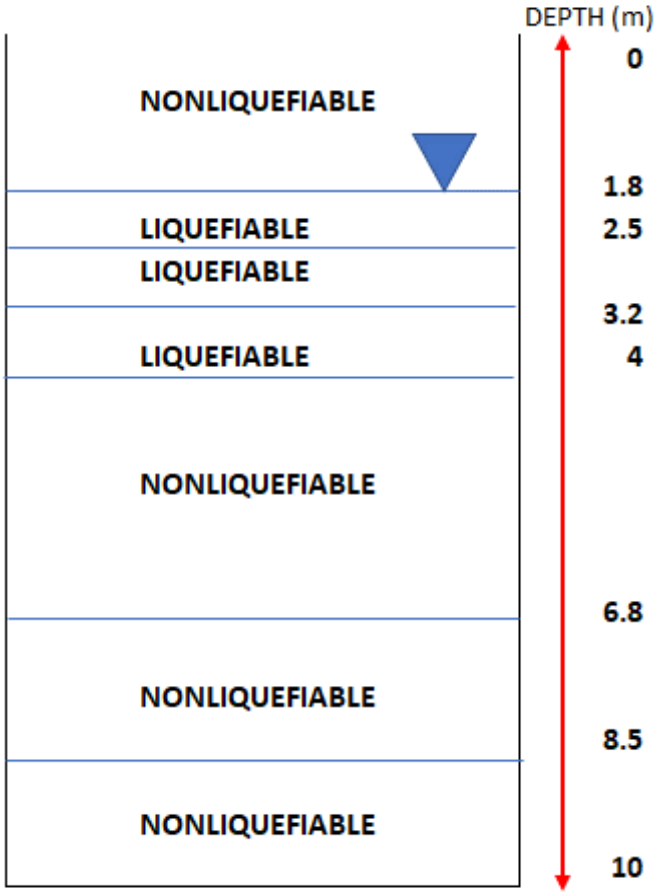

Figure 4.85. Schematic YY2 soil profile to perform shear strength sensitivity analysis.

Table 4.15 provides the shear strength or stress for the original as well as the new YY2 profile for both the 2010 and 2011 earthquakes (shear stresses are computed only for liquefiable layers). Increasing the shear strength of the non-liquefiable layer from 134 kPa to 196 kPa can stop the liquefaction surface manifestation as seen based on the displacement vectors not extending to the ground surface either the 2010 or 2011 earthquakes in Figures 4.86 and 4.87, respectively.

Table 4.15. Shear stress/strength of YY2 model (green numbers are shear strength and red numbers are shear stress).

Layer Essence	Thickness	Original Shear strength/Shear stress	New Shear strength/Shear stress
NL	1.8	98.00	196.00
L	0.7	55 122	55 122
L	0.7	65 122	65 122
L	0.8	80 122	80 98
NL	2.8	158.65	158.65
NL	1.7	179.90	179.90
NL	1.5	203.30	203.30
		Liquefaction surface manifestation	NO Liquefaction surface manifestation

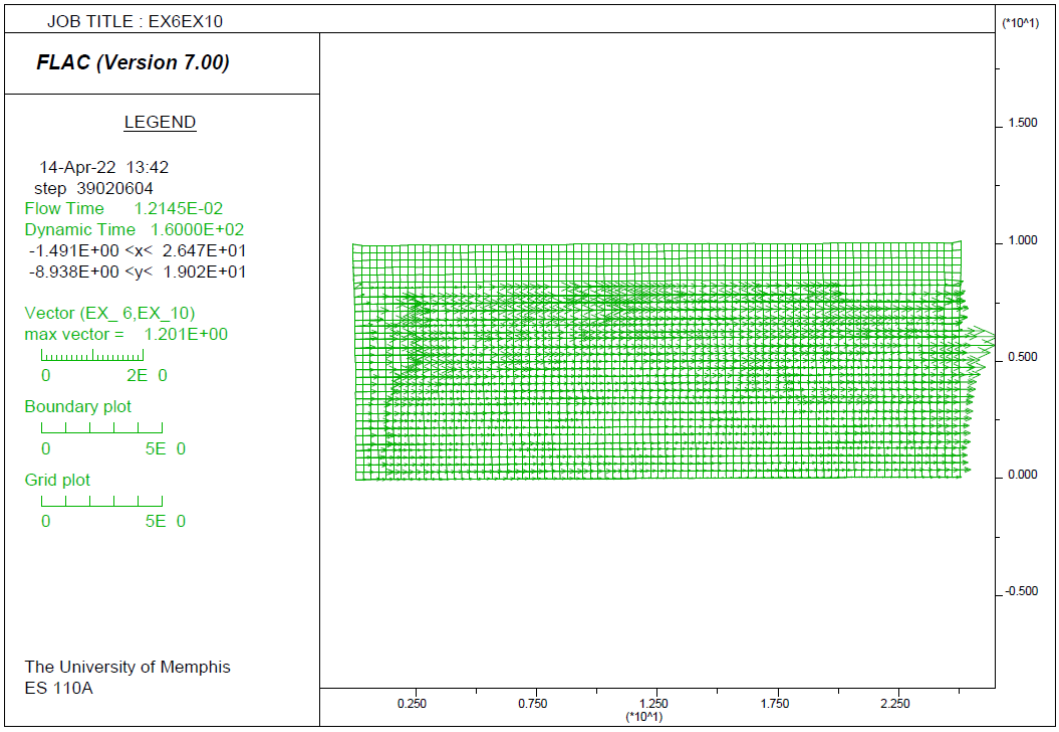

Figure 4.86. Displacement vector map of soil particles of the critical zone due to dynamic loading of 2010 in shear strength sensitivity analysis.

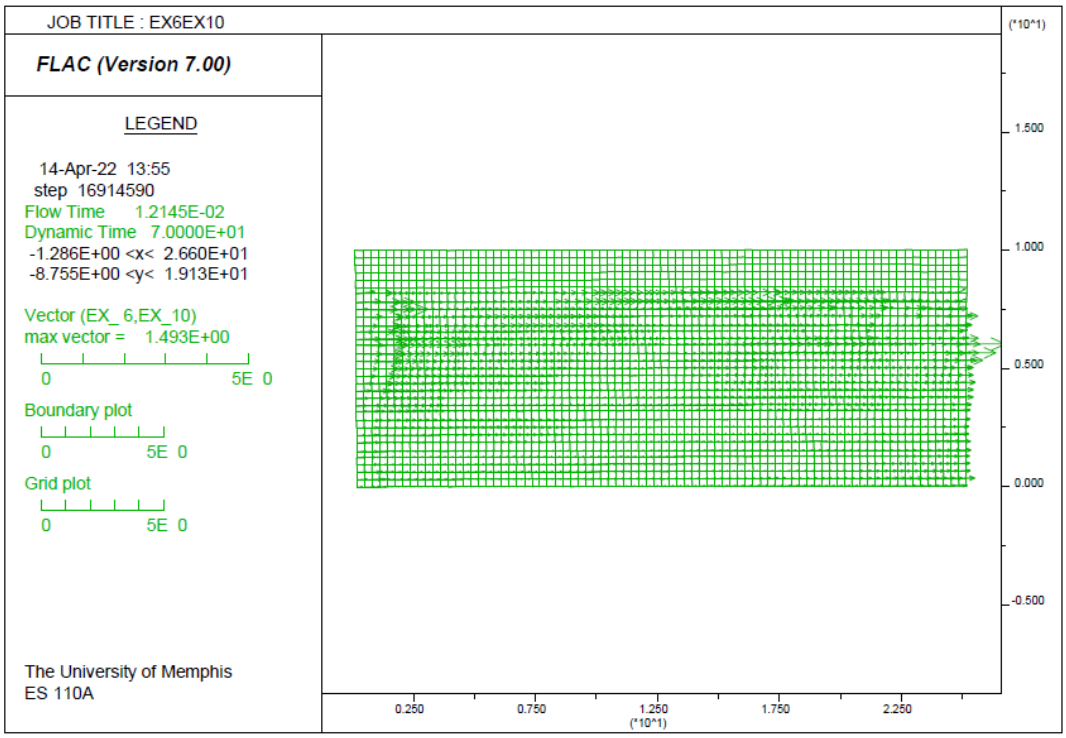

Figure 4.87. Displacement vector map of soil particles of the critical zone due to dynamic loading of 2011 in shear strength sensitivity analysis.

The liquefaction occurrence in the liquefiable soil layers is obvious in Figures 4.88 and 4.89, which indicate pore pressure ratios of less than 1 in the upper layer of the YY2 model in 2010 and 2011 earthquakes, respectively.

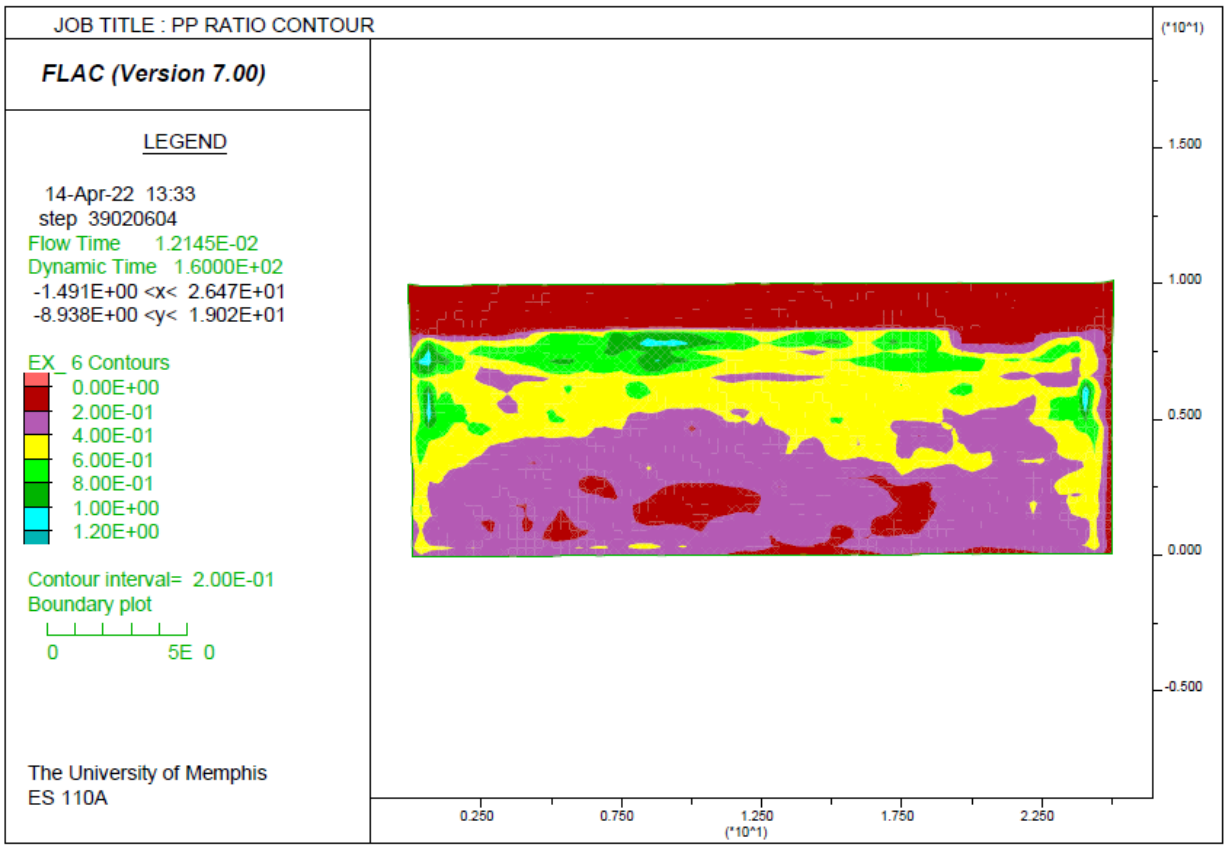

Figure 4.88. Pore pressure ratio contour map of 2010.

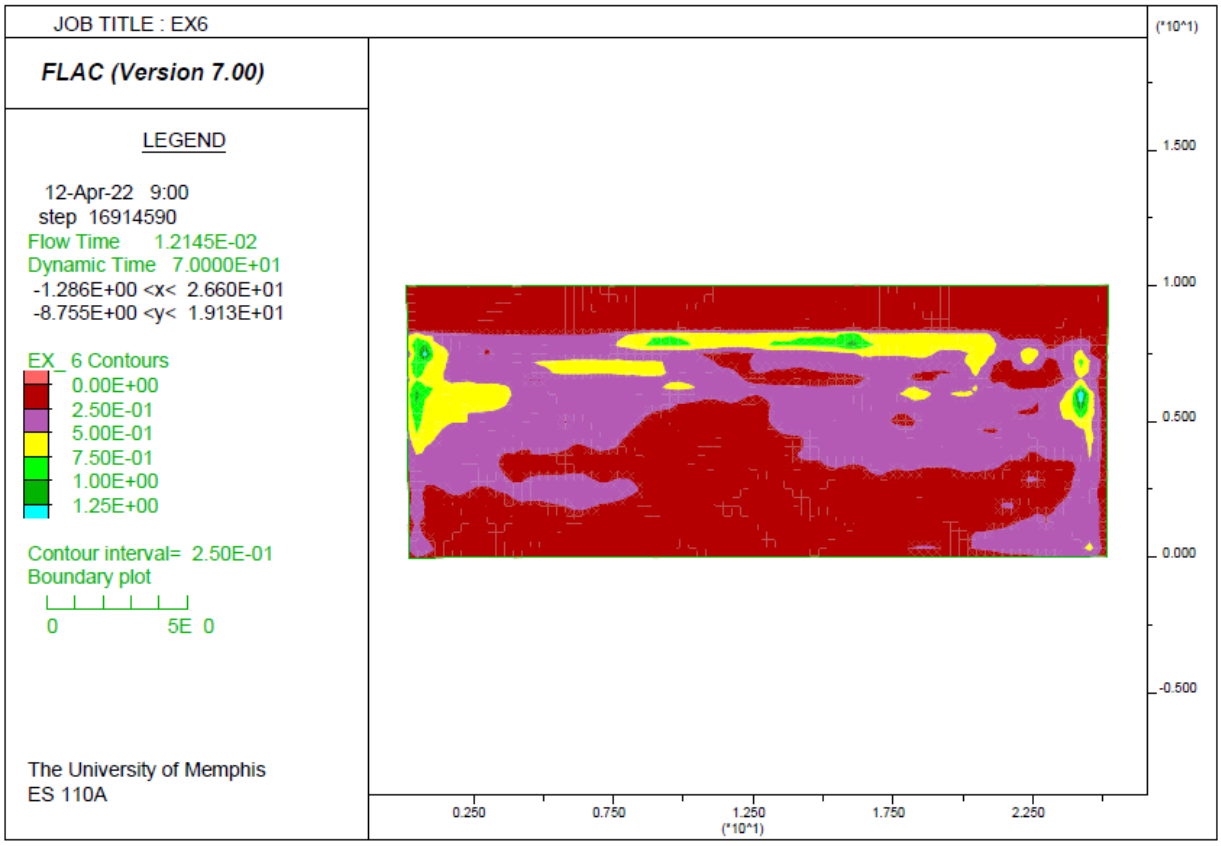

Figure 4.89. Pore pressure ratio contour map of 2011.

4.5.3. NN1

The original NN1 model did not show any liquefaction surface manifestation during the 2010 and 2011 earthquakes of New Zealand. However, the obtained results from analyzing the sensitivity of NN1 to shear strength prove that this model is also sensitive to the shear strength of the upper non-liquefiable crust. As shown in Figure 4.90, the soil layers of the NN1 soil profile are the same thickness as in the original NN1 soil profile, but the shear strength of the upper non-liquefiable soil layers was decreased from 132.84 kPa to 98 kPa as shown in Table 4.16 (shear stresses are computed only for liquefiable layers).

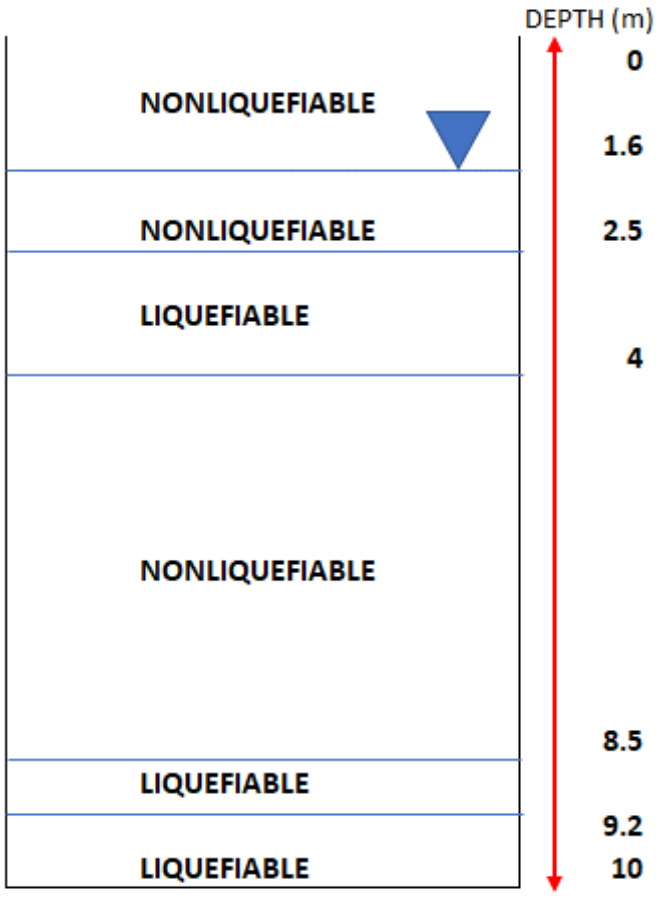

Figure 4.90. Schematic NN1 soil profile to perform shear strength sensitivity analysis.

Table 4.16. Shear stress/strength of NN1 model (green numbers are shear strength and red numbers are shear stress).

Layer Essence	Thickness	Original Shear strength/Shear stress	New Shear strength/Shear stress
NL	1.6	132.84	98.00
NL	0.9	147.58	98.00
L	1.5	50 49.00	50 147
NL	4.5	178.54	178.54
L	0.7	60 96.78	60 96.78
L	0.8	50 71.74	50 71.74
		NO Liquefaction surface manifestation	Liquefaction surface manifestation

The displacement vector maps of the NN1 model after the dynamic analysis show that, by decreasing the shear strength in the upper non-liquefiable soil layers, the liquefied soils in the liquefiable soil layers can penetrate through the non-liquefiable crust and show evidence of liquefaction at the ground surface. Figures 4.91 and 4.92 show displacement vectors extending to the ground surface in the NN1 profile for the earthquakes of 2010 and 2011, respectively.

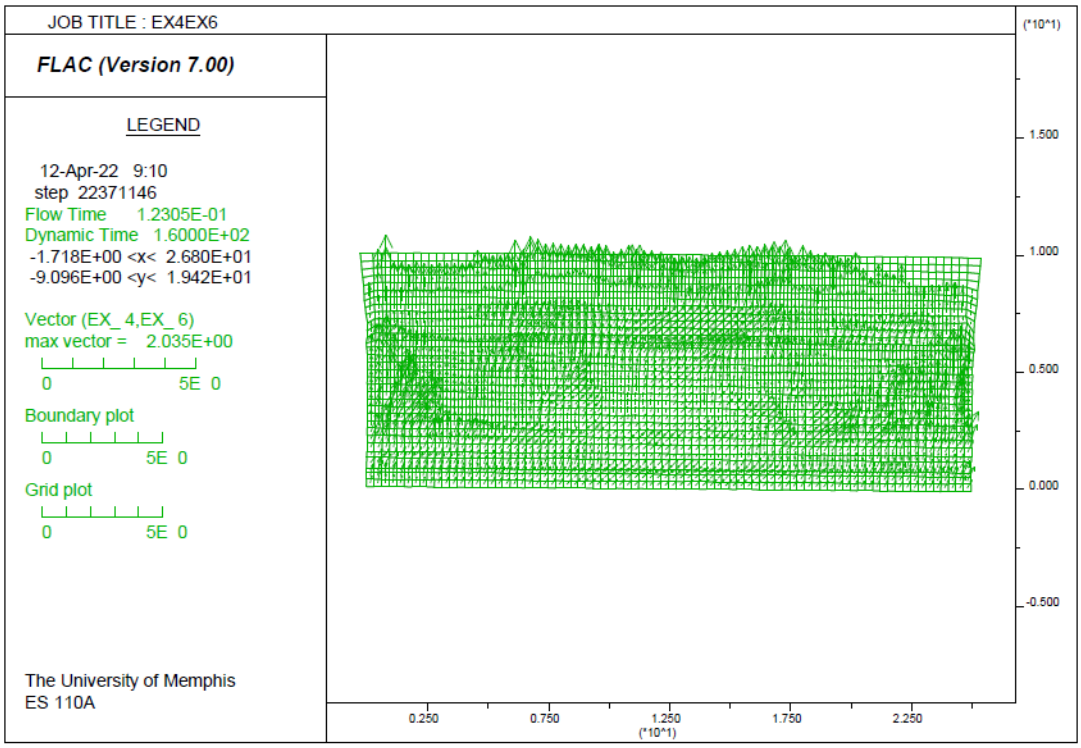

Figure 4.91. Displacement vector map of soil particles of the critical zone due to dynamic loading of 2010 in shear strength sensitivity analysis.

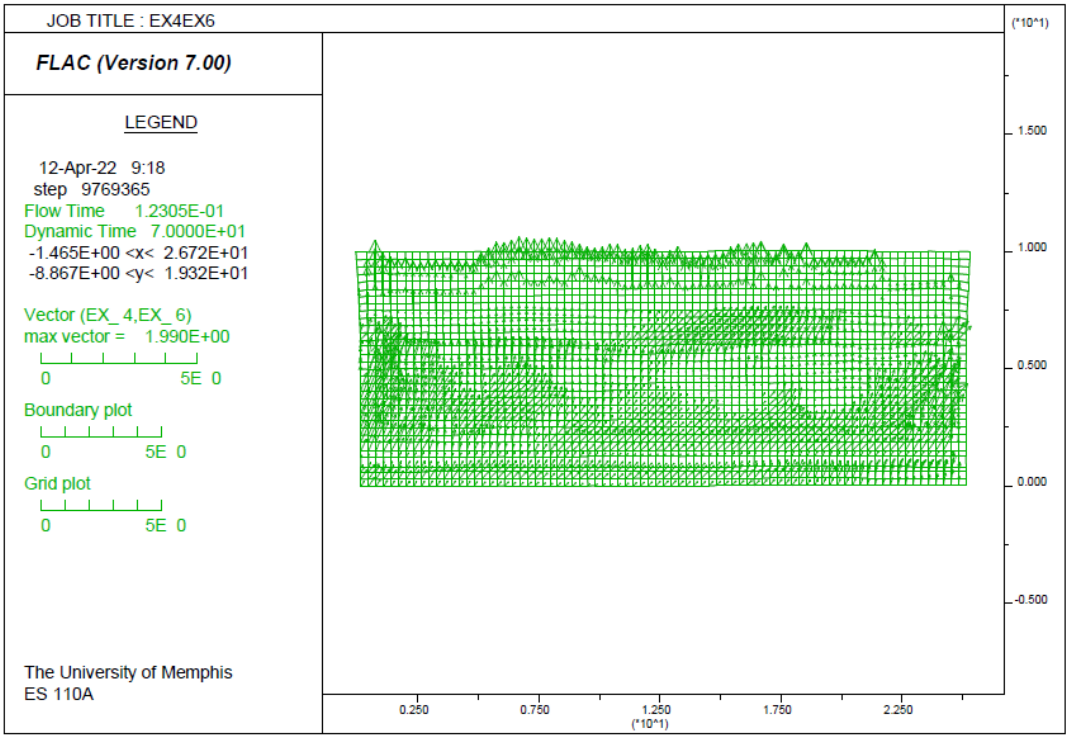

Figure 4.92. Displacement vector map of soil particles of the critical zone due to dynamic loading of 2011 in shear strength sensitivity analysis.

To confirm the occurrence of liquefaction in the liquefiable soil layers, the pore pressure ratio contour maps of NN1 were developed after the dynamic analysis of the 2010 and 2011 earthquake sequences. Figures 4.93 and 4.94 confirm liquefaction in the liquefiable soil layers where the pore pressure ratio is one or higher.

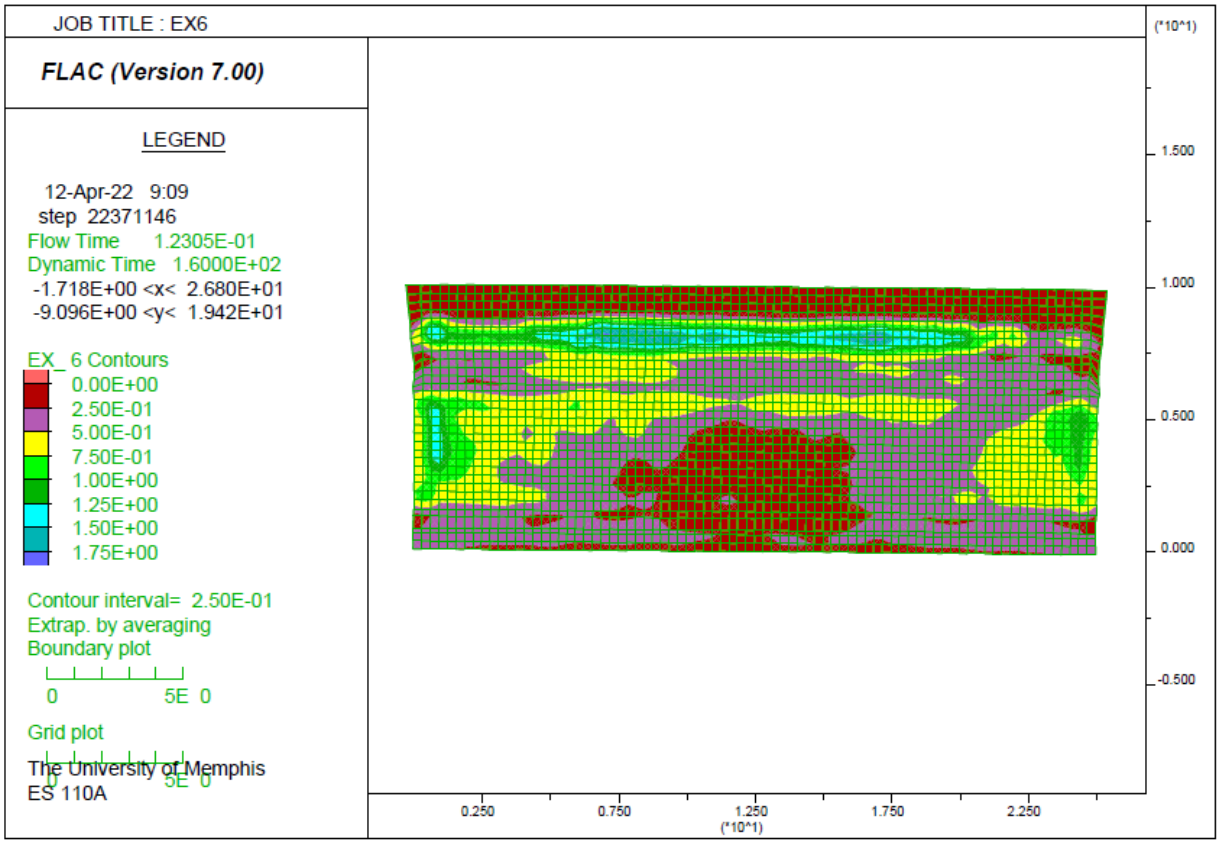

Figure 4.93. Pore pressure ratio contour map of 2010.

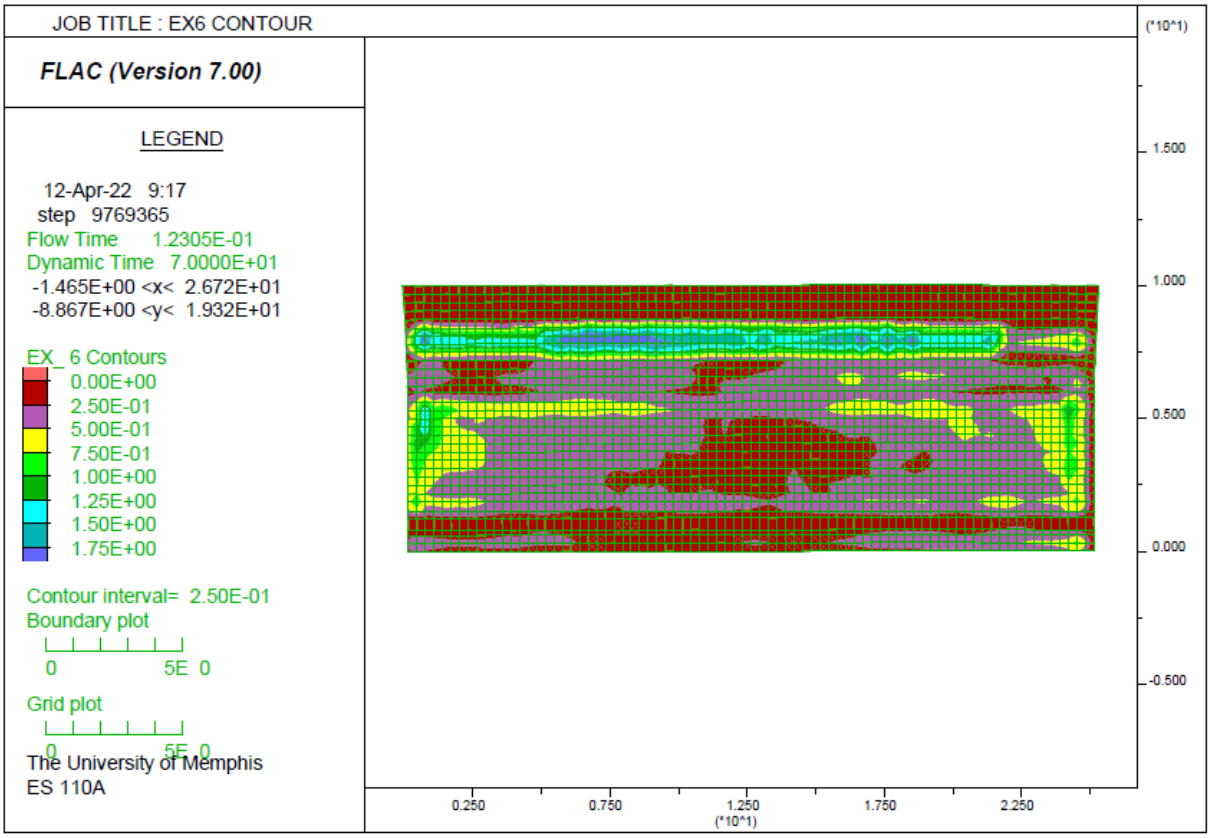

Figure 4.94. Pore pressure ratio contour map of 2011.

4.5.4. Summary of Shear Strength Sensitivity Analysis

In summary, Section 4.5 reveals that the shear strength of the upper non-liquefiable soil layer has a significant impact on the occurrence of liquefaction surface manifestation. In Section 4.5 it was observed that an increase in the shear strength of the upper non-liquefiable soil layer can stop the occurrence of liquefaction surface manifestation. Additionally, sensitivity analysis of the NN1 soil profile to changes in shear strength proved that, by decreasing the shear strength of the upper non-liquefiable soil layer, the liquefied soils in underlying liquefiable soil profiles can break through the upper non-liquefiable soil layers and liquefaction surface manifestation occurs.

4.6. Shear Strength and Thickness Correlation

To adjust the LPI_{ISH} method by considering the impact of shear strength and thickness of upper non-liquefiable layers based on the results presented in this chapter, a relationship between shear strength, thickness, and liquefaction surface manifestation occurrence had to be found.

According to the series of analyses that were conducted and described in Chapter 3 on New Zealand soil profiles of YY1, YY2, NN1, and a partial analysis on NN2, it was found that in all models and for all earthquake scenarios liquefaction surface manifestation occurrence is very sensitive to the thickness and shear strength of the upper non-liquefiable soil layers.

By an engineering analysis of Figure 4.95 it can be concluded that if the upper non-liquefiable layer is more than 1.5 m thicker than the underlying liquefiable layers, liquefaction does not occur. Also, for the models in which the thickness of the upper non-liquefiable layer is less than 1.5 m thicker than the underlying liquefiable layer, Figure 4.95 shows the occurrence of liquefaction. There are two points that do not obey the above rule. Those two points belong to the NN2 soil profile which had 11 soil layers in 10 meters which was excluded from the sensitivity analyses and rest of the numerical analysis of this study.

Based on the correlation methodology (Chapter 3) and according to the provided results in this chapter, correlations between shear strength, thickness, and liquefaction surface manifestation were found. The correlation analyses were conducted between three variables of shear strength, thickness, and liquefaction occurrence. First, the correlation was investigated between each two of the three variables and finally a multi-correlation analysis was done on all three parameters in which the soil layer thickness and shear strength are defined as independent variables and liquefaction was defined as the dependent variable.

The results of the two-variable correlation analysis is provided in Table 4.17 As provided in Table, the correlation between the occurrence of liquefaction and thickness of the upper non-liquefiable soil layer is 0.8 (80%) and the correlation between the occurrence of liquefaction and shear strength of the upper non-liquefiable layer is 0.75 (75%).

Table 4.17. Correlation coefficient between each two variables.

	x=Soil layer thickness	y=Shear strength	z=Liquefaction
x=Soil layer thickness	**1**		
y=shear strength	**0.7**	**1**	
z=Liquefaction	**0.8**	**0.75**	**1**

The result of the multi-variable correlation analysis on three parameters using Equation 3.41 and the results in Table 4.17 shows a correlation of 0.843 (84.3%) between the soil layer thickness and shear strength (independent variables) and liquefaction (dependent variable).

Although in this study it was tried to come up with a new procedure in which the impact of thickness and shear strength of upper non-liquefiable soil layer be considered simultaneously, it was concluded that more cases studies are required for a stronger statistical and engineering analyses to develop a new procedure of liquefaction evaluation.

4.7. Summary of Chapter

Chapter 4 provided the results of a liquefaction hazard analysis of West Tennessee followed by the results of a numerical analysis of the Wildlife CA and New Zealand soil profiles. Continuing in this chapter, the results of the sensitivity analysis of thickness and shear strength were provided followed by a correlation analysis of shear strength and soil layer thickness.

As a part of the HUD project, liquefaction hazard maps were developed for all five counties of Lake, Dyer, Lauderdale, Tipton, and Madison. For all five counties of the HUD project, it was observed that the LPI method predicts significantly higher liquefaction probability than the LPI_{ISH} method. Two primary reasons that the LPI-based LPC predicts a higher probability of liquefaction surface manifestation than the LPI_{ISH}-based LPC are proposed herein. First, the LPI_{ISH} method includes the impact of non-liquefiable layers on liquefaction surface manifestation by incorporating a limiting non-liquefiable layer thickness whereby surficial manifestation is not expected to puncture through the non-liquefiable layer regardless of the thickness of the underlying liquefiable layer while LPI does not consider the impact of non-liquefiable soil layers. Second, LPI_{ISH} incorporates a power-law depth weighting function that provides for shallower liquefiable layers to contribute more to surficial manifestation than deeper layers.

Additionally, Chapter 4 provided and discussed the results of numerical liquefaction analysis including analysis of the Wildlife, California, and New Zealand sites, and sensitivity analysis of the models to the thickness and shear strength of the upper surficial non-liquefiable layers. From the analysis of the Wildlife site, the liquefaction occurrence in the soil layers was captured based on the distribution of excess pore-pressure ratio. Also, by comparing the obtained excess pore pressure from the dynamic analysis of the Wildlife site with the actual measurements

of excess pore pressure from installed piezometers at the Wildlife site during the Superstition earthquake, it was revealed that the numerical analysis provided reliable results.

The developed numerical model of this study was also utilized to investigate the liquefaction surface manifestation occurrence for four soil profiles from New Zealand. The results showed that the numerical analysis agreed with actual site observations in all four models. Furthermore, the LPI and LPI_{ISH} were calculated for the four soil profiles, and it was observed that the LPI- and LPI_{ISH}-based liquefaction predictions are not consistent with site observations. Both the LPI and LPI_{ISH} approaches showed some significant over/under predictions.

Soil layer thickness sensitivity analysis showed that the thickness of different soil layers plays an important role in the occurrence or non-occurrence of liquefaction surface manifestation in a soil profile. Increasing or decreasing the thickness of the upper non-liquefiable soil layers in different soil profiles can stop the occurrence of liquefaction at the ground surface or cause the occurrence of liquefaction at the ground surface. The results of the shear strength sensitivity analysis revealed that the shear strength of the upper non-liquefiable soil layer has a significant impact on the occurrence of liquefaction surface manifestation. It was observed that an increase in the shear strength of the upper non-liquefiable soil layer in those soil profiles that showed liquefaction at the ground surface, can stop the occurrence of liquefaction surface manifestation.

CHAPTER 5. CONCLUSIONS AND FUTURE WORK

5.1. Conclusion

An investigation of the impact of shear strength and thickness of non-liquefiable soil layers on the surface manifestation of liquefaction based on finite difference numerical methods and to investigate the liquefaction potential of the West Tennessee area was performed by (1) analyzing the liquefaction potential of Lake, Dyer, Lauderdale, and Tipton Counties, which are in West Tennessee and within or near the New Madrid Seismic Zone, based on the liquefaction potential indices of LPI and LPI_{ISH} methods; (2) developing a numerical model to perform liquefaction analysis; (3) validating the developed numerical model in FLAC based on the evaluation of New Zealand data and observations; (4) performing sensitivity analyses of the overall FLAC model to the shear strength and thickness of the non-liquefiable soil layers; (5) analyzing statistical correlation of shear strength, thickness and liquefaction surface manifestation occurrence.

A comparison of the LPI- and LPI_{ISH}-based LPCs for $P[LPI\text{-}LPI_{ISH}>5]$, which provides the probability that liquefaction surface manifestation can occur based on the threshold of 5, revealed that the probability of liquefaction surface manifestation provided by the LPI_{ISH} method is significantly lower than the probability of liquefaction surface manifestation provided by the LPI-based LPC, especially at higher ratios of PGA/MSF, i.e., more intense earthquake scenarios. The maximum difference between the two LPCs is about 45% for $P[LPI\text{-}LPI_{ISH}>5]$.

The results of the study indicate two primary reasons that the LPI-based LPC predicts a higher probability of liquefaction surface manifestation than the LPI_{ISH}-based LPC. First, the LPI_{ISH} method includes the impact of non-liquefiable layers on liquefaction surface manifestation

by incorporating a limiting non-liquefiable layer thickness whereby surficial manifestation is not expected to puncture through the non-liquefiable layer regardless of the thickness of the underlying liquefiable layer while LPI does not consider the impact of non-liquefiable soil layers. Second, LPI_{ISH} incorporates a power-law depth weighting function that provides for shallower liquefiable layers to contribute more to surficial manifestation than deeper layers. Therefore, because the weighting function between the two methods is based on different statistical methods, the contribution of soil layers to liquefaction surface manifestation is different between LPI and LPI_{ISH} methods.

The study also revealed that the consistency between LPI and LPI_{ISH} values is higher for lower ranges of PGA and decreases as the PGA increases. Therefore, the lower the PGA the better the agreement between the LPI and LPI_{ISH} methods. However, the change in the consistency between PGA values is negligible from PGA of 0.5 to PGA of 1.0. Therefore, at PGA values greater than 0.5, the difference between LPI and LPI_{ISH} methods is most likely the result of the two primary reasons noted above.

As part of a five-year seismic and liquefaction hazard mapping project for five western Tennessee counties of Lake, Dyer, Lauderdale, Tipton, and Madison, both LPI and LPI_{ISH}-based LPCs were utilized to develop liquefaction hazard maps. For all five counties of the HUD project, it was observed that the LPI method predicts significantly higher liquefaction probability than the LPI_{ISH} method. The effect of upper non-liquefiable soil layers on the surface manifestation of liquefiable soil layers is the most notable difference between the LPI and LPI_{ISH} methods. LPI does not consider the impact of non-liquefiable soil layers while LPI_{ISH} considers it. Thus, considering the impact of non-liquefiable layers causes lower liquefaction surface manifestation probability.

Furthermore, in this study, a numerical model was developed in FLAC to conduct dynamic analysis on various soil profiles. The numerical model was verified by testing it on soil profiles that had a history of showing or not showing liquefaction during actual earthquakes. By evaluating the results of numerical dynamic analyses of four sites in New Zealand it was concluded that the results of the numerical model agree with site observations of all four sites. Additionally, for the four sites in New Zealand, the LPI and LPI_{ISH} were computed, and it was concluded that the LPI and LPI_{ISH}-based liquefaction predictions are not consistent with site observations. Both LPI and LPI_{ISH} approaches showed some significant over/under predictions.

In addition to the numerical analysis of the original soil profiles of New Zealand, two sensitivity analyses of liquefaction surface manifestation of models to the thickness and shear strength of upper non-liquefiable layers were done in this study. According to the 18 analyses that were conducted and described in Chapter 3 on New Zealand soil profiles of YY1, YY2, NN1, and a partial analysis on NN2, it was concluded that in all models and for all earthquake scenarios liquefaction surface manifestation occurrence is very sensitive to the thickness and shear strength of upper non-liquefiable soil layers. Thus, there is a strong relationship between shear strength, thickness, and liquefaction surface manifestation.

Although in this study it was tried to come up with a new procedure in which the impact of thickness and shear strength of upper non-liquefiable soil layer be considered simultaneously, it was concluded that more cases studies are required for a stronger statistical and engineering analyses to develop a new procedure of liquefaction evaluation.

5.2.Future Work

This study has attempted to consider the impact of non-liquefiable soil layers on liquefaction surface manifestation in the West Tennessee region by adjusting the LPI_{ISH} method. In future work, by adding more sites to the numerical analysis and performing more sensitivity analyses to the thickness, shear strength, fines content of the soil, and different earthquake parameters, a better adjustment to the LPI_{ISH} method can be made and possibly a new index can be developed to be utilized to evaluate liquefaction surface manifestation globally. Furthermore, this method has the potential to be utilized for site-specific liquefaction analysis since the results of numerical modeling were able to catch liquefaction features in deeper layers such as lateral spread.

REFERENCES

Andrus, R. D., and Stokoe, K. H., II (1997). ‘‘Liquefaction resistance based on shear wave velocity.’’ Proc., NCEER Workshop on Evaluation of Liquefaction Resistance of Soils, Nat. Ctr. for Earthquake Engrg. Res., State Univ. of New York at Buffalo, 89–128.

Arango, I. (1996). ‘‘Magnitude scaling factors for soil liquefaction evaluations.’’ J. Geotech. Engrg., ASCE, 122(11), 929–936.

Christopher BR, Schwartz C. Geotechnical aspects of pavement reference manual, USDOT. *pub no FHWA NHI-05-037, FHA, May, NHI Course no 132040, 888p*. 2006.

Chung J, Rogers D. Deterministic and Probabilistic Assessment of Liquefaction Hazards Using the Liquefaction Potential Index and Liquefaction Reduction Number. *Journal of Geotechnical and Geoenvironmental Engineering*. 2017;143(10):04017073. doi:10.1061/(ASCE)gt.1943-5606.0001772.

Clark, B. (2011). *Groundwater Availability of the Mississippi Embayment*.

Clark, B. R., and Hart, R. M. (2009). *The Mississippi Embayment Regional Aquifer Study (MERAS): Documentation of a groundwater-flow model constructed to assess water availability in the Mississippi embayment*. *The Mississippi Embayment Regional Aquifer Study (MERAS): Documentation of a groundwater-flow model constructed to assess water availability in the Mississippi embayment*, Scientific Investigations Report, USGS Numbered Series, U.S. Geological Survey, Reston, VA.

Cramer, C. H., and Arellano, D. (2015). Updating Liquefaction Probability Curves, Seismic Hazard Model, and Urban Seismic Hazard Maps with Public Outreach for Memphis and Shelby County, Tennessee.” USGS.

Cramer CH., Van Arsdale RB., Harrison V., Arellano D., Tohidi H., and Bhattarai R., 2021, Madison County seismic and liquefaction hazard maps, CERI Report, 90 pp.

Cramer CH., Van Arsdale RB., Harrison V., Arellano D., Tohidi H., Pezeshk S., Senejani M., and Bhattarai R., 2021, Tipton County seismic and liquefaction hazard maps, CERI Report.

Cramer, C. H., Van Arsdale, R. B., Reichenbacher, R., Arellano, D., Tohidi, H., Pezeshk, S., Horton, S. P., Bhattarai, R., Nazemi, N., and Farhadi, A. (2020a). *Dyer County Seismic and Liquefaction Hazard Maps* (Rep.).

Cramer, C. H., Van Arsdale, R. B., Harrison, V., Bouzeid, K., Arellano, D., Tohidi, H., Pezeshk, S., Horton, S. P., Bhattarai, R., Nazemi, N., and Farhadi, A. (2020b). *Lauderdale County Seismic and Liquefaction Hazard Maps* (Rep.).

Cramer, C., Arsdale, R. B. V., Arellano, D., Pezeshk, S., Horton, S. P., Weathers, T., Nazemi, N., Jimenez, J., Tohidi, H., and Ogweno, L. P. (2019). "Seismic and Liquefaction Hazard Maps for Lake County, Northwestern Tennessee."

Cramer, C. H., Dhar, M. S., and Arellano, D. (2018). "Update of the Urban Seismic and Liquefaction Hazard Maps for Memphis and Shelby County, Tennessee: Liquefaction Probability Curves and 2015 Hazard Maps." Seismological Research Letters, 89(2A), 688–701.

Golesorkhi, R. (1989). ''Factors influencing the computational determination of earthquake-induced shear stresses in sandy soils.'' Ph.D. dissertation, University of California at Berkeley.

FLAC: Fast lagrangian analysis of Continua. (2011). Itasca Consulting Group, Minneapolis, Minn.

Franke K, Ulmer K, Ekstrom L, Meneses J. Clarifying the Differences Between Traditional Liquefaction Hazard Maps and Probabilistic Liquefaction Reference Parameter Maps. Soil Dynamics and Earthquake Engineering 2016, 90, 240-249.

Green, R. A., and Bommer, J. J. (2019). "What is the Smallest Earthquake Magnitude that Needs to be Considered in Assessing Liquefaction Hazard?" *Earthquake Spectra*, 35(3), 1441–1464.

Green RA, Cubrinovski M, Cox B, et al. Select Liquefaction Case Histories from the 2010–2011 Canterbury Earthquake Sequence. *Earthquake Spectra*. 2014;30(1):131-153. doi:10.1193/030713eqs066m.

Hosman, R.L., Long, A.T., Lambert, T.W., and others, 1968. Tertiary aquifers in the Mississippi embayment, with discussions of Quality of water by H.G. Jeffery. U.S. Geological Survey Professional Paper 448-D, 29 p.

Idriss, I. M. (1999). An update to the Seed-Idriss simplified procedure for evaluating liquefaction potential, in Proceedings, TRB Workshop on New Approaches to Liquefaction, Publication No. FHWARD- 99-165, Federal Highway Administration, January.

Ishihara, K.,1985. Stability of natural deposits during earthquakes. In: Proceedings of the 11th International Conference on Soil Mechanics and Foundation Engineering. San Francisco, CA, USA,1, pp.321–376.

Iwasaki, T., Tatsuoka, F., Tokida, K. and Yasuda, S. A practical method for assessing soil liquefaction potential based on case studies at various sites in Japan, Second International Conference on Mierozonation for Safer Construction Research and Application 1978.

Iwasaki, T. and Tokida, K. Soil liquefaction potential evaluation with use of the simplified procedure, Proc. International Conference on Recent Advances in Geotechnical L2zrthquake Engineering and Soil Dynamics, 1981.

Iwasaki, T., Tokida, K., Tatsuoka, F., Watanabe, S., Yasuda, S., and Sato, H. (1982). Microzonation for soil liquefaction potential using simplified methods. Proceedings 3rd International Conference on Microzonation, Seattle, USA. 1319-1330.

Iwasaki, T., Arakawa, T., and Tokida, K.-I. (1984). "Simplified procedures for assessing soil liquefaction during earthquakes." International Journal of Soil Dynamics and Earthquake Engineering, 3(1), 49–58.

Liao, S., and Whitman, R. V. (1986a). ''Overburden correction factors for SPT in sand.'' J. Geotech. Engrg., ASCE, 112(3), 373–377.

Liao, S. S. C., and Whitman, R. V. (1986b). ''Catalogue of liquefaction and non-liquefaction occurrences during earthquakes.'' Res. Rep., Dept. of Civ. Engrg., Massachusetts Institute of Technology, Cambridge, Mass.

Lumsden DN, Cox RT, Van Arsdale RB, Cupples WB. Petrology of Pliocene Mississippi River Alluvium: Provenance Implications. *The Journal of Geology*. 2016;124(4):501-517. doi:10.1086/686997.

Maurer, B. W., Green, R. A., and Taylor, O.-D. S. (2015). "Moving towards an improved index for assessing liquefaction hazard: Lessons from historical data." *Soils and Foundations*, 55(4), 778–787.

Maurer BW, Green RA, Cubrinovski M, Bradley BA. Evaluation of the Liquefaction Potential Index for Assessing Liquefaction Hazard in Christchurch, New Zealand. *Journal of Geotechnical and Geoenvironmental Engineering*. 2014;140(7):04014032. doi:10.1061/(ASCE)gt.1943-5606.0001117.

Mayne, P.W., Peuchen, J., 2013. Unit weight trends with con resistance in soft to firm clays. Geotechnical and Geophysical Site Characterization 4. Taylor & Francis Group, London, 903-910.

Moon, S. W., and Ku, T. (2016). "Empirical estimation of soil unit weight and undrained shear strength from shear wave velocity measurements." Geotechnical and Geophysical Site Characterisation 5, Australian Geomechanics Society.

National Academies of Sciences, Engineering, and Medicine. 2016. State of the Art and Practice in the Assessment of Earthquake-Induced Soil Liquefaction and Its Consequences. Washington, DC: The National Academies Press. DOI: 1017226/23474.

(n.d.). Water Resources of the United States-National Water Information System (NWIS) Mapper, <https://maps.waterdata.usgs.gov/> (Feb. 1, 2019).

Odom W, Hofmann F, Van Arsdale R, Granger D. New 26Al/10Be and (U-Th)/He constraints on the age of the Upland Complex, central Mississippi River Valley. *Geomorphology*. 2020;371:107448. doi:10.1016/j.geomorph.2020.107448.

Rittenour TM, Blum MD, Goble RJ. Fluvial evolution of the lower Mississippi River valley during the last 100 k.y. glacial cycle: Response to glaciation and sea-level change. *Geological Society of America Bulletin*. 2007;119(5-6):586-608. doi:10.1130/b25934.1.

Rix, G. J., 2001, Liquefaction Susceptibility Mapping in Memphis/Shelby County, TN, USGS Award No. 01-HQ-AG-0019.

Rix, G. J., and S. Romero-Hudock, 2006, Liquefaction potential mapping in Memphis and Shelby County, Tennessee, unpublished Rept. To the U.S. Geol. Surv., Denver Colorado, 27 pp.

Rhodes A. Liquefaction evaluation in stratified soils. 2017.

Rodbell DT. Subdivision, subsurface stratigraphy, and estimated age of fluvial-terrace deposits in northwestern Tennessee. *US Geologic Survey Bulletin*. 1996. doi:10.3133/b2128.

Saucier RT. Geomorphology and Quaternary Geologic History of the Lower Mississippi Valley: Vicksburg, Mississippi. *US Army Engineer Waterways Experiment Station*. 1994.

Saucier RT. Geomorphological interpretations of late Quaternary terraces in western Tennessee and their regional tectonic implications. *Professional Paper*. 1987. doi:10.3133/pp1336a.

Schrader, T.P., 2008a. Potentiometric surface in the Sparta-Memphis aquifer of the Mississippi embayment, Spring 2007, U.S. Geological Survey Scientific Investigations Map 3014.

Schrader, T.P., 2013, Water levels and water quality in the Sparta-Memphis aquifer (middle Claiborne aquifer) in Arkansas, spring-summer 2009: U.S. Geological Survey Scientific Investigations Report 2013–5100, 53 p., 2 plates, https: //pubs.usgs.gov/sir/2013/5100/.

Seed, H. B., and Idriss, I. M. (1971). ‘‘Simplified procedure for evaluating soil liquefaction potential.’’ J. Geotech. Engrg. Div., ASCE, 97(9), 1249–1273.

Seed, H. B., and Idriss, I. M. (1982). ‘‘Ground motions and soil liquefaction during earthquakes.’’ Earthquake Engineering Research Institute Monograph, Oakland, Calif.

Seed, H. B., Idriss, I. A., and Arango, I. (1985). “Closure to ‘Evaluation of Liquefaction Potential Using Field Performance Data’ by H. Bolton Seed, I. M. Idriss, and Ignacio Arango, (March 1983).” Journal of Geotechnical Engineering, 111(11), 1346–1346.

Seed, H. B., Tokimatsu, K., Harder, L. F., and Chung, R. M. (1985). ‘‘The influence of SPT procedures in soil liquefaction resistance evaluations.’’ J. Geotech. Engrg., ASCE, 111(12), 1425–1445.

Seed, H. B., and Idriss, I. M. (1967). "Analysis of liquefaction: Niigata earthquake." Proc., ASCE, 93(SM3), 83-108.

Seed, H. B., and Idriss, I. M. (1971). "Simplified procedure for evaluating soil liquefaction potential." J. Soil Mechanics and Foundations Div., ASCE **97**(SM9), 1249–273.Seed, H. B., and Idriss, I. M. (1982). Ground Motions and Soil Liquefaction During Earthquakes, Earthquake Engineering Research Institute, Oakland, CA, 134 pp.

Seed, H. B., Tokimatsu, K., Harder, L. F. Jr., and Chung, R. (1984). The influence of SPT procedures in soil liquefaction resistance evaluations. Earthquake Engineering Research Center, University of California, Berkeley, Report No. UCB/EERC-84/15, 50 pp.

Tohidi H, Arellano D, Cramer CH. Initial Liquefaction Hazard Mapping of Northwest Tennessee. *Geo-Extreme 2021*. https://doi.org/10.1061/9780784483695.029.

Toprak, S., and Holzer, T. L. (2003). "Liquefaction potential index: Field assessment." Journal of Geotechnical and Geoenvironmental Engineering, ASCE, 129(4), 315-322.

Tuttle MP. Observations and Comparisons of Liquefaction Features and Related effects induced by the Bhuj Earthquake. *Earthquake Spectra*. 2002:79-100.

Van Arsdale RB, Arellano D, Stevens KC, et al. Geology, Geotechnical Engineering, and Natural Hazards of Memphis, Tennessee, USA. *Environmental & Engineering Geoscience*. 2012;18(2):113-158. doi:10.2113/gseegeosci.18.2.113.

Van Arsdale R, Bresnahan R, McCallister N, Waldron B. Upland Complex of the central Mississippi River valley: Its origin, denudation, and possible role in reactivation of the New Madrid seismic zone. *Continental Intraplate Earthquakes: Science, Hazard, and Policy Issues*. 2007. doi:10.1130/2007.2425(13).

Youd, T. L., Idriss, I. M., Andrus, R. D., Arango, I., Castro, G., Christian, J. T., Dobry, R., Finn, W. D. L., Harder, L. F., Hynes, M. E., Ishihara, K., Koester, J. P., Liao, S. S. C., Marcuson, W. F., Martin, G. R., Mitchell, J. K., Moriwaki, Y., Power, M. S., Robertson, P. K., Seed, R. B., and Stokoe, K. H. (2001). Liquefaction resistance of soils: summary report from the 1996 NCEER and 1998 NCEER/NSF workshops on evaluation of liquefaction resistance of soils, J. Geotechnical, and Geoenvironmental Eng., ASCE 127(10), 817–33.

Youd, T. L., and Noble, S. K., 1997a, Magnitude scaling factors, Proc., NCEER Workshop on Evaluation of Liquefaction Resistance of Soils, Nat. Ctr. for Earthquake Engrg. Res., State Univ. of New York at Buffalo, 149–165.

Youd, T. L., and Noble, S. K., 1997b, Liquefaction criteria based on statistical and probabilistic analyses, Proc., NCEER Workshop on Evaluation of Liquefaction Resistance of Soils, Nat. Ctr. for Earthquake Engrg. Res., State Univ. of New York at Buffalo, 201–215.

Youd, T. L., and Idriss, I. M. (2001). "Liquefaction Resistance of Soils: Summary Report from the 1996 NCEER and 1998 NCEER/NSF Workshops on Evaluation of Liquefaction Resistance of Soils." Journal of Geotechnical and Geoenvironmental Engineering, 127(4), 297–313.

Youd, T. L., Idriss, I. M., Andrus, R. D., Arango, I., Castro, G., Christian, J. T., Dobry, R., Finn, W. D. L., Harder, L. F., Hynes, M. E., Ishihara, K., Koester, J. P., Liao, S. S. C., Marcuson, W. F., Martin, G. R., Mitchell, J. K., Moriwaki, Y., Power, M. S., Robertson, P. K., Seed, R. B., and Stokoe, K. H. (2003). "Closure to 'Liquefaction Resistance of Soils: Summary Report from the 1996 NCEER and 1998 NCEER/NSF Workshops on Evaluation of Liquefaction Resistance of Soils' by T. L. Youd, I. M. Idriss, Ronald D. Andrus, Ignacio Arango, Gonzalo Castro, John T. Christian, Richardo Dobry, W. D. Liam Finn, Leslie F. Harder Jr., Mary Ellen Hynes, Kenji Ishihara, Joseph P. Koester, Sam S. C. Liao, William F. Marcuson III, Geoffrey R. Martin, James K. Mitchell, Yoshiharu Moriwaki, Maurice S. Power, Peter K. Robertson, Raymond B. Seed, and Kenneth H. Stokoe II." Journal of Geotechnical and Geo-environmental Engineering, 129(3), 284–286.

APPENDIX A. MATLAB CODES USED IN THIS STUDY

MATLAB CODE TO GENERATE SPT-BASED LPC

```
clc
close all
clear all


% Moment Magnitude
%M =8;
%Acceleration in g
%pga = 0.5;

%n=5
M_m = [ 5
    5.5
    6
    6.5
    7
    7.5
    8];

% M_m = [
%     6
%     6
% ];
pga_m = [0.1
    0.2
    0.3
    0.4
    0.5
    0.6
    0.7
    0.8
    0.9
    1.0];


% pga_m = [
%     0.3
%     0.3
%     ];

kk_c=1;
```

```
for ii_c=1:size(M_m,1)

    for jj_c=1:size(pga_m,1)

        % Moment Magnitude
        M = M_m(ii_c,1);
        %Acceleration in g
        pga = pga_m(jj_c,1);


%MSF= 0.94
amax_over_g = pga;

%Assumed GW depth in ft

D_gw = load ('Qal_dtw.txt');


%Pa in lbf/ft^2
Pa= 2088; % (100 kPa)

FC= load('Qal_USCS.txt');

Depth = load ('Depth.txt');
N = load ('Qal_N.txt');

N;

%Number of wells
well= length(N(:,1));

%For Unit weight (Bowels, 1977)
%condition N= N60 (no correction values Cr, Cs, Ce, Cb)

N60=N;

for j= 1:well
     for k = 1:length (Depth)

%for cohesive soils
         if  FC(j,k)>=50 & N60(j,k) <= 4
             Unit_wt (j,k) =110;
         elseif  FC(j,k)>=50 &N60(j,k) > 4 && N60(j,k) <=8
             Unit_wt (j,k) =120;
         elseif  FC(j,k)>=50 &N60(j,k) > 8 && N60(j,k) <=32
             Unit_wt (j,k) =130;
         elseif  FC(j,k)>=50 &N60(j,k) > 32
             Unit_wt (j,k) =140;
```

```
%for granular soils

         elseif N60(j,k) <= 4
             Unit_wt (j,k) =85;
         elseif N60(j,k) > 4 && N60(j,k) <=10
              Unit_wt (j,k) = 102.5;
         elseif N60(j,k)>10 && N60(j,k) <=30
            Unit_wt (j,k) = 120;
         elseif N60(j,k) > 30 && N60(j,k) <= 50
            Unit_wt (j,k) = 125;
         elseif N60(j,k)>50;
            Unit_wt(j,k)= 140;
         end
     end
end
Unit_wt;


% total Pressure (con_press)

 for i= 1: length (Depth)
    for k = 1:well
        %con_press (k,1) = (Depth (2,1)-Depth (1,1))* Unit_wt (k,1);
            if Depth(1,i) < D_gw(k,1) && Depth(2,i) <= D_gw(k,1)
                con_press (k,i) = (Depth (2,i)-Depth(1,i)).* Unit_wt(k,i);% +
con_press(k, i-1);

            elseif Depth(1,i) <= D_gw(k,1) && Depth(2,i) > D_gw(k,1)
                con_press (k,i)= ((D_gw(k,1) -Depth(1,i))*Unit_wt(k,i))+
((Depth (2,i)-D_gw(k,1))*Unit_wt(k,i));%+ con_press(k,i-1);

           elseif Depth(1,i) > D_gw(k,1) && Depth(2,i) > D_gw(k,1)
                con_press (k,i)= (Depth (2,i)-Depth(1,i)).* Unit_wt(k,i);%+
con_press (k,i-1);
            end

% % % Effective  Pressure  (eff_con_press)
       % eff_con_press(k,1) = con_press(k,1);
%
           if Depth(1,i) < D_gw(k,1) && Depth(2,i) <= D_gw(k,1)
                eff_con_press(k,i) = con_press(k,i);
           elseif Depth(1,i) <= D_gw(k,1) && Depth(2,i) > D_gw(k,1)
                eff_con_press (k,i)= ((D_gw(k,1) -Depth(1,i))*Unit_wt(k,i))+
((Depth (2,i)-D_gw(k,1))*(Unit_wt(k,i)-62.4));%+ eff_con_press(k,i-1);
           elseif Depth(1,i) > D_gw(k,1) && Depth(2,i) > D_gw(k,1)
               eff_con_press (k,i)= (Depth (2,i)-Depth(1,i)).* (Unit_wt(k,i)-
62.4);%+ eff_con_press(k,i-1);
```

```
                %eff_con_press (k,i)= ((Depth (2,i)-Depth(1,i)).*
Unit_wt(k,i))-((Depth (2,i)- D_gw(k,1)).*62.4);%+ eff_con_press(k,i-1);
            end

    end
 end

% cummulative total pressure
for k = 1:well

    cum_con_press(k,1 ) = con_press (k,1);
    cum_eff_con_press(k,1 ) = eff_con_press (k,1);
    for i= 2: length (Depth)

         cum_con_press(k,i ) = con_press (k, i) + cum_con_press (k, i-1);
         cum_eff_con_press(k,i ) = eff_con_press (k, i) + cum_eff_con_press
(k, i-1);

    end
end


% %try
%
% % Effective  Pressure  (eff_con_press)
%Effective Stress = Total stress - pore pressure


% %eff_con_press(k,1) = con_press(k,1);
% %
%            if Depth(1,i) < D_gw && Depth(2,i) <= D_gw
%                 eff_con_press(k,i) = con_press(k,i);
%            elseif Depth(1,i) <= D_gw && Depth(2,i) > D_gw
%                 eff_con_press (k,i)= con_press(k,i)-  (Depth(2,i)-
D_gw).*62.4;
%
%
%            elseif Depth(1,i) > D_gw && Depth(2,i) > D_gw
%                 eff_con_press (k,i)= con_press (k,i) -((Depth (2,i)-
D_gw).*62.4);
%
%
%
%            end
%     end
%  end
```

```
 con_press;
 eff_con_press;

 %rd value

% for k = 1:well
%     for j= 1: length (Depth)
%         if Depth (1,j)* 0.3048  <= 9.15 ;
%         rd(k,j)= 1.0-0.00765* Depth (1,j)*0.3048;
%         else
%         rd(k,j)= 1.174-0.0267* Depth (1,j)*0.3048;
%         end
%     end
% end
% rd;
for k = 1:well
  for j= 1: length (Depth)
alphaz(1,j)=-1.012-1.125*sin((Depth(1,j)/11.7)+5.133);
betaz(1,j)=0.106+0.118*sin((Depth(1,j)/11.3)+5.142);
rd(k,j)=exp(alphaz(1,j)+(betaz(1,j)*M));
  end
end
rd;
%Cyclic Stress Ration CSR

for j= 1: length (Depth)
    for k = 1:well
        CSR (k,j) =
0.65*(amax_over_g).*(cum_con_press(k,j)./cum_eff_con_press(k,j)).*rd (k,j);

 %Correction for effective overburden stress, Cn

        Cn(k,j) = (Pa./cum_eff_con_press(k,j)).^0.5;
        Cn(Cn>1.7)= 1.7;

 % Corrected Penetration Resistance for overburden effect N1
       N1(k,j)= round(N(k,j).*Cn(k,j));

%The resulting N1 values were then further corrected for energy, equipment,
and procedural effects to fully standardized N160 values
%N160 = N1*CR*CS*CB*CE.
%Since we do not have all parameters

      N160 (k,j) = N1(k,j);

    end
```

```
 end
CSR;
Cn;
N160;

%Fine Correction
%Assumed fine content percent for GW,GP,SW, SP = 0
%Assumed fine content percent for GM,GCGC-GM, SC, SM, SC-SM = 12
%Assumed fine content percent for  GW-GM, GW-GC, GP-GM, GP-GC, SW-SM, SW-SC,
SP-SM, SP-SC= 5
%Assumed fine content percent for  ML,CL,OL,MH,CH,OH,CL-ML, PT = 50

for j= 1: length (Depth)
    for k = 1:well
        if FC(k,j) <= 5
            alpha(k,j) = 0;
            beta (k,j) = 1;
        elseif FC(k,j) >5 && FC(k,j)< 35
            alpha(k,j) = exp(1.76-(190./FC(k,j).^2));
            beta(k,j) = (0.99+((FC(k,j).^1.5)/1000));
        elseif FC(k,j) >= 35
            alpha(k,j) = 5;
            beta (k,j)= 1.2;
        end
    end
end
alpha;
beta;

for j= 1: length (Depth)
    for k = 1:well
        N160_cs(k,j) = round(alpha(k,j) + beta(k,j).*N160(k,j));
        N160_cs(N160_cs>30)=30;

%Cyclic Resistance Ratio

        CRR7_5(k,j)= 1./(34- N160_cs(k,j))+ N160_cs(k,j)./135 +
50./((10.*N160_cs(k,j)+45).^2)-1/200;

% Magnitude Scaling Factor
       if M<5.2
           MSF=1.82;
       elseif M>5.2
           MSF = 6.9*exp(-M/4)-0.06;
       end


%Factor of Safty FS
```

```
        FS(k,j)= (CRR7_5(k,j)./CSR(k,j) ).*MSF;

    end
end
MSF;
N160_cs;
CRR7_5;

%Making FS>1 for the layers with fine contnets 50 or higher %
for j=1:length (Depth);
    for k = 1: well
        if FC(k,j)>=50
            FS(k,j)=1;

        end
    end
end



%Making FS>1 for the layer above GW level
    for k = 1: well
        for j=1:max(find(Depth(2,:)<D_gw(k,1))) ;
        FS(k,j)=1;
    end
end

FS;
%for LPI calculation

for j=1:length(Depth)
    for k = 1:well
        if FS(k,j)<0
            F(k,j)=0;
        elseif FS(k,j) <= 1
            F(k,j)  = 1-FS(k,j);
        elseif FS(k,j)> 1
            F(k,j) = 0;
        end

%For weighting factor w

% for j= 1: length(Depth)
%   if Depth (1,j) >20
%        Depth (1,j)=20;
%    end
%  end
```

```
    w(1,j) = 10 - 0.5 * Depth(1,j)*0.3048;
    w(w<0)= 0;

    end
end
Depth;
F;
w;

%For thickness dz

for j= 1: length (Depth);
    %dz(1,1)=Depth (1,2);
    dz (1,j) = Depth(2,j) - Depth (1,j);
end

dz= dz*0.3048;

%LPI element in each layer

for j= 1: length(Depth)
    for k = 1:well

    LPI_layer(k,j) = F(k,j)*w(1,j)*dz(1,j);
    end
end

%LPI elememt of each layer of a well
LPI_layer= LPI_layer;


%LPI of a well
LPI = sum(LPI_layer,2);

LPI_layer;
LPI

%probability of exceeding LPI greater than n
n=15;
LPI_gr_n = numel(LPI(LPI>n))/numel(LPI);
seismic_demand= pga/MSF;

fprintf('%s%2.2f%s%2.2f%s%2.4f%s%2.4f\n','Magnitude: ',M,' PGA:', pga, '
PGA/MSF: ', seismic_demand,' LPI:', LPI_gr_n )
%fprintf('%s%2.2f%s%2.2f%s%2.4f%s%2.4f\n','Magnitude: ',M,' PGA:', pga, '
PGA/MSF: ', seismic_demand,' LPI:', LPI_gr_n )
```

```
        final_results(kk_c,1) = seismic_demand
        final_results(kk_c,2) =LPI_gr_n

    kk_c  = kk_c +1;

    end




end

scatter (final_results(:,1),  final_results(:,2))

%plot ((sort(final_results(:,2))), (sort(final_results(:,1))))


% binranges= 0:33;
% [bincounts,ind] = histc(LPI,binranges);
% bar(binranges,bincounts,'histc')
% xlabel ('Liquefaction Potential Index', 'fontsize',14)
% ylabel('Frequency', 'fontsize',14)
%
% for ii = 1:34
%     text(ii-0.8,bincounts(ii)+0.7,num2str((bincounts(ii))))
% end
%
%
```

MATLAB CODE TO GENERATE V_s-BASED LPC

```
clc
close all
clear all


% Moment Magnitude
%M =8;
%Acceleration in g
%pga = 0.5;

%n=5
M_m = [ 5
    5.5
```

```
    6
    6.5
    7
    7.5
    8];

% M_m = [
%     6
%     6
% ];
pga_m = [0.1
    0.2
    0.3
    0.4
    0.5
    0.6
    0.7
    0.8
    0.9
    1.0];



% pga_m = [
%     0.3
%     0.3
%     ];

kk_c=1;

for ii_c=1:size(M_m,1)

    for jj_c=1:size(pga_m,1)

        % Moment Magnitude
        M = M_m(ii_c,1);
        %Acceleration in g
        pga = pga_m(jj_c,1);


%MSF= 0.94
amax_over_g = pga;

%Assumed GW depth in ft

D_gw = load ('Qal_dtw.txt');
```

```
%Pa in lbf/ft^2
Pa= 2088; % (100 kPa)

FC= load('Qal_USCS.txt');

Depth = load ('Depth.txt');
N = load ('Qal_N.txt');
vs = load ('Qal_vs.txt');
N;
vs;
%Number of wells
well= length(N(:,1));

%For Unit weight (Bowels, 1977)
%condition N= N60 (no correction values Cr, Cs, Ce, Cb)

N60=N;

for j= 1:well
     for k = 1:length (Depth)

%for cohesive soils
         if  FC(j,k)>=50 & N60(j,k) <= 4
             Unit_wt (j,k) =110;
         elseif  FC(j,k)>=50 &N60(j,k) > 4 && N60(j,k) <=8
             Unit_wt (j,k) =120;
         elseif  FC(j,k)>=50 &N60(j,k) > 8 && N60(j,k) <=32
             Unit_wt (j,k) =130;
         elseif  FC(j,k)>=50 &N60(j,k) > 32
             Unit_wt (j,k) =140;

%for granular soils

         elseif N60(j,k) <= 4
             Unit_wt (j,k) =85;
         elseif N60(j,k) > 4 && N60(j,k) <=10
              Unit_wt (j,k) = 102.5;
         elseif N60(j,k)>10 && N60(j,k) <=30
            Unit_wt (j,k) = 120;
         elseif N60(j,k) > 30 && N60(j,k) <= 50
            Unit_wt (j,k) = 125;
         elseif N60(j,k)>50;
            Unit_wt(j,k)= 140;
         end
     end
end
Unit_wt;
```

```
% total Pressure (con_press)

 for i= 1: length (Depth)
    for k = 1:well
        %con_press (k,1) = (Depth (2,1)-Depth (1,1))* Unit_wt (k,1);
            if Depth(1,i) < D_gw(k,1) && Depth(2,i) <= D_gw(k,1)
                con_press (k,i) = (Depth (2,i)-Depth(1,i)).* Unit_wt(k,i);% +
con_press(k, i-1);

            elseif Depth(1,i) <= D_gw(k,1) && Depth(2,i) > D_gw(k,1)
                con_press (k,i)= ((D_gw(k,1) -Depth(1,i))*Unit_wt(k,i))+
((Depth (2,i)-D_gw(k,1))*Unit_wt(k,i));%+ con_press(k,i-1);

           elseif Depth(1,i) > D_gw(k,1) && Depth(2,i) > D_gw(k,1)
                con_press (k,i)= (Depth (2,i)-Depth(1,i)).* Unit_wt(k,i);%+
con_press (k,i-1);
           end

% % % Effective  Pressure  (eff_con_press)
       % eff_con_press(k,1) = con_press(k,1);
%
           if Depth(1,i) < D_gw(k,1) && Depth(2,i) <= D_gw(k,1)
                eff_con_press(k,i) = con_press(k,i);
           elseif Depth(1,i) <= D_gw(k,1) && Depth(2,i) > D_gw(k,1)
                eff_con_press (k,i)= ((D_gw(k,1) -Depth(1,i))*Unit_wt(k,i))+
((Depth (2,i)-D_gw(k,1))*(Unit_wt(k,i)-62.4));%+ eff_con_press(k,i-1);
           elseif Depth(1,i) > D_gw(k,1) && Depth(2,i) > D_gw(k,1)
               eff_con_press (k,i)= (Depth (2,i)-Depth(1,i)).* (Unit_wt(k,i)-
62.4);%+ eff_con_press(k,i-1);
                 %eff_con_press (k,i)= ((Depth (2,i)-Depth(1,i)).*
Unit_wt(k,i))-((Depth (2,i)- D_gw(k,1)).*62.4);%+ eff_con_press(k,i-1);
           end

    end
 end

% cummulative total pressure
for k = 1:well

    cum_con_press(k,1 ) = con_press (k,1);
    cum_eff_con_press(k,1 ) = eff_con_press (k,1);
    for i= 2: length (Depth)

         cum_con_press(k,i ) = con_press (k, i) + cum_con_press (k, i-1);
         cum_eff_con_press(k,i ) = eff_con_press (k, i) + cum_eff_con_press
(k, i-1);
```

```
    end
end


% %try
%
% % Effective  Pressure  (eff_con_press)
%Effective Stress = Total stress - pore pressure


% %eff_con_press(k,1) = con_press(k,1);
% %
%             if Depth(1,i) < D_gw && Depth(2,i) <= D_gw
%                  eff_con_press(k,i) = con_press(k,i);
%             elseif Depth(1,i) <= D_gw && Depth(2,i) > D_gw
%                  eff_con_press (k,i)= con_press(k,i)-  (Depth(2,i)-
D_gw).*62.4;
%
%
%             elseif Depth(1,i) > D_gw && Depth(2,i) > D_gw
%                  eff_con_press (k,i)= con_press (k,i) -((Depth (2,i)-
D_gw).*62.4);
%
%
%
%             end
%     end
%  end




 con_press;
 eff_con_press;

 %rd value

% for k = 1:well
%     for j= 1: length (Depth)
%         if Depth (1,j)* 0.3048  <= 9.15 ;
%         rd(k,j)= 1.0-0.00765* Depth (1,j)*0.3048;
%         else
%         rd(k,j)= 1.174-0.0267* Depth (1,j)*0.3048;
%         end
%     end
% end
% rd;
for k = 1:well
```

```
  for j= 1: length (Depth)
alphaz(1,j)=-1.012-1.125*sin((Depth(1,j)/11.7)+5.133);
betaz(1,j)=0.106+0.118*sin((Depth(1,j)/11.3)+5.142);
rd(k,j)=exp(alphaz(1,j)+(betaz(1,j)*M));
  end
end
rd;
%Cyclic Stress Ration CSR

for j= 1: length (Depth)
    for k = 1:well
        CSR (k,j) =
0.65*(amax_over_g).*(cum_con_press(k,j)./cum_eff_con_press(k,j)).*rd (k,j);

 %Correction for effective overburden stress, Cn

        Cn(k,j) = (Pa./cum_eff_con_press(k,j)).^0.25;


 % Corrected Penetration Resistance for overburden effect N1
       N1(k,j)= round(N(k,j).*Cn(k,j));

       vs1(k,j)= round(vs(k,j).*Cn(k,j));
       vs1(k,j)=vs1(k,j).*0.3048;
%The resulting N1 values were then further corrected for energy, equipment,
and procedural effects to fully standardized N160 values
%N160 = N1*CR*CS*CB*CE.
%Since we do not have all parameters

      N160 (k,j) = N1(k,j);

    end
 end
CSR;
Cn;
N160;
vs1;
%Fine Correction
%Assumed fine content percent for GW,GP,SW, SP = 0
%Assumed fine content percent for GM,GCGC-GM, SC, SM, SC-SM = 12
%Assumed fine content percent for  GW-GM, GW-GC, GP-GM, GP-GC, SW-SM, SW-SC,
SP-SM, SP-SC= 5
%Assumed fine content percent for  ML,CL,OL,MH,CH,OH,CL-ML, PT = 50

for j= 1: length (Depth)
    for k = 1:well
        if FC(k,j) <= 5
            c(k,j) = 215;
```

```
%             beta (k,j) = 1;
        elseif FC(k,j) >5 && FC(k,j)< 35
            c(k,j) = 215-(0.5.*(FC(k,j)-5));
%             beta(k,j) = (0.99+((FC(k,j).^1.5)/1000));
        elseif FC(k,j) >= 35
            c(k,j) = 200;
%             beta (k,j)= 1.2;
        end
    end
end
c;
% beta;

for j= 1: length (Depth)
    for k = 1:well
        vs1(k,j) = round(vs1(k,j));
        vs1(vs1>210)=210;

%Cyclic Resistance Ratio

        CRR7_5(k,j)=(0.022.*((vs1(k,j)./100)^2))+(2.8.*((1./( c(k,j)-
vs1(k,j)))-(1./c(k,j))));

% Magnitude Scaling Factor
        MSF = 6.9*exp(-M/4)-0.06;

%Factor of Safty FS

        FS(k,j)= (CRR7_5(k,j)./CSR(k,j) ).*MSF;

    end
end
MSF;
% N160_cs;
CRR7_5;

%Making FS>1 for the layers with fine contnets 50 or higher %
for j=1:length (Depth);
    for k = 1: well
        if FC(k,j)>=50
            FS(k,j)=1;
        end
    end
end



%Making FS>1 for the layer above GW level
```

```
    for k = 1: well
        for j=1:max(find(Depth(2,:)<D_gw(k,1))) ;
        FS(k,j)=1;
    end
end

FS;
%for LPI calculation

for j=1:length(Depth)
    for k = 1:well
        if FS(k,j)<0
            F(k,j)=0;
        elseif FS(k,j) <= 1
            F(k,j)  = 1-FS(k,j);
        elseif FS(k,j)> 1
            F(k,j) = 0;
        end

%For weighting factor w

% for j= 1: length(Depth)
%   if Depth (1,j) >20
%        Depth (1,j)=20;
%    end
%  end

    w(1,j) = 10 - 0.5 * Depth(1,j)*0.3048;
    w(w<0)= 0;

    end
end
Depth;
F;
w;

%For thickness dz

for j= 1: length (Depth);
    %dz(1,1)=Depth (1,2);
    dz (1,j) = Depth(2,j) - Depth (1,j);
end

dz= dz*0.3048;

%LPI element in each layer

for j= 1: length(Depth)
```

```
    for k = 1:well

    LPI_layer(k,j) = F(k,j)*w(1,j)*dz(1,j);
    end
end

%LPI elememt of each layer of a well
LPI_layer= LPI_layer;


%LPI of a well
LPI = sum(LPI_layer,2);

LPI_layer;
LPI

%probability of exceeding LPI greater than n
n=15;
LPI_gr_n = numel(LPI(LPI>n))/numel(LPI);
seismic_demand= pga/MSF;

fprintf('%s%2.2f%s%2.2f%s%2.4f%s%2.4f\n','Magnitude: ',M,' PGA:', pga, '
PGA/MSF: ', seismic_demand,' LPI:', LPI_gr_n )
%fprintf('%s%2.2f%s%2.2f%s%2.4f%s%2.4f\n','Magnitude: ',M,' PGA:', pga, '
PGA/MSF: ', seismic_demand,' LPI:', LPI_gr_n )

        final_results(kk_c,1) = seismic_demand
        final_results(kk_c,2) =LPI_gr_n

    kk_c  = kk_c +1;

    end




end

scatter (final_results(:,1),  final_results(:,2))

%plot ((sort(final_results(:,2))), (sort(final_results(:,1))))


% binranges= 0:33;
% [bincounts,ind] = histc(LPI,binranges);
% bar(binranges,bincounts,'histc')
% xlabel ('Liquefaction Potential Index', 'fontsize',14)
```

```
% ylabel('Frequency', 'fontsize',14)
%
% for ii = 1:34
%     text(ii-0.8,bincounts(ii)+0.7,num2str((bincounts(ii))))
% end
%
%
```

APPENDIX B. FLAC CODES USED IN THIS STUDY

```
; Source: <no name>

config gwflow dynamic extra 20

grid 80,32

gen 0.0,0.0 0.0,10.0 25.0,10.0 25.0,0.0 i=1,81 j=1,33

model elastic i=1,80 j=1,32

; Fixed boundary conditions

fix x i=1 j=1,33

fix x i=81 j=1,33

fix x y i=1,81 j=1

gen line 0.0,1.5 25.0,1.5

gen line 0.0,3.2 25.0,3.2

gen line 0.0,6.0 25.0,6.0

gen line 0.0,6.8 25.0,6.8

gen line 0.0,7.5 25.0,7.5

gen line 0.0,8.2 25.0,8.2

group 'User:1.8-0' region 30 30

group 'User:2.5-1.8' region 46 26
```

group 'User:3.2-2.5' region 47 24

group 'User:4-3.2' region 43 21

group 'User:6.8-4' region 42 16

group 'User:8.5-6.8' region 40 8

group 'User:10-8.5' region 43 3

model mohr notnull group 'User:10-8.5'

prop density=1937.5 bulk=3.167E7 shear=1.46169E7 cohesion=116012.5 friction=40.4 dilation=0.0 tension=0.0 notnull group 'User:10-8.5'

model mohr notnull group 'User:8.5-6.8'

prop density=1937.5 bulk=2.85033E7 shear=1.31554E7 cohesion=104412.5 friction=40.6 dilation=0.0 tension=0.0 notnull group 'User:8.5-6.8'

model mohr notnull group 'User:6.8-4'

prop density=1937.5 bulk=2.692E7 shear=1.24246E7 cohesion=98612.5 friction=41.7 dilation=0.0 tension=0.0 notnull group 'User:6.8-4'

model mohr notnull group 'User:4-3.2'

prop density=1937.5 bulk=2.53367E7 shear=1.16938E7 cohesion=92812.5 friction=42.9 dilation=0.0 tension=0.0 notnull group 'User:4-3.2'

model mohr notnull group 'User:3.2-2.5'

prop density=1937.5 bulk=1.10867E7 shear=5.11692E6 cohesion=40612.5 friction=39.3 dilation=0.0 tension=0.0 notnull group 'User:3.2-2.5'

model mohr notnull group 'User:2.5-1.8'

prop density=1937.5 bulk=6.33667E6 shear=2.92462E6 cohesion=23212.5 friction=37.0 dilation=0.0 tension=0.0 notnull group 'User:2.5-1.8'

model mohr notnull group 'User:1.8-0'

prop density=1835.5 bulk=3.167E7 shear=1.46169E7 cohesion=116012.5 friction=49.0 dilation=0.0 tension=0.0 notnull group 'User:1.8-0'

set gravity=9.81

```
prop por=0.3 perm=4.0E-6 region 39 30
prop por=0.3 perm=4.0E-6 region 36 26
prop por=0.3 perm=4.0E-6 region 37 23
prop por=0.3 perm=1.0E-4 region 38 21
prop por=0.3 perm=2.0E-4 region 35 16
prop por=0.3 perm=3.0E-4 region 29 9
prop por=0.3 perm=3.0E-4 region 34 4
set flow=off
water density=1000.0
; directory is changed to call file in case of nested calls
set cd name 'C:\Program Files (x86)\Itasca\FLAC700\gui\fishlib\Groundwater\'
call 'Ininv.fis'
set cd back
set wth=8.2 k0x=0.5 k0z=0.5
ininv
set dyn=off
history 999 unbalanced
solve  elastic
apply pp 0.0 var 0.0 80442.0 from 1,28 to 81,1
fix  pp i 81 j 1 28
history 1 gwtime
history 2 pp i=39, j=31
history 3 pp i=39, j=25
```

```
history 4 pp i=39, j=21
history 5 pp i=39, j=16
history 6 pp i=39, j=13
history 7 pp i=39, j=11
history 8 pp i=39, j=7
history 9 pp i=39, j=1
set flow=on
water bulk=1.96E9
set fastwb=on
set step=100000000
solve
set flow=off
water density=1000.0
; directory is changed to call file in case of nested calls
set cd name 'C:\Program Files (x86)\Itasca\FLAC700\gui\fishlib\Groundwater\'
call 'Ininv.fis'
set cd back
set wth=8.2 k0x=0.5 k0z=0.5
ininv
set dyn=off
history 999 unbalanced
solve  elastic
apply pp 0.0 var 0.0 80442.0 from 1,28 to 81,1
```

```
fix  pp i 81 j 1 28
history 1 gwtime
history 2 pp i=39, j=31
history 3 pp i=39, j=25
history 4 pp i=39, j=21
history 5 pp i=39, j=16
history 6 pp i=39, j=13
history 7 pp i=39, j=11
history 8 pp i=39, j=7
history 9 pp i=39, j=1
set flow=on
water bulk=1.96E9
set fastwb=on
set step=100000000
solve
set dyn=on
set =large
call 'TABLE215CACSVELOCITYN40E3-24-21.dat'
initial xdisp 0 ydisp 0
initial xvel 0 yvel 0
set echo=off
;Name:strain_hist
 def strain_ini_hist
```

```
  str_40_26=0.0
end
strain_ini_hist
;
def strain_hist
array arr1(4)
while_stepping
dum1 = fsr(40,26,arr1)
str_40_26=str_40_26 + 2.0*arr1(4)
end
strain_hist
set echo=off
;Name:reldispx
def reldispx
   reldispx = xdisp(40,26) - xdisp(40,1)
   reldispy = ydisp(40,26) - ydisp(40,1)
end
reldispx
set echo=off
;Name:inipp
def inipp
   ppini   = pp(40,26)
end
```

```
inipp
set echo=off
;Name:excpp
def excpp
   excpp = pp(40,26) - ppini
end
excpp
set echo=off
history 5 dytime
history 6 vsxy i=42, j=30
history 7 vsxy i=42, j=17
history 8 vsxy i=42, j=2
history 9 ssi i=42, j=31
history 10 ssi i=42, j=17
history 11 ssi i=42, j=2
history 12 sxy i=42, j=31
history 13 sxy i=42, j=17
history 14 sxy i=42, j=2
history 15 xaccel i=42, j=32
history 16 xaccel i=42, j=17
history 17 xaccel i=42, j=2
history 18 xvel i=41, j=31
history 19 xvel i=41, j=17
```

```
history 20 xvel i=41, j=2
history 21 xdisp i=41, j=31
history 22 xdisp i=41, j=17
history 23 xdisp i=41, j=2
history 24 esyy i=41, j=31
history 25 esyy i=41, j=16
history 26 esyy i=41, j=2
history 27 reldispx
history 28 reldispy
history 29 excpp
history 30 str_40_26
history nstep 100
;Name:mon_ex
def _ini_ex
  loop i (1,izones)
   loop j (1,jzones)
    if model(i,j) # 1
      ex_9(i,j)=0.
      ex_10(i,j)= 0.
    endif
   endloop
  endloop
end
```

```
_ini_ex
def mon_ex
  array arr(4)
  while_stepping
  loop i (1,izones)
    loop j (1,jzones)
      if model(i,j) # 1
        dum = fsr(i,j,arr)
        ex_9(i,j)=ex_9(i,j) + 2.0 * arr(4)
        ex_10(i,j)= max(ex_10(i,j),abs(ex_9(i,j)))
      endif
    endloop
  endloop
end
mon_ex
history 36 sxy i=36, j=32
history 37 sxy i=36, j=29
history 38 sxy i=36, j=27
history 39 sxy i=36, j=25
history 40 sxy i=36, j=23
history 41 sxy i=36, j=19
history 42 sxy i=36, j=16
history 43 sxy i=36, j=14
```

```
history 44 sxy i=36, j=11
history 45 sxy i=36, j=8
history 46 sxy i=36, j=6
history 47 sxy i=36, j=3
history 48 sxy i=36, j=1
apply ffield
apply sxy -589000.0 hist table 215 from 1,1 to 81,1
apply xquiet  from 1,1 to 81,1
apply yquiet  from 1,1 to 81,1
def getExcesspp
  whilestepping
  if nstep = nsample then
  loop i (1,izones)
    loop j (1,jzones)
    if model(i,j) # 1
      if pp(i,j) > ex_2(i,j) then
        ex_5(i,j) = pp(i,j) - ex_2(i,j)
      else
        ex_5(i,j) = 0.0
      endif
      ex_4(i,j) = abs(ex_5(i,j)/ex_3(i,j))
      ex_6(i,j)= max(ex_6(i,j),abs(ex_4(i,j)))
    endif
```

```
    endloop
  endloop
  nstep = 1
  endif
  nstep = nstep + 1
end
def excpp
  excpp = pp(49,23) - ppini
end
def inipp
  ppini   = pp(49,23)
end
def savepp
  loop i (1,izones)
    loop j (1,jzones)
      ex_2(i,j) = pp(i,j)
      ex_3(i,j) = (sxx(i,j)+syy(i,j)+szz(i,j))/3.0 + pp(i,j)
      ex_6(i,j) = 0.0
    endloop
  endloop
end
def strain_ini_hist
 str_77_20=0.0
```

```
end
strain_ini_hist
;
def strain_hist
array arr1(4)
while_stepping
dum1 = fsr(77,20,arr1)
str_77_20=str_77_20 + 2.0*arr1(4)
end
def reldispx
   reldispx = xdisp(62,29) - xdisp(62,1)
   reldispy = ydisp(62,29) - ydisp(62,1)
def integrate
  command
     table int_out erase
  end_command
  nitem = table_size(int_in)
;
  xold  = xtable(int_in,1)
  yold  = ytable(int_in,1)
  val = 0.0
  xtable(int_out,1) = xold
  ytable(int_out,1) = val
```

```
  loop ii (2,nitem)
    xnew = xtable(int_in,ii)
    ynew = ytable(int_in,ii)
    val = val + 0.5*(yold + ynew)*(xnew-xold)
    xtable(int_out,ii) = xnew
    ytable(int_out,ii) = val
    xold = xnew
    yold = ynew
  end_loop
;
end
end
def _ini_ex
   loop i (1,izones)
    loop j (1,jzones)
     if model(i,j) # 1
       ex_9(i,j)=0.
       ex_10(i,j)= 0.
     endif
    endloop
   endloop
end
_ini_ex
```

```
def mon_ex
  array arr(4)
  while_stepping
  loop i (1,izones)
   loop j (1,jzones)
    if model(i,j) # 1
      dum = fsr(i,j,arr)
      ex_9(i,j)=ex_9(i,j) + 2.0 * arr(4)
      ex_10(i,j)= max(ex_10(i,j),abs(ex_9(i,j)))
    endif
   endloop
  endloop
end
def baseline
  npnts = table_size(itab_unc)
;
  loop ii (1,npnts)
    tt = float(ii-1) * ttime / float(npnts)
    vv = pi * tt / ttime
    cor_d = drift * pi / (2.0 * ttime)
    ytable(itab_corr,ii) = -(cor_d*sin(vv))
    xtable(itab_corr,ii) = tt
    ytable(itab_cmot,ii) = ytable(itab_corr,ii) + ytable(itab_unc,ii)
```

```
      xtable(itab_cmot,ii) = xtable(itab_unc,ii)
    endloop
end
;Code: FLAC


;***** ini_pp ******
; Initializes zone pore pressures
; parameters (SET):
;          wth ..... height of the water table
def ini_pp
loop i (1,igp)
  loop j (1,jgp)
    if y(i,j)>wth then
      sat(i,j)=0.0
    else
      sat(i,j)=1.0
      gpp(i,j)=-1.0*abs((y(i,j)-wth))*wdens*ygrav
    end_if
  end_loop
end_loop
loop i (1,izones)
  loop j (1,jzones)
    pp(i,j)=0.25*(gpp(i,j)+gpp(i,j+1)+gpp(i+1,j+1)+gpp(i+1,j))
```

```
  end_loop
end_loop
end
;**** ini_syy ******
; Initializes vertical stresses
; variables:
;          h ..... height of zone j
;          bot ..... vertical stress at the bottom of zone j
;          top ..... vertical stress at the top of zone j
def ini_syy
top = 0.0
loop jj (1,jzones)
  j=jgp-jj
  h=abs(y(1,j)-y(1,j+1))
  bot=top+ygrav*h*(density(1,j)+porosity(1,j)*0.5*(sat(1,j)+sat(1,j+1))*wdens)
  loop i (1,izones)
    syy(i,j)=0.5*(bot+top)
  end_loop
  top=bot
end_loop
end
;**** ini_shor ******
; Initializes horizontal stresses
```

```
; variables:
;          k0x..... ratio of effective sxx to effective syy
;          k0z..... ratio of effective szz to effective syy
; parameters (SET):
;             k0x
;          k0z
def ini_shor
loop i (1,izones)
  loop j (1,jzones)
    sxx(i,j)=k0x*(syy(i,j)+pp(i,j))-pp(i,j)
    szz(i,j)=k0z*(syy(i,j)+pp(i,j))-pp(i,j)
  end_loop
end_loop
end

def ininv
  ini_pp
  ini_syy
  ini_shor
end
set flow=off
solve dytime 160.0
```

APPENDIX C. ALL LPCS DEVELOPED FOR THIS STUDY

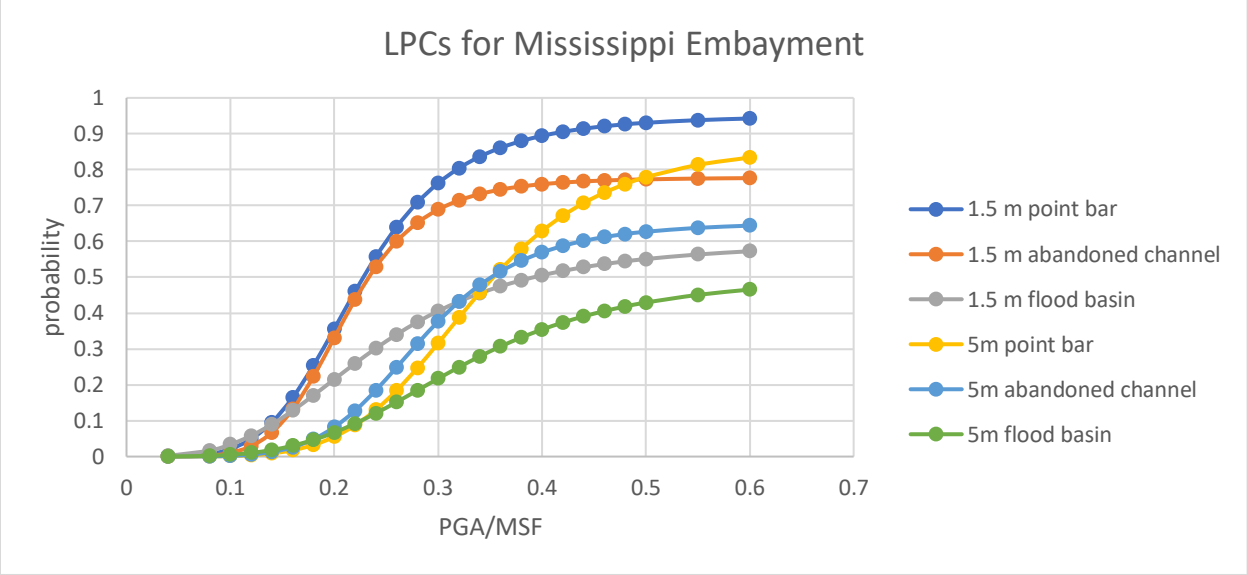

Figure C.1. LPCs for LPI>15 for Mississippi embayment from Holzer's study (2011).

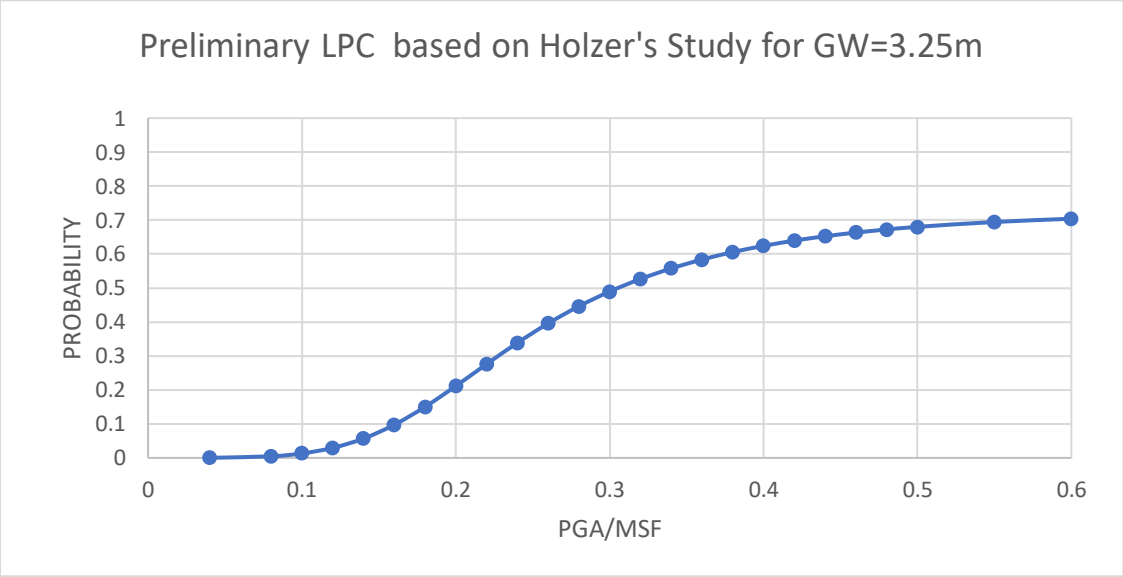

Figure C.2. Liquefaction Probability Curve from Holzer's Study.

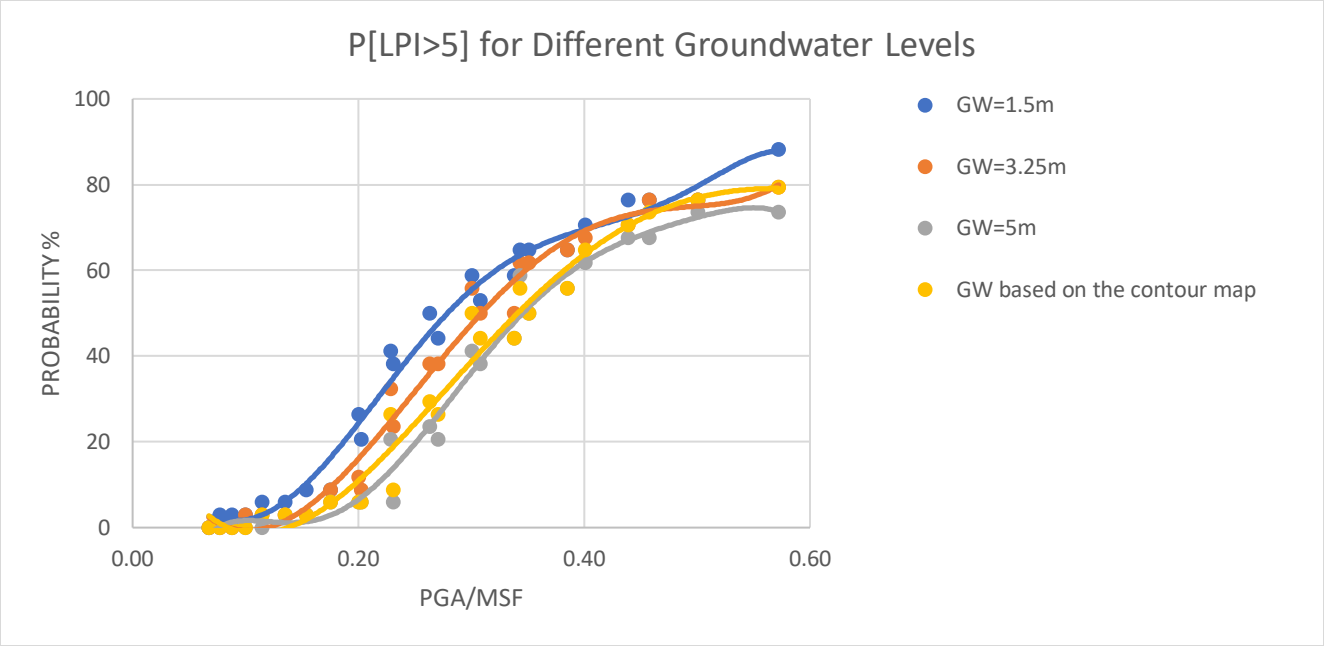

Figure C.3. LPCs from SPT data for LPI>5.

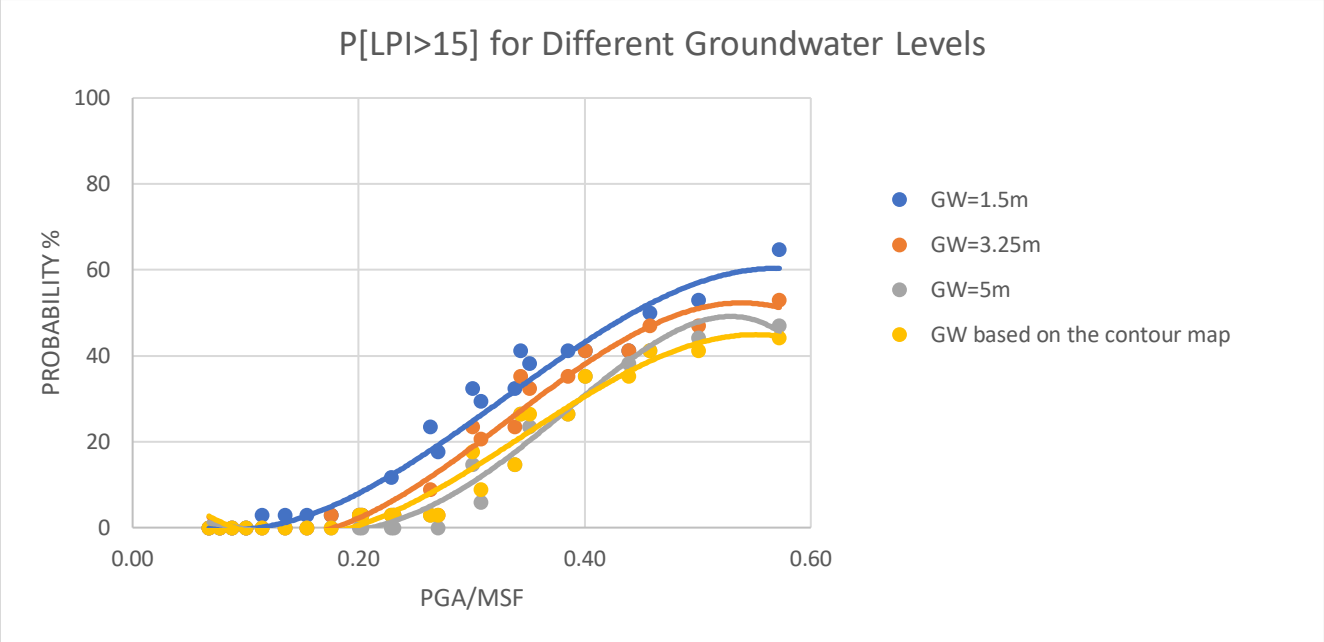

Figure C.4. LPCs from SPT data for LPI>15.

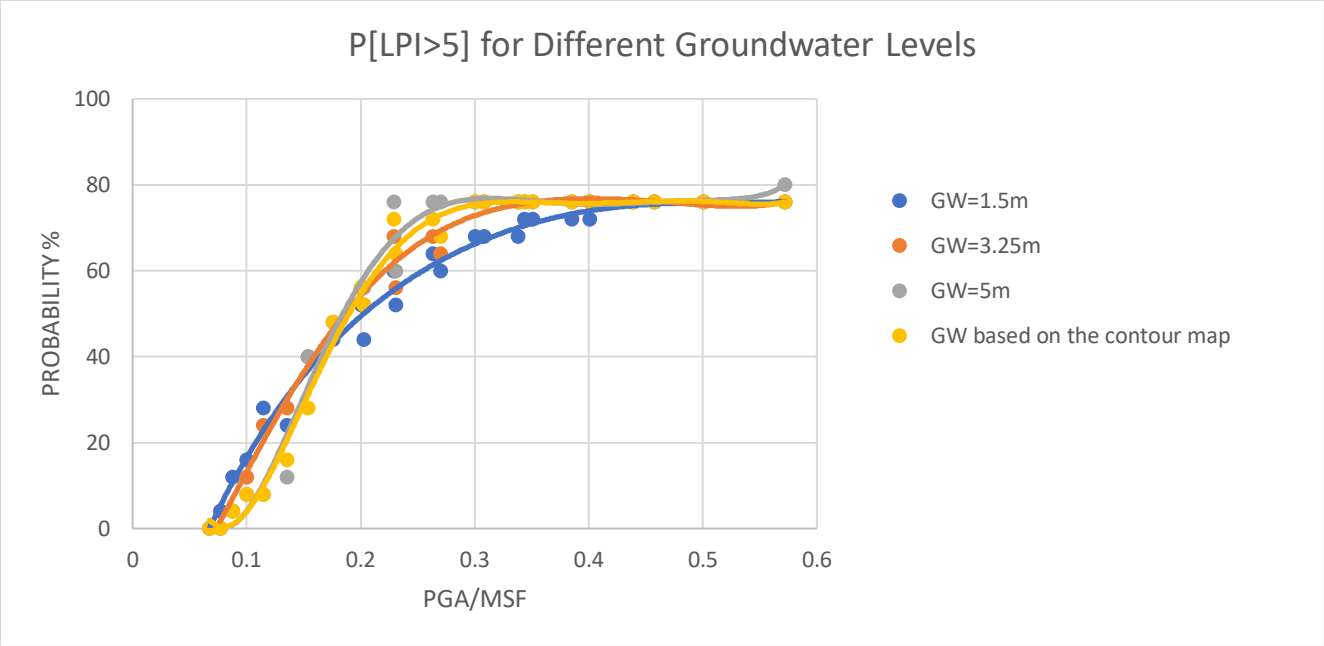

Figure C.5. LPCs from shear wave velocity data for LPI>5.

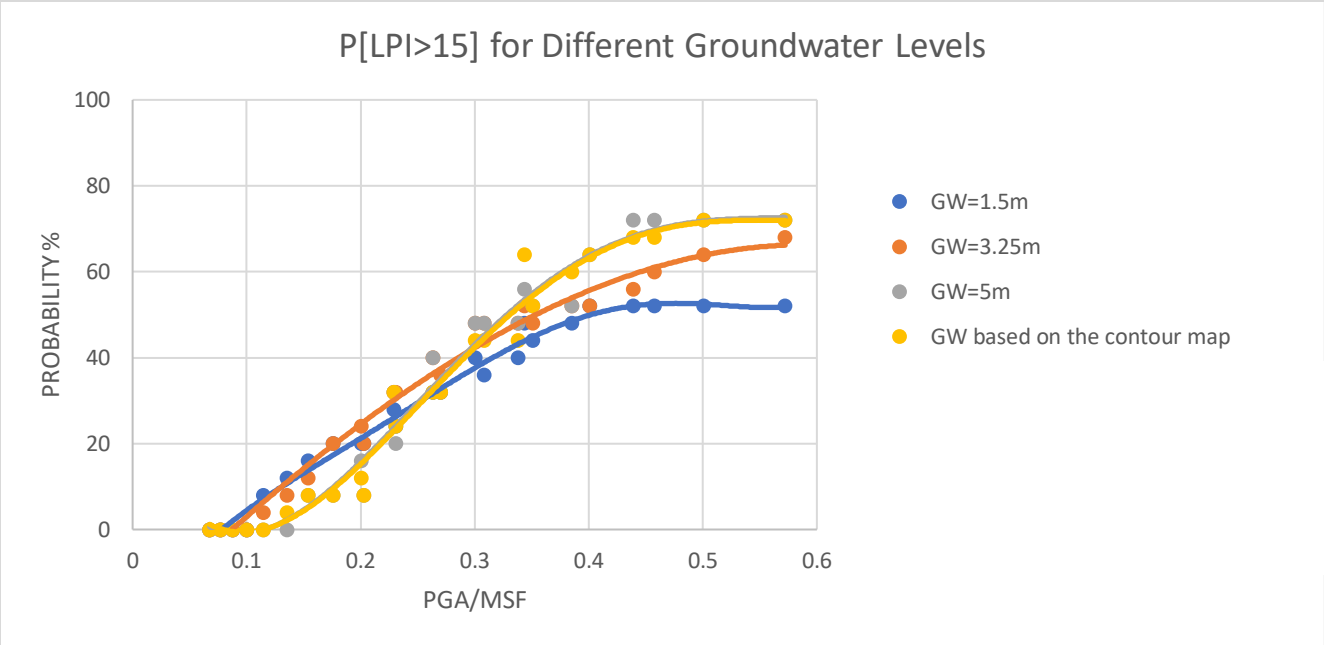

Figure C.6. LPCs from shear wave velocity data for LPI>15.

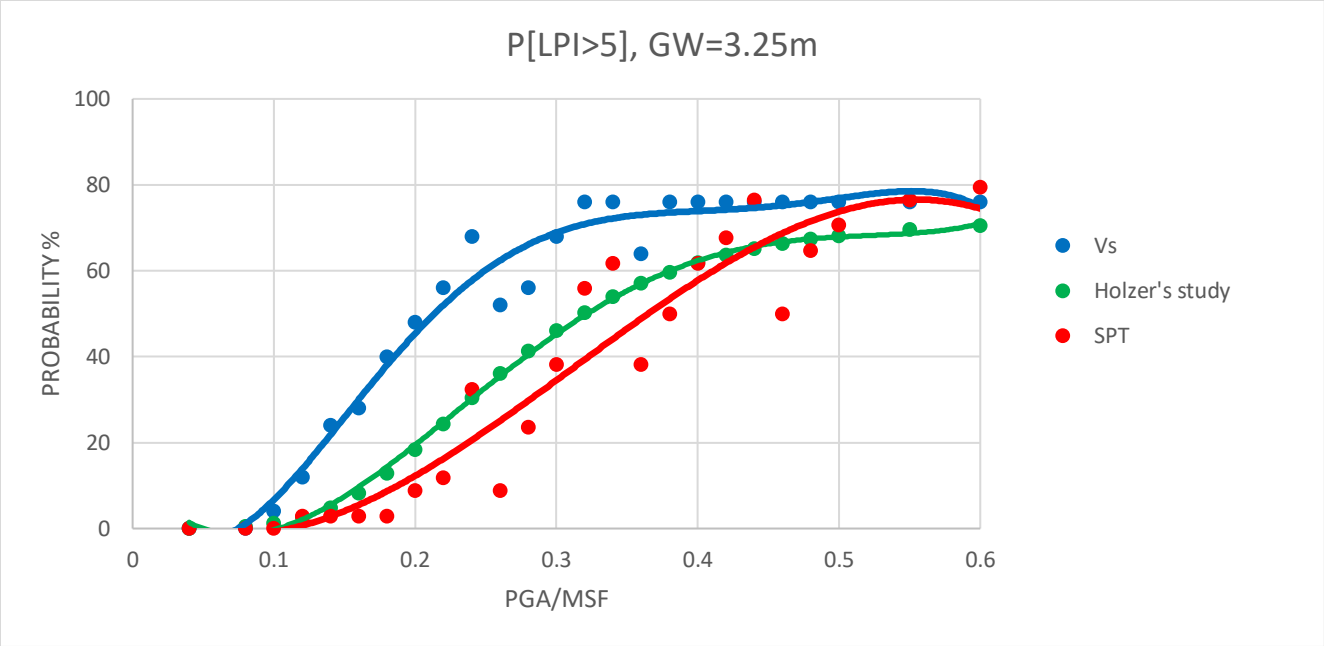

Figure C.7. Comparison of obtained LPCs based on SPT data, shear wave velocity profiles and Holzer's study for GW=3.25m.

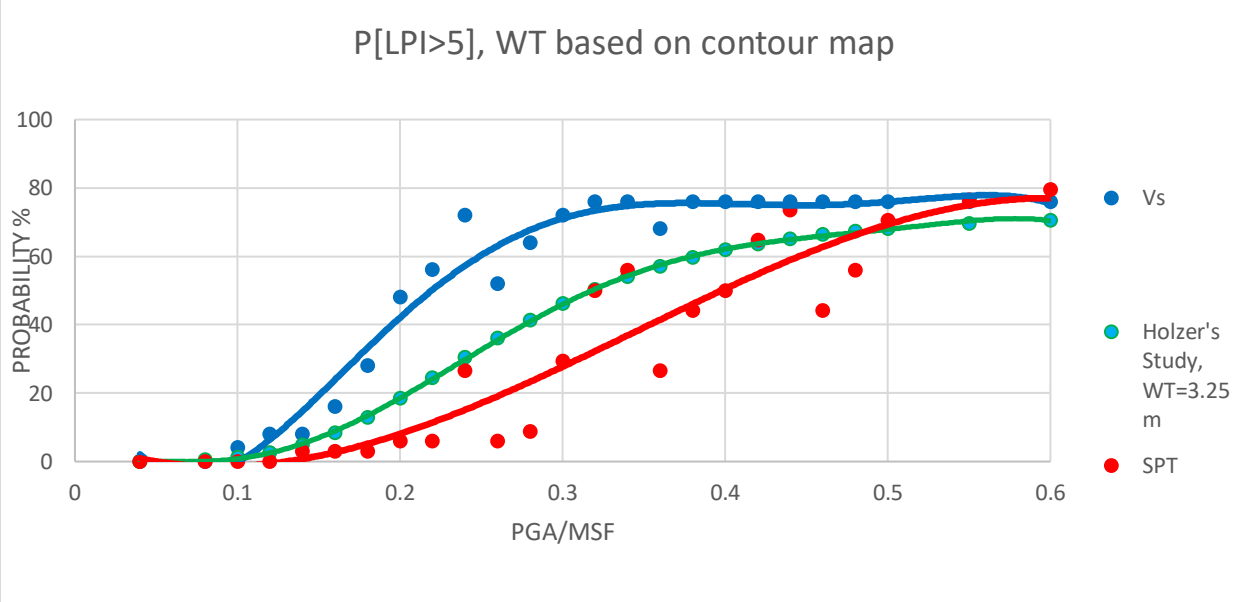

Figure C.8. Comparison of obtained LPCs based on SPT data, shear wave velocity profiles (groundwater level based on the contour map) and Holzer's study (GW=3.25m).

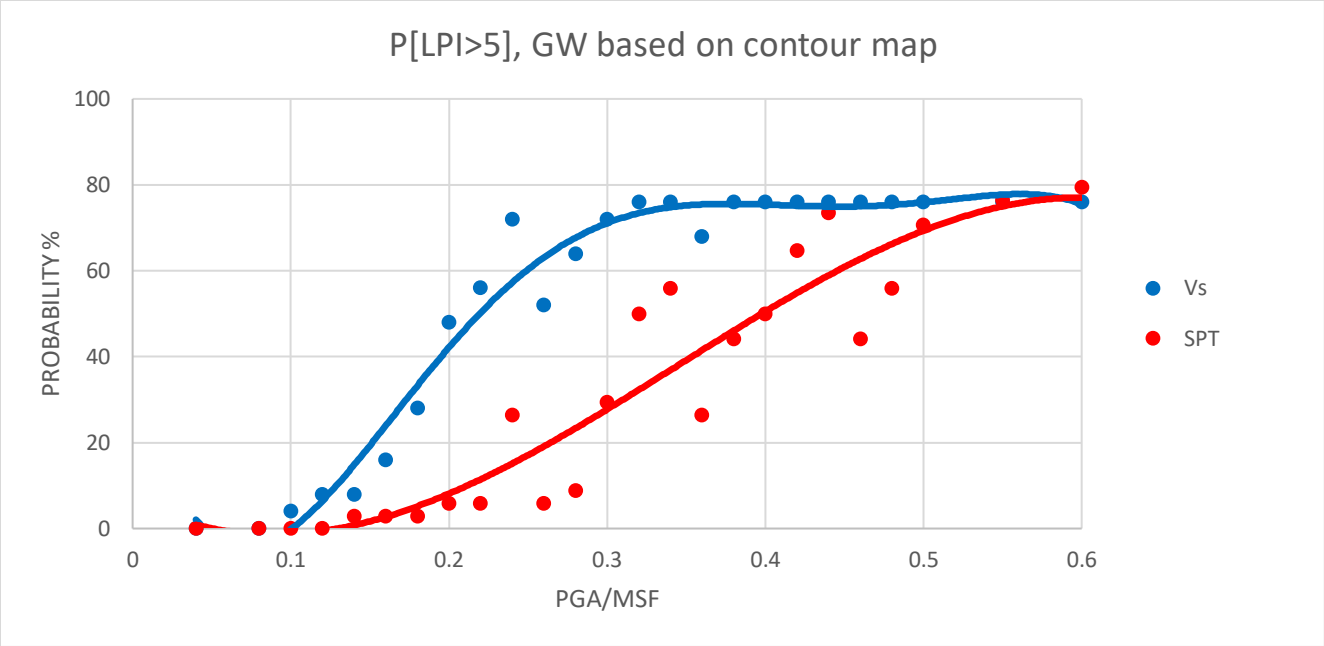

Figure C.9. Comparison of obtained LPCs based on SPT data and shear wave velocity profiles for LPI>5.

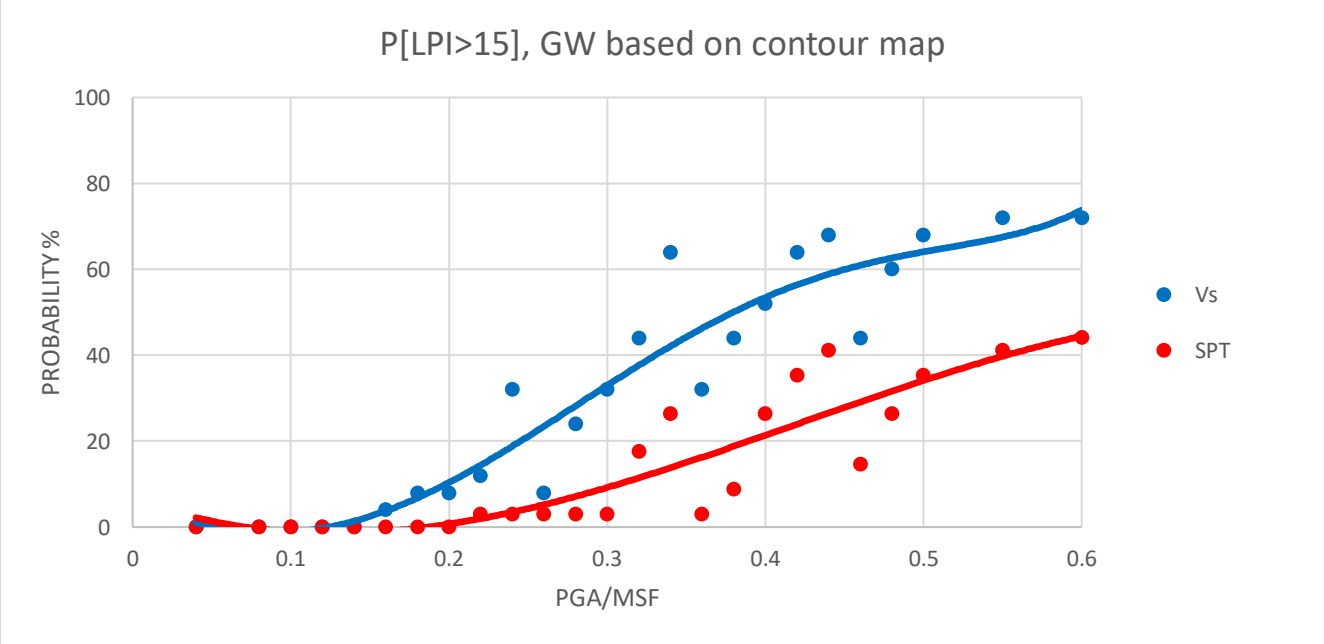

Figure C.10. Comparison of obtained LPCs based on SPT data and shear wave velocity profiles for LPI>15.

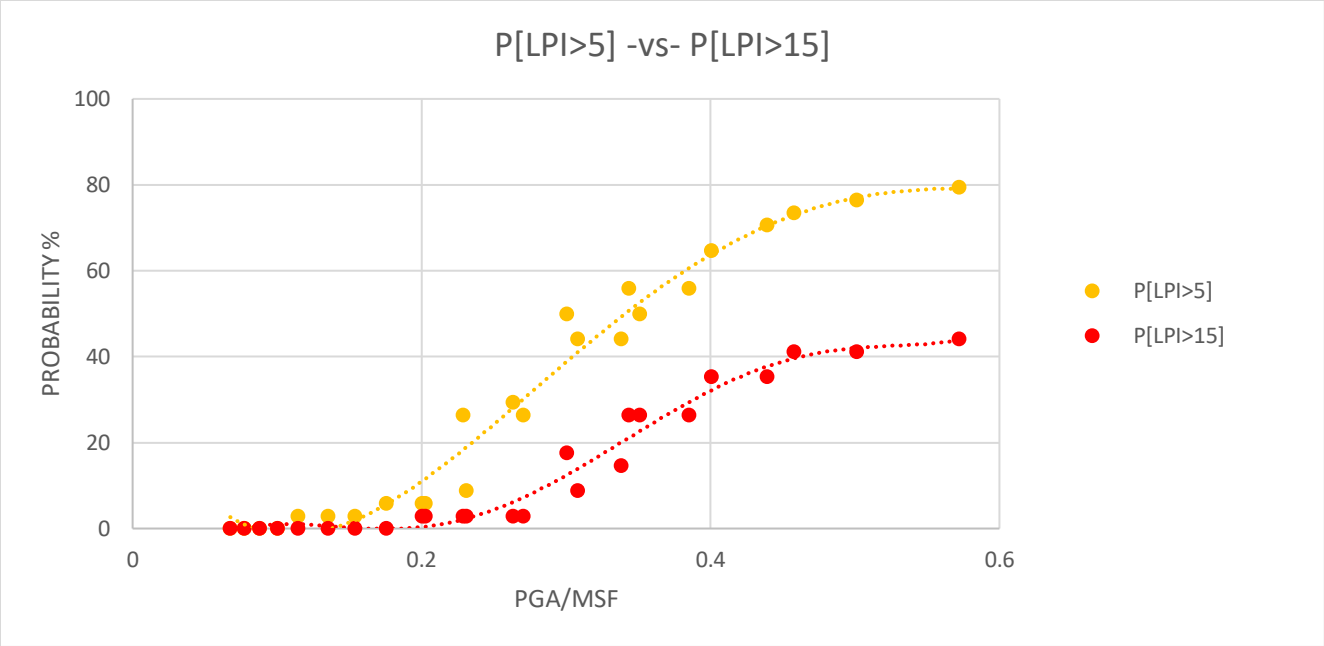

Figure C.11. Liquefaction probability curves using SPT boring data.

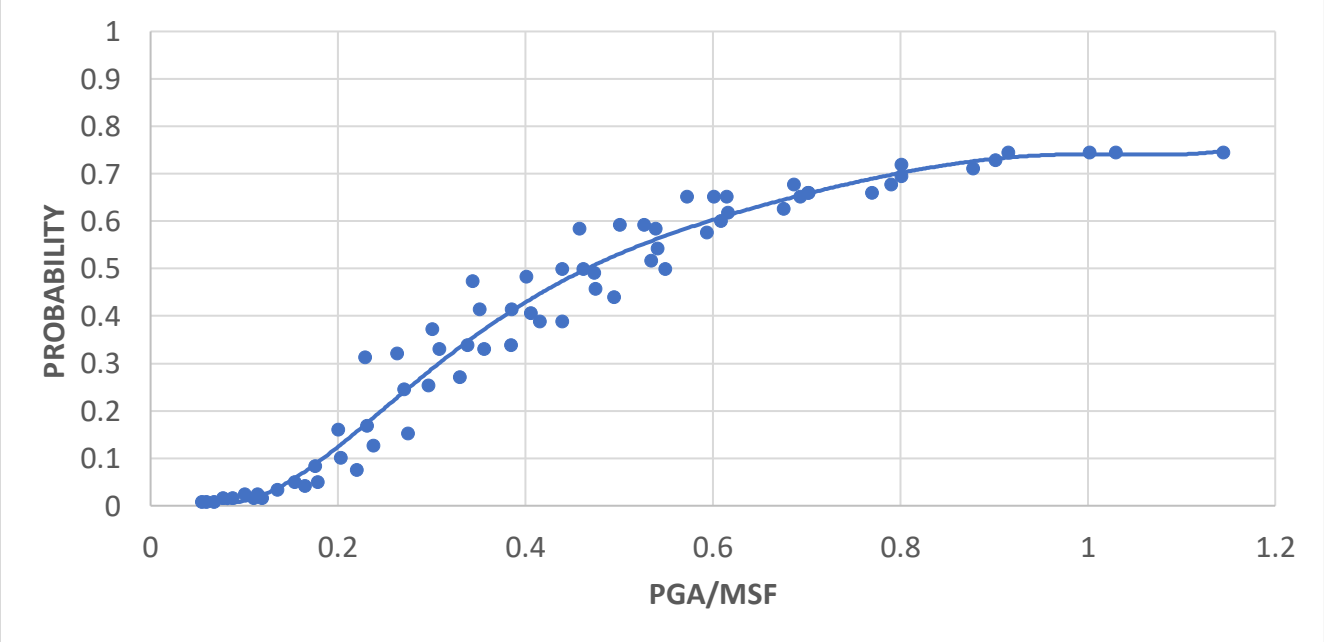

Figure C.12. Lowland LPC from SPT data for P[LPI>5].

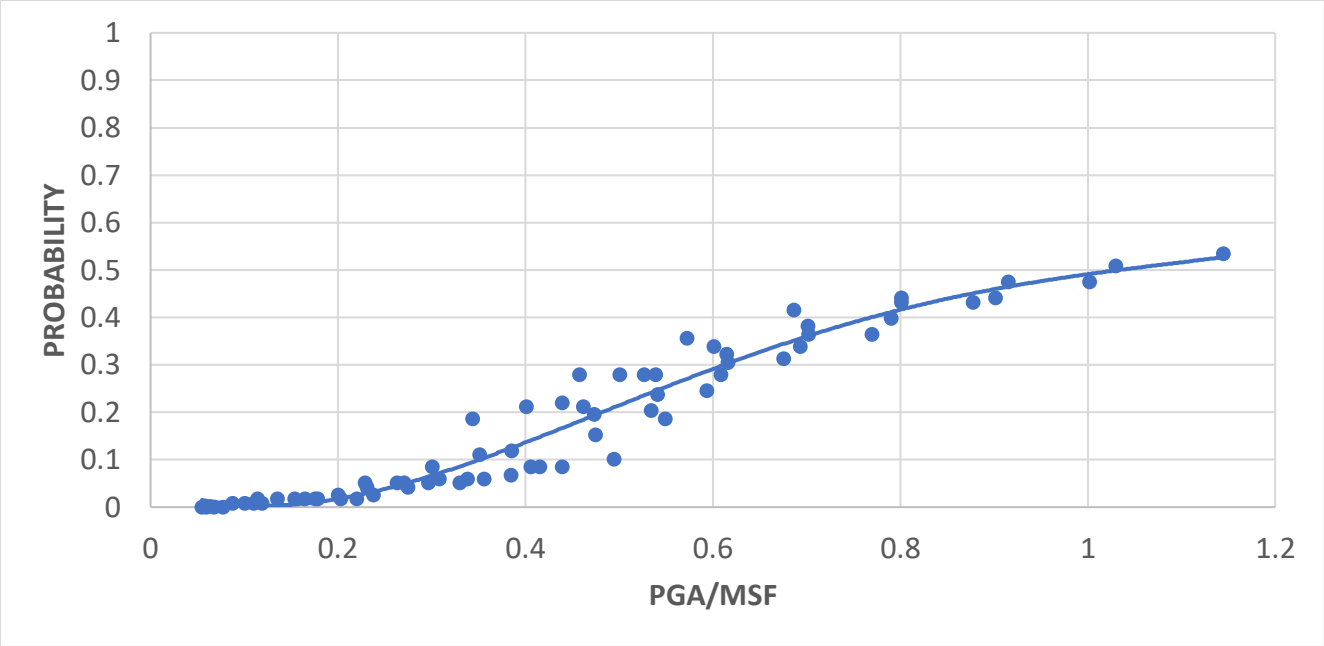

Figure C.13. Lowland LPC from SPT data for P[LPI>15].

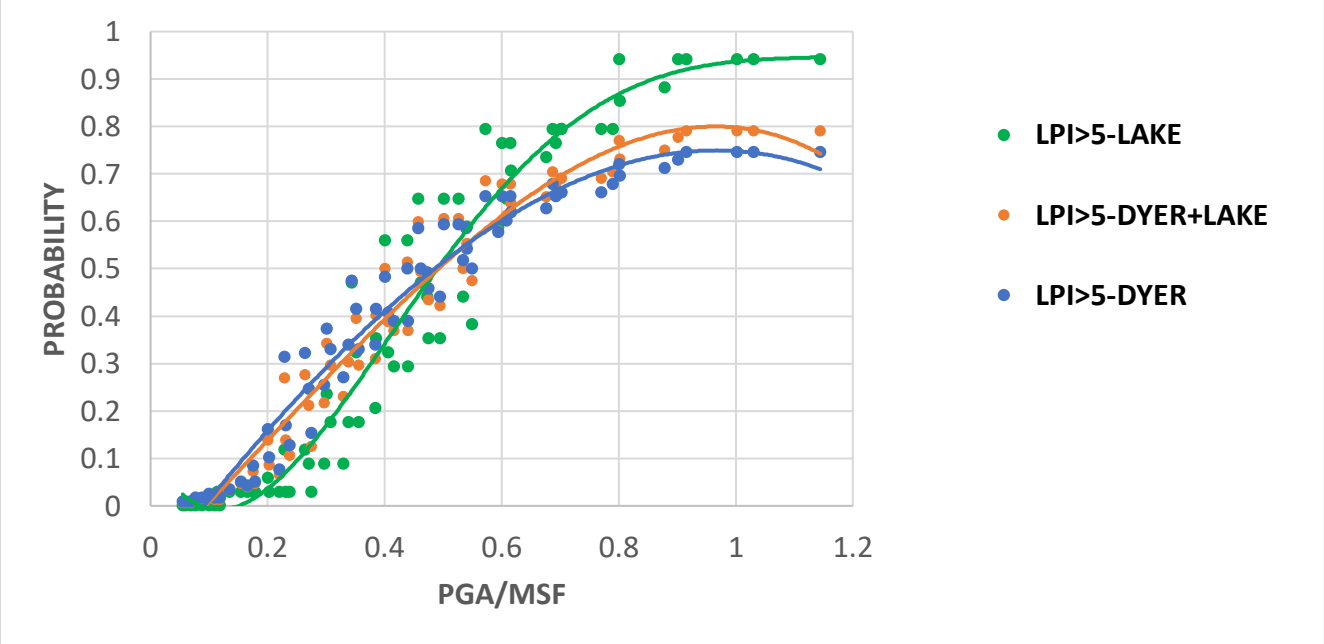

Figure C.14. Comparison and combination of lowland LPCs of Lake and Dyer Counties for P[LPI>5].

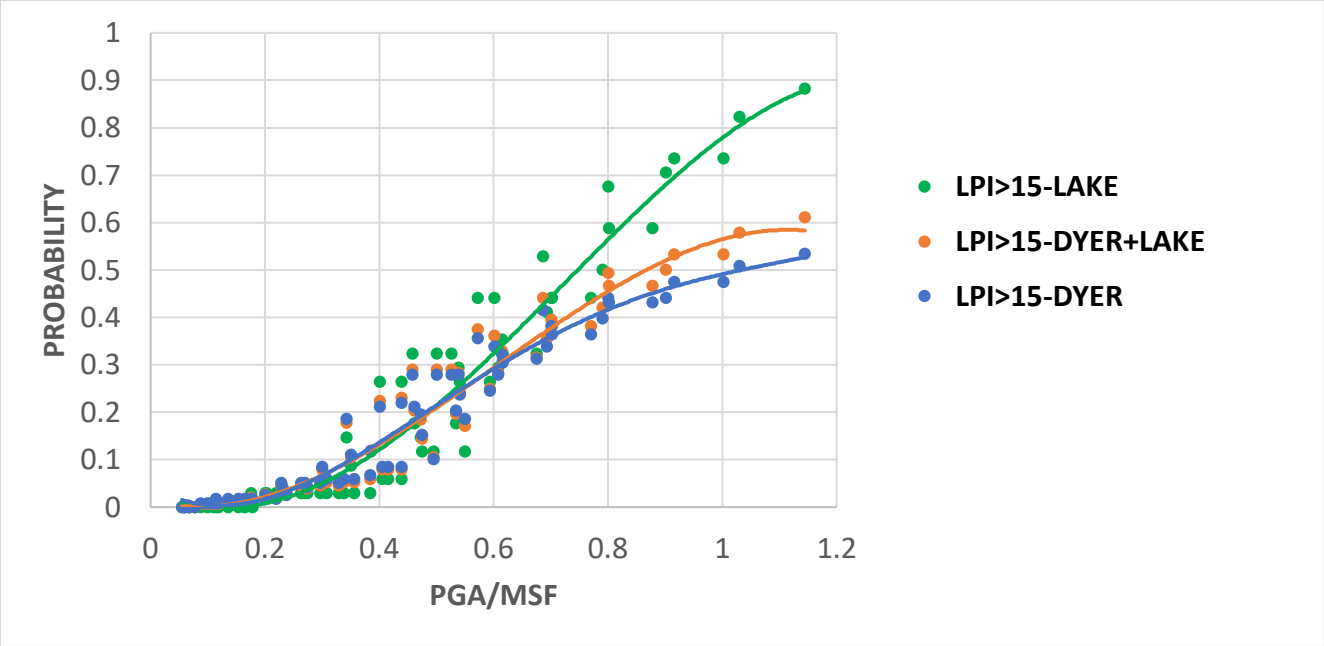

Figure C.15. Comparison and combination of lowland LPCs of Lake and Dyer Counties for P[LPI>15].

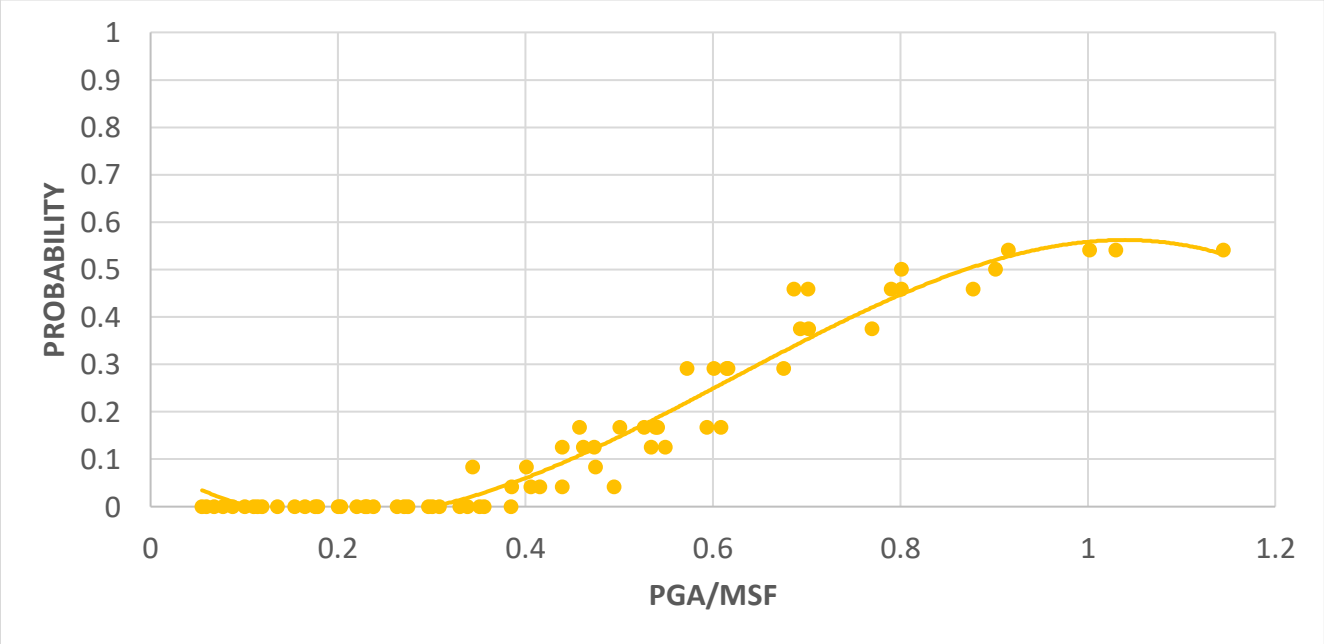

Figure C.16. Non-lowland LPC from SPT data for P[LPI>5].

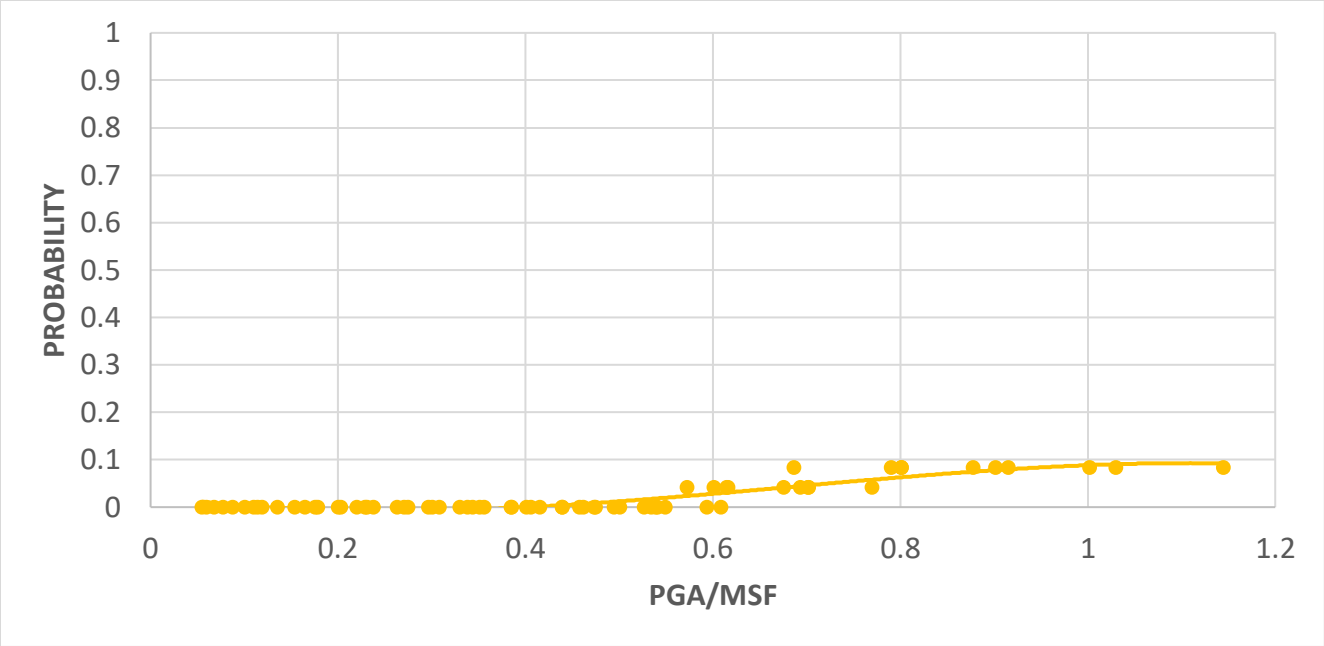

Figure C.17. Non-lowland LPC from SPT data for P[LPI>15].

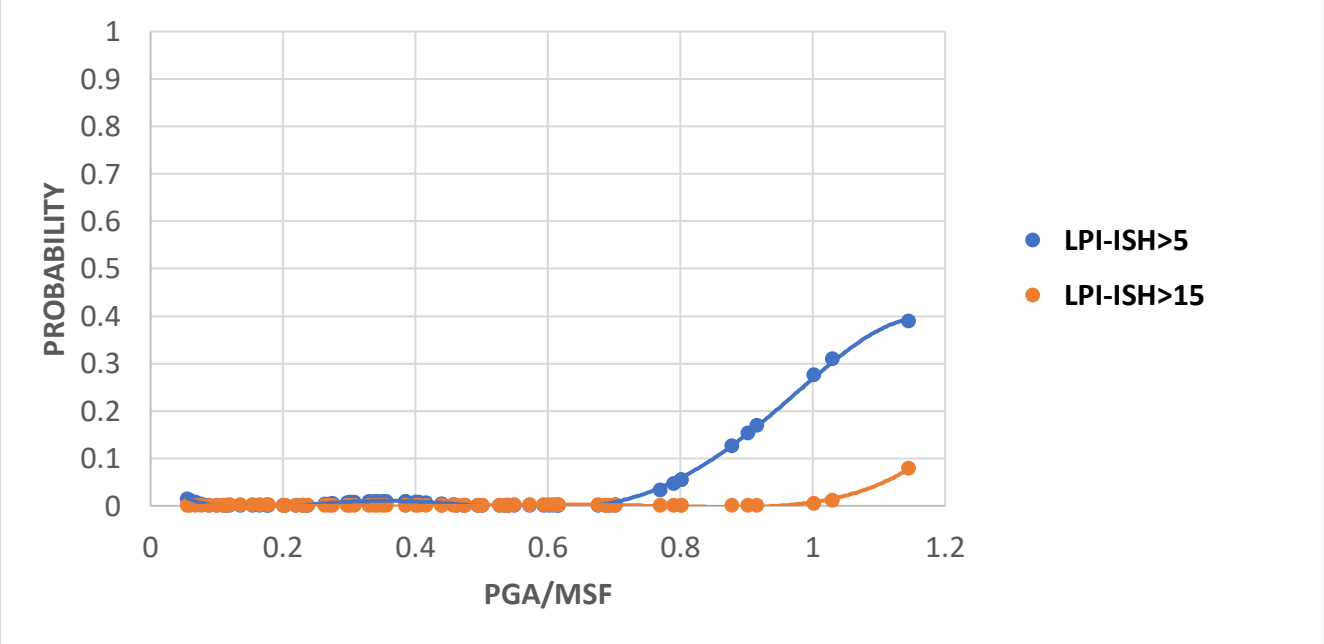

Figure C.18. LPI_{ISH} based LPCs of lowland geologic unit.

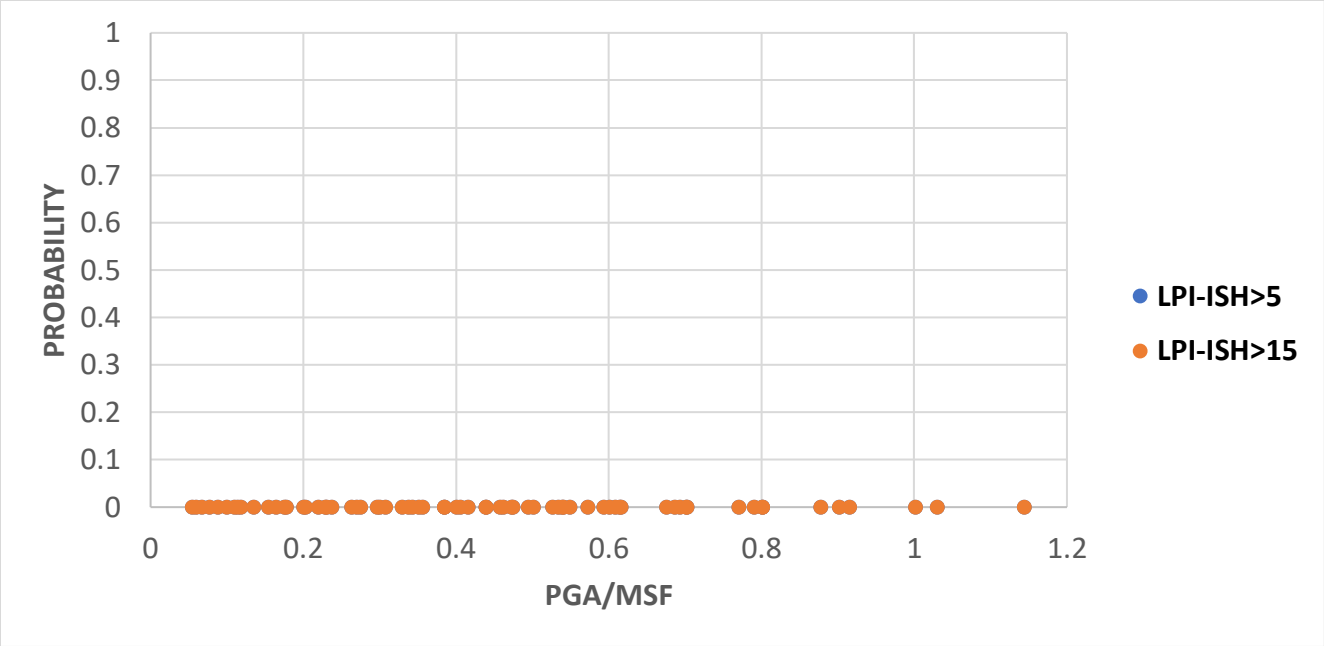

Figure C.19. LPI_{ISH} based LPCs of non-Lowland geologic units.

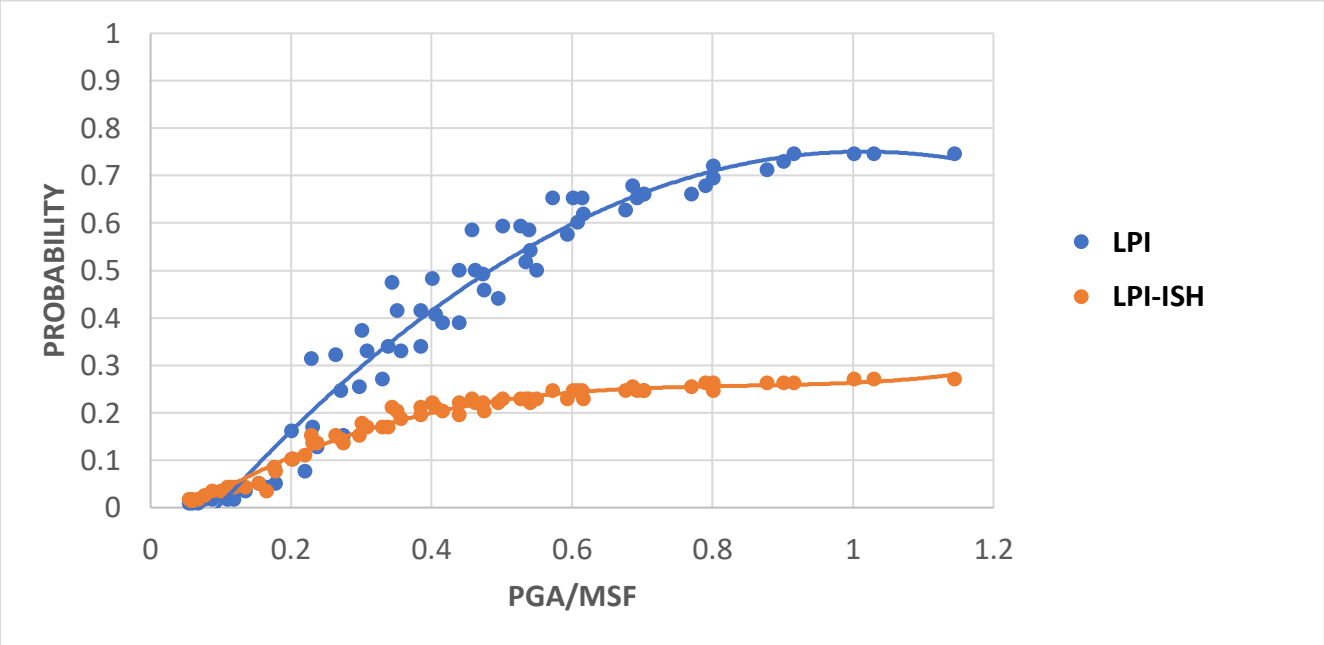

Figure C.20. Comparison of LPI- and LPI_{ISH}-based lowland LPCs for P[LPI>5].

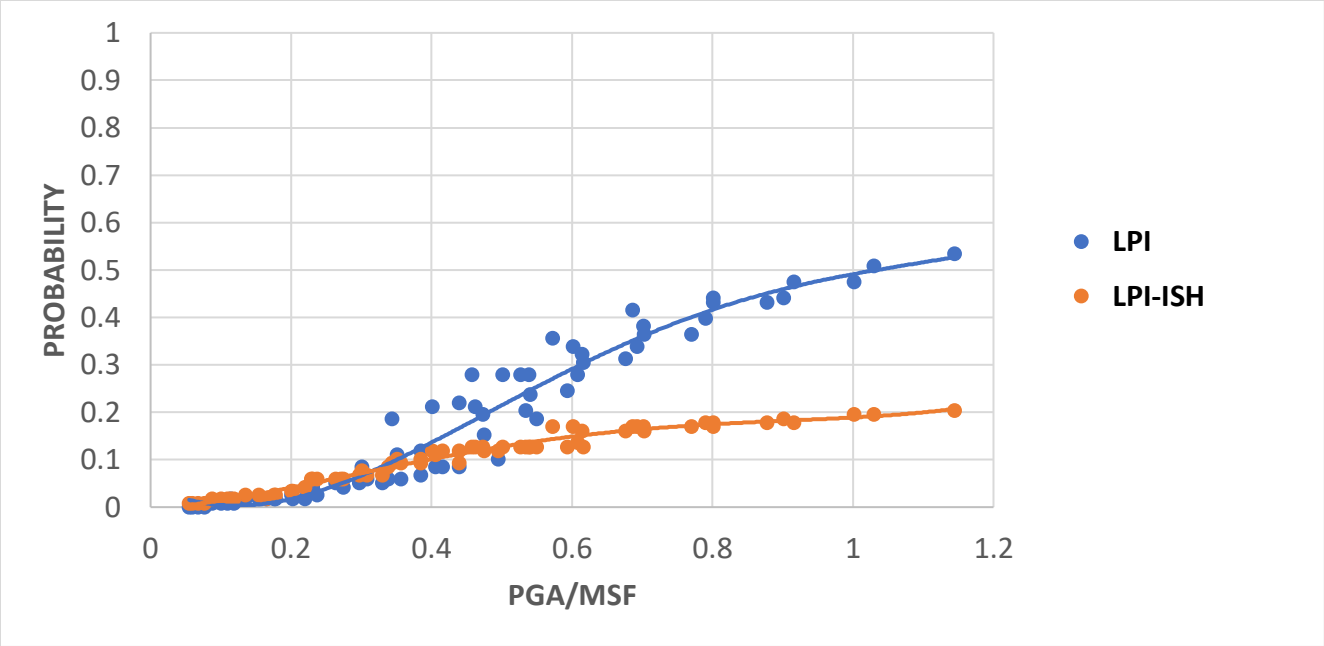

Figure C.21. Comparison of LPI- and LPI_{ISH}-based lowland LPCs for P[LPI>15].

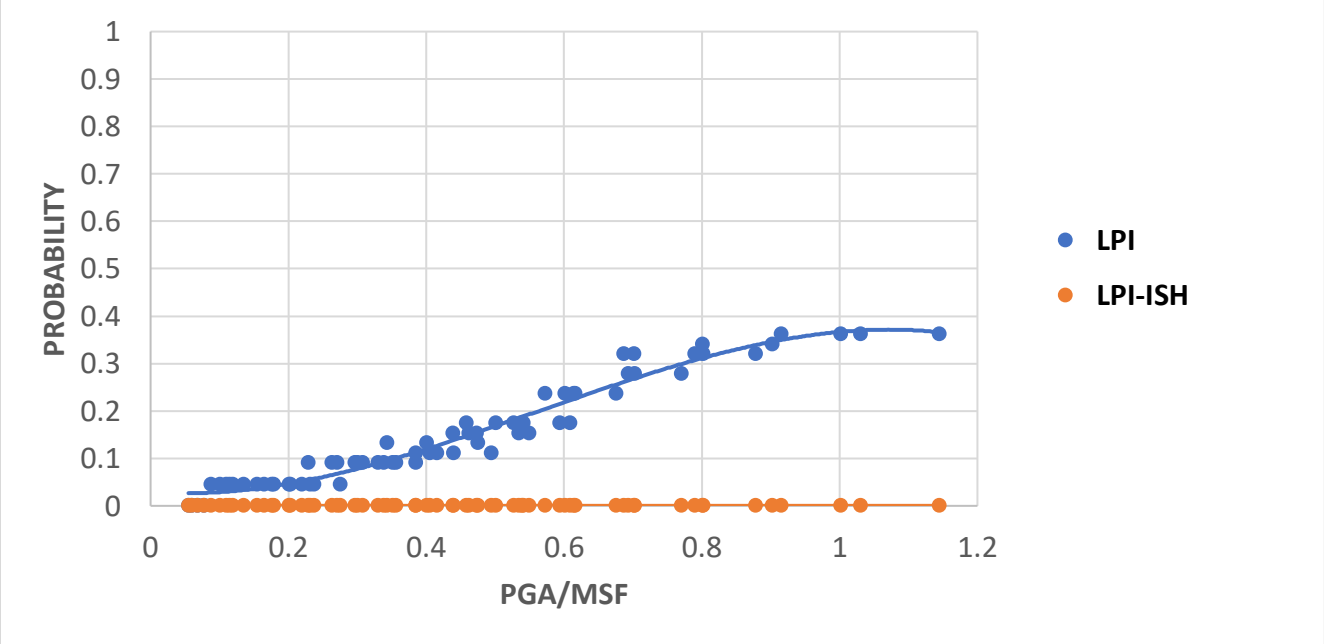

Figure C.22. Comparison of LPI- and LPI_{ISH}-based non-lowland LPCs for P[LPI>5].

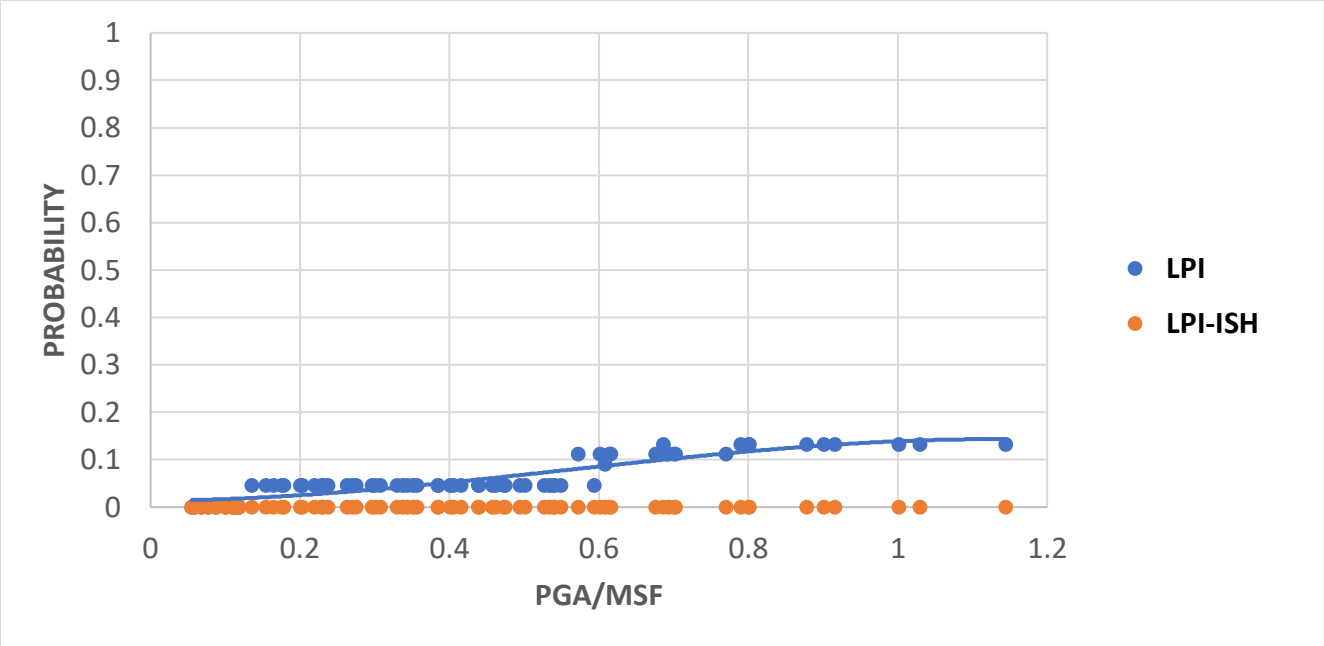

Figure C.23. Comparison of LPI- and LPI_{ISH}-based non-lowland LPCs for P[LPI>15].

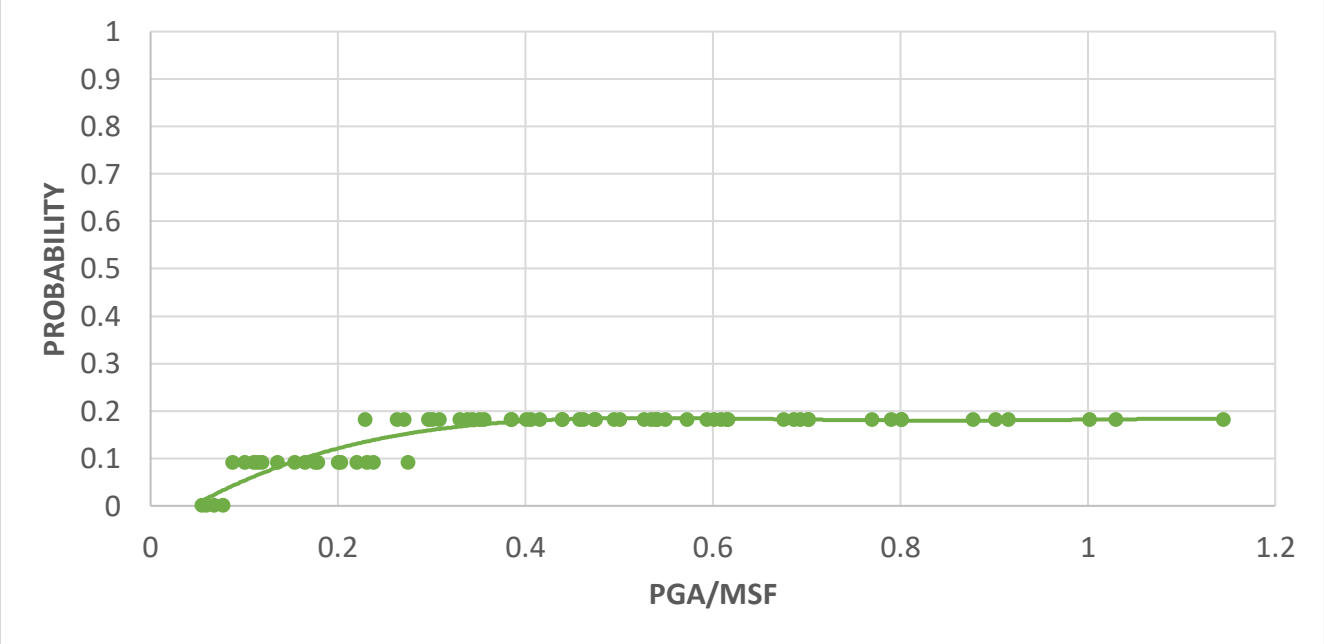

Figure C.24. Non-lowland *Vs* based LPCs for P[LPI>5].

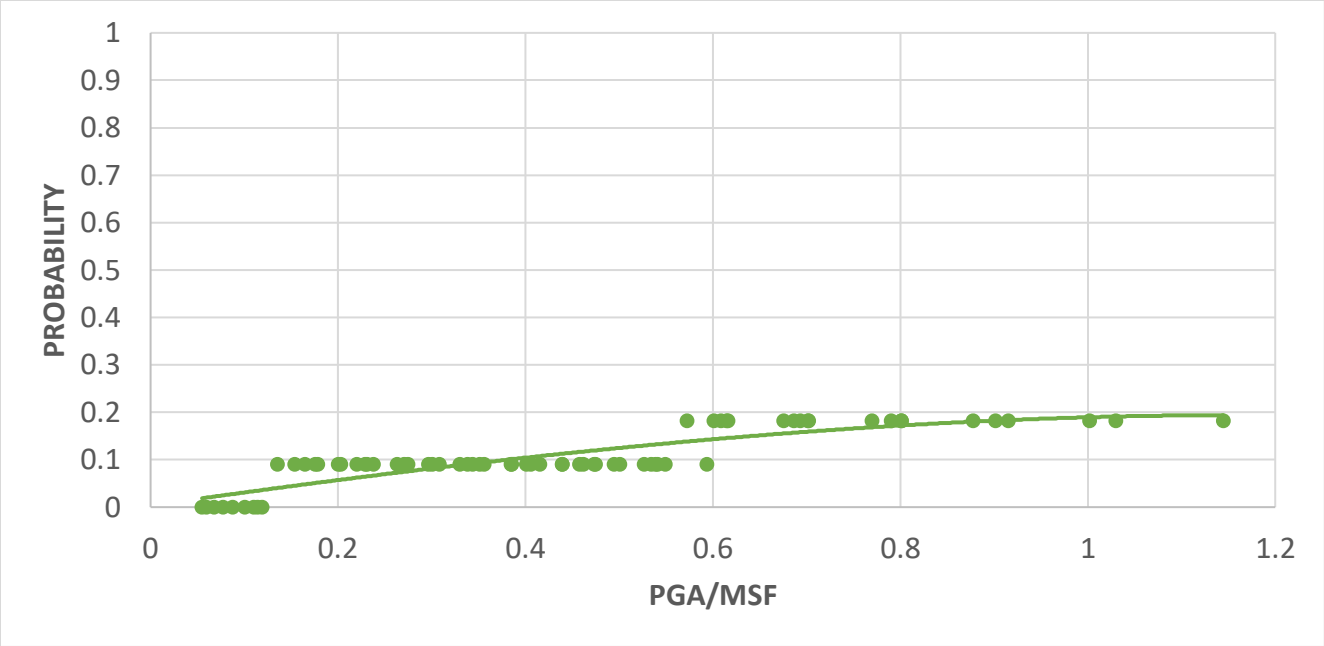

Figure C.25. Non-lowland *Vs* based LPCs for P[LPI>15].

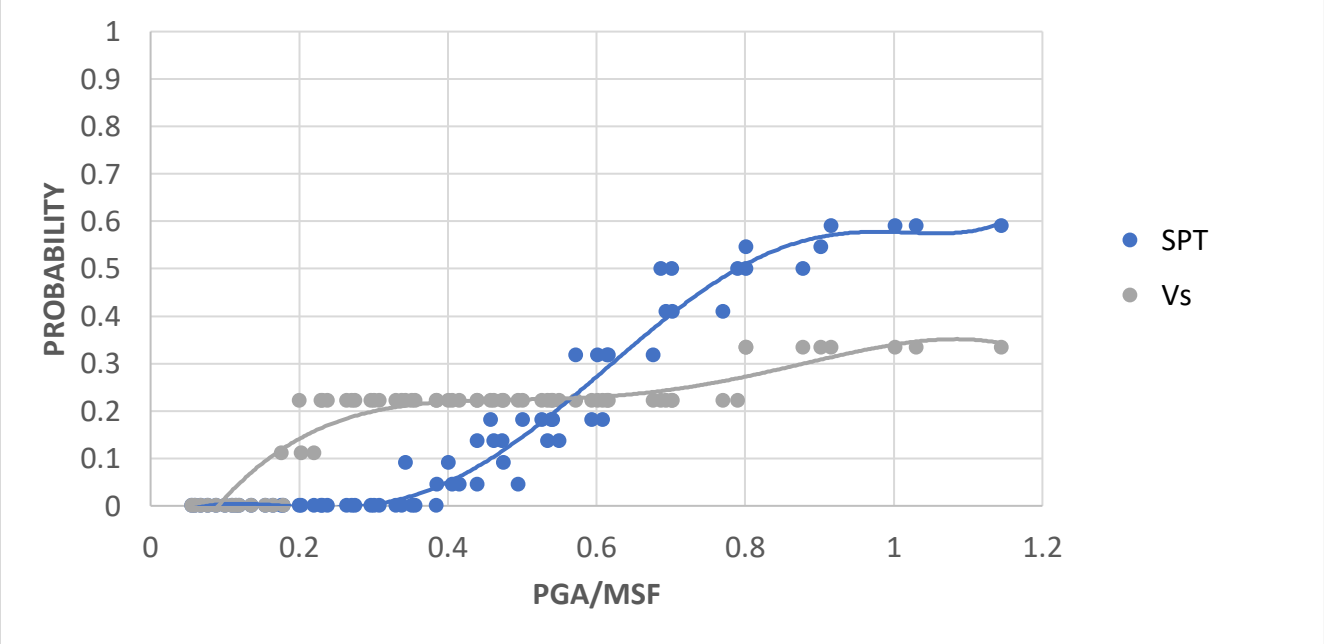

Figure C.26. Comparison of LPCs based on SPT data and shear wave velocity profiles for P[LPI>5] for non-lowland parts of Dyer County.

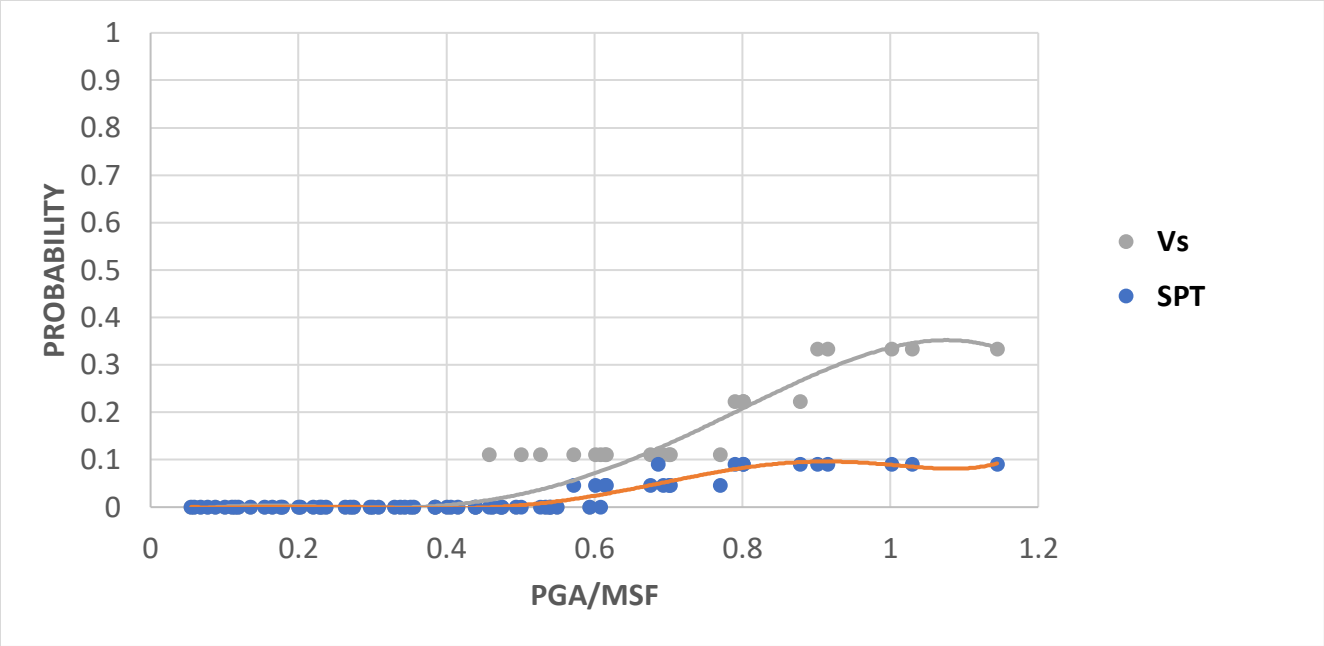

Figure C.27. Comparison of LPCs based on SPT data and shear wave velocity profiles for P[LPI>15].

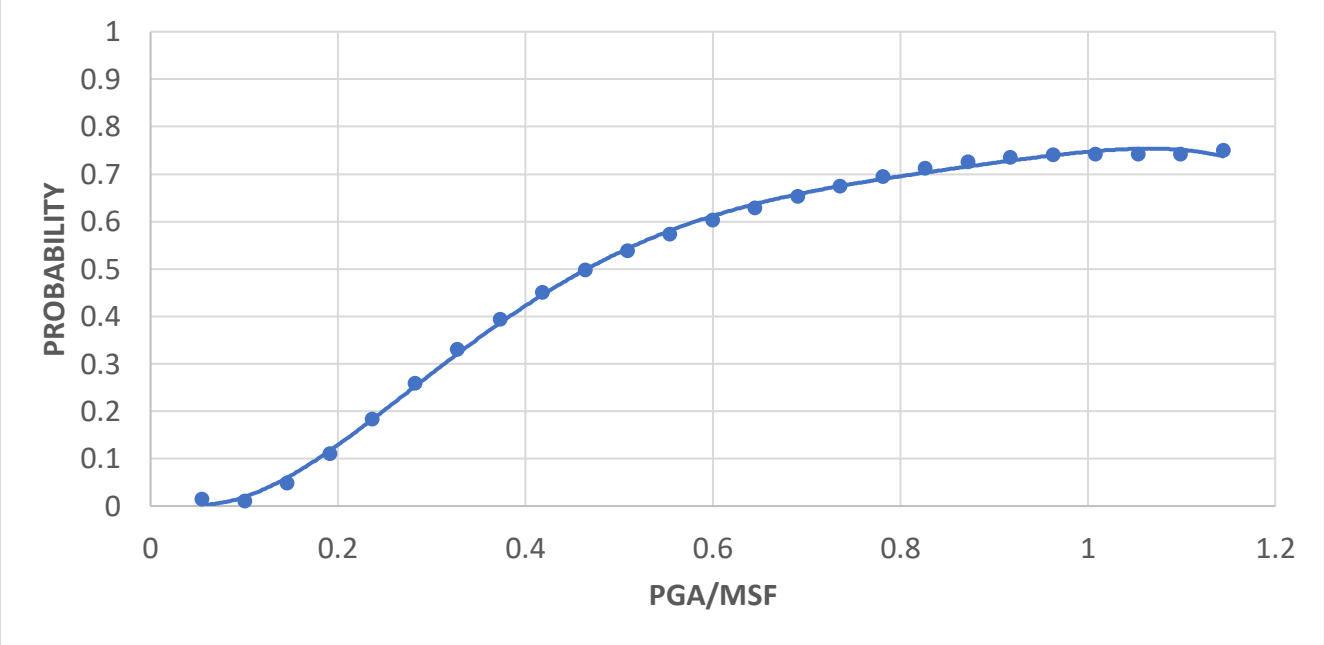

Figure C.28. SPT-based LPC for P[LPI>5] of the lowland part of Dyer County.

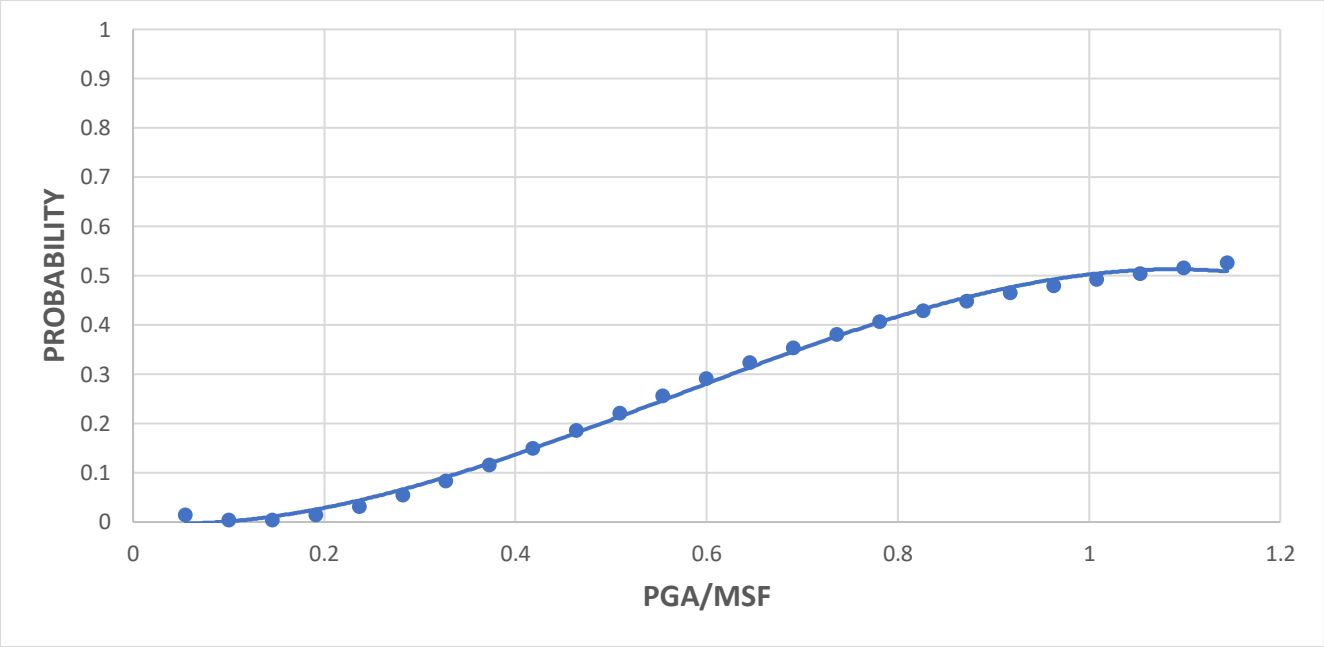

Figure C.29. SPT-based LPC for P[LPI>15] of the lowland part of Dyer County.

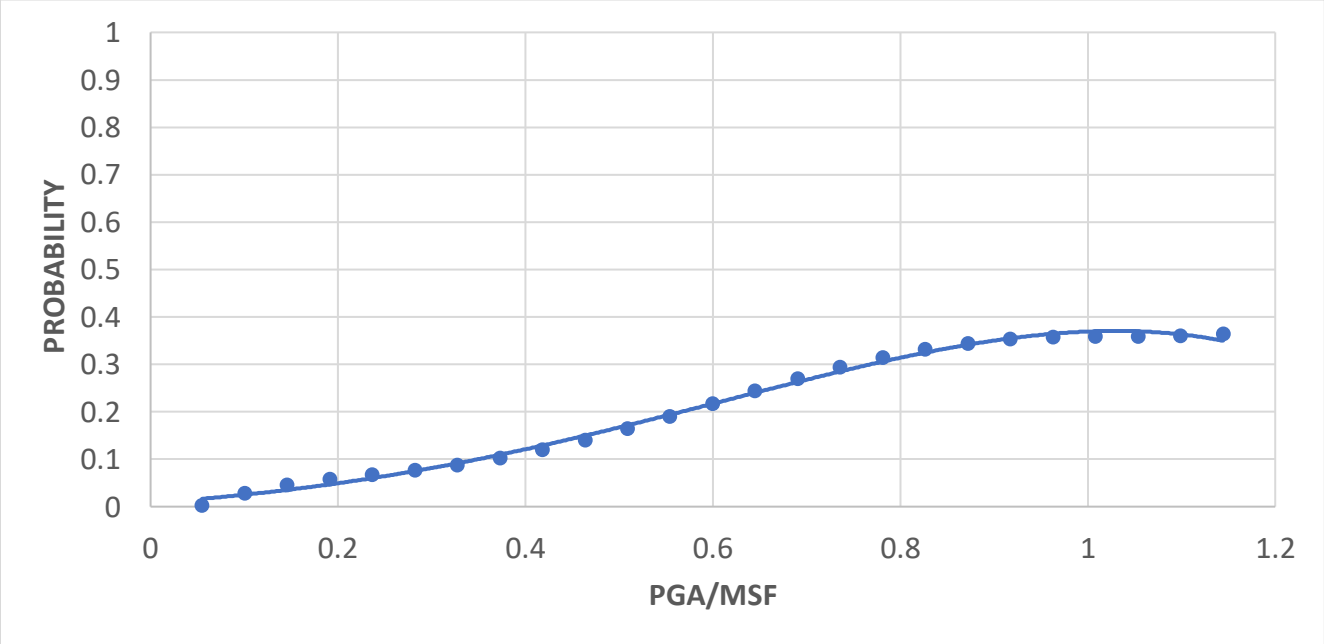

Figure C.30. LPC for P[LPI>5] of non-lowland part of Dyer County.

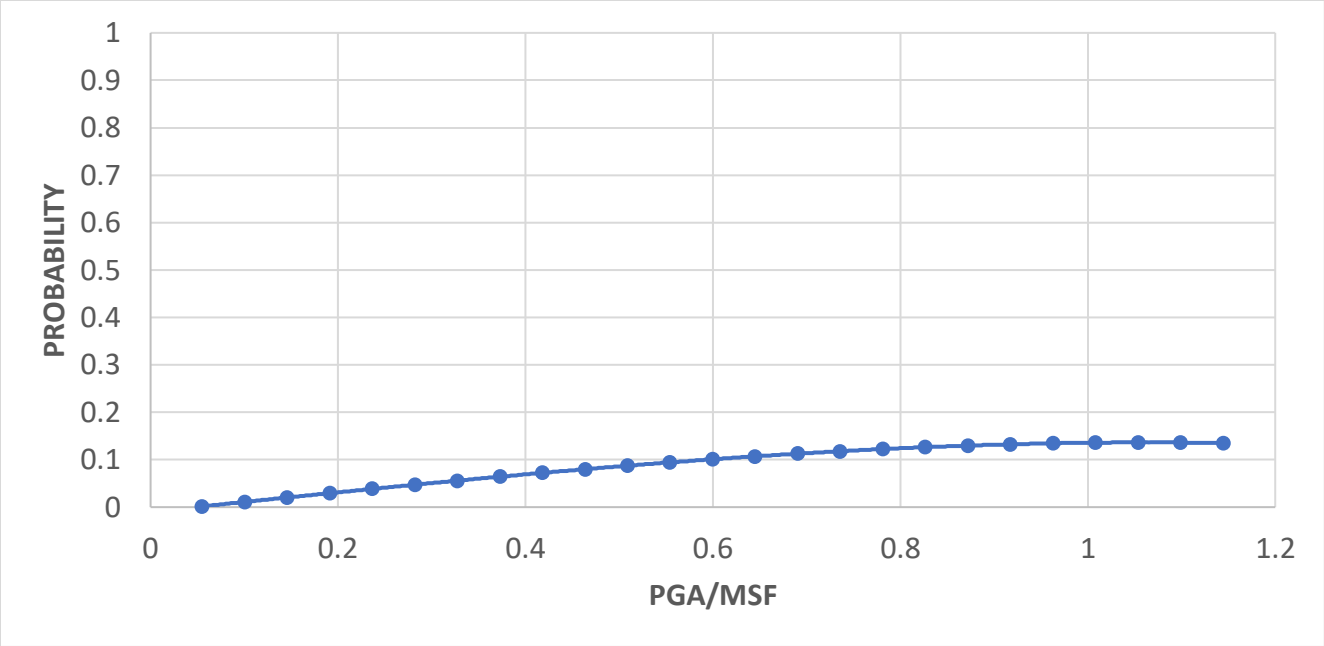

Figure C.31. LPC for P[LPI>15] of non-lowland part of Dyer County

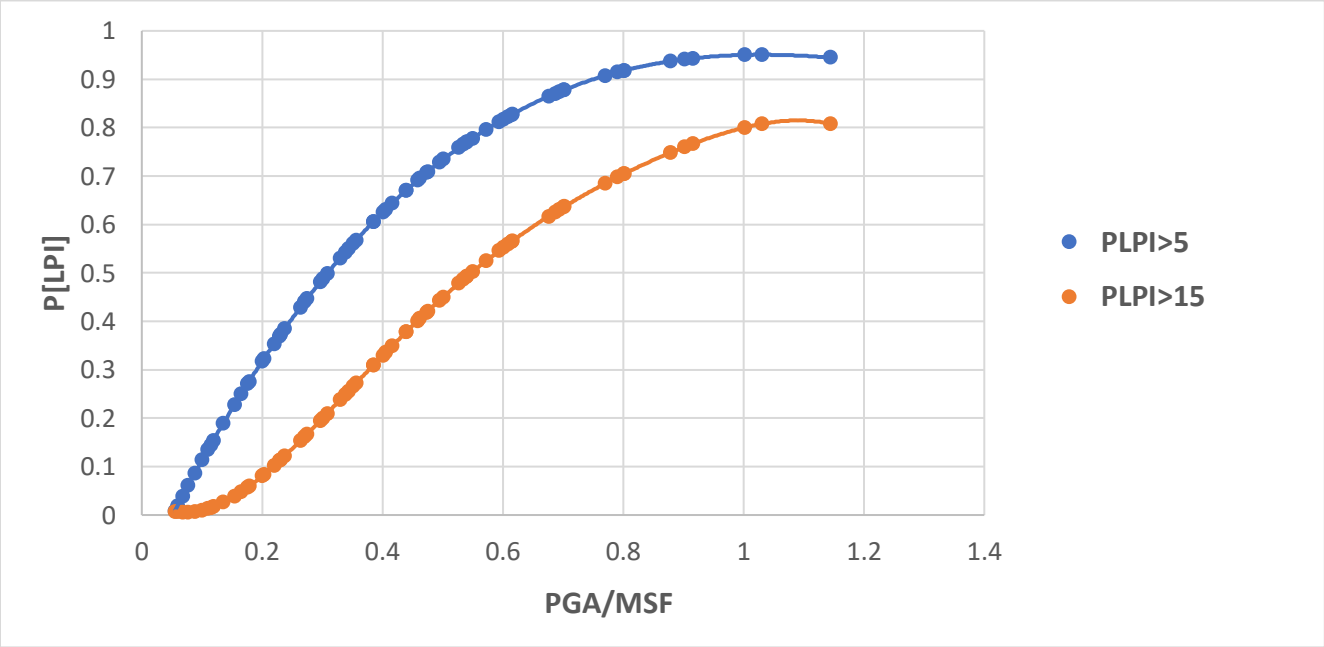

Figure C.32. LPI-based lowland LPCs from SPT data

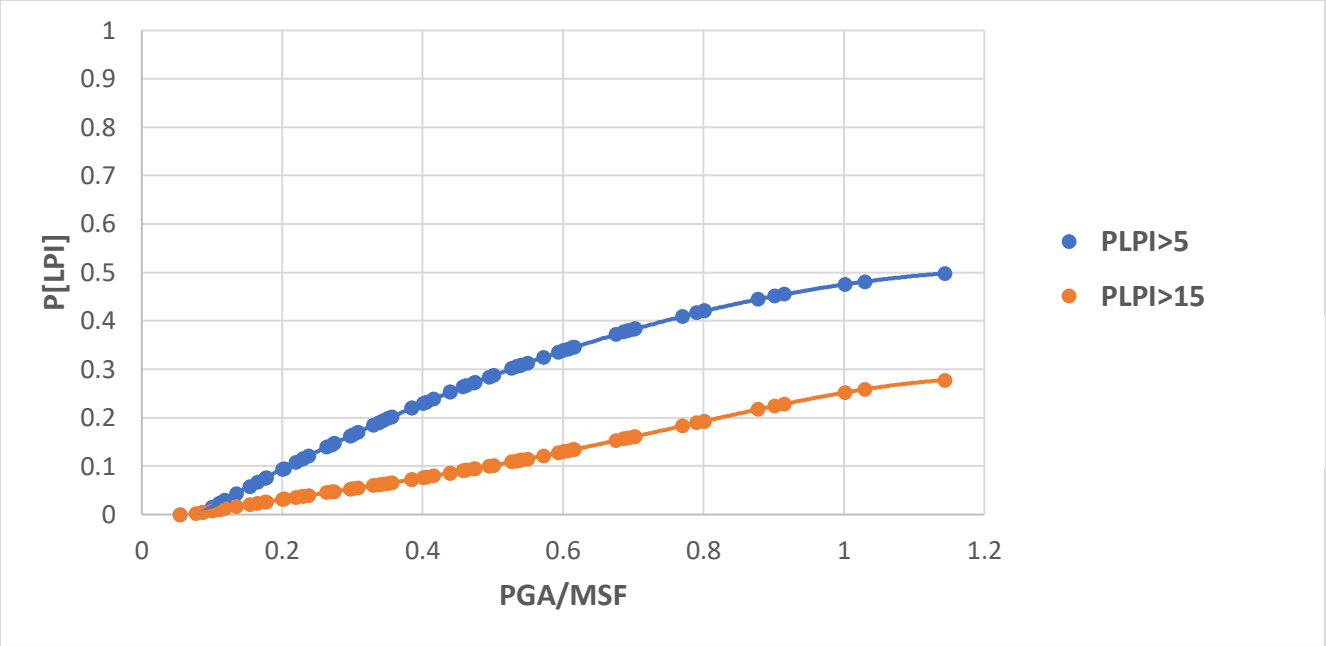

Figure C.33. LPI-based intermediate LPCs from SPT data

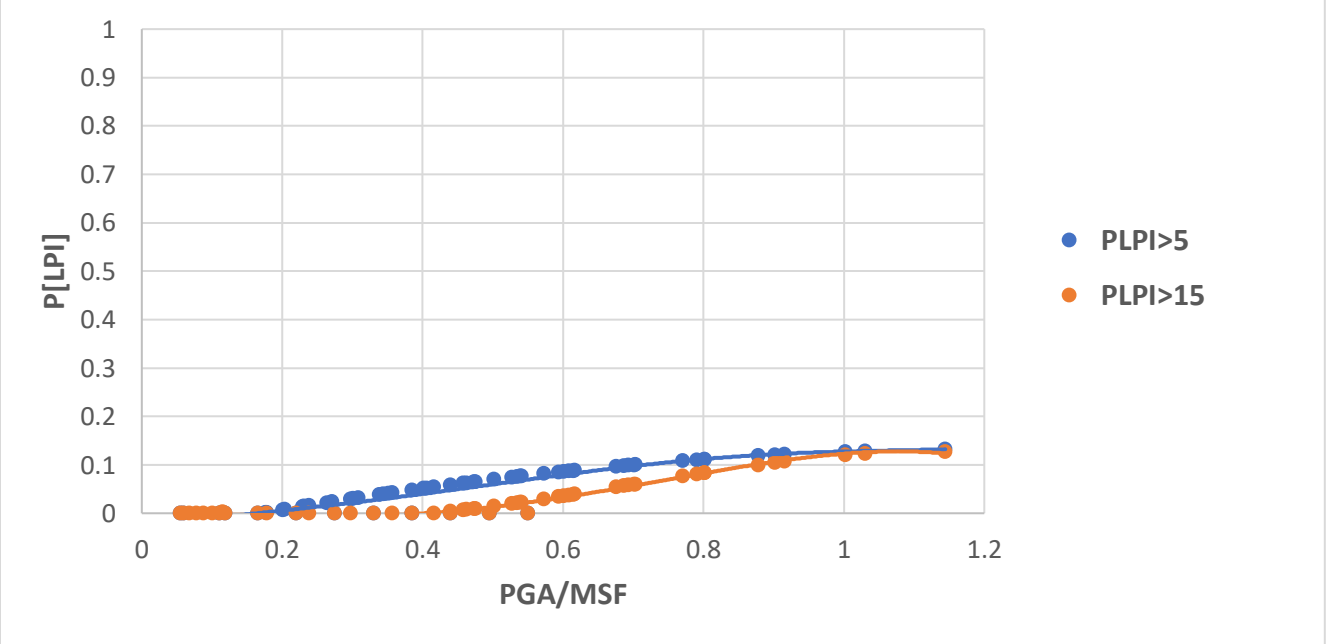

Figure C.34. LPI-based upland LPCs from SPT data

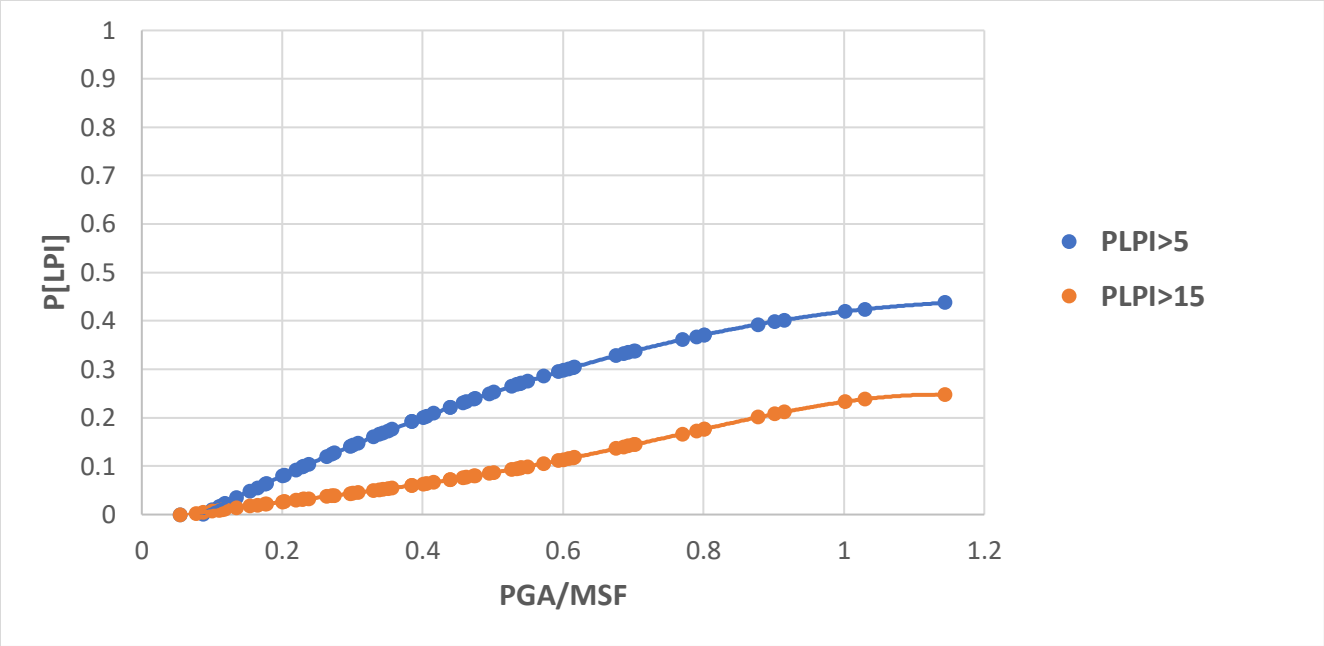

Figure C.35. LPI-based non-Lowland LPCs from SPT data

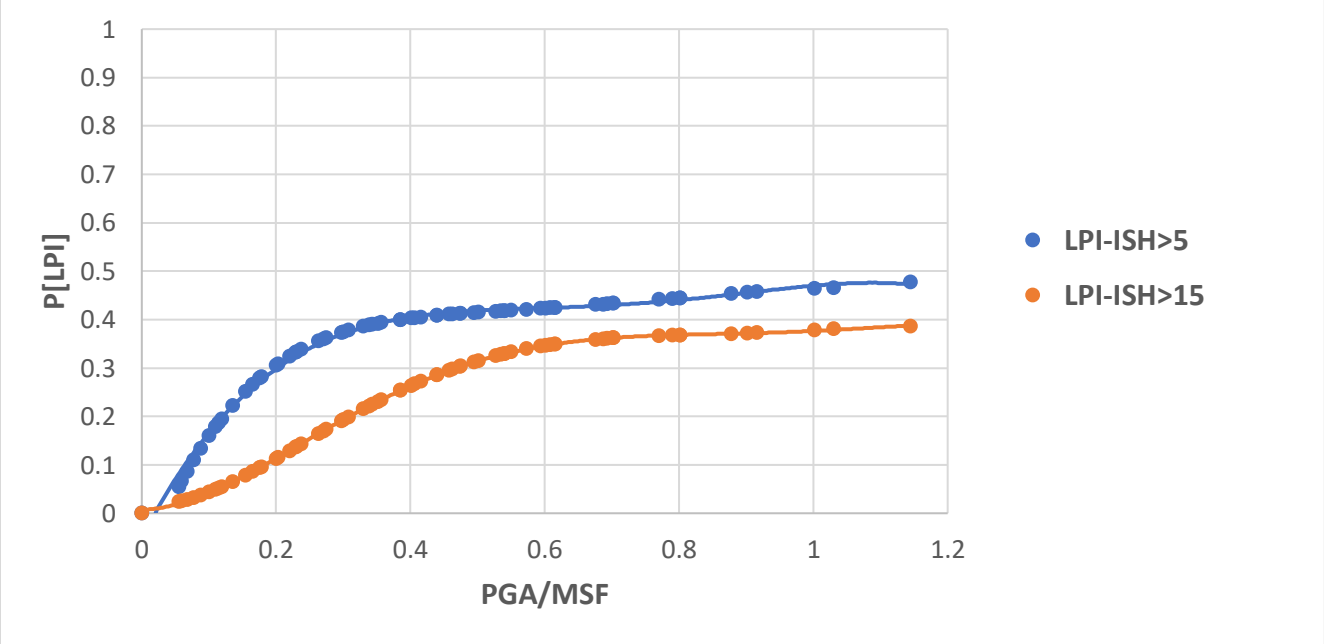

Figure C.36. LPI_{ISH} based LPCs of lowland from SPT data

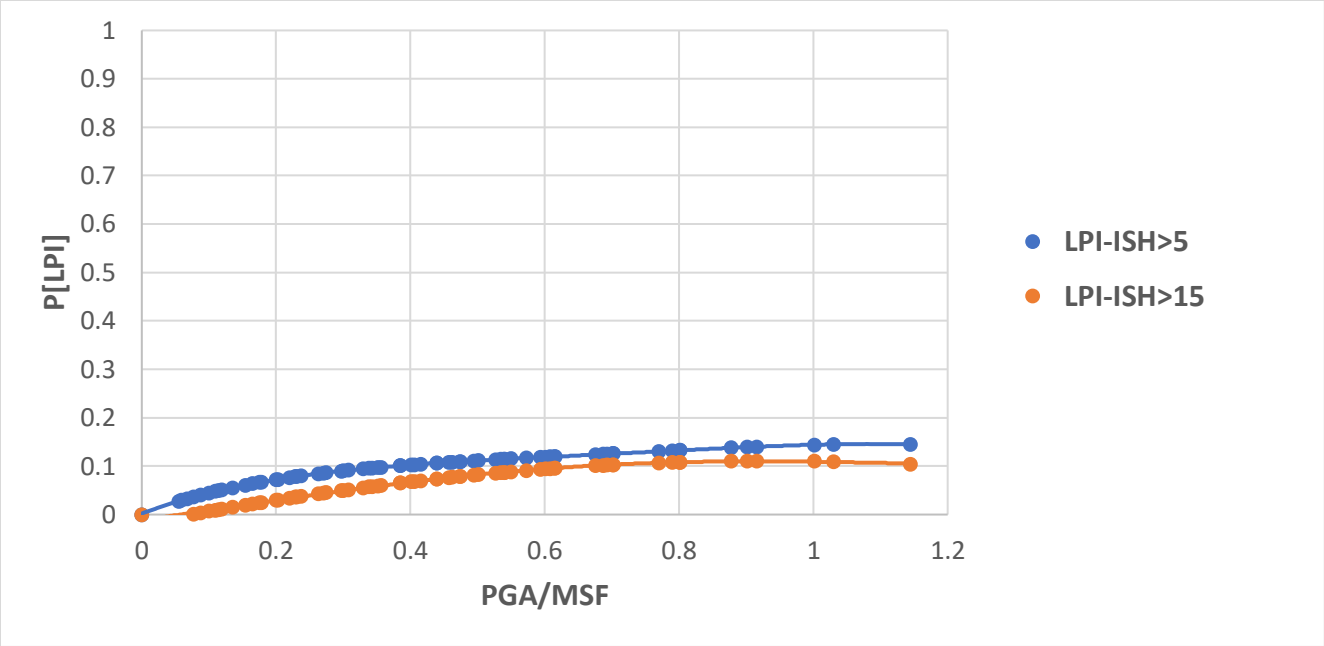

Figure C.37. LPI_{ISH} based LPCs of non-Lowland from SPT data

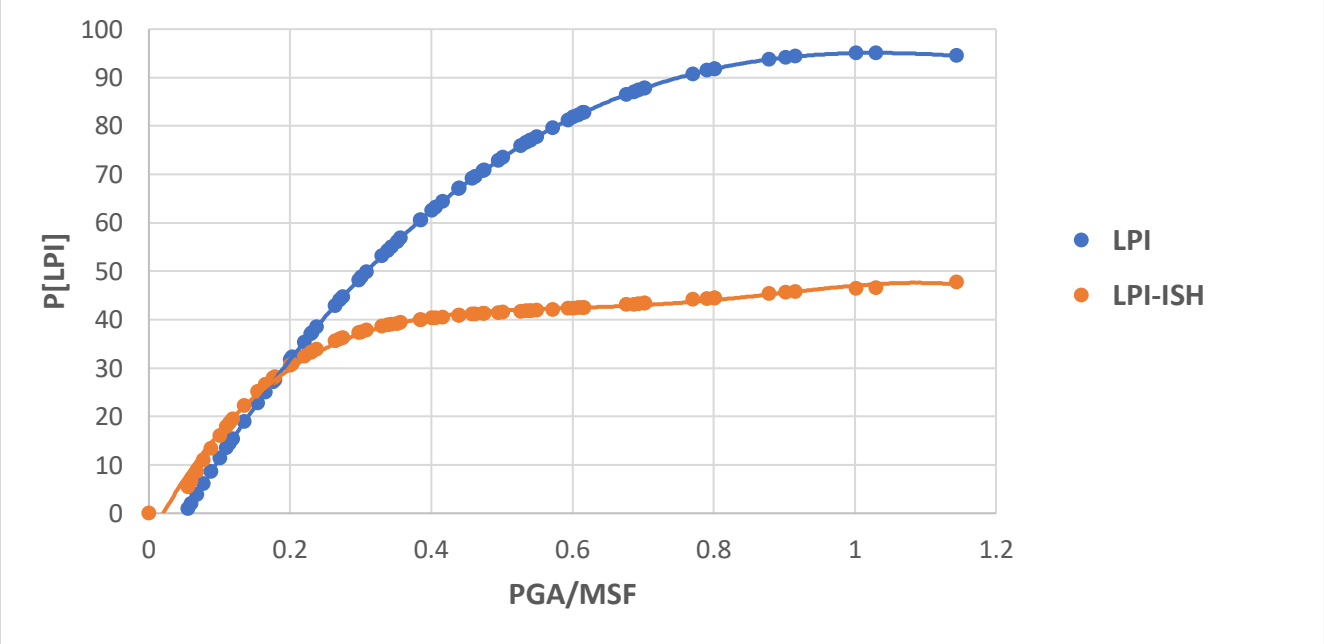

Figure C.38. LPI- and LPI_{ISH}-based lowland LPCs for P[LPI>5]

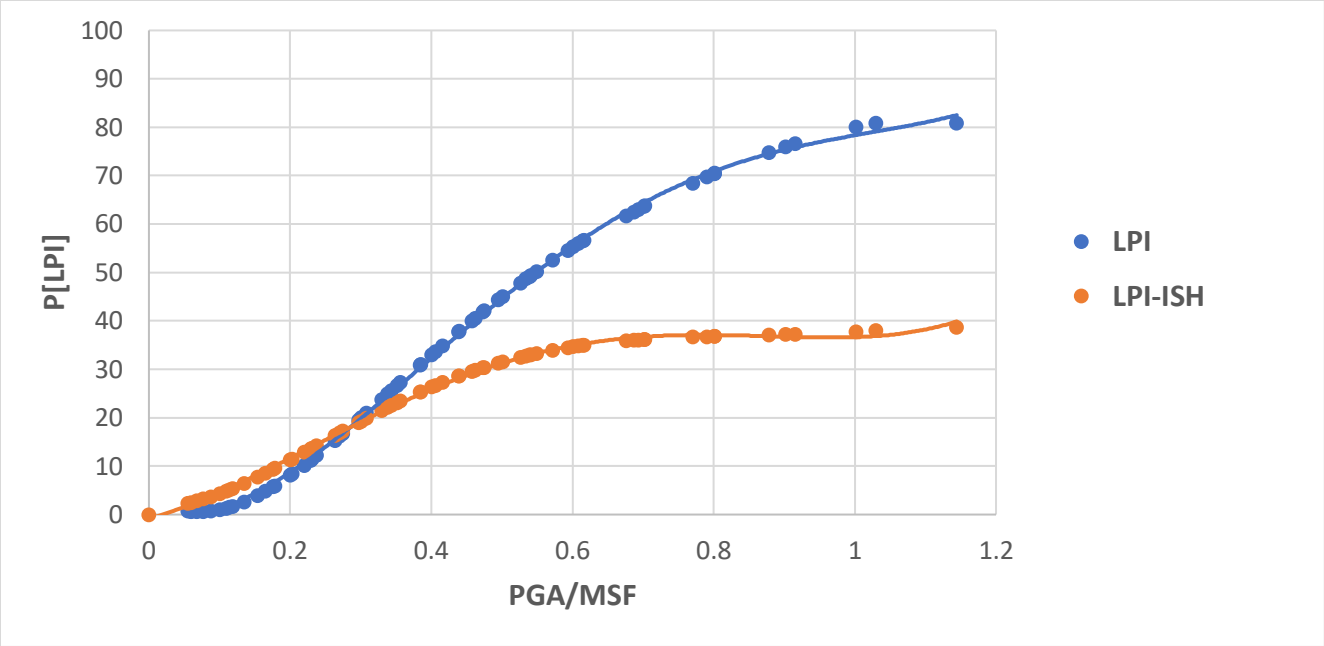

Figure C.39. LPI- and LPI_{ISH}-based lowland LPCs for P[LPI>15]

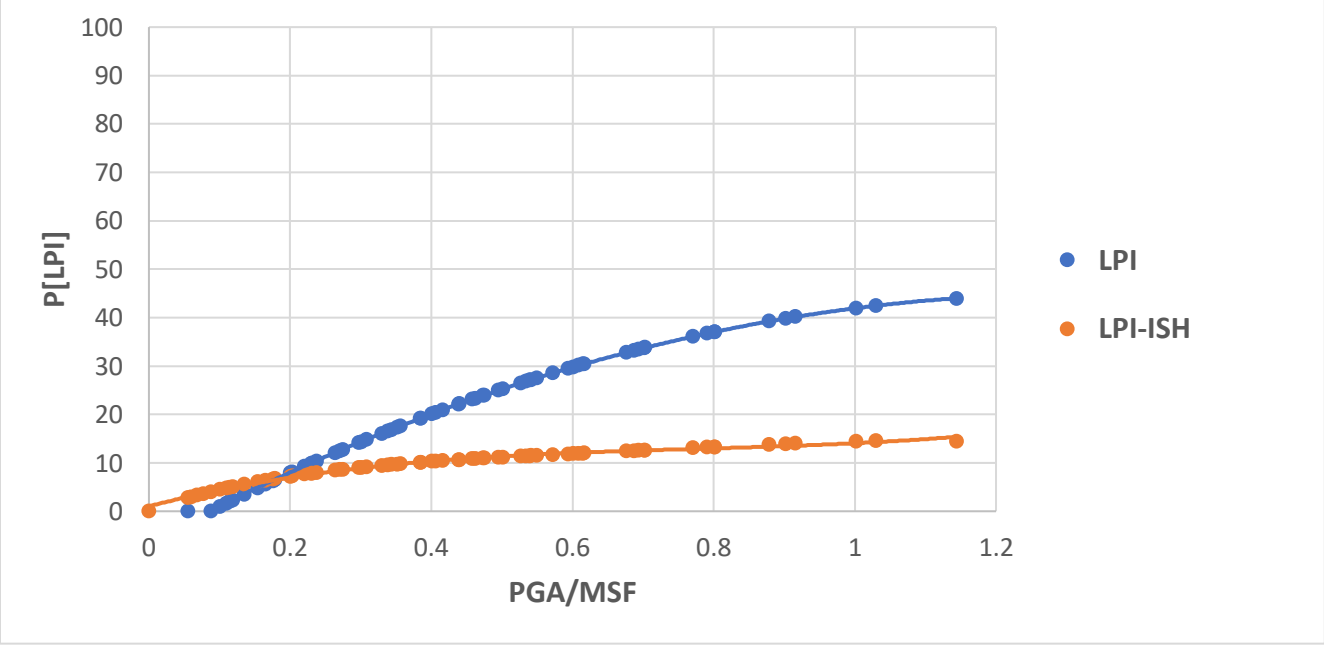

Figure C.40. LPI- and LPI_{ISH}-based non-lowland LPCs for P[LPI>5]

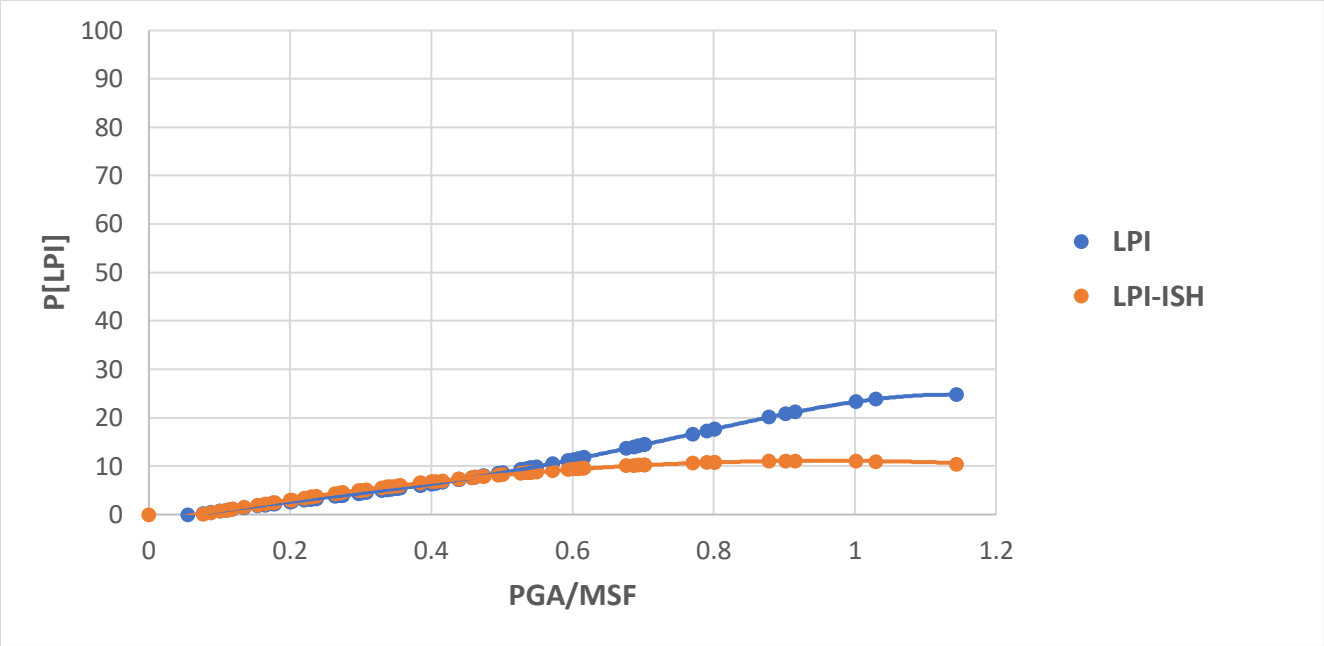

Figure C.41. LPI- and LPI_{ISH}-based non-lowland LPCs for P[LPI>15]

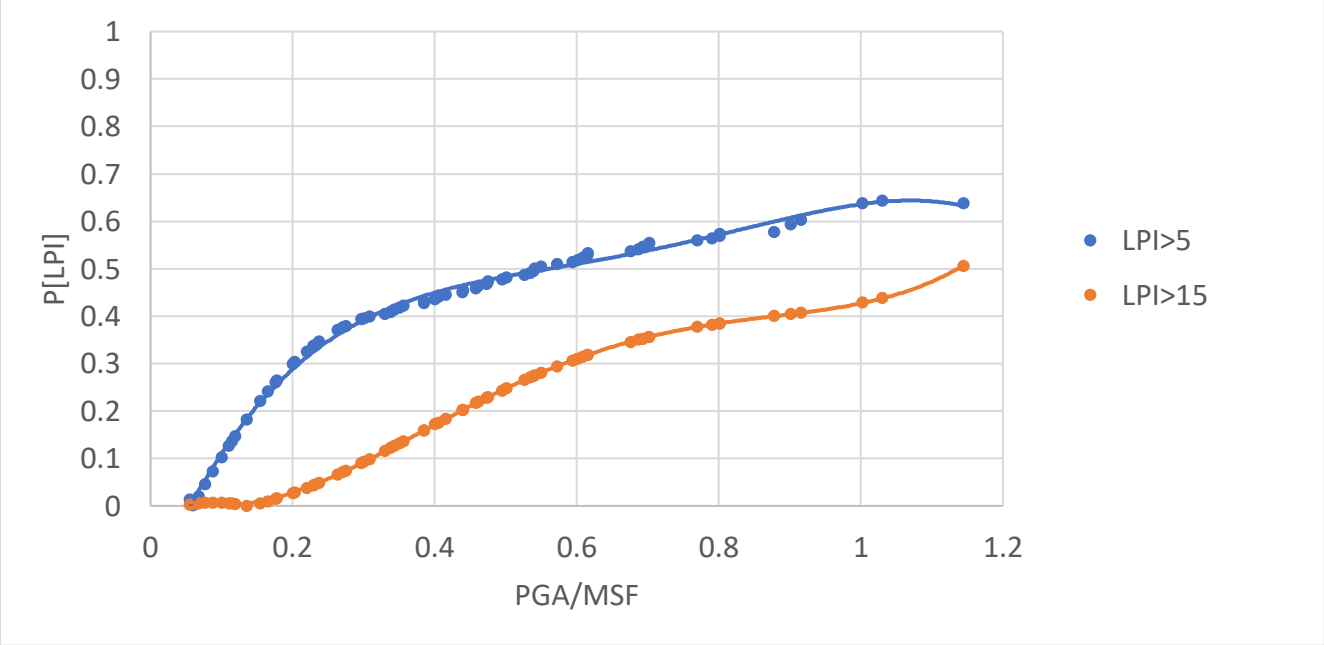

Figure C.42. LPI-based lowland LPCs from SPT data.

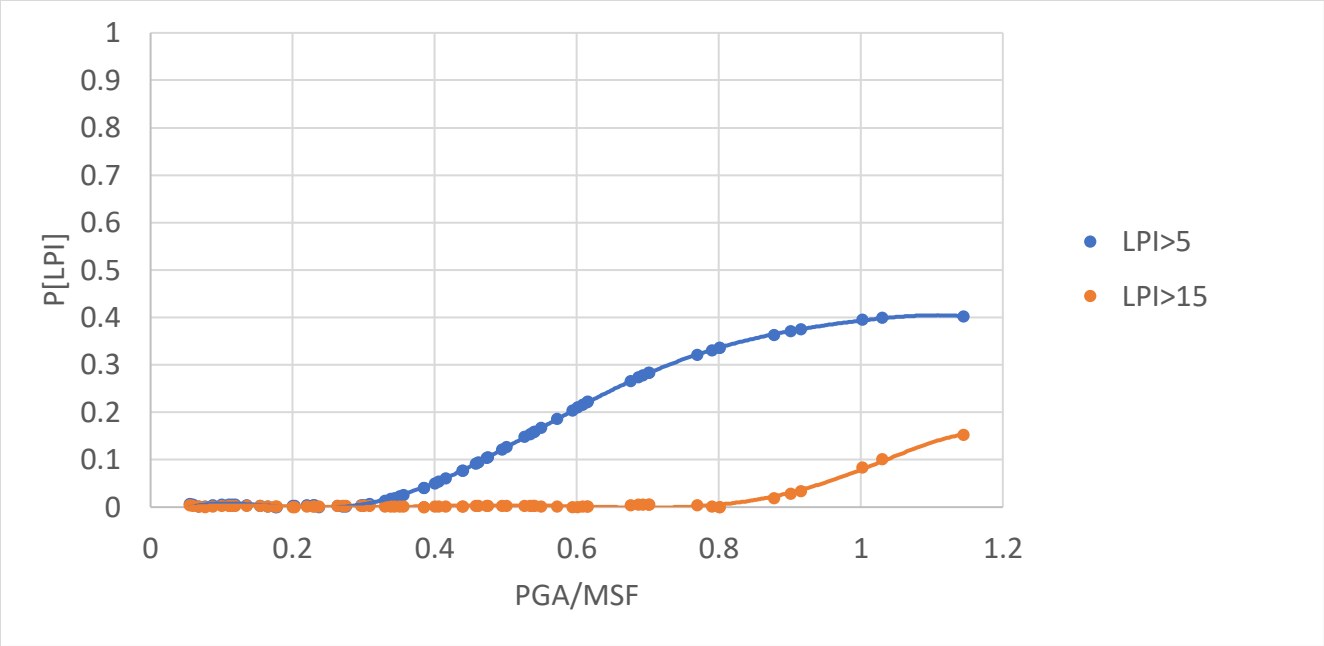

Figure C.43. LPI-based intermediate LPCs from SPT data.

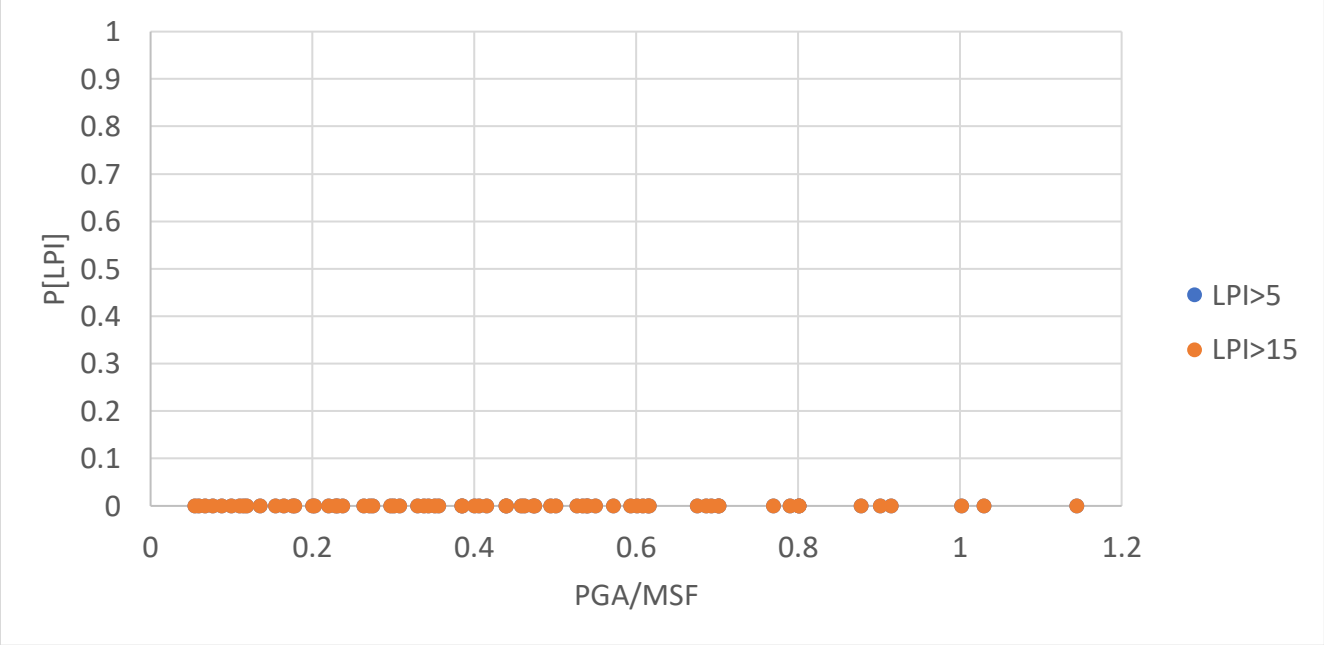

Figure C.44. LPI-based upland LPCs from SPT data.

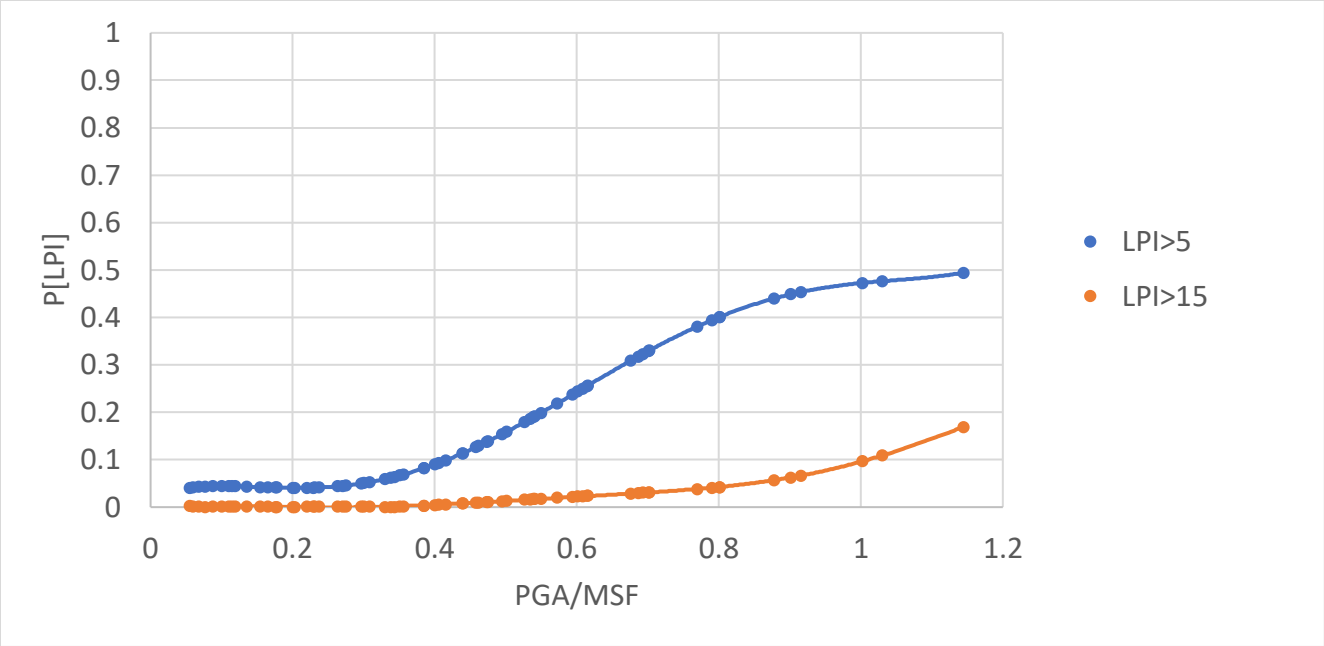

Figure C.45. LPI-based non-Lowland LPCs from SPT data.

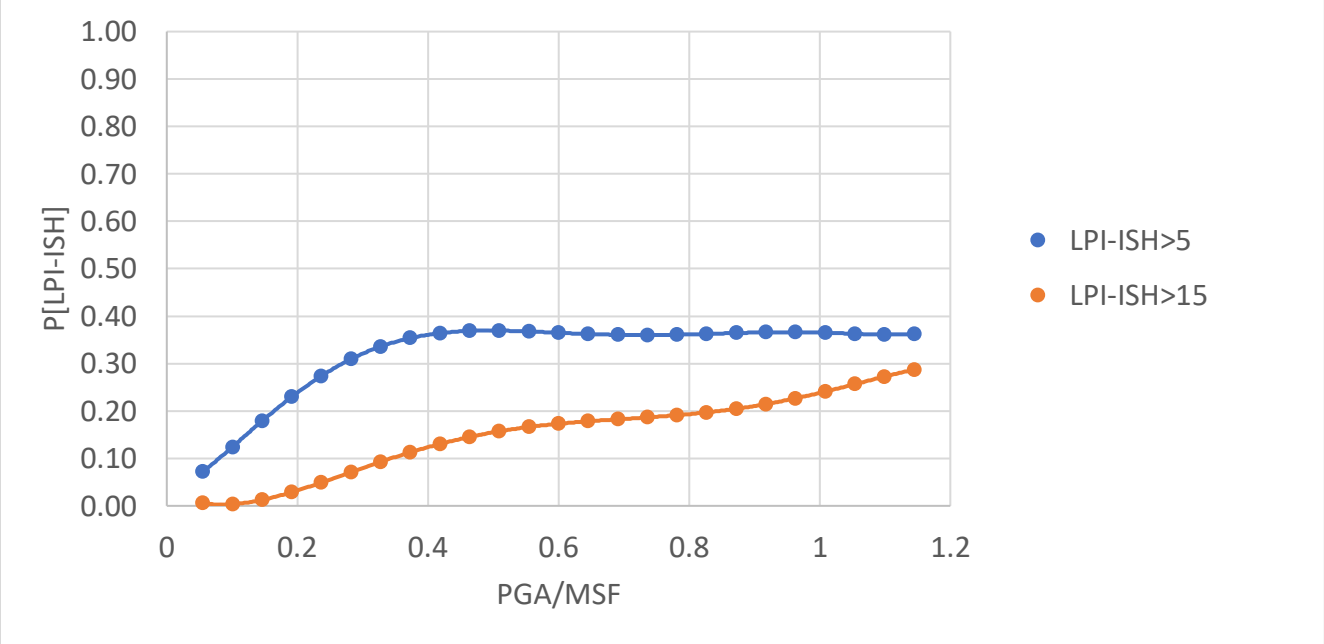

Figure C.46. LPI_{ISH} based LPCs of lowland from SPT data

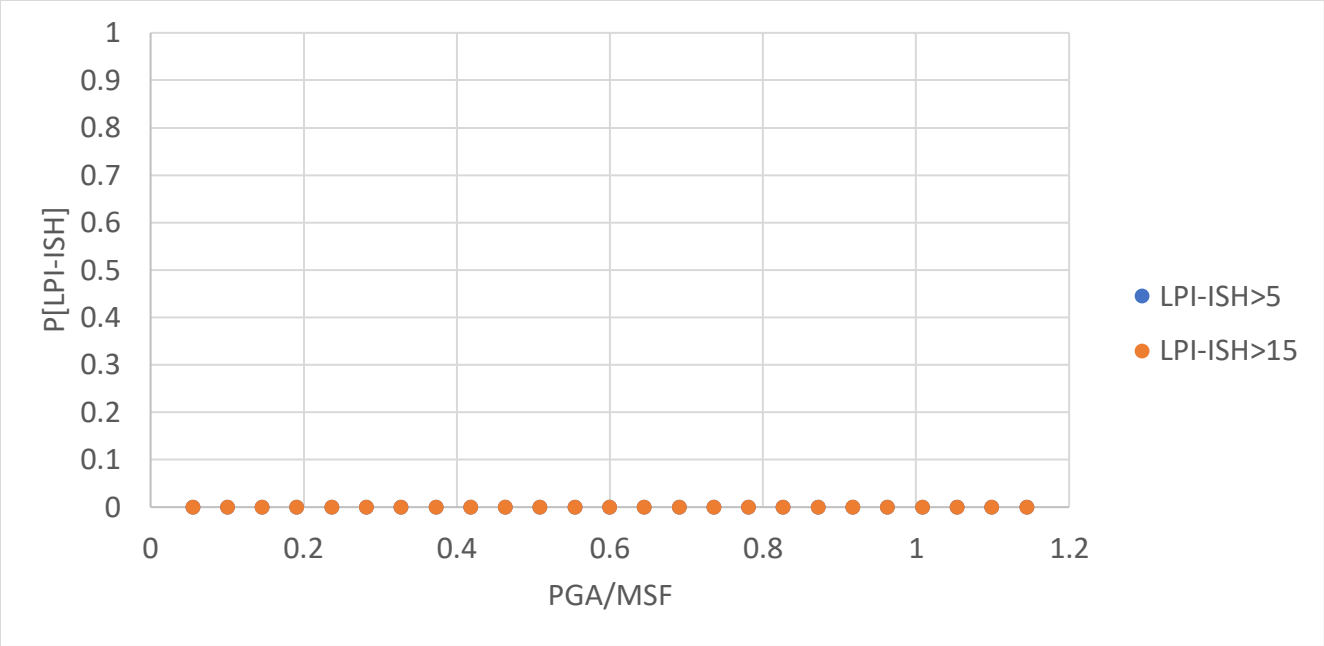

Figure C.47. LPI_{ISH} based LPCs of non-Lowland from SPT data.

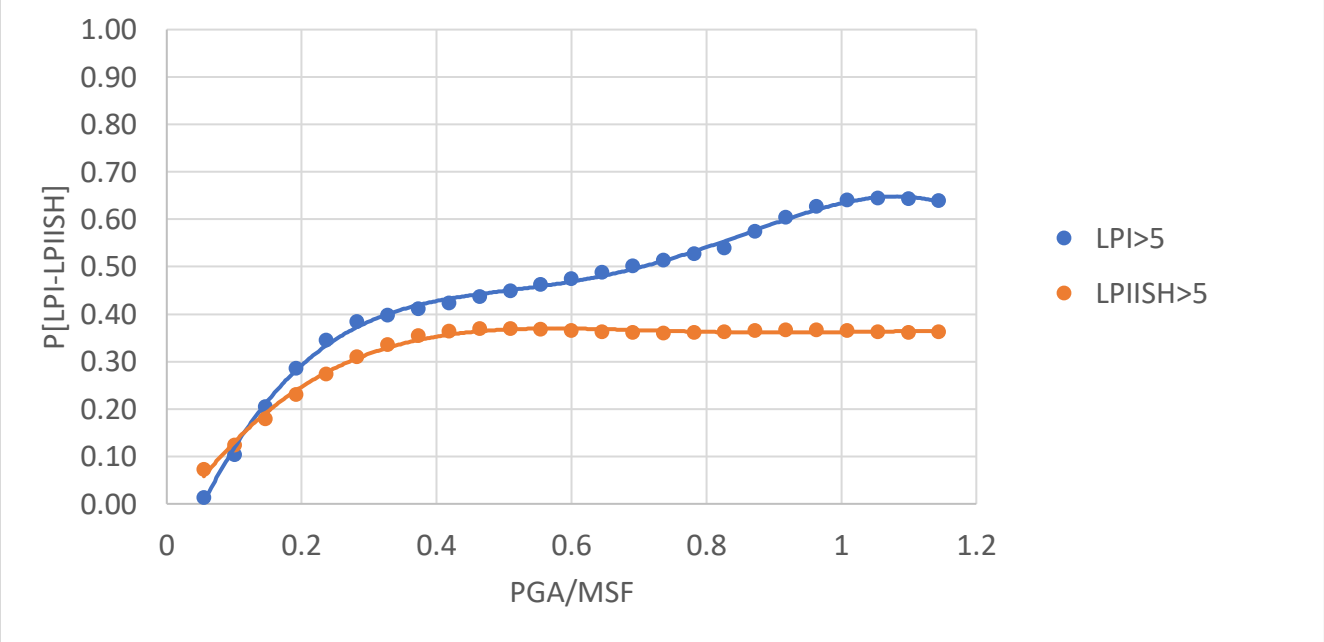

Figure C.48. LPI- and LPI_{ISH}-based lowland LPCs for P[LPI>5].

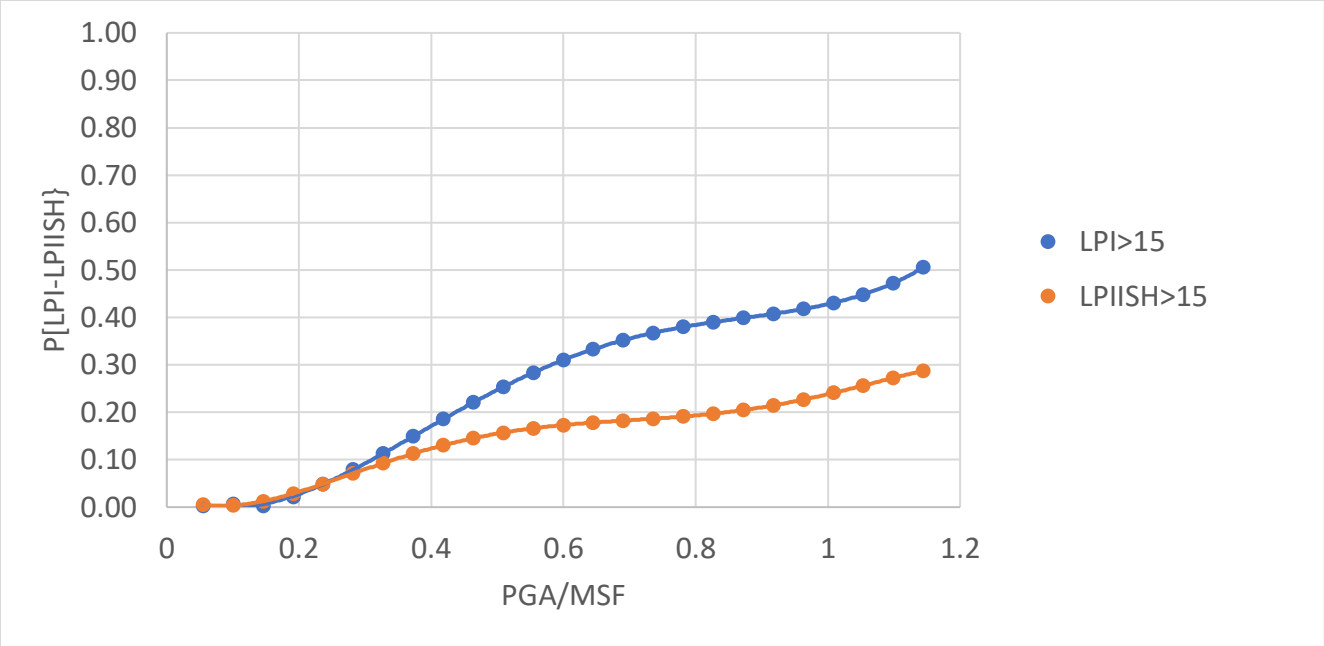

Figure C.49. LPI- and LPI_{ISH}-based lowland LPCs for P[LPI>15].

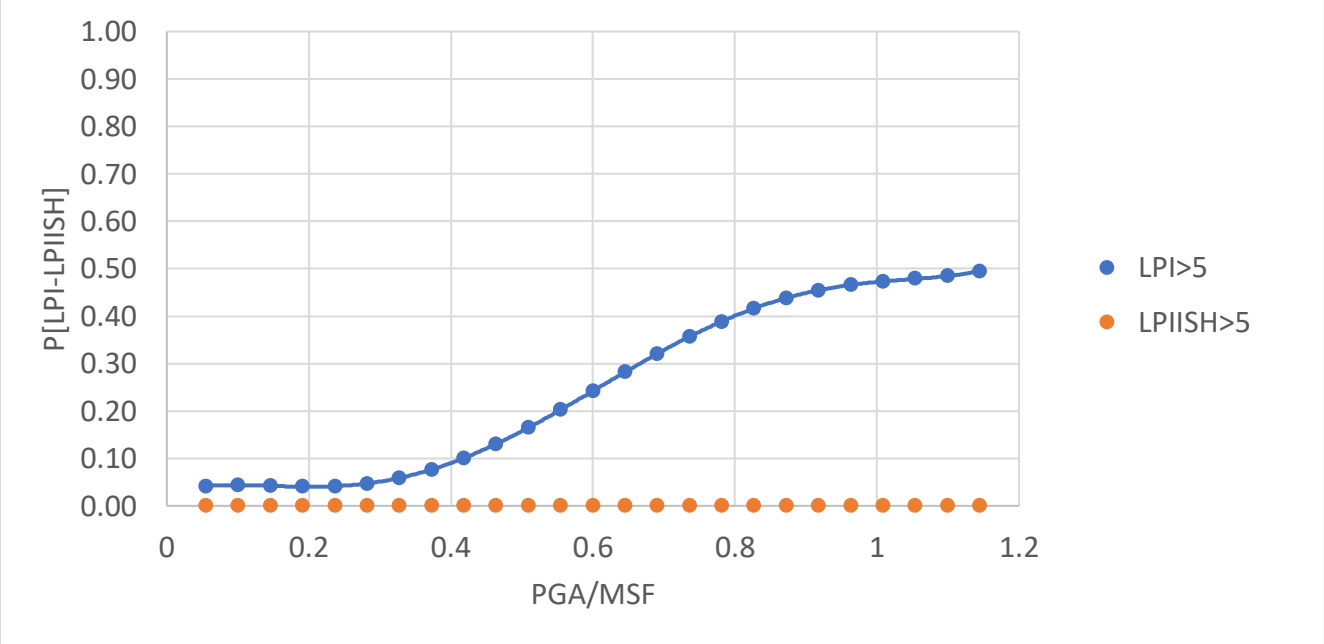

Figure C.50. LPI- and LPI_{ISH}-based non-lowland LPCs for P[LPI>5].

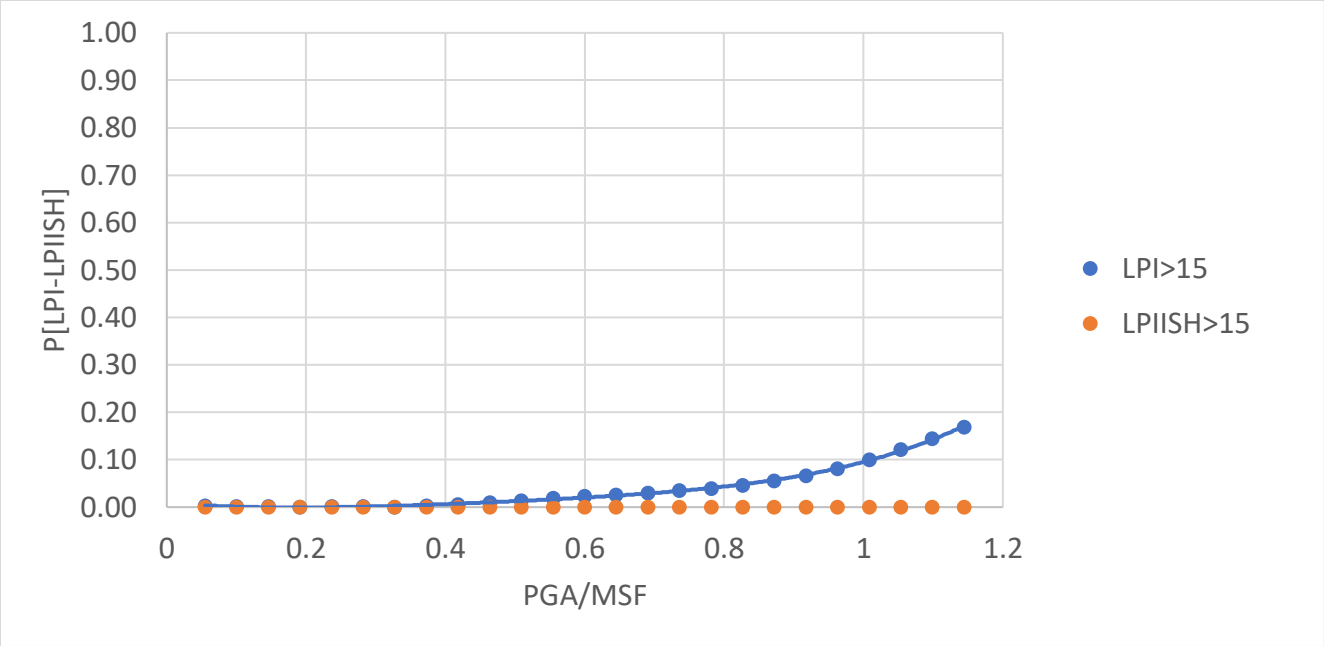

Figure C.51. LPI- and LPI_{ISH}-based non-lowland LPCs for P[LPI>15].

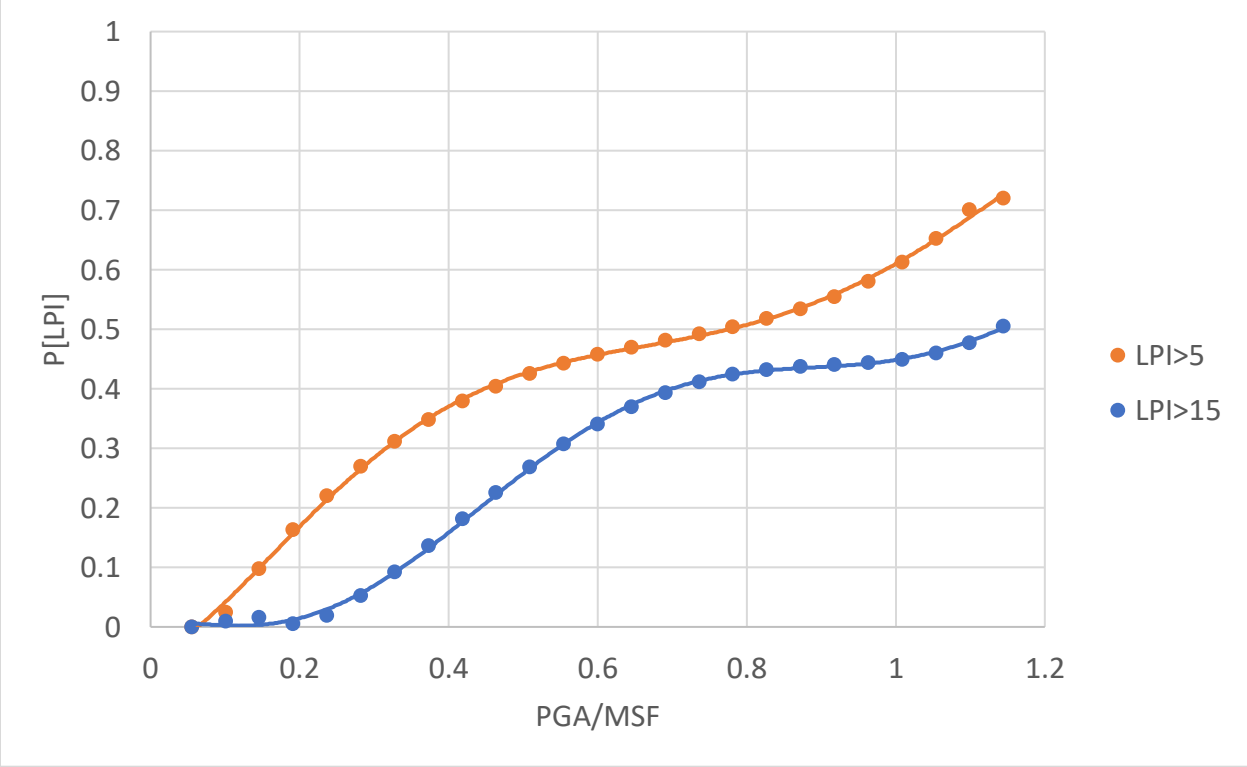

Figure C.52. LPI-based LPCs of floodplains from SPT data.

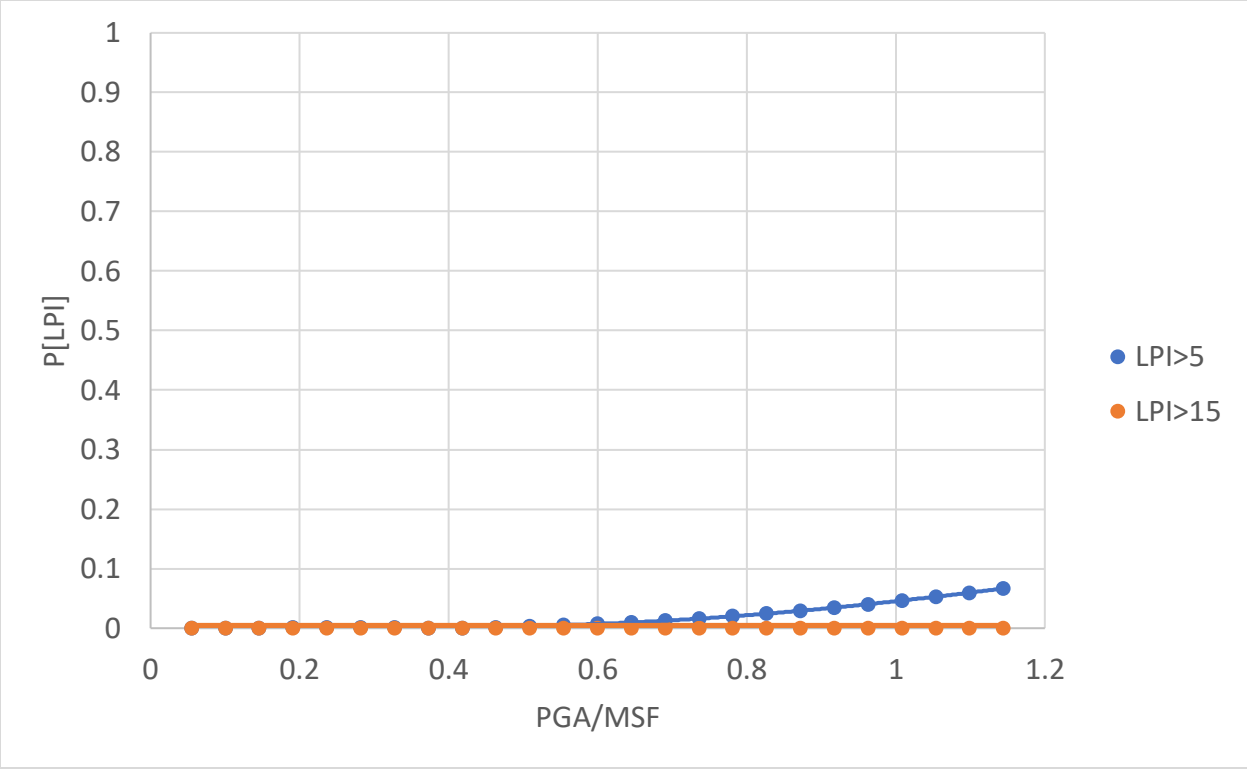

Figure C.53. LPI-based LPCs of non-floodplains from SPT data.

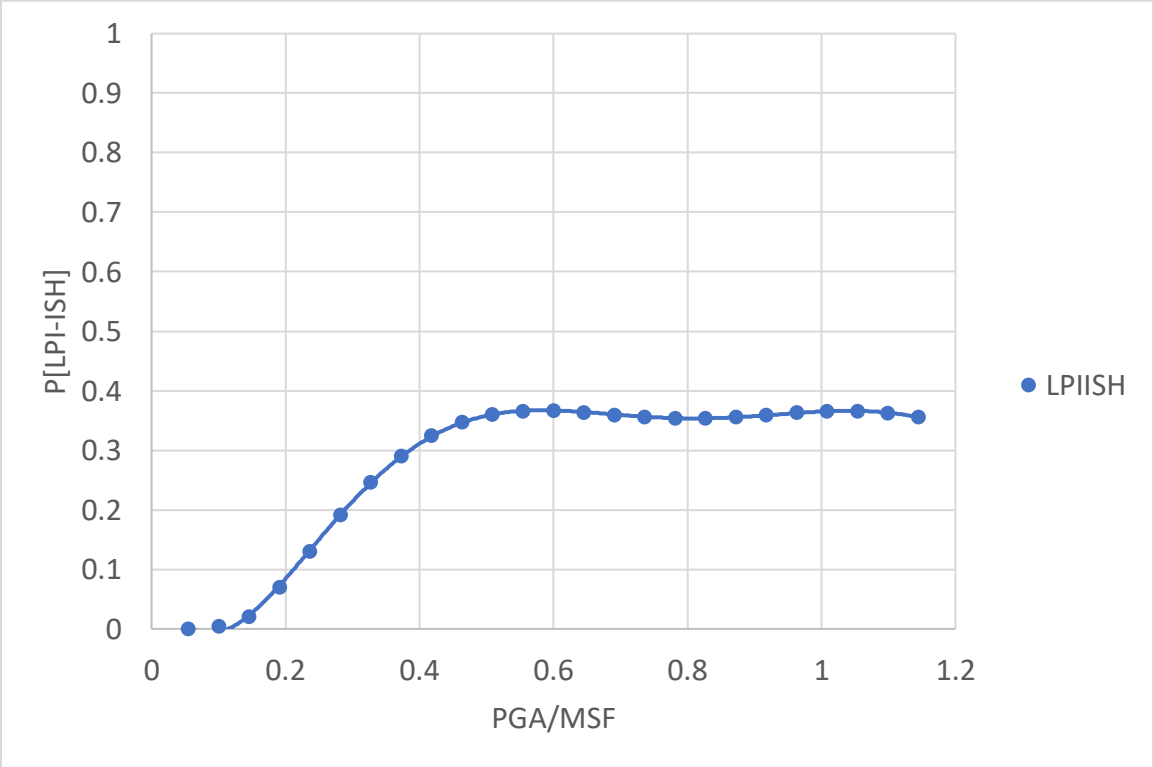

Figure C.54. LPI_{ISH} based LPCs of the floodplain from SPT data.

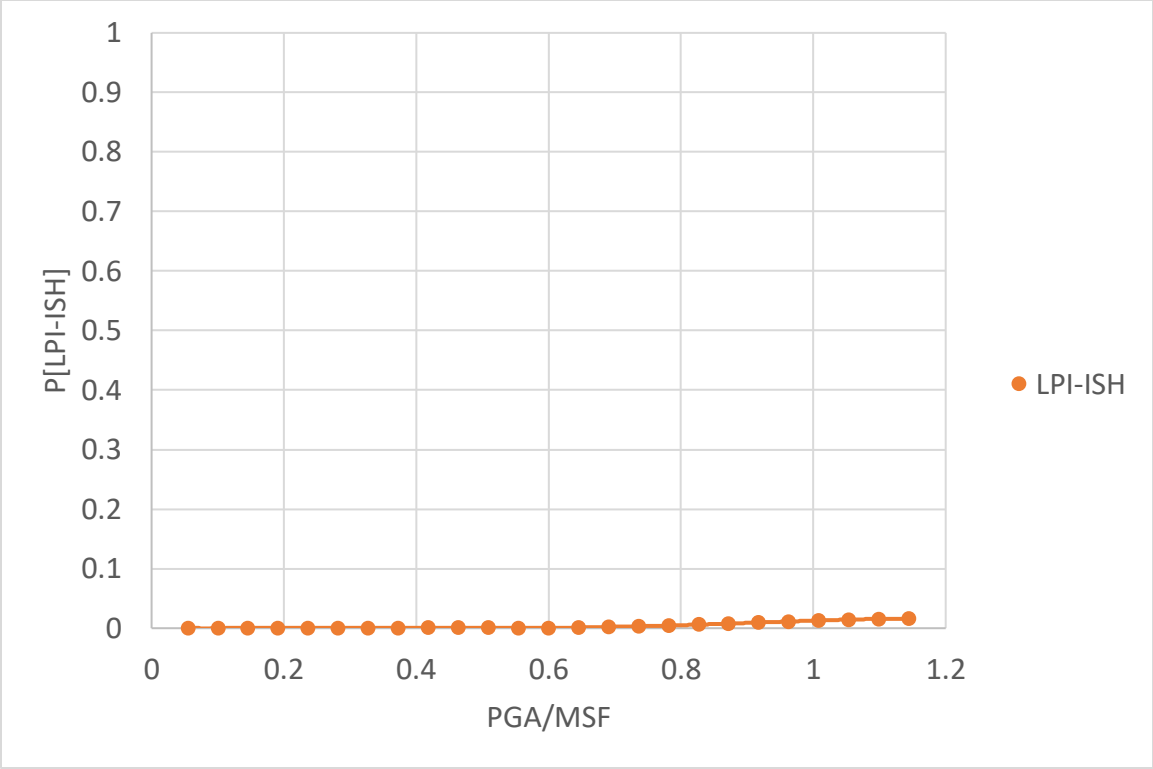

Figure C.55. LPI_{ISH} based LPCs of non-floodplain from SPT data.

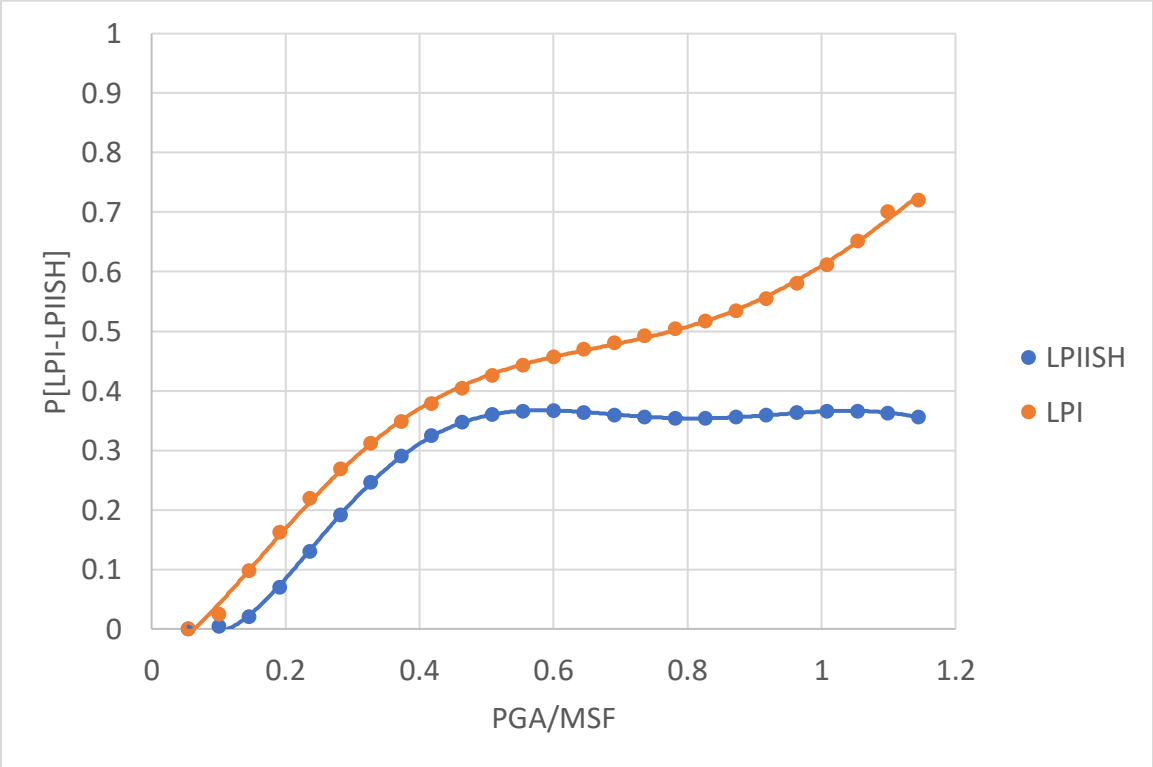

Figure C.56. LPI- and LPI_{ISH}-based floodplain LPCs for $P[LPI/LPI_{ISH}>5]$.

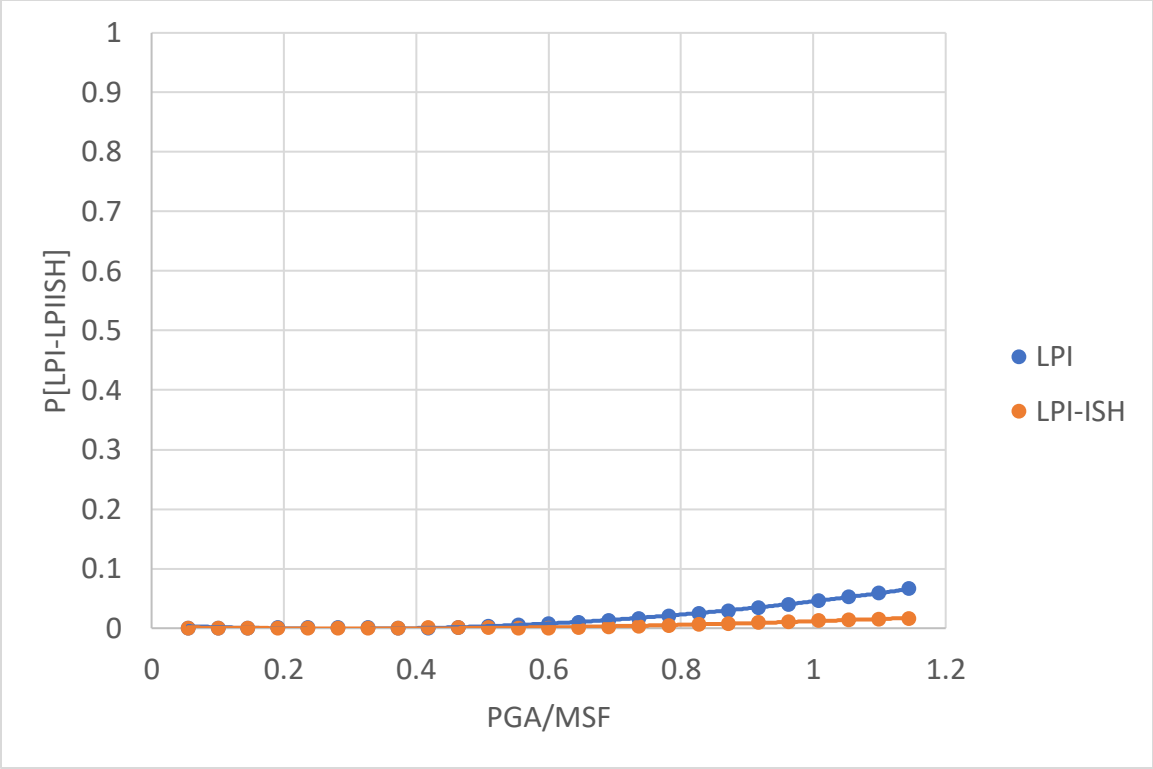

Figure C.57. LPI- and LPI_{ISH}-based non-floodplain LPCs for $P[LPI/LPI_{ISH}>5]$.